Computational Studies of the Effects of Pressure on Reaction Kinetics and Reaction Mechanisms

by

Jacob A. Spooner

B.Sc., University of the Fraser Valley, 2011

Thesis Submitted in Partial Fulfillment of the
Requirements for the Degree of
Doctor of Philosophy

in the
Department of Chemistry
Faculty of Science

SIMON FRASER UNIVERSITY

Fall 2017

Approval

Name: **Jacob A. Spooner**

Degree: **Doctor of Philosophy (Chemistry)**

Title: ***Computational Studies of the Effects of Pressure on Reaction Kinetics and Reaction Mechanisms***

Examining Committee: **Chair:** Dr. Hua-Zhong Yu
Professor

Dr. Michael H. Eikerling
Senior Supervisor
Professor

Dr. Charles J. Walsby
Supervisor
Associate Professor

Dr. Andrew J. Bennet
Supervisor
Professor

Dr. Noham Weinberg
Supervisor
Associate Faculty

Dr. Gary W. Leach
Internal Examiner
Associate Professor

Dr. Thomas W. Swaddle
External Examiner
Professor Emeritus
Chemistry
University of Calgary

Date Defended/Approved: October 10, 2017

Abstract

Both experiment and first principles calculations unequivocally indicate that properties of elements and their compounds undergo a tremendous transformation at ultra-high pressures due to the fact that the difference between intra- and intermolecular interactions disappears under such conditions. Yet, even at much milder pressures, when molecules still retain their individual identity, their chemical properties and reactivity change dramatically. We propose a set of techniques, based on molecular dynamics simulations and quantum mechanical calculations, which can aid in the understanding and prediction of the behavior of chemical systems over a wide range of high pressures.

Experimentally, the effects of pressure on reaction rates and equilibrium constants are described by their pressure derivatives, known as volumes of activation and reaction volumes respectively. These quantities are directly linked to partial molar volumes of reactants, transition states, and products. We formulate a molecular dynamics method for the accurate calculation of molecular volumes. This method can be applied to both stable and transient species, which makes it suitable for quantitative analysis of experimental volumes of activation and reaction volumes. The calculated partial molar volumes, as well as reaction and activation volumes obtained from them, agree well with experimental data. To assess the reliability of the experimental activation and reaction volumes, we also present an analysis of the most common empirical analytical functions used to obtain them from pressure dependences of the rate and equilibrium constants.

Since mechanisms of chemical reactions are often described in terms of properties of their potential energy surfaces (PES) or Gibbs energy surfaces (GES), we present an analysis of pressure-induced deformations of GES of solvated reaction systems and use quantum mechanical and molecular dynamics simulations to construct energy surfaces and reaction profiles of compressed species, and to analyze how their shapes and topography change in response to compression. We also discuss the important role of volume profiles in assessing pressure-induced deformations of GES.

Keywords: high pressure effects; molecular volume; activation volume; reaction volume; volume profile; energy surface.

Acknowledgements

It is my pleasure to thank my supervisor, Dr. Noham Weinberg, for everything that he has given me throughout my time as a researcher in his lab. My experience working with Noham has been extremely fulfilling, and all the knowledge and skills I have gained from this time are the result of his expert and thoughtful guidance. I will be forever grateful for the immense effort and countless hours that he has dedicated to ensuring my success in my graduate studies.

I would like to thank my supervisory committee members, Dr. Michael Eikerling, Dr. Charles Walsby, and Dr. Andrew Bennet for their valuable suggestions and advice throughout these years. I extend my thanks to Dr. Gary Leach and Dr. Thomas Swaddle for being my internal and external examiners of this thesis. I would also like to express my gratitude to the past and present members of Dr. Weinberg's research group for their valuable friendship and support.

Outside of the university, I would also like to acknowledge the support of my friends and family, especially my parents for all their help and encouragement. Having a very cheap but very comfortable place to live throughout my studies was a huge help, so for that, and also for the many valuable conversations we have had over the years, I must thank Dr. Wes Neumeier. Finally, and most importantly, I thank my partner Christine for her love and support which were crucial during the writing of this thesis.

Table of Contents

List of Tables

List of Figures

List of Abbreviations

Abbreviation	Definition
B3LYP	Becke, 3-Parameter, Lee-Yang-Parr
BEBO	Bond energy bond order
GES	Gibbs energy surface
HF	Hartree-Fock
LJ	Lennard-Jones
MC	Monte Carlo
MD	Molecular dynamics
OPLS	Optimized potential for liquid simulations
PBE	Perdew–Burke-Ernzerhof
PES	Potential energy surface
PME	Particle mesh ewald
QM	Quantum mechanics
QSAR	Quantitative structure-activity relationships
SPC	Simple point charge
TIP4P	4-Site (4-Point) transferable interaction potential
TS	Transition state
TST	Transition state theory

List of Symbols

Symbol	Definition
$\Delta V_{\infty}^{\neq}$	Activation volume at infinite pressure
$\Delta \xi_{0}^{\neq}$	Hypercompressibility coefficient of activation
$\Delta V_{solv}^{\neq}$	Solvation contribution to activation volume
$\Delta V^{\neq}$	Activation volume
$\Delta \beta^{\neq}$	Compressibility coefficient of activation
d_{ab}	Mean of relative differences
$\Delta L^{\neq}$	Length change of activation
$\Delta G_{IR,}{}^{\neq}$, $\Delta G_{SR}{}^{\neq}$, $\Delta G_{COUL}{}^{\neq}$, $\Delta G_{DH}{}^{\neq}$	Contributions to $\Delta G^{\neq}$ of electron transfer due to internal rearrangement, solvent rearrangement, coulombic interaction, and ionic strength
$\Delta G^{\neq}$	Gibbs energy of activation
ΔV	Reaction volume
$\Delta V^{\neq}{}_{\text{struc}}$	Structural contribution to activation volume
$\Delta V_{IR,}{}^{\neq}$, $\Delta V_{SR}{}^{\neq}$, $\Delta V_{COUL}{}^{\neq}$, $\Delta V_{DH}{}^{\neq}$	Contributions to $\Delta V^{\neq}$ of electron transfer due to internal rearrangement, solvent rearrangement, coulombic interaction, and ionic strength
ε_{ij}	LJ interaction parameter
E_a	Activation energy
ε_0	Vacuum permittivity
F	Force
G	Gibbs energy
H	Enthalpy
K	Equilibrium constant
k	Rate constant
k_b	Stretching force constant
K_{ow}	Octanol-water partition coefficient
k_θ	Bending force constant
$\kappa(P)$	Ideal rate constant

$L(x)$	System length
$L^{\neq}$	Length of TS
L_R	Length of reactant
m	Mass
N	Number of particles
N_{conf}	Number of conformations
n_x	Number of moles of the solute
η	Packing coefficient
P	Pressure
$\Phi(P)$	El'yanov-Gonikberg function
q_i	Charge
r	Probe sphere radius
R	Gas constant
R_{C}	Carbon van der Waals radius
R_{H}	Hydrogen van der Waals radius
ρ	Isodensity cut off value
σ_{ij}	LJ interaction parameter
s_d	Standard deviation of relative differences
$S_{no,}$ $S_{nw,}$	Hydrophobic surface area in octanol and water
S_{po}, S_{pw}	Hydrophilic surface area in octanol and water
σ	Cross sectional area
T	Temperature
t	Time
τ	Paired t-statistic
U	Potential energy
U^{inter}	Intermolecular potential energy
U^{intra}	Intramolecular potential energy
V	Volume
V_{exp}	Experimental volume
V_n	Dihedral force constant
V_P	Volume of product

V_R	Volume of reactant
V_{SE}	Solvent excluded volume
V_W	Van der Waals volume
x_{octane}	Mole fraction of octane
z	Random number drawn from normal distribution

Preface

The contents of this thesis represent a collection of works with the overarching goal of developing computational methodologies for the study of the effects of high pressure on chemical reactions. Major parts of this thesis have been published or submitted for publication and are presented here as revised versions of these publications as follows:

Chapter 2: J. Spooner, H. Wiebe, N. Boon, E. Deglint, E. Edwards, B. Yanciw, B. Patton, L. Thiele, P. Dance and N. Weinberg, "Molecular dynamics calculation of molecular volumes and volumes of activation" *Physical Chemistry Chemical Physics*, 2012, **14**, 2264; H. Wiebe, J. Spooner, N. Boon, E. Deglint, E. Edwards, P. Dance, N. Weinberg, "Calculation of molecular volumes and volumes of activation using molecular dynamics simulations" *Journal of Physical Chemistry C*, 2012, **116**, 2240; P. Ebrahimi, J. Spooner,N. Weinberg, E. Plettner, *Chemosphere*, 2013, **93**, 54.

Chapter 3: J. Spooner, H. Wiebe, M. Louwerse, B. Reader and N. Weinberg, "Theoretical analysis of high pressure effects on conformational equilibria" *Canadian Journal of Chemistry*, 2017, in review.

Chapter 4: J. Spooner, B. Yanciw, B. Wiebe and N. Weinberg, "Reaction Profiles and Energy Surfaces of Compressed Species" *Journal of Physical Chemistry A*, 2014, **118**, 765; J. Spooner, B. Smith and N. Weinberg, "Effect of high pressure on the topography of potential energy surfaces" *Canadian Journal of Chemistry*, 2016, **94**, 1057

Chapter 5: J. Spooner, and N. Weinberg, "A comparative analysis of empirical equations describing pressure dependence of equilibrium and reaction rate constants" *Canadian Journal of Chemistry*, 2017, **95**, 149.

Chapter 1.

Introduction

1.1. Effect of Pressure on Reaction Kinetics and Equilibria: Activation and Reaction Volumes

Along with temperature, pressure is one of the most important physical parameters significantly affecting reaction rates and equilibria over even a relatively modest range of 1−10 kbar[1-2]. The sign and magnitude of the pressure effects vary with the type of reaction. For example, compared to their values at ambient conditions, the rate of the Diels-Alder dimerization of cyclopentadiene increases by a factor of 30 at 4 kbar[3], the rate of Menshutkin reaction between dimethylanaline and isopropyliodide is increased by a factor of 25 at 3 kbar[4], whereas the rate of decomposition of benzoyl peroxide is decreased by 20% at 1.5 kbar[5].

The thermodynamic expressions describing the effect of pressure on chemical equilibria is given by van't Hoff equation[6]

$$\left(\frac{\partial lnK}{\partial P}\right)_T = -\frac{\Delta V}{RT} \qquad (1.1)$$

where ΔV, known as the reaction volume, is the difference:

$$\Delta V = V_P - V_R \qquad (1.2)$$

between the product and reactant partial molar volumes, V_P and V_R. Similarly, the pressure dependence of the reaction rate constant is given by

$$\left(\frac{\partial lnk}{\partial P}\right)_T = -\frac{\Delta V^{\neq}}{RT} \qquad (1.3)$$

where $\Delta V^{\neq}$ is the so called activation volume[1]. Although equation (1.3) was already known to van't Hoff in the late 1800's[7], there was no theory available at that time capable of providing a physical interpretation of the activation volume term. In fact, it would be more than thirty years later that Evans and Polanyi could provide a molecular interpretation of the activation volume within the framework of transition state theory (TST)[1a], and identified $\Delta V^{\neq}$ as the difference in volume between transition states (TS) and reactants:

$$\Delta V^{\neq} = V^{\neq} - V_R \qquad (1.4)$$

When solvent-solute interactions are strong, as in the case of polar reactions in polar media, solvent restructuring in response to the solute rearrangement can result in substantial volume effects[1]. In recognition of this fact, the overall activation (or reaction) volume is frequently presented as a sum of two terms – a structural contribution, $\Delta V^{\neq}_{\text{struc}}$, and the solvation contribution, $\Delta V^{\neq}_{\text{solv}}$:

$$\Delta V^{\neq} = \Delta V^{\neq}_{struc} + \Delta V^{\neq}_{solv} \qquad (1.5)$$

In some cases, $\Delta V^{\neq}_{solv}$ can be the dominant component of $\Delta V^{\neq}$, and can reverse its sign. Thus, the activation volume of a homolytic bond cleavage, where $\Delta V^{\neq}_{solv}$ is expected to be negligible (and thus $\Delta V^{\neq} \approx \Delta V^{\neq}_{struc}$), is around 10 cm^3/mol, whereas the activation volume for an ionic dissociation dominated by $\Delta V^{\neq}_{solv}$ is about -20 cm^3/mol[2a].

1.2. Mechanistic Application of Activation Volumes

In combination with reactant volumes V_R, readily available experimentally, activation volumes $\Delta V^{\neq}$ give a useful piece of mechanistic information in the form of the transition state volumes $V^{\neq}$, thus providing a valuable insight into the mechanistic details of organic and inorganic reactions[1-2,8]. In general, interpretation of experimental

activation volumes is done at a qualitative level, where different types of reactions and processes are characterized by typical ranges of activation volumes (Tables 1 and 2).

Table 1.1. Activation volume contributions from different processes (adapted from Ref. 2a)

Type of Reaction	$\Delta V^{\neq}$ (cm^3/mol)
Bond Cleavage	+10
Bond Formation	-10
Displacement	-5
Ionic Dissociation	-20
Ion Recombination	+20
Charge Dispersal	+5
Charge Concentration	-5

Table 1.2. Typical ranges of activation volumes for different types of reactions (adapted from Ref. 8g)

Type of Reaction	$\Delta V^{\neq}$ (cm^3/mol)
Homolysis	5 to 20
Radical Polymerization	≈ -20
Diels-Alder Cycloadditions	-25 to -40
Intramolecular Cycloadditions	-25 to -30
Dipolar Cycloadditions	-40 to -50
Ester Hydrolysis (basic)	-10 to -15
Ester Hydrolysis (acidic)	> -10

An important example of the utility of activation volumes in the mechanistic context is their application to the discussion of the mechanism of cycloaddition reactions[9]. As illustrated in Scheme 1 for the case of the Diels-Alder reaction of ethene and butadiene, there are two possible pathways for cycloaddition reactions – concerted and stepwise. For the concerted pathway, the TS is product-like with both new bonds being nearly formed, which means that $V^{\neq} \approx V_P$. In accordance with equations (1.2) and (1.4) this implies that $\Delta V^{\neq} \approx \Delta V$. On the other hand, the transition state for the stepwise diradical pathway is considerably less compact so $\Delta V^{\neq}$ is expected to be less negative: (both $\Delta V^{\neq}$ and ΔV are negative). Therefore, the ratio of $\Delta V^{\neq}/\Delta V$ can be used to

discriminate between these two pathways, since this ratio is expected to be considerably less than 1 for the stepwise mechanism.

Scheme 1.1. Concerted (top) and stepwise (bottom) mechanisms of the Diels-Alder reaction between butadiene and ethene.

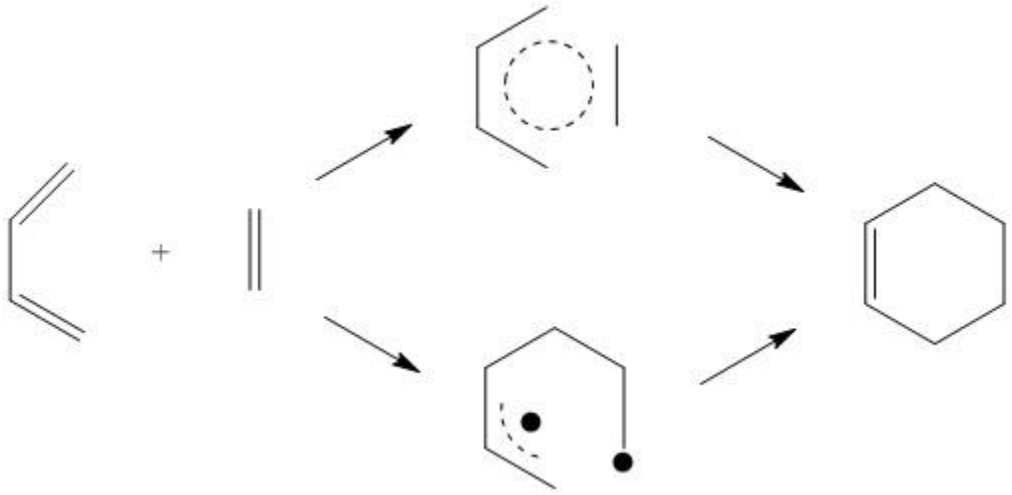

The dimerization of chloroprene (2-chloro-1,3-butadiene) **1**[10] serves as an excellent example. As shown in Scheme 1.2, this reaction leads to a complex product mixture that includes a [2+2] cycloadduct **2**, and three different [4+2] cycloadducts **3-5**. The activation and reaction volume for each of these products are listed in Table 1.3. Inspection of the $\Delta V^{\neq}/\Delta V$ ratios given in the last column of the table shows that mechanisms of the [2+2] cycloaddition leading to products **2** is stepwise, while the [4+2] cycloaddition forming **3** and **4** is concerted, which is consistent with the predictions of the Woodward-Hoffmann rules.[11] The case of product **5** is quite interesting because, in accordance with these rules, it can be expected to be formed through a concerted [4+2] cycloaddition, which is inconsistent with a relatively low $\Delta V^{\neq}/\Delta V$ ratio of 0.69. Subsequent detailed stereochemical studies of dimerization of deuterated chloroprene confirmed that formation of product **5** is indeed a result of a stepwise process[12].

Scheme 1.2. Dimerization of chloroprene.

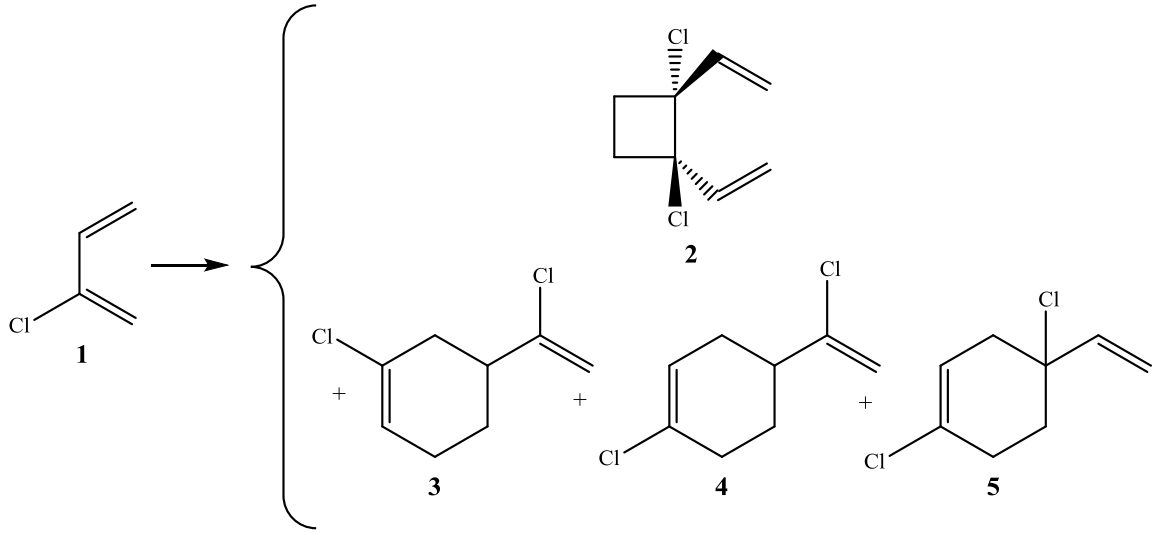

Table 1.3. Activation and reaction volumes for the product of chloroprene dimerization

Product	ΔV (cm^3/mol)	$\Delta V^{\neq}$ (cm^3/mol)	$\Delta V^{\neq}/\Delta V$
2	-27	-10	0.37
3	-32	-31	0.97
4	-32	-29	0.91
5	-32	-22	0.69

The first attempt at rationalizing activation volumes from a microscopic molecular point of view was made by Stearn and Eyring[1b], who proposed a model considering a reaction system as a cylinder of constant cross section σ and variable length *L*. The volume of the system could then be obtained as a product of these parameters

$$V = \sigma L \tag{1.6}$$

Cross section σ is estimated from eq. (1.6) by dividing the experimental value *V* of the reaction system by the length parameter *L* found as the sum of incremental contributions of constituent bonds. On the assumption that σ does not change in the course of reaction, the activation volume can then be found as

$$\Delta V^{\neq} = \sigma \Delta L^{\neq} \tag{1.7}$$

where $\Delta L^{\neq}$ is the change in length of the reaction system between the reactant and transition state: $\Delta L^{\neq} = L^{\neq} - L_R$ (see Fig. 1.1).

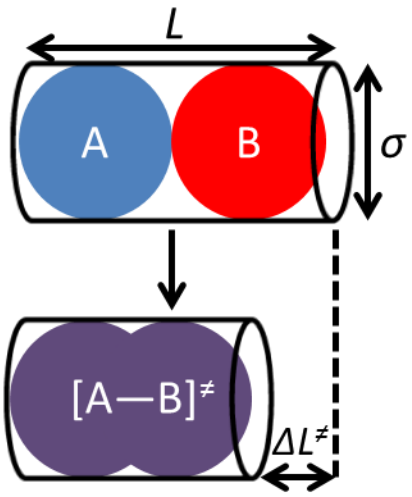

Figure 1.1. Cylindrical Stearn-Eyring model for a simple reaction A+B → AB: the length of the system L changes on going from the reactant (top) to transition state (bottom), whereas its cross section σ remains constant, which allows the activation volume to be obtained as $\Delta V^{\neq} = \sigma \Delta L^{\neq}$

Although this model has proven to be useful in qualitative and semi-quantitative discussions of pressure effects on reaction kinetics[13], its validity is limited to relatively simple reaction systems as it completely ignores the complexity of molecular shape. Figure 1.2 illustrates an example of a reaction where this model would significantly overestimate the activation volume due to unevenness of the cross section along the molecular axis. Obviously, the "proper" cross section that needs to be used in eq. (1.7) is the cross section σ_1 near the reaction center, whereas the cross section σ estimated from eq. (1.6) is closer to σ_2 describing a much wider part of the molecule.

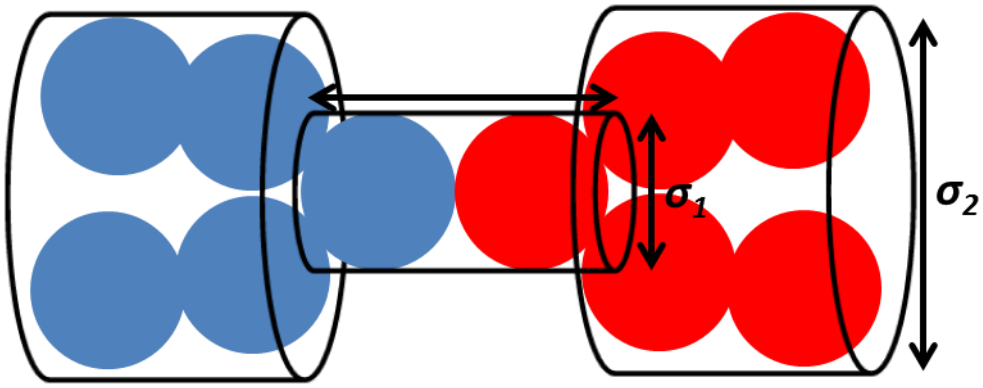

Figure 1.2. Cylindrical model for a system of complex shape, where the choice of σ becomes ambiguous. If σ_2 is used for calculation, the activation volume will be significantly overestimated.

To avoid this problem, Gonikberg and Kitaigorodskii[14] proposed to calculate activation volumes by focusing only on the parts of the molecules which overlap upon reaction and to use for that the change in van der Waals volume of a hard sphere model of the reaction system (Figure 1.3).

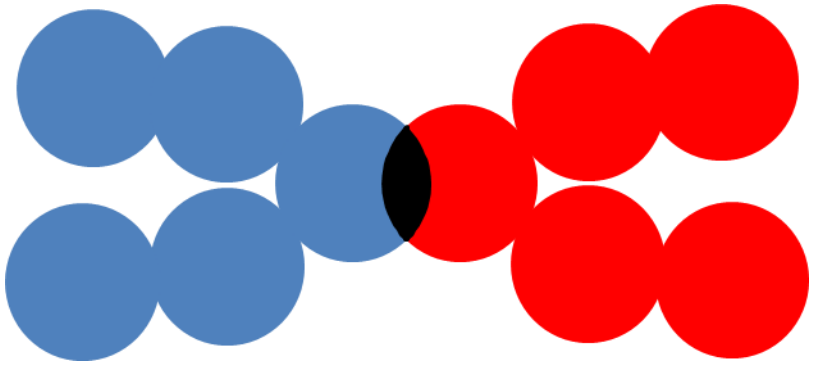

Figure 1.3. Illustration of the Gonikberg-Kitaigorodskii model where the activation volume is calculated as the volume of the overlapping van der Waals spheres (black).

Although this method could be expected to offer an improved structure-sensitive alternative to the Stearn-Eyring model, in reality it provides very poor estimates of the activation volume, even in comparison with the latter[15.] This is due to the fact that this approach completely ignores the effects of packing (the void volume) and of thermal expansion (the expansion volume), which are shown to give substantial contributions to

the volumes of activation[16]. Figure 1.4 illustrates a case where the neglect of the void volume contribution in the Gonikberg-Kitaigorodskii model results in a significant underestimation of the activation volume.

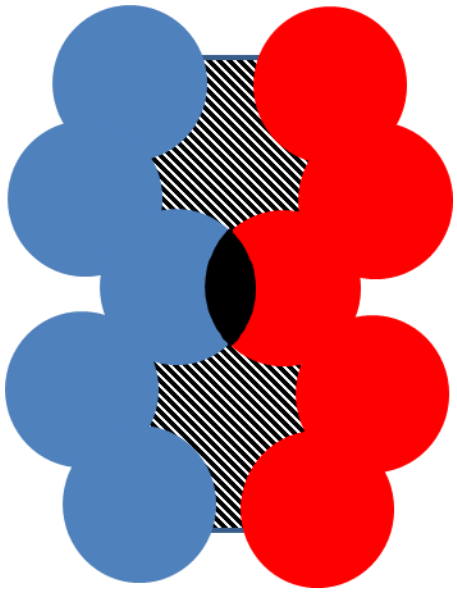

Figure 1.4. The void volume contribution is the volume of the shaded part of space outside the van der Waals spheres of constituent atoms, which is inaccessible to solvent molecules in a course of reaction. In this example, the void volume significantly exceeds the volume of the van der Waals overlap (black) used by Gonikberg and Kitaigorodski to estimate the activation volume.

Subsequently, a number of more refined models became available for the calculation of molecular volumes[17], however most of them were never used for calculation of activation volumes. Most of these models treat a molecule as an object with distinct geometrical boundaries defined by model-specific parameters and, with the exception of the Stranks-Hush-Marcus thermodynamic model[17c], do not account for solvent effects[18]. Poor accuracy combined with inadequate structural sensitivity is the common problem of these models, severely limiting their applicability as a mechanistic tool. We provide a full review of these models in Chapter 2 of this thesis. We also outline a new volume calculation method, which utilizes constant pressure molecular dynamics (MD), and show that this method allows one to obtain accurate partial molar volumes with appropriate sensitivity to molecular geometry and specific solvent-solute interactions.

1.3. Volume Profiles

In discussing reaction mechanisms, activation and reaction volumes are frequently presented in the form of three-state diagrams visually comparing volumes or reactants, products, and transition states[2]. Examples of such diagrams, usually referred to as volume profiles, are shown in Fig 1.5. In general, the concept of a volume profile does not have to be limited to a discrete case of these three-state diagrams. The notion of a continuous volume profile[13,19] generalizes this concept and defines it as a continuous function *V(x)* describing the evolution of volume *V* of the reaction system along its reaction coordinate *x*. The schematic continuous volume profiles corresponding to discrete diagrams of Fig. 1.5 are shown in Fig. 1.6. Construction of such continuous volume profile for a reaction system requires a series of volume calculations for its various configurations along the reaction coordinate.

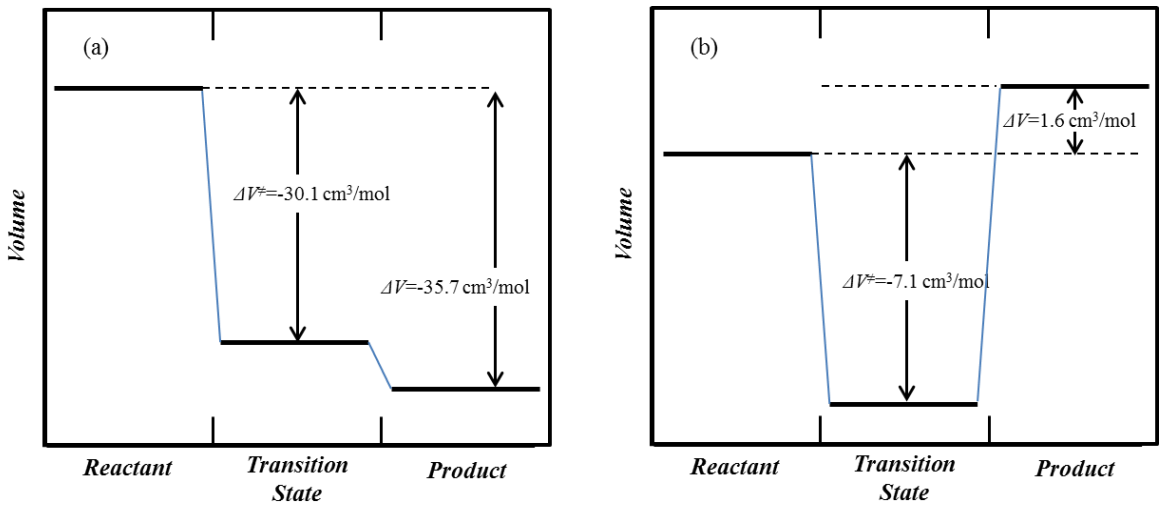

Figure 1.5. Three-state volume profile diagrams for Diels-Alder addition of methyl acrylate to cyclopentadiene[20] (a), and ligand exchange reaction of $Cu(tren)H_2O^{2+}$ and pyridine[21](tren=tris-(2-aminoethyl)amine) (b). Horizontal bars represent the volumes of the reactant, transition, and product states; the connecting blue lines serve merely as logical links between these states and do not represent any physical quantities.

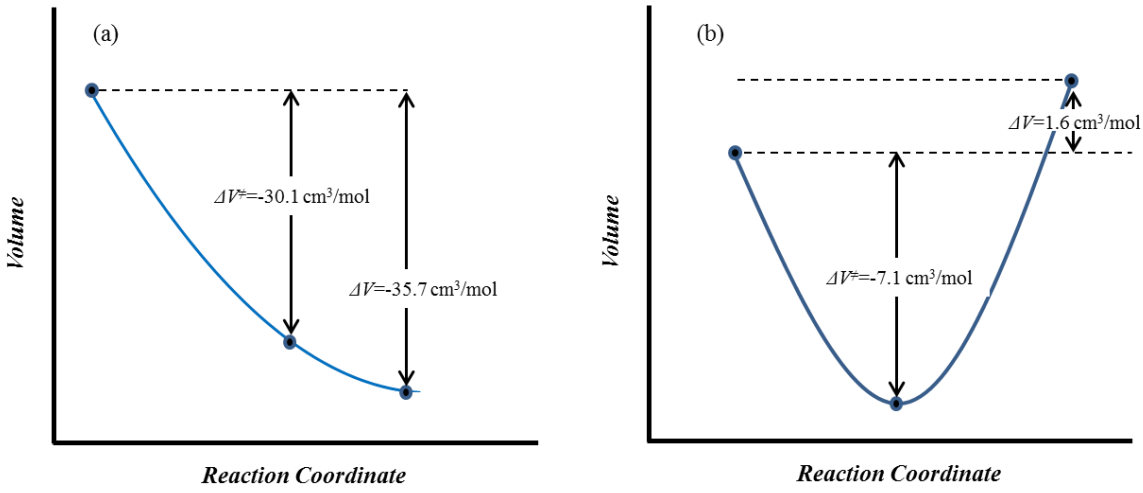

Figure 1.6. Schematic continuous volume profiles (blue lines) corresponding to discrete diagrams of Fig. 1.5: (a) Diels-Alder addition of methyl acrylate to cyclopentadiene, (b) ligand exchange reaction of $Cu(tren)H_2O^{2+}$ and pyridine. Now the blue lines represent actual volumes of transient species encountered along the reaction path that connects the reactant, transition, and product states (shown on the profiles as filled circles)

In the past, continuous volume profiles *V(x)* were used to assess the effects of pressure on the energy profiles of chemical reactions[13]. Pressure-dependent enthalpy profiles

$$H(x,P) \cong U(x) + PV(x) \tag{1.8}$$

were used for this purpose, obtained by a combination of the zero-pressure energy profile *U*(*x*) with the expansion work term *PV*(*x*). Significant pressure-induced deformations of the reaction energy profiles were predicted, but the scope of this early work was severely limited by the lack of a dependable method of generating volume profiles. We will show in Chapter 4 of this thesis that reliable volume profiles can be constructed using our MD volume calculation method outlined in Chapter 2. We then further expand this approach by introducing the concept of a volume surface *V(**x**)*, where ***x*** is a multidimensional coordinate of the reaction system, and show that this concept offers a powerful tool for generating high pressure energy surfaces and for studying pressure induced deformations of their landscapes.

1.4. Experimental Determination of Activation and Reaction Volumes

In accordance with eq. (1.3), the experimental values of activation volumes $\Delta V^{\neq}$ are obtained as the logarithmic derivatives of the observed pressure dependencies of the rate constants $k(P)$. Similarly, when the direct determination of reaction volumes ΔV as the difference of V_P and V_R is impossible, as in the case of fast conformational equilibria, the values of ΔV are obtained as the logarithmic derivatives of the equilibrium constants $K(P)$ from equation (1.1)[1-2]. The difficulty arising in these cases is the inaccuracy of numerical differentiation of $k(P)$ or $K(P)$ due to experimental errors. Therefore, the $\Delta V^{\neq}$ values are typically obtained by differentiation of empirical analytical functions ln $k(P)$ fitted to the experimental data. With few exceptions, these functions can be presented in the form[22]

$$\ln k = a_0 + a_1 P + a_2 f(P) + a_3 P f(P) \tag{1.9}$$

with one of the following three choices of $f(P)$:

$$f(P) = P^2 \tag{1.10a}$$

$$f(P) = 1/(1 + a_4 P) \tag{1.10b}$$

$$f(P) = \ln(1 + a_4 P) \tag{1.10c}$$

The eleven most common functions used in the literature are listed in Table 1.4.

Table 1.4. Most common empirical equations describing pressure dependence of rate and equilibrium constants and their classification.

	Equation	Type
E1	$\ln k/k_0 = a_1P + a_2P^2$	Polynomial
E2	$\ln k/k_0 = a_1P + a_3P^3$	
E3	$\ln k/k_0 = a_1P + a_2P^2 + a_3P^3$	
E4	$\ln k/k_0 = a_3P/(1+a_4P)$	Hyperbolic
E5	$\ln k/k_0 = a_1P + a_3P/(1+a_4P)$	
E6	$\ln k/k_0 = a_2\ln(1+a_4P)$	Logarithmic
E7	$\ln k/k_0 = a_1P + a_2\ln(1+a_4P)$	
E8	$\ln k/k_0 = a_1P + a_3P\ln(1+a_4P)$	
E9	$\ln k/k_0 = a_1P + a_2(1+a_4P)\ln(1+a_4P)$	
E10	$\ln k/k_0 = a_1P + a_2\ln(1+a_4P) + a_3P\ln(1+a_4P)$	
E11	$\ln k/k_0 = a_1P + a_2P^{1.523}$	Pseudo-logarithmic

Since the above analytical expressions are quite different, the values of $\Delta V^{\neq}$ obtained from the same experimental data set using different equations can turn out to be different. This creates an additional problem in the context of the use of activation volumes as a tool for mechanistic insight. We address this matter in Chapter 5, where we present a detailed analysis of the situation and suggest the ways of mitigating the problem.

1.5. Computational Methods

The two principal computational tools used in this thesis are classical MD simulations and quantum mechanical (QM) calculations. These techniques allow us to relate changes in molecular structure to the resulting changes in energy, volume, and other properties. Although first principles (or QM) MD simulations can provide a more accurate description of the systems of interest, they become prohibitively expensive when system sizes are large or the required dynamic trajectories are long. Classical MD offers a reasonable and much less computationally expensive alternative when knowledge of the

electronic structure is not required, however its accuracy critically depends on the quality of the utilized empirical force field. In our studies, we tried to maintain a proper balance in using static QM and classical MD to obtain appropriately accurate results at a reasonable computational expense. A brief outline of specific computational details pertaining to these two methods is presented below.

1.5.1. MD Simulations

Classical MD simulations[23] were used to obtain volumes, energies, free energies, and other thermodynamic properties of pure liquid substances and solutions, as well as to assess dynamic behavior and microscopic parameters of the systems of interest. These properties were obtained by averaging over an MD trajectory **r**(*t*) in the 3N-dimensional coordinate space of a system of N particles (atoms, molecules, or ions). The time dependence of the multidimensional coordinate vector **r** was obtained by leap-frog integration[24] of coupled Newtonian equations of motion

$$m_i \frac{\partial^2 r_i}{\partial t^2} = F_i \tag{1.11}$$

where t is time, and m_i and F_i are the mass and force associated with coordinate r_i. The flow chart of an MD run is shown in Fig. 1.7. Unless stated otherwise, a time step of 1 fs was used for numerical integration of eqs. (1.11). Forces F_i are calculated as components of the negative gradient of potential energy function $U(\mathbf{r})$

$$F_i = -\frac{\partial U}{\partial r_i} \tag{1.12}$$

The functional form and parameters of $U(\mathbf{r})$ are determined by the choice of an empirical force field used in MD simulations. For organic systems, we used the popular OPLS (Optimized Potential for Liquid Simulations) force field[25] the functional form of which is given by eq. (1.13)

$$
\begin{aligned}
U &= U_{bond} + U_{angle} + U_{torsion} + U_{vdW} + U_{es} \\
U_{bond} &= \sum_{bonds} k_b (b - b_0)^2 \\
U_{angle} &= \sum_{angles} k_\theta (\theta - \theta_0)^2 \\
U_{torsion} &= \sum_{torsions} \sum_{n=1}^{4} \frac{V_n}{2} [1 + (-1)^{n+1} cos\{n(\varphi - \varphi_0)\}] \\
U_{oop} &= \sum_{angles} k_\psi (\psi - \psi_0)^2 \\
U_{vdW} = U_{LJ} &= \sum_{i=1}^{N} \sum_{j=i+1}^{N} \left(4\varepsilon_{ij} \left[\left(\frac{\sigma_{ij}}{r_{ij}} \right)^{12} - \left(\frac{\sigma_{ij}}{r_{ij}} \right)^{6} \right] \right) \\
U_{es} &= \sum_{i=1}^{N} \sum_{j=i+1}^{N} \frac{q_i q_j}{4\pi\varepsilon_0 r_{ij}}
\end{aligned}
\tag{1.13}
$$

The bond and angle contributions, U_{bond} and U_{angle}, are modelled by a quadratic dependence of the energy on the deviation of a bond length b or a bond angle θ from their equilibrium values b_0 and θ_0. Due to its periodic nature with respect to dihedral angles φ, the torsion contribution $U_{torsion}$ is described by the first four cosine terms of its Fourier series. Out of plane bending, U_{oop}, is treated using a quadratic dependence of the so-called improper torsions angle ψ. The nonbonded interactions are represented by the van der Waals term U_{vdW} modelled by a 6-12 Lennard Jones (LJ) potential and an electrostatic term U_{es} described by a Coulomb potential. In principle, the summation in nonbonded terms should be extended over all pairs of atoms i and j in the system, however the strength of van der Waals interactions rapidly approaches zero as the distances between atoms increase. Therefore, for computational efficiency, these interactions are assumed to be zero for the distances exceeding an established cutoff. In this work, this cutoff distance was set at 1 nm. The same cutoff was used for electrostatic interactions in nonpolar systems. In cases of polar systems, where long-range electrostatic interactions converge

much slower, we employed the particle mesh Ewald (PME) method [26] extending summation over the entire space.

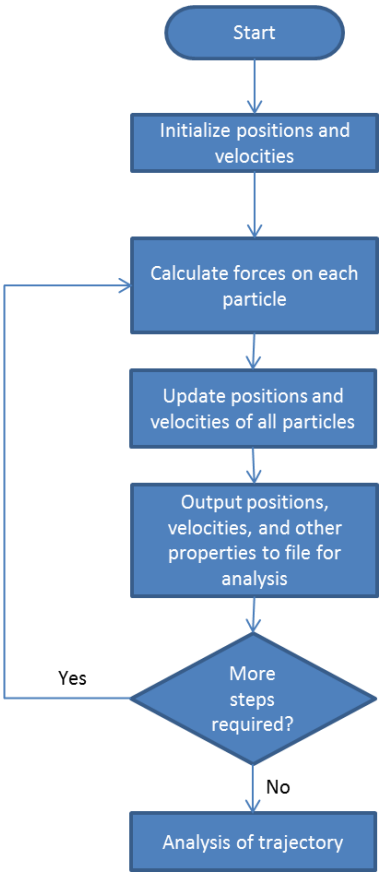

Figure 1.7. Flowchart of MD simulation.

The water force field was predominantly described by the SPC (single point charge) model[27], although TIP4P (4-point-transferable intermolecular potential)[28] and flexible SPC[29] models were occasionally used as well (Figure 1.8). In some instances we also used a model solvent composed of monoatomic LJ particles with parameters m = 40 amu, $\sigma = 0.35$ nm, $\varepsilon = 2.0$ kJ $mol^{-1.}$

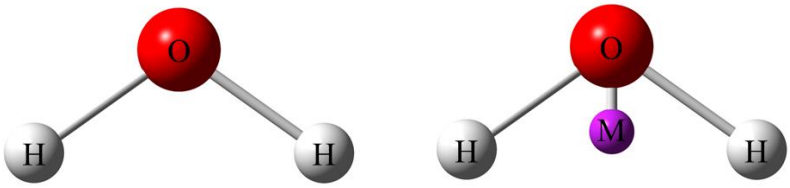

Figure 1.8. SPC (left) and TIP4P (right) models for the water molecule. In the SPC model, the charges are localized on the three constituent atoms, whereas in the TIP4P models, the negative charge of the oxygen atom is offset to the dummy atom M to provide a better description of the electrostatic properties of the molecule.

All MD calculations were performed using the GROMACS package[30]. Periodic boundary conditions were utilized for a cubic cell. All simulations were run in the NPT ensemble. In all cases Berendsen temperature coupling[31] was used with a coupling constant τ_T = 0.1ps. This was typically combined with Berendsen pressure coupling[31] with τ = 0.5ps, however in some instances which will be indicated, the Parinello-Rahman barostat[32] was employed with τ_P = 1ps. Solvent excluded volumes were calculated using the g_sas program included in the GROMACS package with van der Waals radii taken from ref 18(d). Graphic presentation of MD trajectories were done using the VMD package[33].

1.5.2. Quantum Mechanical Calculations

QM calculations were used in this work to construct potential energy surfaces of chemical species at zero and elevated pressures and to generate the missing force field parameters for MD simulations. All QM calculations were performed with the Gaussian 09 suite[34], usually at the B3LYP/6-31++G(d,p) level. In some cases, the calculations were done at the HF/6-31G level, which offered a reasonable compromise between computational cost and quality, adequate for the exploratory nature of those calculations.

1.6. Brief Outline of this Work

We begin Chapter 2 with a review of the existing models of molecular volume and then proceed to the formulation of a new approach toward calculation of such volumes based on the constant pressure MD simulations of the solute-solvent systems of interest. Further in that chapter we present the evidence of the efficiency of this method in generating accurate molar and partial molar volume values consistent with the experimental data and propose a method of assessing molecular surfaces that incorporates this technique.

In Chapter 3 we expand the application of our MD method to the calculation of reaction and activation volumes and discuss the QM based approach for evaluating the MD force field parameters for TSs, required to perform our $\Delta V^{\neq}$ calculations.

As a further extension of our approach, in Chapter 4 we discuss calculations of volume profiles and volume surfaces of reactions, and their use in constructing high pressure reaction profiles and energy surfaces. We illustrate our methodology by its application to study of pressure induced deformations of energy profiles and surfaces in a number of hydrogen and methyl transfer reactions.

In Chapter 5 the general properties of the empirical analytical functions used to describe the effect of pressure on rate and equilibrium constants in solution are reviewed and the effects of experimental errors on the accuracy of activation and reaction volumes predicted by these equations are compared. Based on the analysis of fitting these equations to simulated and experimental data, we propose a set of general recommendations for using them as a tool for obtaining accurate activation and reaction volumes.

1.7. References

1. (a) M. J. Evans and M. Polanyi, *Trans. Faraday Soc.* **1935,** *31*, 875; (b) A. E. Stearn, and H. Eyring, *Chem. Rev.* **1941**, *29*, 509; (c) S. D. Hamann, *Physico-Chemical Effects of Pressure*; Academic Press: New York, **1957**; (d) M. G. Gonikberg, *Chemical equilibria and reaction rates at high pressures*; National Science Foundation: Washington, **1963**; (e) N. S. Isaacs, *Liquid Phase High Pressure Chemsitry*; Wiley: New York, **1981.**
2. (a) W.J. le Noble, *Prog. Phys. Org. Chem.*, 1967, **5**, 207; (b) T. Asano and W.J. le Noble, *Chem. Rev.*, 1978, **78**, 407; (c) R. van Eldik, T. Asano and W.J. le Noble, *Chem. Rev*., 1989, **89**, 549; (d) A. Drljaca, C.D. Hubbard, R. van Eldik, T. Asano, M.V. Basilevsky and W.J. le Noble, *Chem. Rev.*, 1998, **98**, 2167.
3. B. Raistrick, R. H. Sapiro and D. M. Newitt, *J. Chem. Soc.*, 1939,**61**, 1761.
4. M.G. Gonikberg and V.M. Zhulin, *Aust. J. Chem.*, 1958, **11**, 285.
5. C. Walling and J. Pellon, *J. Am. Chem. Soc*., 1957, **79**, 4786.
6. P. W. Atkins and J. De Paula, *Physical Chemistry*, 9th ed.; Oxford University Press: New York, 2010.
7. K. Laidler, *Arch. Hist. Exact Sci.*, 1985, **32**, 43.
8. For recent reviews see, for example, (a) T. W. Swaddle, P.A. Tregloan, *Coord. Chem. Rev.* 1999, **187,** 255; (b) G. Stochel, R. van Eldik, *Coord. Chem. Rev.*, 1999, **187**, 329; (c) F.-G. Klärner, V. Brietkopf, *Eur. J. Org. Chem.*, 1999, **11**, 2757; (d) F.-G. Klärner, F. Wurche, *J. Prakt. Chem.*, 2000, **342**, 609; (e) T.W. Swaddle, *Chem. Rev.* 2005, **105**, 2573; (f) C.D. Hubbard and R. van Eldik, *J.*

Coord. Chem., 2007, **60**, 1; (g) Schettino, V.; Bini, R. *Chem. Soc. Rev*, 2007, **36**, 869.

9. (a) K. N. Houk, J. González, Y. Li, *Acc. Chem. Res.*, 1995, **28**, 81 and references therein. See also a more recent discussion on that matter in: (b) K. A. Swiss and R.A. Firestone, *J. Phys. Chem. A* 2000, **104**, 3057; (c) W.J le Noble and T. Asano, *J. Phys. Chem. A* 2001, **105**, 3428; (d) K. A. Swiss and R.A. Firestone, *J. Phys. Chem. A*, 2001, **105**, 3430; (e) C.F. Weber, and R.J. van Eldik, *Phys. Chem. A*, 2002, **106**, 6904; (f) K.A. Swiss and R.A. Firestone, *J. Phys. Chem. A*, 2002, **106**, 6909; (g) S.D. Hamann, and W.J. le Noble, *J. Phys. Chem. A*, ***2004***, **107**, 7121; (h) K.A. Swiss and R.A. Firestone, *J. Phys. Chem. A*, 2004, **108**, 7124.
10. C.A. Stewart, *J. Am. Chem. Soc.*, 1972, **94**, 635.
11. R. Hoffmann and R.B. Woodward, *J. Am. Chem. Soc.*, 1965, **87**, 2046; R. B. Woodward and R. Hoffmann; *The conservation of orbital symmetry***,** Academic Press: New York, **1970**; Ian Fleming, *Pericyclic Reactions*; Oxford University Press: New York, **1999.**
12. F.-G. Klarner, V. Ruster, B. Zimny, and D. Hochstrate, *High Press. Res.*, 1991, **7**, 133.
13. M. Basilevsky, N. Weinberg and V. Zhulin, *J. Chem. Soc. Faraday Trans.* 1, 1985, **81**, 875.
14. M. Gonikberg and A. Kitaigorodskii, *Proc Acad. Sci. USSR*, 1958, **122**, 665.
15. M.G. Gonikberg, V. M. Zhulin and B. S. El'yanov, in *The Physics and Chemistry of High Pressure*; Soc. Chem. Industry, London, 1963.

16. (a) T. Asano and W. J. le Noble, *Rev. Phys. Chem. Jpn.*, 1973, **43**, 82; (b) M. V. Basilevsky, N. N. Weinberg, and V.M. Zhulin, *J. Mol. Liquids*, 1986, **33**, 29; (c) N. Weinberg, *Rev. High Pressure Sci. Tech.,* 1998, **8,** 86.

17. See, for example, (a) A. I. Kitaigorodskii, *Organic Chemical Crystallography*, Consultants Bureau: New York, **1961**; (b) A. J. Bondi, *Phys. Chem.,* **1964**, *68*, 441; (c) D.R. Stranks, *Pure Appl. Chem.*, 1974, **38**, 303; (d) A. Gavezzotti, *J. Am. Chem. Soc.,* 1983, **105**, 5220; (e) F.M. Richards, *Methods Enzymol.* 1985, **115**, 440; (f) M. L. Connolly, *J. Am. Chem. Soc.,* 1985, **107**, 1118; (g) R. Bader, M. Carroll, J. Cheeseman and C. Chang, *J. Am. Chem. Soc.,* 1987, **109**, 7968; (h) M. W. Wong, K. B. Wiberg and M. J. Frisch, *J. Comp. Chem.,* 1995, **16**, 385; (i) F.-G. Klärner, B. Krawczyk, V. Ruster and U. K. Deiters, *J. Am. Chem. Soc.,* 1994, **116**, 7646; 1995, **117**, 576; (k) B. J. Smith and N. E. Hall, *J Comput. Chem.,* 1998, **19**, 1482; (l) J. A. Grant and B.T Pickup, *J. Phys. Chem.,* 1995, **99**, 3503; (m) A. S. Mitchell and M.A. Spackman, *J. Comput. Chem.,* 2000, **21**, 933; (m) L. D. Gong, and Z.Z. Yang, *J. Comp. Chem.,* 2010, **31**, 2098.

18. J. Spooner, H. Wiebe, N. Boon, E. Deglint, E. Edwards, B. Yanciw, B. Patton, L. Thiele, P. Dance, N. Weinberg, *Phys. Chem. Chem. Phys.*, 2012, **14**, 2264.

19. W.J. le Noble, *Rev. Phys. Chem. Jap.,* 1980, **50**, 207.

20. K. Seguchi, A. Sera, and K. Maruyama, *Bull. Chem. Soc. Jap.*, 1974, **47**, 2242.

21. D. Powell, A. Merbach, I. Fábián, S. Schindler, and R. van Eldik, *Inorg. Chem.*, 1994, **33**, 4468.

22. C.A.N. Viana and J.C.R.Reis, *Pure Appl. Chem.,* 1996, **68**, 1541 and references therein.

23. (a) M.P. Allen, D.J. Tildesley, *Computer Simulation of Liquids*, Oxford Univ. Press: N.Y., **1989**; (b) D.C. Rapaport, *The Art of Molecular Dynamics Simulations*, Cambridge Univ. Press: Cambridge, **2004**.

24. R.W. Hockney, and J.W. Eastwood; *Computer Simulation using Particles*, Taylor & Francis: New York, **1988**.

25. (a) W.L. Jorgensen and J. Tirado-Rives, *J. Am. Chem. Soc.*, 1988, **110**, 1657; (b) W.L. Jorgensen, D.S. Maxwell and J. Tirado-Rives, *J. Am. Chem. Soc.*, 1996, **118**, 11225.

26. (a) T. Darden, D. York and L. Pedersen, *J. Chem. Phys.*, 1993, **98**, 10089; (b) U. Essmann, L. Perera, M.L. Berkowitz, T. Darden, H. Lee and L.G. Pedersen, *J. Chem. Phys.*, 1995, **103**, 8577.

27. H.J.C. Berendsen, J.P.M. Postma, W.F. van Gunsteren and J. Hermans, *Jerusalem Symposia on Quantum Chemistry and Biochemistry*, 1981, Reidel, Dordrecht, Holland, 331-342.

28. W.L. Jorgensen, J. Chandrasekhar, J.D. Madura, R.W. Impey and M.L. Klein, *J. Chem. Phys.*, 1983, **79**, 926.

29. K.Toukan and A. Rahman, *Phys. Rev. B*, 1985, **31**, 2643.

30. (a) H.J.C. Berendsen, D. van der Spoel and R. van Drunen, *Comp. Phys. Comm.*, 1995, **91**, 43; (b) E. Lindahl, B. Hess and D. van der Spoel, *J. Mol. Mod.*, 2001, **7**, 306; (c) D. van der Spoel, E. Lindahl, B. Hess, G. Groenhof, A.E. Mark and H.J.C. Berendsen, *J. Comp. Chem.*, 2005, **26**, 1701; (d) B. Hess, C. Kutzner, D.van der Spoel and E. Lindahl, *J. Chem. Theory Comut.*, 2008, **4**, 435.

31. H.J.C. Berendsen, J.P.M. Postma, W.F. van Gunsteren, A. DiNola and J.R. Haak, *J. Chem. Phys.*, 1984, **81**, 3684.

32. M. Parrinello and A. Rahman, Phys. Rev. Lett., 1980, **45**, 1196; *J. Appl. Phys.*, 1981, **52**, 7182; *J. Chem. Phys.*, 1982, **76**, 2662.

33. W. Humphrey, A. Dalke and K. Schulten, *J. Molec. Graphics*, 1996, **14**, 33.

34. Gaussian 09, Revision **E.01**, M. J. Frisch, G. W. Trucks, H. B. Schlegel, G. E. Scuseria, M. A. Robb, J. R. Cheeseman, G. Scalmani, V. Barone, B. Mennucci, G. A. Petersson, H. Nakatsuji, M. Caricato, X. Li, H. P. Hratchian, A. F. Izmaylov, J. Bloino, G. Zheng, J. L. Sonnenberg, M. Hada, M. Ehara, K. Toyota, R. Fukuda, J. Hasegawa, M. Ishida, T. Nakajima, Y. Honda, O. Kitao, H. Nakai, T. Vreven, J. A. Montgomery, Jr., J. E. Peralta, F. Ogliaro, M. Bearpark, J. J. Heyd, E. Brothers, K. N. Kudin, V. N. Staroverov, R. Kobayashi, J. Normand, K. Raghavachari, A. Rendell, J. C. Burant, S. S. Iyengar, J. Tomasi, M. Cossi, N. Rega, J. M. Millam, M. Klene, J. E. Knox, J. B. Cross, V. Bakken, C. Adamo, J. Jaramillo, R. Gomperts, R. E. Stratmann, O. Yazyev, A. J. Austin, R. Cammi, C. Pomelli, J. W. Ochterski, R. L. Martin, K. Morokuma, V. G. Zakrzewski, G. A. Voth, P. Salvador, J. J. Dannenberg, S. Dapprich, A. D. Daniels, Ö. Farkas, J. B. Foresman, J. V. Ortiz, J. Cioslowski, and D. J. Fox, Gaussian, Inc., Wallingford CT, 2009.

Chapter 2.

Molecular Dynamics Calculation of Molecular Volumes

As outlined in Chapter 1, the concept of molecular volume is crucial for microscopic interpretation of activation and reaction volumes. It is also widely used in rheology, QSAR (quantitative structure-activity relationships), biochemistry, and many other chemical applications[1]. In most of the existing approaches a molecule is treated as an object with geometrical boundaries. Four examples of that kind are shown for a benzene molecule in Fig. 2.1.

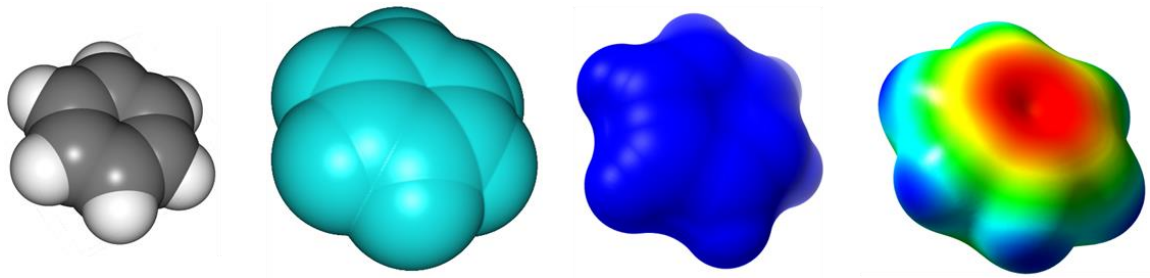

(a) (b) (c) (d)

Figure 2.1. Four most common geometrical models of benzene molecule defined by the following types of molecular boundaries: (a) van der Waals (R_C = 0.17 nm, R_H = 0.12 nm), (b) solvent-accessible (R_C = 0.17 nm, R_H = 0.12 nm, $R_{solvent}$ = 0.14 nm); (c) solvent-excluded (R_C = 0.17 nm, R_H = 0.12 nm, $R_{solvent}$ = 0.14 nm); (d) isodensity (ρ = 0.01). See the text below for a detailed description of these models and their comparison.

Although molecular volume as a geometrical concept is intuitively appealing, it is not well defined, primarily because molecules do not actually possess distinct geometrical boundaries. In addition, the definitions of these boundaries are often rather arbitrary and are not transferable to volume calculations in different solvents or under different physical conditions, and are thus insensitive to the context of their environment.

Molecular dynamics serves as an excellent instrument that properly places molecules in this context. In this chapter we formulate a MD method for the accurate calculation of molecular volumes[2]. The calculated volumes are sensitive to the molecular geometry as well as to the specifics of physical conditions and solvent-solute interactions, and thus are perfectly suited to microscopic interpretation of experimental and reaction activation volumes.

The outline of this chapter is as follows: In Section 2.1, a review of available molecular volume models is given, along with a discussion of their limitations. The concept and procedure of our MD method for calculating molecular volumes is outlined in detail in Section 2.2. In Sections 2.3 and 2.4, the performance of the method is tested for the calculation of volumes of various systems. Technical aspects are discussed in Section 2.5. In Section 2.6, we show that our method, in combination with a geometrical model, can be used in calculations of molecular surface areas that are sensitive to physical conditions. Finally, in Section 2.7, the results and conclusions of this chapter are summarized.

2.1. Review of Molecular and Activation Volume Models

2.1.1. Cylindrical Model

As discussed in Section 1.3 the earliest approach toward molecular interpretation of activation volumes was formulated by Stearn and Eyring[3], who proposed to consider a reaction system as a cylinder of constant cross section σ and variable length L (Fig. 1.1). The volume of the system was then presented as a product of these parameters, with the volume change in the course of reaction being proportional to the change in L.

Despite its utmost simplicity, this model proved to be useful in describing the effects of pressure on reaction kinetics at a qualitative and semi-quantitative level[3-6]. However, although this model is able to predict how volume of a relatively simple

reaction system would change in response to its structural changes, it is obviously unsuited for calculation of molecular volumes based on molecular structure.

2.1.2. Van der Waals Volume

Hard sphere models of molecular volume[7-9] offer a more refined approach with a stronger connection between molecular structure and molecular volume. The simplest model of that kind defines the volume of a molecular system, which in this case is referred to as the van der Waals volume, as the total volume of the set of overlapping van der Waals spheres centered at the nuclei of constituent atoms. The van der Waals volumes can be easily calculated either numerically[7c,d,g-j] or analytically.[7e,f,k-m] However, the choice of van der Waals radii is rather arbitrary[10]. More importantly, van der Waals volumes completely ignore the effects of packing and of thermal expansion thus seriously underestimating the value of the molecular volume. As can be seen from the example shown in Table 2.1, the contributions of van der Waals volume to the total molar volume vary over a wide range depending on solute, solvent, and temperature conditions and can be as low as 25% as in the case of methane in hexane solvent.

Table 2.1. Experimental (V_{exp}) and van der Waals (V_W) volumes and their ratios for methane, ethane and benzene in various solvents at 1 bar.

Hydrocarbon	V_W, cm^3/mol	Solvent	T	V_{exp}, cm^3/mol	V_W/V_{exp}
Methane	15.6	*n*-Hexane	25°C	60.0[a]	26%
		Water	25°C	37.3[b]	42%
Ethane	26.2	*n*-Hexane	25°C	69.3[a]	38%
		Water	25°C	51.12[b]	51%
Benzene	62.1	Water	25°C	83.1[b]	75%
		Benzene	50°C	92.3[c]	67%
			90°C	97.1[c]	64%
			130°C	103.2[c]	60%

[a] data from Ref 11
[b] data from Ref 12
[c] data from Ref 13

As discussed in Section 1.3, the idea of using van der Waals volumes for activation volume calculations was proposed by Gonikberg and Kitaigorodskii[14] as a structure-sensitive alternative to the Stearn-Eyring model. However, since the void and expansion volume contributions are not included in the model, despite being the main components,[15] van der Waals volumes considerably underestimate the values of reaction and activation volumes. For example, the reaction volume of the Diels alder reaction of ethene and 1,3-butadiene to form cyclohexene calculated using van der Waals volumes is found to be only -11.2 cm^3/mol compared to the actual experimental value of -41.7 cm^3/mol,[16i] i.e. the van der Waals contribution constitutes only 27% of the total value.

2.1.3. Solvent Accessible and Solvent Excluded Volumes

An alternative definition of the molecular boundary that takes the finite size of the solvent particles into consideration and thus properly accounts for the contribution of the void volume was proposed by Lee and Richards[8]. The molecular surface, known as the solvent accessible surface, is traced by the center of a probe sphere, representing the solvent, rolling over the van der Waals surface of the molecule (see Fig. 2.2).

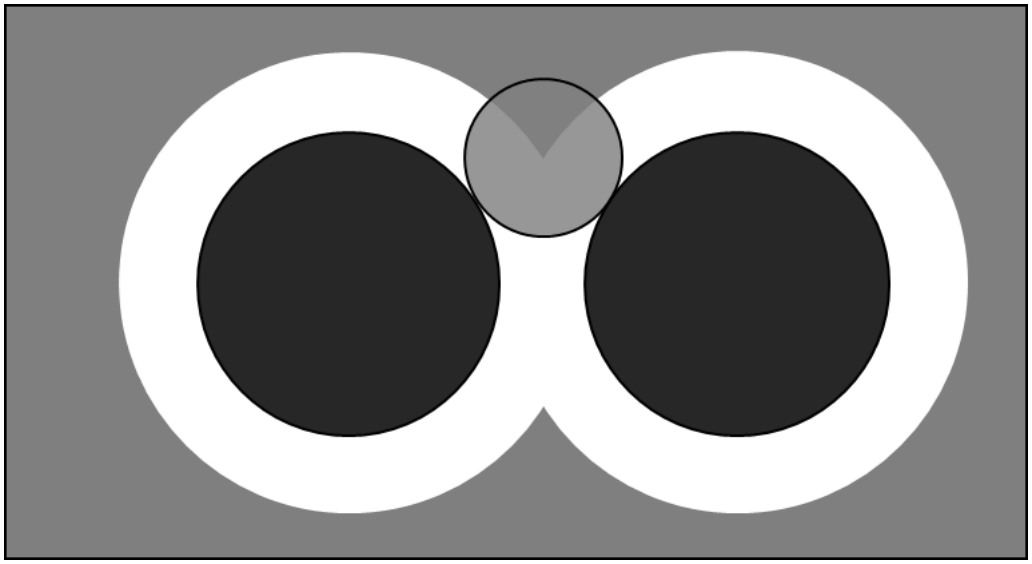

Figure 2.2. Illustration of a section through the solvent accessible surface for a set of two van der Waals spheres. The solvent accessible surface is defined by the locus of the centre of the probe sphere (gray circle) as it rolls around the van der Waals surface (black circles).

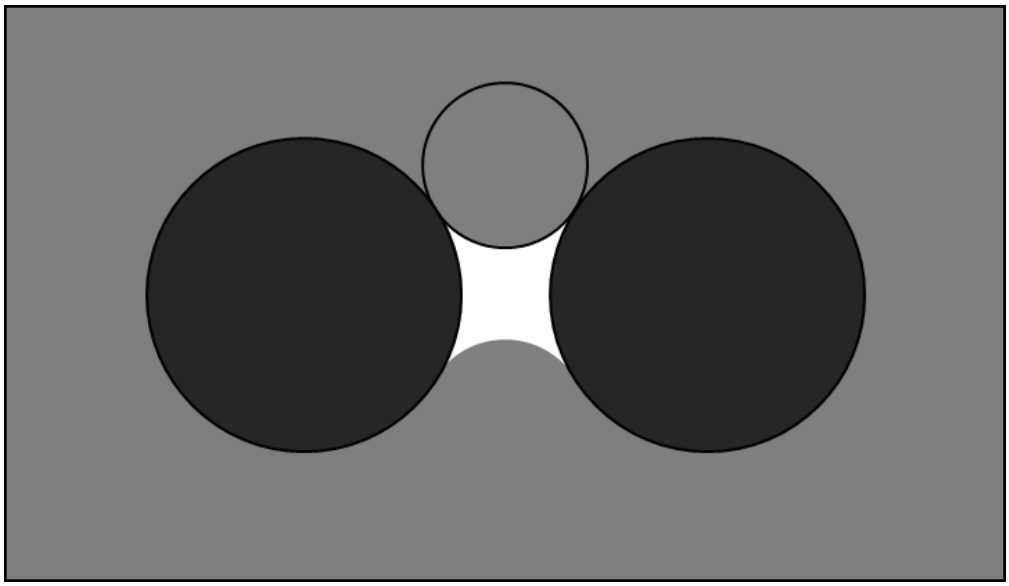

Figure 2.3. Illustration of a section through the solvent excluded surface for a set of two van der Waals spheres. The solvent excluded surface is defined by the the boundary of the region inaccessible to the probe sphere.

The solvent accessible volume outlined by this surface clearly overestimates the molecular volume, which is better approximated by the so-called solvent excluded volume,[9] defined as the volume of the region inaccessible to the probe sphere (Fig. 2.3). The results in both models crucially depend on the choice of the probe sphere radius, representing properties of the solvent. In addition, neither of them includes the effects of thermal expansion. A possible fix to the latter problem lies in the use of a temperature-adjusted probe sphere radius. The data in Table 2.2 indicate that with properly chosen probe sphere radii, specifically adjusted for each solvent-solute system at a given temperature, the calculated solvent excluded volumes can be made equal to the experimental values. It is also important to emphasise, however, that this match is achieved through a highly empirical *ad hoc* fitting process, and the wide range of variation the adjusted probe radii is hard to rationalize. The lack of a properly defined procedure of choosing the probe radius makes application of the excluded volume model to calculation of molecular volumes somewhat problematic.

Table 2.2. Experimental (V_{exp}) and solvent excluded (V_{SE}) volumes of methane, ethane and benzene in various solvents at 1 bar, along with the adjusted probe sphere radii (r).

Hydrocarbon	Solvent	T	V_{exp}, cm^3/mol	V_{SE}, cm^3/mol	r, nm
Methane	*n*-Hexane	25°C	60.0[a]	60.1	0.103
	Water	25°C	37.3[b]	37.1	0.052
Ethane	*n*-Hexane	25°C	69.3[a]	69.5	0.085
	Water	25°C	51.12[b]	51.2	0.052
Benzene	Water	25°C	83.1[b]	82.6	0.019
	Benzene	50°C	92.3[c]	92.0	0.030
		90°C	97.1[c]	96.6	0.035
		130°C	103.2[c]	102.9	0.041

[a] data from Ref 11
[b] data from Ref 12
[b] data from Ref 13

2.1.4. Quantum Mechanical Models

The hard sphere models described previously depend heavily on the selection of a set of van der Waals and probe sphere radii in their definition of molecular surface. Quantum mechanics offers an alternative approach based on electronic properties of a molecule[17]. Bader[17a-b] proposed to use electron density for this purpose and defined molecular boundaries by an isodensity surface. The method has been used to calculate molecular surfaces and volumes for systems of different complexity[17c-g]. The isodensity level (usually 0.001 a.u.) is the only parameter needed in the model; however, this parameter is not universal[17d-f] and its different values are necessary to describe different molecular species.[18,19] When compared with experimental molar volumes for a large selection of organic compounds it was found that molecular volumes calculated using the isodensity surface model with the typical 0.001 a.u. envelope tended to significantly underestimate the volume by about 25%.[17f] The quality of the fit can be improved by choosing an isodenisty level different from 0.001 a.u., but that would break the

universality of that parameter and make it hard to define *a priori*. Even at that cost, the model remains insensitive to the temperature and solvent effects.

Another quantum mechanical approach is based on the concept of molecular face[20], a surface defined by the classical turning point of electron movement in the molecule. The volumes confined by these surfaces show a strong linear correlation with those calculated using the electron isodensity model[20d]and suffer from the same limitations.

2.1.5. Emperical Scaling

The calculation of $\Delta V^{\neq}$ using the volumes provided by any of the above models ignores the effects of thermal expansion as well as the effects of the changes in the surrounding medium. A scaling procedure has been suggested[21] to relate geometrically defined volumes, such as van der Waals volumes V_w, to the observed partial molar volumes V by so-called packing coefficients $\eta = V_w/V$. This ratio gives an indication of the amount of the volume that can be attributed to contributions from the void volume and thermal expansion. The value of η for neutral molecules in the liquid phase ranges from about 0.4-0.6, and tends to be larger for cyclic compounds when compared to their acyclic analogues.[16]

If packing coefficients are the same for the reactant and transition states, they can be obtained from the experimental partial molar volumes of reactants and then used to calculate activation volume $\Delta V^{\neq}$ from its van der Waals component $\Delta V_w^{\neq}$ as $\Delta V^{\neq} = \eta \Delta V_w^{\neq}$. If the values of η and $\eta^{\neq}$ are different, the latter can be either approximated by the packing coefficients for the similar stable species or estimated by computer simulations,[16] however the quality of such determination is rather poor.

2.1.6. Stranks-Hush-Marcus Thermodynamic Model

All of the above models, even with empirical adjustments to their parameters, are hardly applicable to polar reactions where significant solvent reorganization gives the

major or a substantial contribution to the activation volume. A typical example of a highly polar reaction is outer-sphere electron transfer. This process is well described by Marcus theory,[22] according to which the total Gibbs energy of activation $\Delta G^{\neq}$ includes contributions of internal reorganization of the reaction system, $\Delta G_{IR}^{\neq}$, reorganization of the surrounding solvent, $\Delta G_{SR}^{\neq}$, the Coulombic work required to bring the reactants together in the transition state, $\Delta G_{COUL}^{\neq}$, and the effect of interionic interactions, $\Delta G_{DH}^{\neq}$. Differentiation of $\Delta G^{\neq}$ with respect to pressure gives the activation volume of the process which in turn can be represented as the sum of four terms: [23]

$$\Delta V^{\neq} = \Delta V_{IR}^{\neq} + \Delta V_{SR}^{\neq} + \Delta V_{COUL}^{\neq} + \Delta V_{DH}^{\neq} \tag{2.1}$$

$$\Delta V_{IR}^{\neq} \approx 0.6\ cm^3/mol \tag{2.2}$$

$$\Delta V_{SR}^{\neq} = \frac{e^2}{4}\left(\frac{1}{r_1} + \frac{1}{r_2} - \frac{1}{\sigma}\right)\frac{\partial}{\partial P}\left(\frac{1}{\varepsilon_o} - \frac{1}{\varepsilon}\right) \tag{2.3}$$

$$\Delta V_{COUL}^{\neq} = \frac{Z_1 Z_2 e^2}{r_1 + r_2}\frac{\partial}{\partial P}\left(\frac{1}{\varepsilon}\right) \tag{2.4}$$

$$\Delta V_{DH}^{\neq} = -RTZ_1Z_2\frac{A\sqrt{I}}{1 + Ba\sqrt{I}}\left(\frac{3}{\varepsilon}\frac{\partial \varepsilon}{\partial P} - \kappa_s\right) \tag{2.5}$$

where σ is the internuclear separation at which the electron transfer occurs and is assumed to be pressure independent along with ionic radii r_1 and r_2; The values of these terms are dependent on the properties of the solvent, as well as the radii of the reactants and the geometry of the reaction system.

Eq. (2.1) was thoroughly examined by Swaddle[24] who showed that the model reproduces well the experimental activation volumes of many outer-sphere self-exchange electron transfer reactions in aqueous solution if $\Delta V_{IR}^{\neq}$ term can be neglected or approximated with a constant value of 0.6 cm^3/mol. However, the predictions become inaccurate when solute restructuring is important or when ion pairing is expected to be significant.[24] Morover, the model is not designed to work for reactions, other than electron transfer processes.

2.1.7. Monte Carlo and MD models

Despite certain success each of the above models might have enjoyed in describing various components of partial molar volume, they all suffer from poor accuracy and/or inadequate structural sensitivity, severely limiting their applicability as mechanistic tools. An attempt to overcome this problem by using Monte Carlo (MC) simulations of solvent-solute systems was made twenty years ago by Klärner *et al*.[21] but their work was never followed up, likely because of insufficient accuracy of calculations affordable at that time. At the current state of computer technology, MC and MD methods reached precision that rivals the experimental level, which has led to a wider use of MD simulations to discuss volumetric properties of chemical and biochemical systems.[25] In the subsequent section we will formulate an MD-based method toward calculation of molecular volumes, which provides an accuracy sufficient for mechanistic applications.

2.2. Displacement Model of Molecular Volume

As discussed in Chapter 1, mechanistic interpretation of activation and reaction volumes requires molecular volume calculations which are sensitive to the structure and specific solvent environment of the solute, as well as temperature and pressure. Constant-pressure MD provides a tool suitable for these purposes. Thermodynamically, the partial molar volume V_X of solute **X** in solvent **S** is defined as

$$V_X = \left(\frac{\partial V}{\partial n_X} \right)_{P,T} \tag{2.6}$$

where V is the total volume of the solution and n_x is the number of moles of the solute. For dilute solutions this can be replaced with a finite-difference expression,

$$V_X = \frac{V(n_S, n_X) - V(n_S, 0)}{n_X} \tag{2.7}$$

and in the limit of infinite dilution represents the change in volume upon addition of a single solute molecule. Using constant-pressure MD we can obtain the volume of a single solute molecule as an Archimedean displacement volume, *i.e.* as the volume difference between a pure solvent (N particles: $N\cdot\mathbf{S}$) and a system containing, in addition, one solute molecule (N+1 particles: $\mathbf{X} + N\cdot\mathbf{S}$):

$$V(\mathbf{X}) = V(\mathbf{X}+N\cdot\mathbf{S}) - V(N\cdot\mathbf{S}) \tag{2.8}$$

This concept is illustrated by Fig. 2.4 for the case of a model diatomic solute in a LJ solvent (described in Section 1.5). The solute, atoms of which are shown as blue balls of van der Waals diameter (assumed here to be equal to the LJ parameter σ), is immersed in the solvent, represented in the figure by small white balls marking positions of the centers of the solvent particles averaged over the entire MD trajectory. The solvent trajectory shows a clear pattern of avoidance due to the short-range solvent-solute repulsion resulting in the formation of a cavity around the solute. The size and the shape of the cavity depend on the geometry of the solute, the strength and type of the solute-solvent interactions, as well as the temperature and pressure. The incremental increase of the volume of the overall system due to cavity formation, described by eq. (2.8), is the partial molar volume of the solute in a given solvent under specified temperature and pressure conditions.

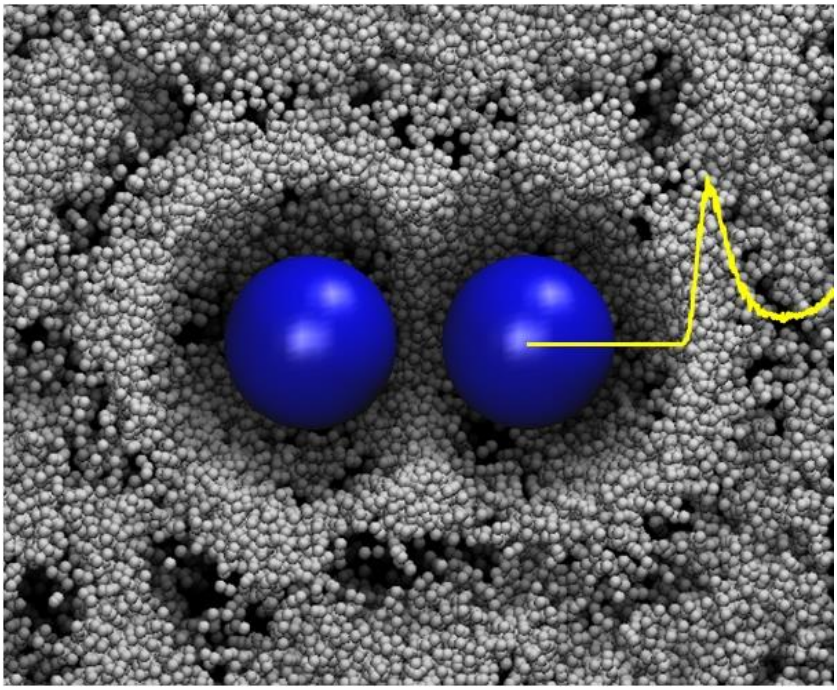

Figure 2.4. Model diatomic in a LJ solvent. The solvent trajectory is represented by an overlay of solvent configurations acquired at different instants of time. The solute atoms are shown as blue balls of van der Waals radii; the small white balls mark instantaneous positions of the solvent particles. The yellow curve is the solute-solvent radial distribution function.

The image in Fig. 2.4 has a remarkable resemblance to that of Fig. 2.2 illustrating the concept of solvent accessible surface. In Fig. 2.4 this surface can be identified with the first coordination sphere, defined by the first maximum of the solute-solvent radial distribution function and seen in the figure as the cavity wall. The appearance of the cavity depends on the rendering chosen for the solvent particles. Thus, when both solute and solvent particles are represented by their van der Waals spheres (Fig. 2.5a), they seem to be tightly packed, leaving no empty space with the exception of the 'void' volume near the geometrical center of the diatomic. The new shape of the solvent cavity can be better seen if the radii of the solute atoms are significantly reduced, just to mark the positions of their centers (Fig. 2.5b).

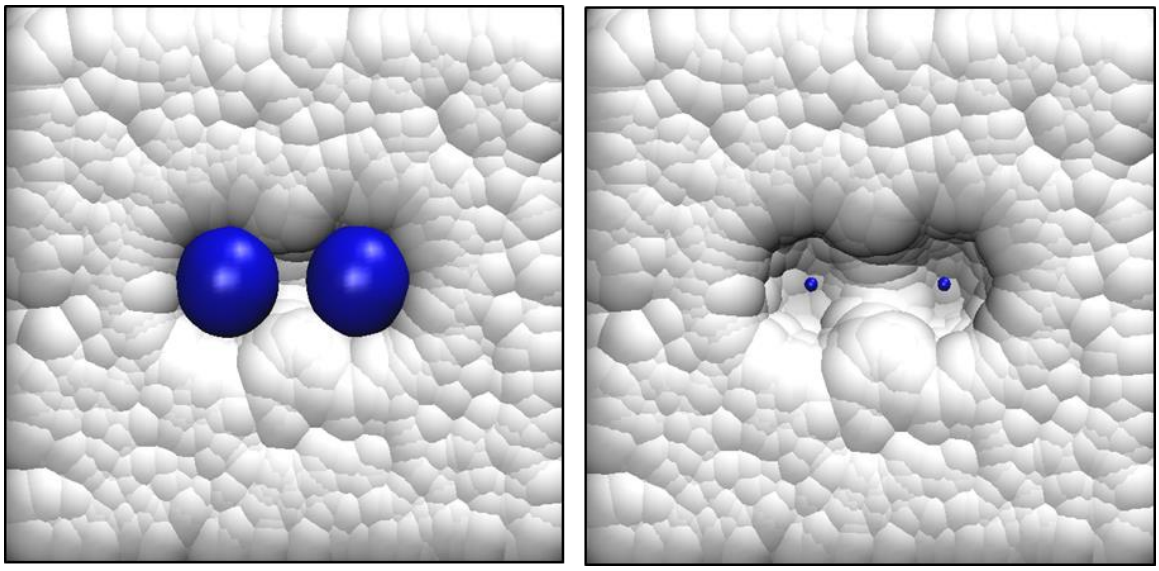

(a) **(b)**

Figure 2.5. Model diatomic in a LJ solvent (the same configuration as in Fig. 2.4): (a) both solute atoms (blue) and solvent particles (white) are shown as balls of van der Waals radii; (b) the small blue balls mark positions of the centers of the solute atoms.

The surface of this cavity matches in its concept and appearance with the solvent excluded surface of Fig. 2.3. Interestingly, as can be seen in Fig. 2.6, the cross-section of the cavity remains constant for interatomic distances R ranging from 0.1 to about 0.25 nm, and its volume is described well by linear eq. (1.6) of the Stearn-Eyring cylindrical model. At longer interatomic distances, a narrowing develops in the middle of the cavity, resulting in a marked nonlinearity of the volume dependence. The radius of the circular cross-section estimated from the linear dependence of Fig. 2.6 is 0.31 nm, which is by a factor of 1.8 greater than the van der Waals radius of the atoms of the diatomic (0.18 nm) estimated by its LJ parameter σ, and constitutes 82% of the radius of the first coordination sphere (0.38 nm) defined by the first maximum of the radial distribution function or 88% of the solvent accessible radius (0.35 nm) defined as the sum of van der Waals radii of the solvent and solute.

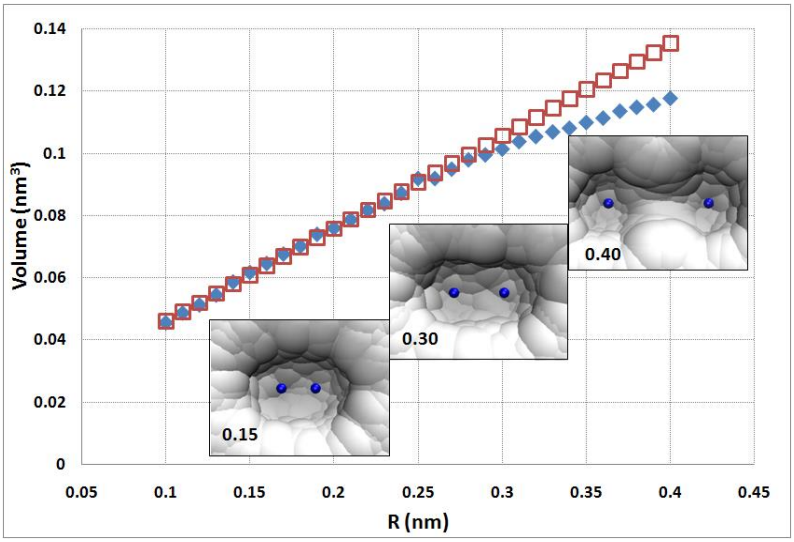

Figure 2.6. Dependence of the displacement volume of the model diatomic on its size measured by the interatomic distance *R* (blue diamonds) in comparison with the straight line (red squares) predicted by Stearn-Eyring model. The insets, labeled by the values of *R*, show the evolution of the sizes and shapes of the solvent cavity.

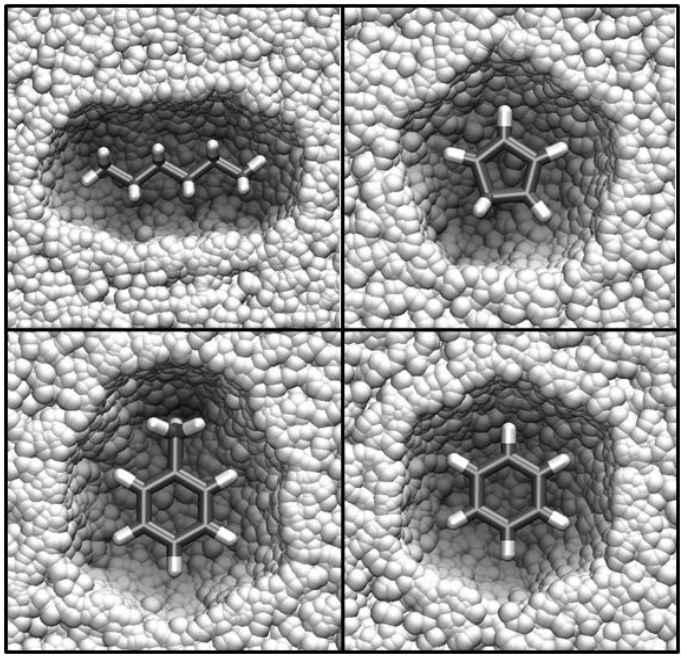

Figure 2.7. Hydrocarbons immersed in LJ solvent (clockwise from the top left corner): hexane, cyclopentadiene, benzene, and toluene. The solvent trajectory is represented by an overlay of solvent configurations acquired at different instants of time. Solvent particles (white) avoid the solute, thus forming a cavity of the matching size and shape.

Fig. 2.7 provides illustration for more structurally complex solutes, showing four hydrocarbons immersed in the LJ solvent. For these molecules we see again that the geometries of the systems are reflected in the size and shape of the solute cavity. Depending on the nature of interactions between the solvent and solute the partial molar volume of a solute may vary substantially (see discussion in Section 2.6). Importantly, while experimental determination of partial molar volumes is limited to stable species, our MD method is equally applicable to calculation of partial molar volumes of stable and short lived and transient species (such as conformers and TS), which is crucial for the theoretical analysis of activation volumes, volume profiles, and conformation equilibria presented in the subsequent chapters.

2.3. MD Volumes

In order to test the suitability of the OPLS force field[26] for the displacement volume calculations we performed MD simulations and obtained the molar volumes for a number of hydrocarbon systems. The results shown in Tables 2.3 and 2.4 demonstrate good agreement between calculated and experimental volumes for pure hydrocarbons and octane-benzene mixtures of various compositions.

Table 2.3. Experimental (V_{exp}) and calculated (V_{calc}) molar volumes (cm^3/mol) of octane-benzene mixtures at 1 bar and 25°C arranged in the order of increasing mole fraction of octane, x_{octane}.

x_{octane}	V_{exp} [a]	V_{calc}
0	89.4	89.7
0.1	97.9	98.4
0.2	105.1	105.2
0.3	112.2	112.4
0.4	120.3	120.4
0.5	127.4	127.5
0.6	133.8	133.8
0.7	141.8	141.5
0.8	148.8	148.2
0.9	156.6	156.1
1	163.5	162.7

[a] data from Ref 27

Table 2.4. Experimental (V_{exp}) and calculated (V_{calc}) molar volumes (cm^3/mol) of pure hydrocarbons at 1 bar.

Hydrocarbon	T	V_{exp} [a]	V_{calc}
Cyclopentadiene	20°C	82.4	83.5
Cyclopentene	20°C	88.2	90.9
Cyclopentane	20°C	94.0	97.8
Benzene	20°C	89.1	89.2
1,3-Cyclohexadiene	20°C	95.3	96.4
Cyclohexene	20°C	101.4	103.8
Cyclohexane	20°C	108.1	109.8
n-Hexane	25°C	130.4	129.3 [b]
Toluene	25°C	106.9	105.0
Methylcyclohexane	20°C	127.6	127.8
n-Octane	25°C	163.5	162.7
n-Dodecane	25°C	227.3	225.8 [b]

[a] data from Ref 28
[b] data from Ref 29

2.4. Displacement Volumes

The molecular volumes were then calculated using eq. (2.8) as differences $V_{257} - V_{256}$ of volumes of 257- and 256-molecule systems. The results are listed in Table 2.5 and are of a comparable quality to the bulk volumes listed in Table 2.4. The convergency of the displacement volumes to the experimental values is good over sufficiently long MD trajectories, as illustrated by Fig. 2.8 for the case of isoprene.

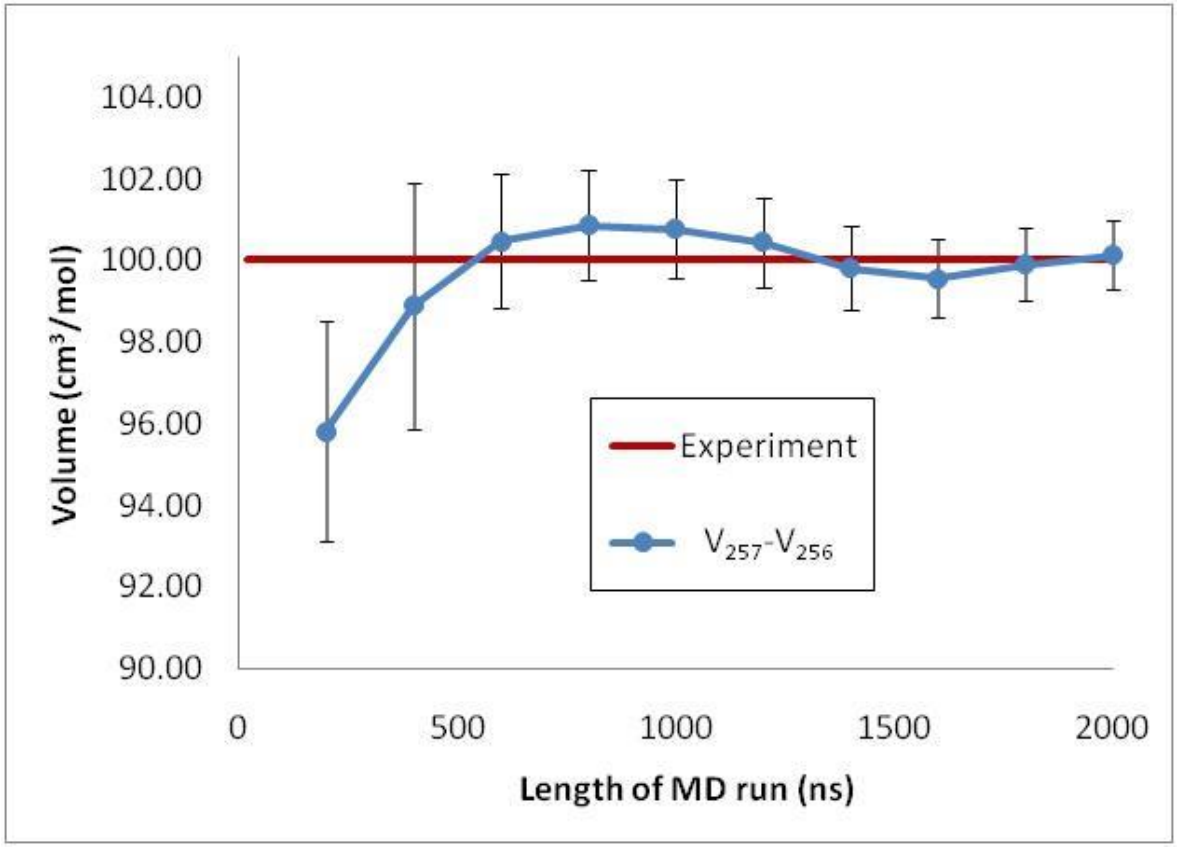

Figure 2.8. Displacement volume of a single isoprene molecule calculated using eq. (2.8) as a difference between volumes of 257- and 256-particle systems in comparison with the experimental molar volume of isoprene.

To study how well the displacement volumes of eq. (2.8) predict the solvent dependence of the partial molar volumes, we performed MD simulations of selected hydrocarbons in polar and nonpolar solvents. Inspection of the results listed in Table 2.5 shows that with the exception of methane in hexane, the experimental partial molar volumes of hydrocarbons in nonpolar solvents are well reproduced by the calculated displacement volume. We believe that the mentioned discrepancy for methane may be due to a somewhat inaccurate experimental value. Indeed, as can be seen from Table 2.6,

Table 2.5. Experimental (V_{exp}) and calculated (V_{calc}) partial molar volumes (cm^3/mol) of some hydrocarbons in nonpolar and polar solvents. The hydrocarbons are arranged in the order of increasing molar mass; the solvents are arranged in the order of increasing polarity.

Hydrocarbon	Solvent	Solvent model	V_{calc} [a]	V_{exp}	T
Methane	*n*-Hexane	OPLS	55.1	60.0 [b]	25°C
	Water	TIP4P [c]	41.4	37.3 [f]	25°C
		SPC [d]	42.5 (42.0)		
		Flexible SPC [e]	36.3		
Ethane	*n*-Hexane	OPLS	69.5	69.3 [b]	25°C
	Water	TIP4P [c]	60.5	51.2 [f]	25°C
		SPC [d]	62.1 (60.3)		
		Flexible SPC [e]	49.4		
Benzene	*n*-Octane	OPLS	92.0 [g]	91.4 [g]	25°C
	Benzene	OPLS	89.7 [h]	89.4 [h]	25°C
	Di-*n*-butyl ether	OPLS	87.4 (90.1)	89.7 [j]	25°C
	Water	TIP4P [c]	93.7	83.1 [f]	25°C
		SPC [d]	96.0 (90.6)		
		Flexible SPC [e]	86.3		
Cyclohexane	Cyclohexane	OPLS	109.8 [i]	108.1 [i]	20°C
	Di-*n*-butyl ether	OPLS	112.6 (110.1)	109.9 [j]	25°C
n-Hexane	*n*-Hexane	OPLS	129.3 [i]	130.4 [i]	25°C
	Di-*n*-butyl ether	OPLS	128.9 (130.9)	131.5 [j]	25°C

[a] Coulombic energies were calculated by direct summation with cut-off radius of 0.9-1.0 nm; the volumes calculated using PME[30] are given in parentheses for comparison;

[b] data from Ref. 11; [c] rigid water model, Ref. 31;

[d] rigid water model, Ref. 32; [e] flexible water model, Ref. 33;

[f] data from Ref. 12; [g] a three-point estimate based on the data of Table 2.3;

[h] data from Table 2.3; [i] data from Table 2.4; [j] data from Ref. 34

Table 2.6. Experimental partial molar volumes (cm^3/mol) of methane and ethane in various solvents at 25°C (adapted from Ref. 11).

Solvent	$V_{methane}$	V_{ethane}
n-perfluoroheptane	68.4	82.9
n-hexane	60.0	69.3
carbon tetrachloride	52.4	65.9
benzene	52.2	66.0
carbon disulphide	56.1	67.4

comparing partial molar volumes of methane and ethane in various solvent, 55-57 cm^3/mol volume may be a more reasonable estimate for methane in hexane, as it fits better with the rest of the data. A greater error in methane data may be attributed to a much lower solubility of methane.[35]

Direct summation of electrostatic interactions with the cut-off radius of 0.9-1.0 nm works reasonably well, although the use of the more accurate PME technique[30] offers some improvement. Thus, in the cases of hexane and cyclohexane (Table 2.5), the use of PME reduces the difference bewteen calculated and experimental molar volumes from 2.6-2.7 cm^3/mol to 0.2-0.6 cm^3/mol. The strongest effect of 5.4 cm^3/mol volume reduction was observed for benzene in water calculations using the SPC[32] model. However, even an improved PME result (90.6 cm^3/mol) is still much greater than the experimental value of 83.1 cm^3/mol. Overall, partial molar volumes for aqueous solutions, obtained with the standard rigid models of water (SPC or TIP4P[31]) appear completely inadequate. However, switching to a flexible water model[33] brings the displacement volumes within a 1-3 cm^3/mol margin of the experimental data and somewhat improve the results of a recent study[25o]. Fig. 2.9 illustrates the difference between the cases of the rigid and flexible water models. Although the cavity sizes seem roughly the same in both cases, their shapes are distinctly different. Flexible water

molecules seem to be able to reach further in some angular directions, thus reducing the overall volume of the cavity. It is interesting to note that this "penetration" effect of the flexible water cannot be detected by comparing C-O radial distribution functions (Fig. 2.10), likely due to spherical averaging of the latter.

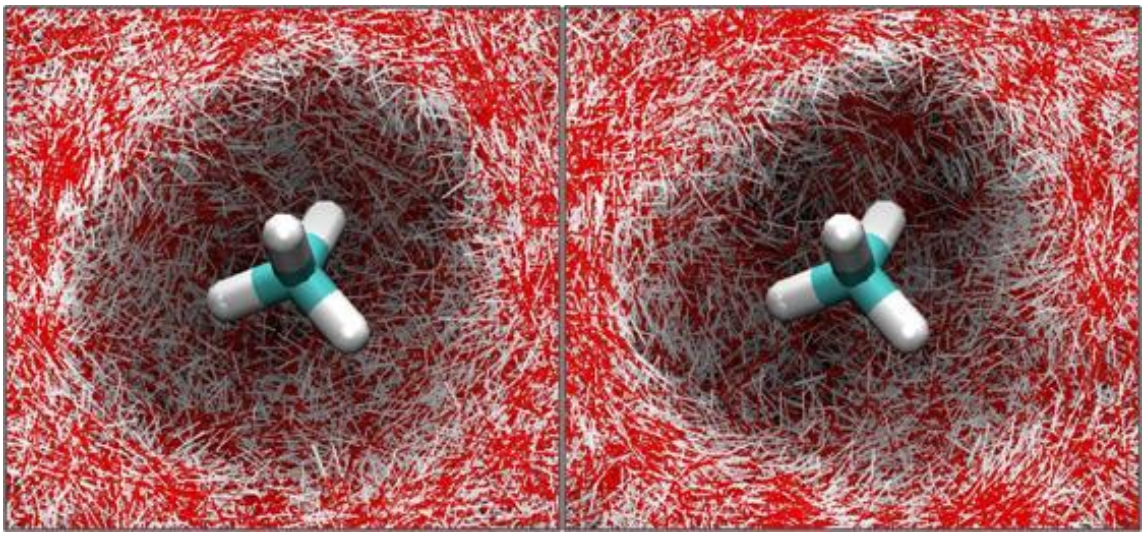

Figure 2.9. Methane molecule in a rigid (left) and flexible (right) water solvent. Although the rough sizes of cavities are equal, their shapes are somewhat different, which results in a 6 cm^3/mol difference in the calculated partial molar volumes.

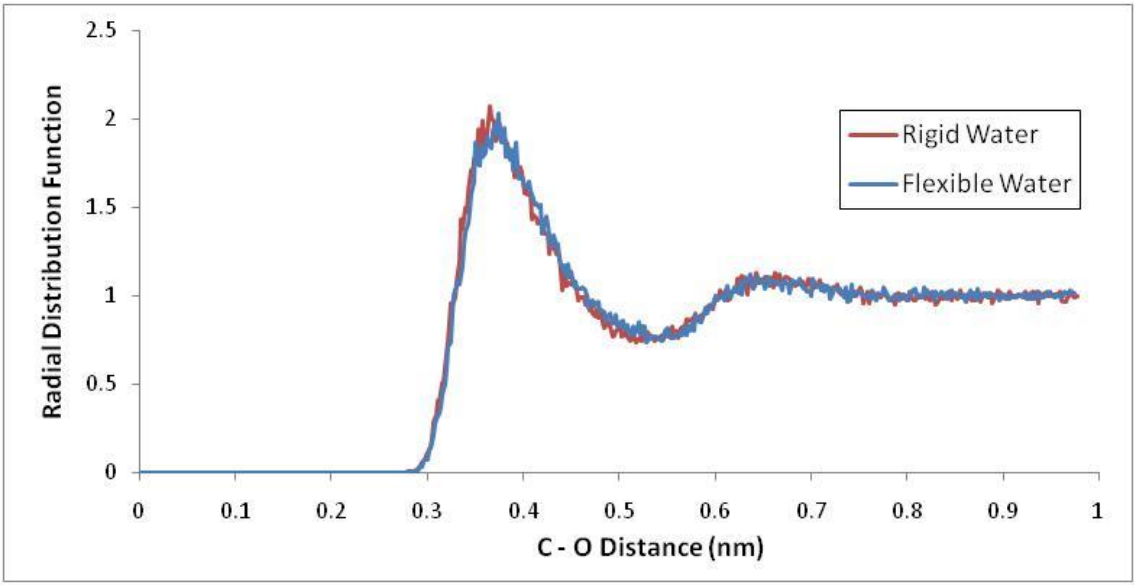

Figure 2.10. Radial distribution functions (C-O distances) for a methane molecule in rigid and flexible water solvents.

We have also applied our method to the calculation of partial molar volumes of polar solutes. The displacement volumes calculated for a number of aqueous amino acids in their zwitterionic forms are given in table 2.7, showing good agreement with the experimental values.

Table 2.7. Experimental (V_{exp}) and calculated (V_{calc}) partial molar volumes (cm^3/mol) of some aqueous amino acids in their zwitterionic forms at 25°C

Zwitterion	V_{calc} [a]	V_{exp} [b]
Glycine	42.4	43.2
Alanine	58.4	60.3
Valine	89.5	91.3
Isoleucine	105.4	106.8
Leucine	107.0	107.5

[a] Coulombic energies were calculated by direct summation with cut-off radius of 0.9-1.0 nm;
[b] data from Ref. 36;

2.5. Technical Aspects

The volume fluctuations in a constant-pressure MD simulation are quite significant. In fact, they exceed the value of an incremental volume increase due to a single molecule (see fig 2.11). These large fluctuations complicate the determination of volumes; however, reasonably short correlation times (Fig. 2.12) allow us to use the standard block-averaging procedure[37] to obtain average volumes with sufficient accuracy. The error of volume determination decreases as the square root of the length of the MD trajectory and, as seen from Fig. 2.13, good convergency can be achieved over a reasonable period of simulation time.

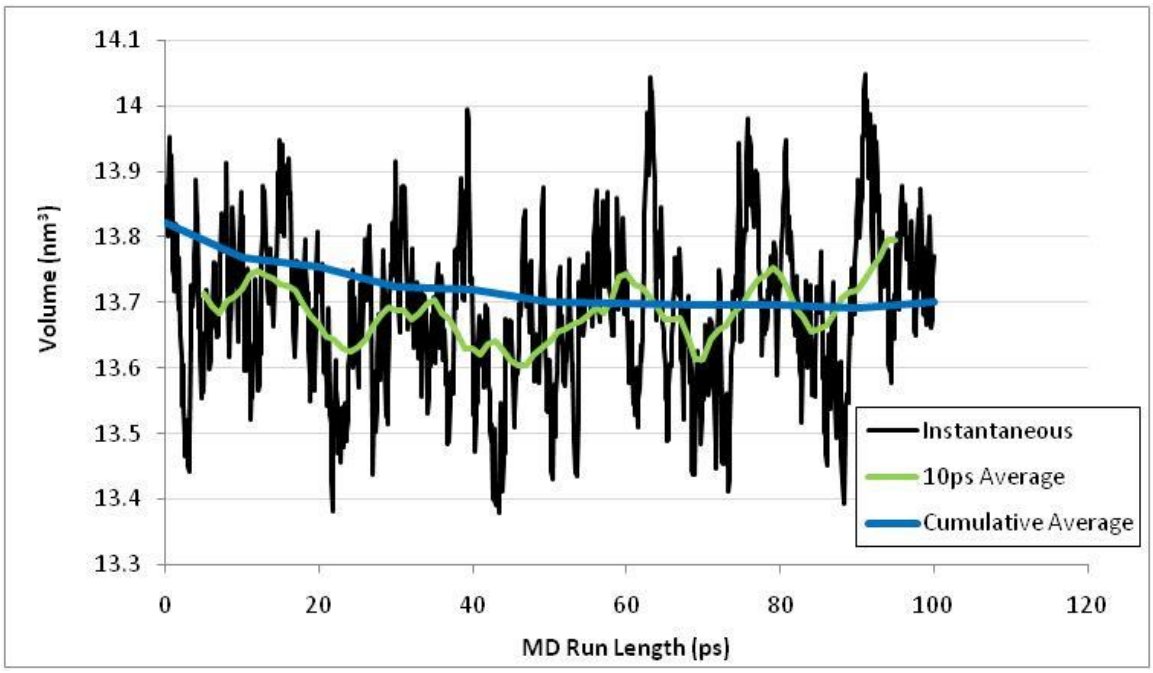

Figure 2.11. The instantaneous and average MD volumes of a system of 256 LJ particles. The incremental contribution from a single particle is *ca.* 0.05 nm^3. Large amplitude fluctuations of the instantaneous volume are somewhat stabilized by averaging over 10 ps intervals. Further improvement is reached by using a cumulative average.

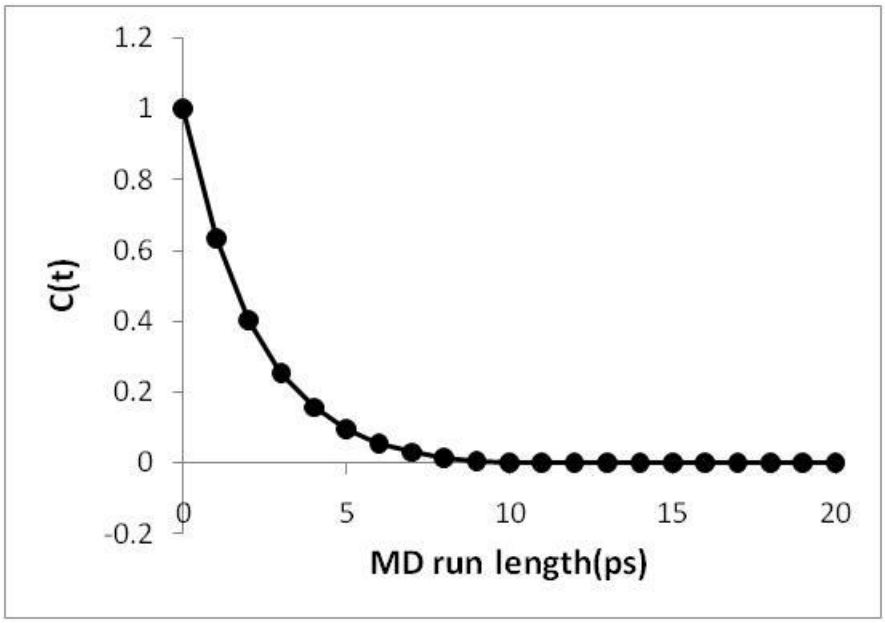

Figure 2.12. Volume autocorrelation function $C(t) = \frac{\langle (V(\tau)-\overline{V})(V(\tau+t)-\overline{V})\rangle_\tau}{\langle (V(\tau)-\overline{V})^2\rangle_\tau}$ for the system of 256 LJ particles at 300 K and 1 kbar.

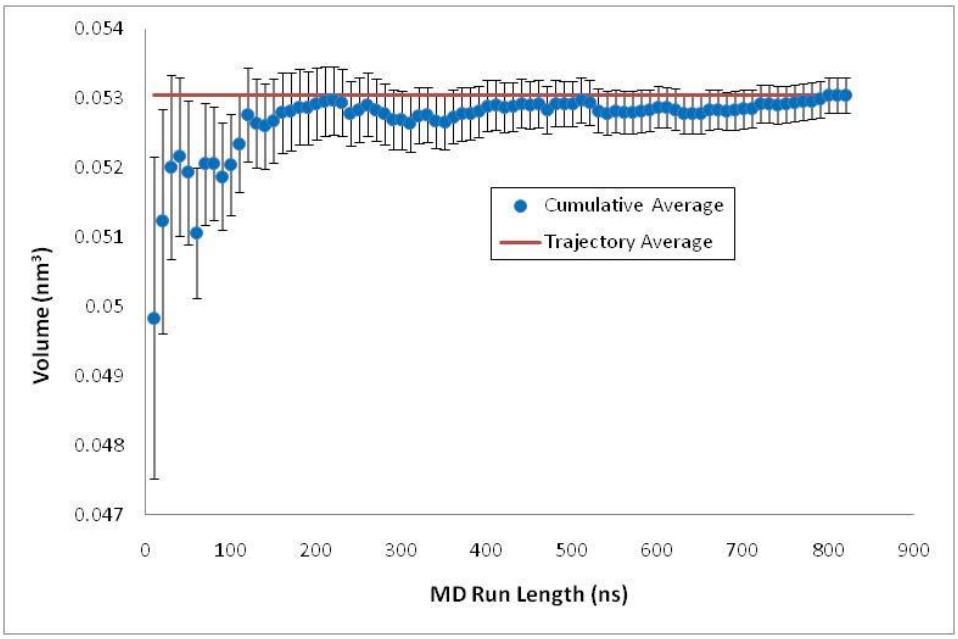

Figure 2.13. Displacement volume of a single LJ solvent particle calculated using eq. (2.8) as a difference between volumes of 257 and 256-particle systems.

2.6. An MD-enhanced Geometrical Model

2.6.1. The MD Based Calculation of Molecular Surface Area

Molecular surface, or more precisely its area, is a concept widely used in various empirical correlations, such as QSAR[38]. Although our MD volume model does not directly provide the value of a physically nonexistent molecular surface area, this area, as an empirical parameter, can be obtained by a combination of the MD volume model with a simple geometrical model, such as solvent accessible model discussed in Section 2.1, where molecular surface plays a key role. The molecular surface and the volume delimited by it depend on the choice of the probe sphere radius, which can be adjusted so that the molecular volume defined by this radius matches the MD-generated volume of the system. The probe radius thus defined emulates the combined effect of solvent, packing, and thermal expansion. Clearly, this eliminates any predictive power of the model with respect to volume, but affords a more reasonable estimate of the molecular surface area matching the proper molecular volume.

2.6.2. Volumes and Surface Areas of Disubstituted Benzenes

The environmental fate of organic compounds, including pesticides and insecticides, is an important problem due to its environmental implications and the resulting economic impact. Partition of these compounds between soil components, biophases, and water is crucial to understanding of their environmental degradation.[39] This interface equilibrium is frequently described in terms of the octanol-water partition coefficient K_{ow},[40] which can be expected to correlate with the hydrophobic (*n=nonpolar*) and hydrophilic (*p=polar*) surface areas of organic compounds in octanol (*o*) and water (*w*) solvents in terms of the following linear QSAR:[41]

$$logK_{ow} = \alpha_{no}S_{no} + \alpha_{po}S_{po} + \alpha_{nw}S_{nw} + \alpha_{pw}S_{pw} + \alpha_{ow} \qquad (2.9)$$

To obtain the molecular surface areas needed in eq. (2.9), we applied the approach described in Section 2.6.1. The compounds of interest were the ortho, meta, and para isomers of diethoxy-, dipropoxy-, and diallyloxy-benzene (Fig. 2.14), which are being developed as new insect behavioral control agents for agricultural applications[42] because they mimic naturally occurring plant odorants and have been shown to affect olfactory responses of moths[38]

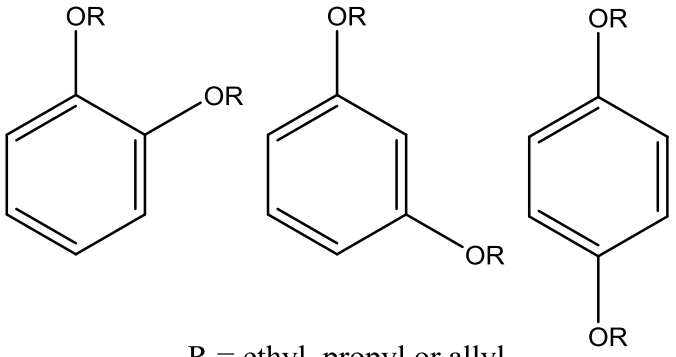

R = ethyl, propyl or allyl

Figure 2.14. Dialkoxybenzenes studied.

Experimental molecular volumes for these compounds were not available, so their partial molar volumes in aqueous solvent and octanol were calculated using the MD displacement volume method. It was then possible to match the accessible surface

volumes to these results by adjusting the probe radii. Using these same radii we were then able to obtain the hydrophobic and hydrophilic surface areas for each compound in water and octanol. The results are listed in Table 2.8.

Table 2.8. Calculated volumes and surface areas for dialkoxybenzenes of Fig. 2.14.

	Volume (cm^3/mol)		Augmenting radii increments (nm)[a]		Hydrophobic Surface Area (nm^2)[b]		Hydrophilic Surface Area (nm^2)[b]	
	octanol	water	octanol	water	octanol	water	octanol	water
1,2-diethoxybenzene	163.4	165.1	0.084	0.085	2.35	2.36	0.15	0.15
1,2-dipropoxybenzene	198.3	197.6	0.088	0.088	2.81	2.81	0.12	0.12
1,2-diallyloxybenzene	182.2	185.4	0.079	0.081	1.86	1.87	0.96	0.98
1,3-diethoxybenzene	165.1	163.2	0.085	0.084	2.36	2.35	0.12	0.12
1,3-dipropoxybenzene	194.5	195.1	0.085	0.086	2.78	2.80	0.11	0.11
1,3-diallyloxybenzene	191.0	183.2	0.084	0.080	1.92	1.88	0.93	0.91
1,4-diethoxybenzene	164.0	165.0	0.085	0.085	2.36	2.36	0.14	0.14
1,4-dipropoxybenzene	197.1	197.5	0.086	0.087	2.76	2.77	0.14	0.14
1,4-diallyloxybenzene	187.1	187.3	0.083	0.083	1.86	1.86	0.98	0.98

The molecular surface areas listed in the table were then used to obtain coefficients α of eq. (2.8) by the least squares fit to the experimental values of partition coefficients. With the exception of *p*-diethoxybenzene, the values of logK_{ow} obtained from eq. (2.9) correlated well with experimental data[39](Fig. 2.15).

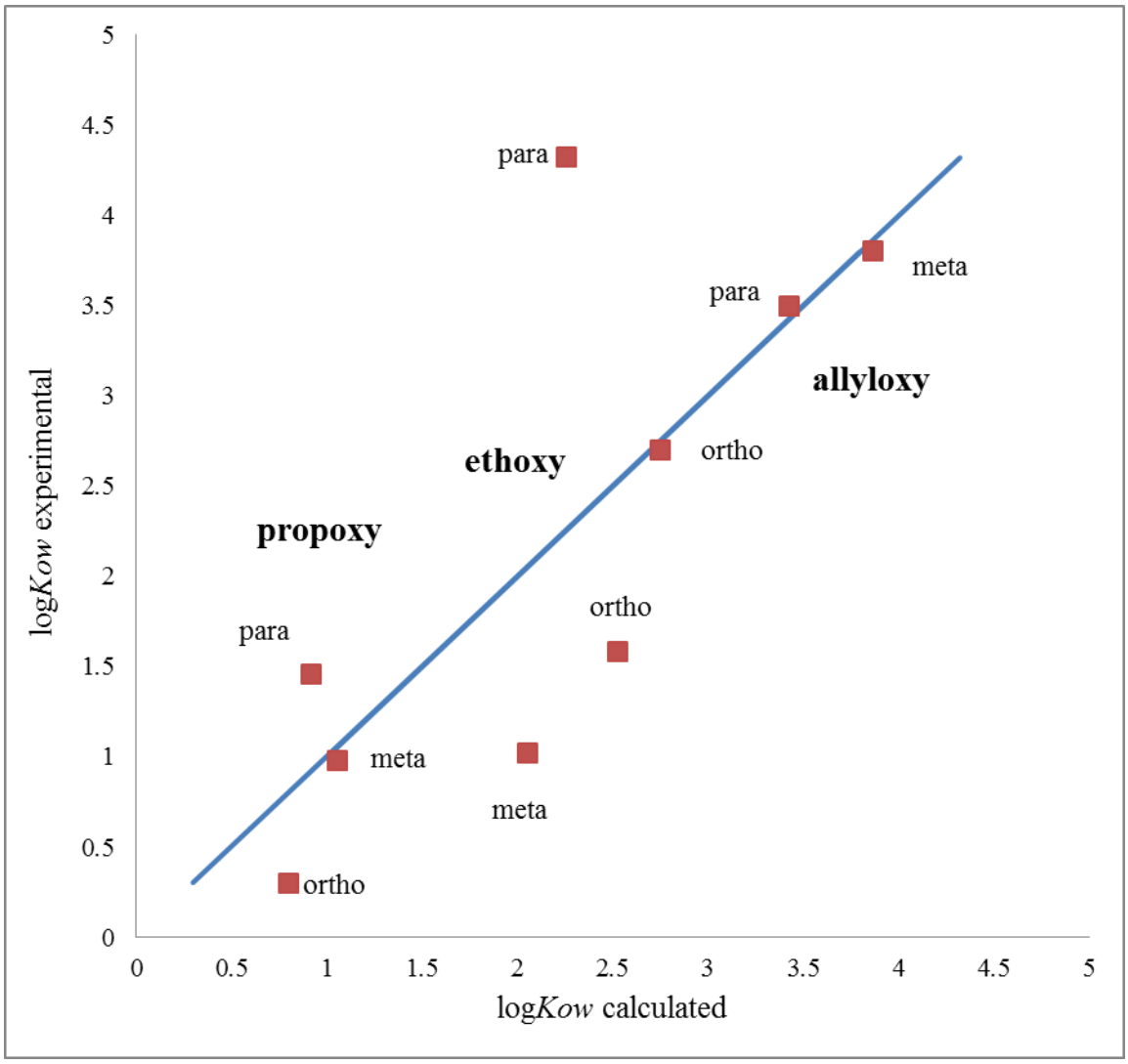

Figure 2.15. Correlation between experimental octanol–water partition coefficients and those estimated from the hydrophobic/hydrophilic molecular surface areas.

2.7. Conclusion

The results presented in this chapter demonstrate that the displacement volume model is sufficiently accurate to be used for theoretical calculation of molecular volumes of stable molecules and that the standard OPLS force field works well for both polar and nonpolar systems. We can therefore proceed to the calculation of theoretical activation and reaction volumes as described in the subsequent chapters. It was also shown that our MD displacement volumes can be used as a tool to improve the performance of the

solvent accessible surface model, allowing for the inclusion of previously neglected effects of the solvent and thermal expansion in the determination of the molecular surface area.

2.8. References

1. J.C.McGowan;A.Mellors, Molecular Volumes in Chemistry and Biology, Wiley: NY, 1986.
2. J. Spooner, H. Wiebe, N. Boon, E. Deglint, E. Edwards, B. Yanciw, B. Patton, L. Thiele, P. Dance, N. Weinberg, *Phys. Chem. Chem. Phys.*, 2012, **14**, 2264.
3. A.E. Stearn and H. Eyring, *Chem. Rev.*, 1941, **29**, 509
4. M. J. Evans and M. Polanyi, *Trans. Faraday Soc*., **1935,** *31*, 875; (b) A. E. Stearn, and H. Eyring, *Chem. Rev.*, **1941**, *29*, 509; (c) S. D. Hamann, *Physico-Chemical Effects of Pressure*; Academic Press: New York, **1957**; (d) M. G. Gonikberg, *Chemical equilibria and reaction rates at high pressures*; National Science Foundation: Washington, **1963**; (e) N. S. Isaacs, *Liquid Phase High Pressure Chemsitry*; Wiley: New York, **1981.**
5. M. Basilevsky, N. Weinberg and V. Zhulin, *J. Chem. Soc. Faraday Trans.* 1, 1985, **81**, 875.
6. J. Spooner, B. Yanciw, B. Wiebe and N. Weinberg, *J. Phys. Chem. A* 2014, **118**, 765.
7. (a) A.I. Kitaigorodskii, Organic Chemical Crystallography, Consultants Bureau: New York, 1961; (b) A. Bondi, *J. Phys. Chem.*, 1964, **68**, 441; (c) A. Gavezzotti, *J. Am. Chem. Soc.*, 1983, **105**, 5220; (d) A. Gavezzotti, *J. Am. Chem. Soc.* 1985, **107**, 962; (e) R. Lustig, *Molec. Phys.*, 1985, **55**, 305; (f) K. Gibson, and H. Scheraga, *Mol. Phys.*, 1987, **62,** 1247; (g) A. Gavezzotti, *Acta. Cryst.*, 1988, **B44**, 427; (h) J. Alejandre, S.E. Martinez-Casas and G.A., Chapela, *Mol. Phys.*, 1988, **65**, 1185; (i) A. Gavezzotti, *J. Am. Chem. Soc*., 1989, 111, 1835; (j) A. Gavezzotti, *J. Am. Chem. Soc.*, 1989, **111**, 1835; (k) L.R. Dodd and D.N.

Theodorou, *Mol. Phys.*, 1991, **72**, 1313; (l) M. Petitjean, *J. Comput. Chem.*, 1994, **15**, 507; (m) M. Irisa, *Comp. Phys. Comm.*, 1996, **98**, 317.

8. B. Lee and F. M. Richards, *J. Mol. Biol.*, 1971, **55**, 379;
9. (a) F. M . Richards, *Annu. Rev. Biophys. Bioeng.*, 1977, **6**, 151; (b) M. Pavlov and B. Federov, *Biopolymers*, 1983, **22**, 1507; (c) T.J. Richmond, *J. Mol. Biol*., 1984, **178**, 63; (d) M.L. Connolly, *J. Appl. Cryst*., 1985, **18**, 499; (e) F.M. Richards, *Methods Enzymol*., 1985, **115**, 440; (f) M.L. Connolly, *Science*, 1983, **221**, 709; (g) M.L. Connolly, *J. Am. Chem. Soc.*, 1985, **107**, 1118; (g) C. Kundrot, J. Ponder and F.M. Richards, *J. Comp. Chem.*, 1991, **12**, 402.
10. S.S. Batsanov, *Inorg. Mat.*, 2001, **37**, 871.
11. J. Chr. Gjaldbaek, and J. H. Hildebrand, *J. Am. Chem. Soc.*, 1950, **72**, 1077.
12. W.L. Masterton, *J. Chem. Phys.*, 1954, **22**, 1830.
13. J L Hales, *J. Phys. E: Sci. Instrum.*, 1970, **3**, 855.
14. M. Gonikberg, and A. Kitaigorodskii, *Doklady Akademii Nauk SSSR*, 1958, **122**, 231.
15. (a) T. Asano and W. J. le Noble, *Rev. Phys. Chem. Jpn.*, 1973, **43**, 82; (b) M. V. Basilevsky, N. N. Weinberg, and V.M. Zhulin: *J. Mol. Liquids*, 33, 29-51(1986), (c) N. Weinberg, Rev. High Pressure Sci. Tech., **1998**, *8***,** 86.
16. F.-G. Klärner, B. Krawczyk, V. Ruster, and U.K. Deiters, *J. Am. Chem. Soc.*, 1994, **116**, 7646
17. (a) R.F.W. Bader, W.H. Henneker and P.E.J Cade, *Chem. Phys.* 1967, **46**, 3341; (b) R.F.W. Bader, M.T. Carroll, J.R. Cheeseman and C. Chang, *J. Am. Chem. Soc.*, 1987, **109**, 7968; (c) P. Walker, and P. Mezey, *J. Am. Chem. Soc.*, 1994, **116**, 12022; (d) K.B. Wiberg, P.R. Rablen, D.J. Rush, and T.A. Keith, *J. Am. Chem. Soc.*, 1995,**117**, 4261; (e) K.B. Wiberg, T.A. Keith, M.J. Frisch, and M. Murcko, *J. Phys. Chem.*, 1995, **99**, 9072; (f) M.W. Wong, K.B. Wiberg and M.J. Frisch, *J. Comp. Chem.*, 1995, **16**, 385; (g) A. Mitchell, and M. Spackman, *J. Comp. Chem.*, 2000, **21**, 933;
18. B.J. Smith and N.E.J. Hall, *J. Comput. Chem.*, 1998, **19**, 1482.

19. C. Lim, S.L. Chan, and P. Tole, In *Structure and Reactivity in Aqueous Solution*, C.J. Cramer and D.G. Truhlar, Eds., ACS, Washington, DC, 1994.
20. (a) D.X. Zhao, L.D. Gong, Z.Z. Yang, *Chem. J. Chin. Univ.*, 2001, **22**, 1893; (b) D.X. Zhao, L.D. Gong and Z.Z. Yang, *Chin. Sci. Bull.*, 2002, **47**, 635; (c) D.X. Zhao, L.D. Gong and Z.Z. Yang, *J. Phys. Chem. A*, 2005, **109**, 10121.; (d) L.D. Gong and Z.Z. Yang, *J. Comp. Chem.*, 2010, **31**, 2098.
21. F.G. Klärner and F. Wurche, *J. Prakt. Chem.*, 2000, **342**, 609.
22. R.A. Marcus, *J. Chem. Phys.*, 1956, **24**, 966, 979; ibid. 1957, **26**, 867; *Discuss. Faraday Soc*., 1960, **29**, 129.; N.S. Hush. Trans. Faraday Soc. **57**, 557 (1961).
23. D.R. Stranks, *Pure Appl. Chem.*, 1974, **38**, 303.
24. (a) T. Swaddle, *Inorg. Chem.*, 1990, **29**, 5018; (b) T. Swaddle, *J. Mol. Liq.*, 1995, **65/66**, 237; (c) T. Swaddle, *Can. J. Chem.*, 1996, **74**, 631; (d) T. Swaddle and P. Tregloan, *Coord. Chem. Rev.*, 1999, **187**, 255; (e) T. Swaddle, *Chem. Rev.*, 2005, **105**, 2573.
25. (a) C. Lin and R. Wood, *J. Phys. Chem.*, 1996**, 100**, 16399; (b) N. Matubayasi and R. Levy, *J. Phys. Chem.*, 1996**, 100**, 2681; (c) D. Lockwood and P. Rossky, *J. Phys. Chem. B*, 1999**, 103**, 1982; (d) C.C. Chai and M.S. Jhon, *Mol. Sim.*, 2000, **23**, 257; (e) T. Imai, M. Kinoshita and F. Hirata, *J. Chem. Phys.*, 2000, **112**, 9469; (f) V.M. Dadarlat and C.B. Post, *J. Phys. Chem. B*, 2001, **105**, 715; (g) R. DeVane, C. Ridley, R. Larsen, B. Space, P. Moore, and S. Chan, *Biophys. Journ.*, 2003, **85**, 2801; (h) F. Floris, *J. Phys. Chem. B*, 2004, **108**, 16244; (i) C. Ridley, A.C. Stern, T. Green, R. DeVane, B. Space, J.Miksosvska and R.W. Larsen, *Chem. Phys. Lett.*, 2006, **418**, 137; (j) M. Sabaye, and H.S. Chan, J. Chem. Phys., 2007, **126**, 114507; (k) A.V. Sangwai and H.S. Ashbaugh, *Ind. Eng. Chem. Res.*, 2008, **47**, 5169; (l) S. Sarupria, T. Ghosh, A. Garcia, and S. Garde, *Proteins*, 2010, **78**, 1641; (m) I. Yu, T. Tasaki, K. Nakada and M. Nagaoka, *J. Phys. Chem. B*, 2010, **114**, 12392; (n) J.B. Rouget, T. Aksel, J. Roche, J.L. Saldana, A.E. Garcia, D. Barrick and C.A. Royer, *J. Am. Chem. Soc.*, 2011, **133**, 6020; (o) N. Patel, D. Dubins, R. Pomès, and T. Chalikian, *J. Phys. Chem. B*, 2011, **115**, 4856;

(p) J. Vilseck, J. Tirado-Rives, W.J. Jorgensen, *Phys. Chem. Chem. Phys.*, 2015, **17**, 8407.

26. (a) W.L. Jorgensen and J. Tirado-Rives, *J. Am. Chem. Soc.*, 1988, **110**, 1657; (b) W.L. Jorgensen, D.S. Maxwell and J. Tirado-Rives, *J. Am. Chem. Soc.*, 1996, **118**, 11225.
27. L. Moravkova, Z. Wagner, and J. Linek, *J. Chem. Thermodyn.*, 2008, **40,** 607.
28. *CRC Handbook of Chemistry and Physics*, ed. D.R. Lide, CRC Press, FL, 90th edn, 2009.
29. J. Ho, S. Reimer and N. Weinberg, *High Press. Res.*, 2009, **29**, 587.
30. (a) T. Darden, D. York and L. Pedersen, *J. Chem. Phys.*, 1993, **98**, 10089; (b) U. Essmann, L. Perera, M.L. Berkowitz, T. Darden, H. Lee and L.G. Pedersen, *J. Chem. Phys.*, 1995, **103**, 8577.
31. W.L. Jorgensen, J. Chandrasekhar, J.D. Madura, R.W. Impey and M.L. Klein, *J. Chem. Phys.*, 1983, **79**, 926.
32. H.J.C. Berendsen, J.P.M. Postma, W.F. van Gunsteren and J. Hermans, *Jerusalem Symposia on Quantum Chemistry and Biochemistry*, 1981, Reidel: Dordrecht, Holland, 331-342.
33. K.Toukan and A. Rahman, *Phys. Rev. B*, 1985, **31**, 2643. We used the following parameters available in Gromacs: OH bond length – 0.10 nm, OH stretch force constant – 345000 kJ $mol^{-1}nm^{-2}$, HOH bond angle – 109.47°, HOH bending force constant – 383 kJ $mol^{-1}rad^{-2}$.
34. L. Bernazzani, N. Ceccanti, G. Conti, P. Gianni, V. Mollica and M.R.Tine, *J. Chem. Thermodynamics*, 2001, **33**, 629.
35. (a) W.J. le Noble, *Prog. Phys. Org. Chem.*, 1967, **5**, 207; (b) T. Asano and W.J. le Noble, *Chem. Rev.*, 1978, **78**, 407; (c) R. van Eldik, T. Asano and W.J. le Noble, *Chem. Rev*., 1989, **89**, 549; (d) A. Drljaca, C.D. Hubbard, R. van Eldik, T. Asano, M.V. Basilevsky and W.J. le Noble, *Chem. Rev.*, 1998, **98**, 2167.
36. F. Millero, A. L. Surdo, and C. Shin, *J. Phys. Chem.*, 1978, **82**, 784.
37. (a) H. Flyvbjerg, and H. Petersen, *J. Chem. Phys.*, 1989, **91**, 461; (b) B. Hess, *J. Chem. Phys.*, 2002, **116**, 209.

38. J. Debruijn, and J. Hermens, *Quant. Struct.-Act. Relat.* 1990, **9**, 11; W. J. Dunn, *Prog. Clin. Biol. Res.* 1989, **291**, 47; W. J. Dunn, M. G. Koehler, and S. Grigoras, *J. Med. Chem.* 1987, **30**, 1121; D. Stanton, B. Mattioni, J. Knittel and P. Jurs, *J. Chem. Inf. Comput. Sci.*, 2004, **44**, 1010.
39. R. D. Wauchope, S. Yeh, J. Linders, R. Kloskowski, K. Tanaka, B. Rubin, A. Katayama, W. Kordel, Z. Gerstl, M. Lane, and J. B. Unsworth, *Pest Man. Sci.*, 2002, **58**, 419.
40. S. H. Yalkowsky and S.C. Valvani, *J. Med. Chem.*, 1976, **19**,727.
41. P. Ebrahimi, J. Spooner,N. Weinberg, E. Plettner, *Chemosphere*, 2013, **93**, 54.
42. (a) E. Plettner and R. Gries, *J. Agric. Food Chem.*, 2010, **58**, 3708; (b) Y. Gong and E. Plettner, *Chem. Senses*, **2011**, *36*, 291.

Chapter 3.

Reaction and Activation Volumes

The utility of reaction and activation volumes as mechanistic tools has been outlined in Chapter 1. As discussed, the main limitation restricting their use to a qualitative level is the lack of a reliable method for relating the volumes of molecular systems to their structure. The displacement model of molecular volume introduced in Chapter 2 resolves this problem, allowing for quantitative analysis of experimental reaction and activation volumes. In this chapter we will show that this method is capable of generating accurate theoretical values of reaction and activation volumes with errors comparable to those of experiment.

3.1. Reaction Volumes

As discussed in Chapter 1, the reaction volume ΔV is defined as the difference $\Delta V = V_P - V_R$ between partial molar volumes of reactants (V_R) and products (V_P). For stable species, the values of V_R and V_P can be directly measured, thus giving ΔV by eq. (1.2). In cases involving unstable and short-lived compounds, as in conformational equilibria where individual conformers cannot be isolated, the value of ΔV is determined by the reversal of eq. (1.1)[1]

$$\Delta V = -RT\left(\frac{\partial lnK}{\partial P}\right)_T \qquad (3.1)$$

as the isothermal logarithmic pressure derivative of the equilibrium constant *K*, usually assessed spectroscopically.[2] The errors of such determination, typically based on a linear

approximation for $K(P)$, can be relatively high in comparison with the values of ΔV, as illustrated in Table 3.1 by the case of *anti-gauche* isomerization of 1,2-dichloroethane.[3]

Table 3.1. Conformational volume changes, ΔV, reported for the *anti-gauche* isomerization of 1,2-dichloroethane by different authors.[3]

Literature source	Solvent	Pressure range, kbar	Rough appearance of $K(P)$	ΔV, cm^3/mol	
				Reported[a]	Linearly estimated[b]
Ref 3a	20% in hexane	0 – 4	linear	–3.5	–3.2
	30% in hexane	0 – 5	linear	–3.8	–3.8
Ref 3b	neat	0 – 2.3	linear	–2.7	–3.1
Ref 3c	2-methylbutane	0 – 7.5	linear	–2.9	–2.7
Ref 3d	diethyl ether	0 – 26.4	nonlinear	–2.4[c]	–
		0 – 5.2	linear	–	–5.1
		0.6 – 5.2	linear	–	–3.7
		5.2 – 26.4	linear	–	–1.4
Ref 3e	neat	0.6 – 5.0	linear	–0.6	–0.6

[a] ΔV value as reported in the literature source
[b] ΔV value obtained in the present work by linear regression based on $K(P)$ values reported in the literature source
[c] ΔV value reported in the literature source based on the exponential fit to $K(P)$ data

Our displacement model of molecular volume[4] is applicable to all molecular species regardless of their stability. It is therefore suitable for calculation of molar volumes of conformers, and thus conformational volume changes. In this section we use this model for calculation of the volume changes for conformational equilibria in 1,2-dichloroethane,[3] 2-chloro- and 2-bromobutane,[5,6] 1-chloro- and 1-bromo-2-methylpropane,[5,6] and 1-bromo-butane, pentane, and hexane.[7] Further, to mimic the experimental procedure and for the purpose of comparison, we also generate theoretical values for the corresponding equilibrium constants over a range of pressures and obtain reaction volumes for these equilibria from eq. (3.1) using a variety of empirical equations describing their pressure dependence.[8]

3.1.1. Direct Calculation of Reaction Volume for Conformational Change

Conformational volume changes were calculated directly from eq. (1.2) using the MD-based displacement volume method,[4] as illustrated by Fig. 3.1 for the case of *anti-gauche* isomerization of 1,2-dichloroethane.

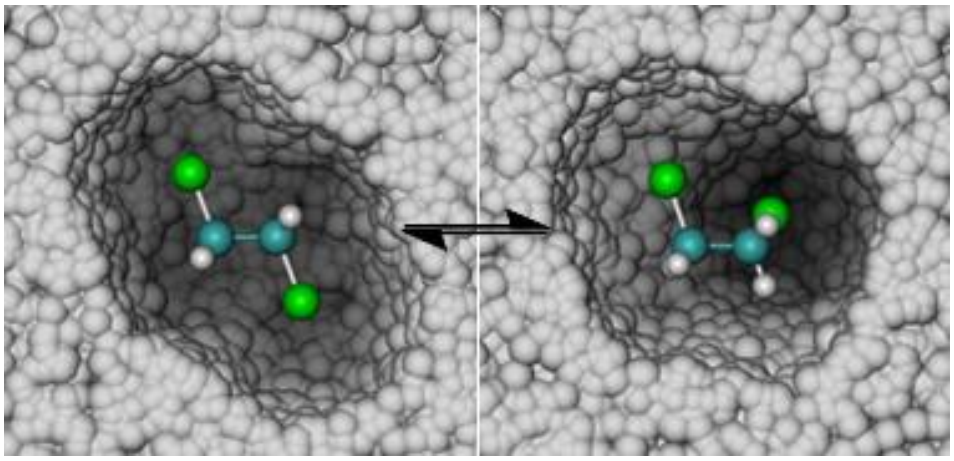

Figure 3.1. 1,2-dichloroethane in *anti* (left) and *gauche* (right) conformations immersed in a solvent (represented here by an overlay of solvent particles, positions of which are sampled along the MD trajectory). Due to a short-range repulsion, the solvent avoids the solute, which results in the creation of a solvent cavity of size and shape specific to the solute conformation. Color scheme: H – white, C – light blue, Cl – green, solvent – light grey.

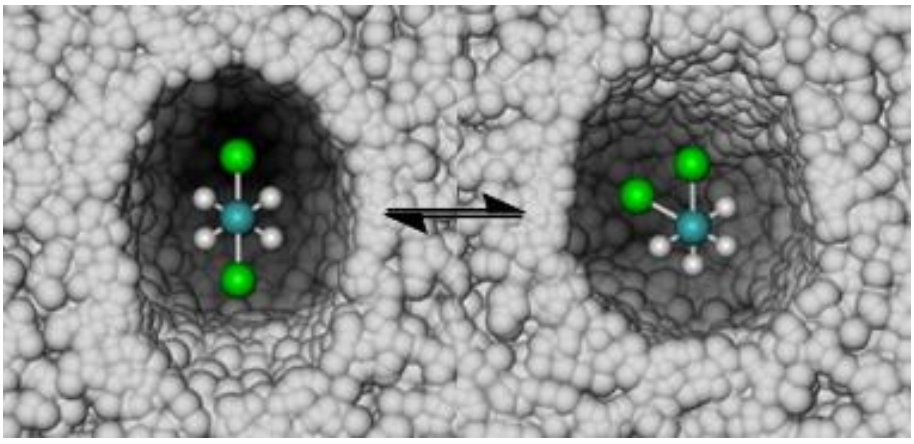

Figure 3.2. Newman projection of *anti* (left) and *gauche* (right) conformations of 1,2-dichloroethane immersed in a solvent (the color scheme is the same as in Fig. 3.1). Despite an obvious difference in the shapes of solvent cavities for these conformations, their volumes do not seem to differ too much.

It is interesting to note that, although the shapes of the solvent cavities differ significantly for the *gauche* and *anti* conformations of 1,2-dichloroethane, their volumes are quite similar (see Fig. 3.2). This situation seems to be quite typical for the observed conformational volume changes, the reported values of which are usually small.[2] Consequently, to obtain these small values theoretically, the volumes of conformers must be calculated with an extreme accuracy, preferably within a fraction of 1 cm^3/mol. As can be seen from the convergency plots of Fig. 3.3, this stringent accuracy requirement was met by our calculations.

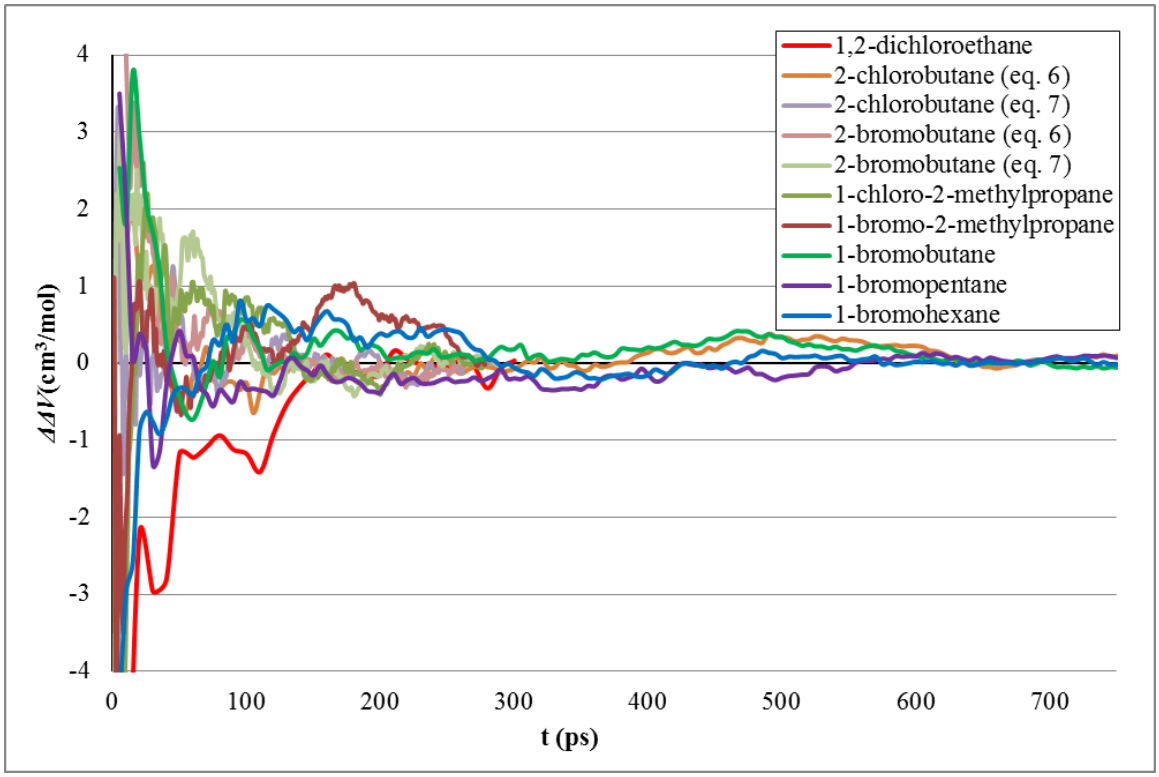

Figure 3.3. Convergency of the conformational volume changes calculated using the displacement volume method.[4] The level of convergency is measured by the deviation $\Delta\Delta V(t) = \Delta V(t) - \Delta V_\infty$ of the cumulative average $\Delta V(t)$ from the trajectory average ΔV_∞.

Table 3.2. Calculated and experimental conformational volume changes, ΔV, for selected neat halogenated hydrocarbons.

Halogenated hydrocarbon	Conformational transformation	ΔV, cm^3/mol		Literature source
		Calculated[a]	Experimental	
1,2-dichloroethane	eq. (3.2)	–3.6	–2.7	Ref 3b
			–0.6	Ref 3e
2-chlorobutane	eq. (3.3)	–0.9	–1.5	Ref 5
	eq. (3.4)	–0.3	–0.8	Ref 5
2-bromobutane	eq. (3.3)	–0.8	2.0	Ref 5
	eq. (3.4)	–0.4	0.6	Ref 5
1-chloro-2-methylpropane	eq. (3.5)	–0.8	0.5	Ref 5
1-bromo-2-methylpropane	eq. (3.5)	–1.2	–1.7	Ref 5
1-bromobutane	eq. (3.6)	–1.0	–0.8	Ref 7
1-bromopentane		–1.0	–1.0	Ref 7
1-bromohexane		–0.9	–0.5	Ref 7

[a] ΔV values calculated using the displacement volume method[4] using eq. (1.2)

Table 3.2 lists the calculated and experimental values of the conformational volume changes for selected neat halogenated hydrocarbons, undergoing conformational transformations described by eqs. (3.2)-(3.6):

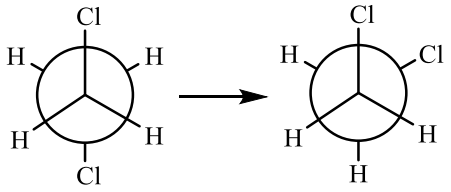

(3.2)

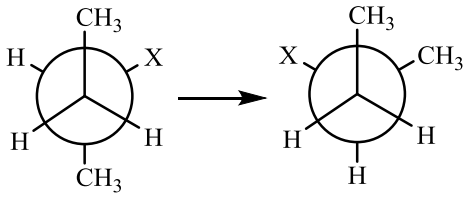

(3.3)

X=Cl,Br

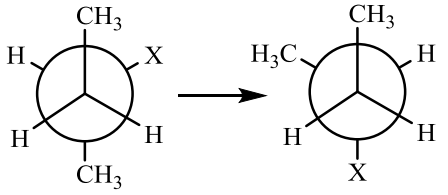

X=Cl,Br (3.4)

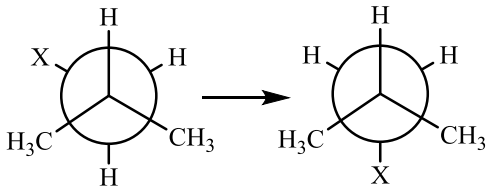

X=Cl,Br (3.5)

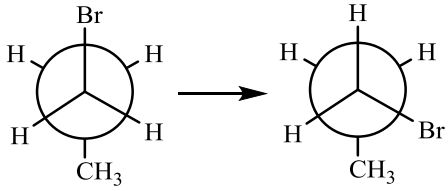

R=C_4H_9, C_5H_{11}, C_6H_{13} (3.6)

Comparison of the experimental and MD calculated ΔV values shows a close match in most cases, with the exception of 2-bromobutane and 1-chloro-2-methylpropane for which the reported experimental ΔV are positive. We believe that these discrepancies are due to inaccuracy in the experimental values. As can be seen in Table 3.3, ΔV values reported for the same transformations in hexane solvent are all negative and are closely matching our values calculated for neat solution. Since such solvent-dependent switch in the sign of the volume changes is not observed for the similar cases of 2-chlorobutane and 1-bromo-2-methylpropane, it seems likely that the positive experimental ΔV values for 2-bromobutane and 1-chloro-2-methylpropane are erroneous.

Table 3.3. Experimental conformational volume changes, ΔV, for selected halogenated hydrocarbons in hexane.

Halogenated hydrocarbon	Conformational transformation	ΔV, cm^3/mol[a]
2-chlorobutane	eq. (3.3)	–1.8
	eq. (3.4)	–0.5
2-bromobutane	eq. (3.3)	–1.4
	eq. (3.4)	–0.9
1-chloro-2-methylpropane	eq. (3.5)	–0.6
1-bromo-2-methylpropane	eq. (3.5)	–0.5

[a] Ref 6

3.1.2. Conformational Volume Changes Obtained From Equilibrium Constants

Due to the small size of the halogenated hydrocarbons considered in our calculations, direct MD simulations of their conformational equilibria was feasible and was performed for temperature and pressures matching the experimental conditions. These calculations were limited to the subset of the systems and processes listed in Table 3.2, for which the experimental $K(P)$ were available. The simulated equilibrium constants were obtained as the ratios of the resident times spent by the systems in the targeted conformations. The convergency trends are shown in Fig. 3.4. The calculated equilibrium constants plotted in Figs. 3.5-3.9 match the experimental constants within the limits of the experimental errors. In all cases the pressure dependences of the equilibrium constants, both experimental and simulated, look roughly linear. The conformational volume changes, ΔV, obtained from the slopes of their linear regressions are also included in the figures.

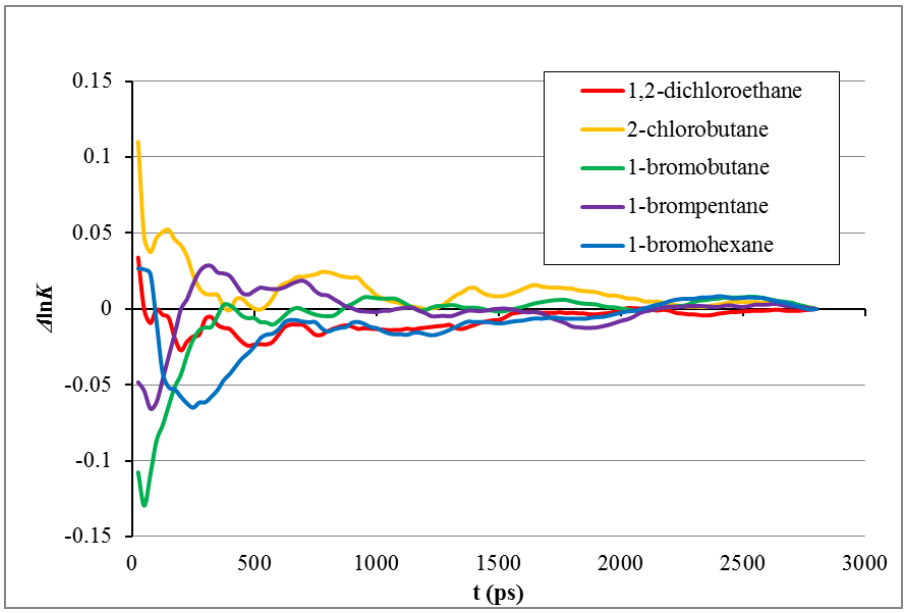

Figure 3.4. Convergency of the ambient pressure equilibrium constants obtained by MD simulations of conformational equilibria. The level of convergency is measured by the deviation $\Delta \ln K(t) = \ln K(t) - \ln K_\infty$ of the cumulative average $K(t)$ from the trajectory average K_∞. In the energy scale, $\Delta \ln K$ = 0.05 corresponds to the Gibbs energy difference of only 0.12 kJ/mol.

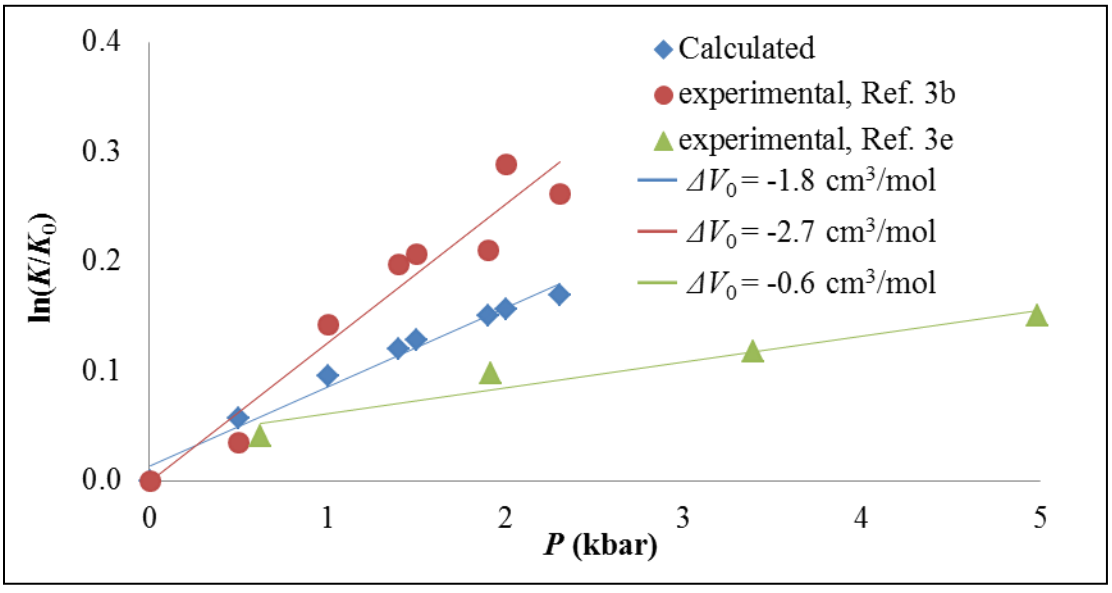

Figure 3.5. Calculated and experimental equilibrium constants at 298K and various pressures for *anti-gauche* conformational equilibrium in 1,2-dichloroethane (eq. 3.2). The indicated values of the conformational volume changes were obtained using eq. (3.1) from the slopes of the respective linear regressions.

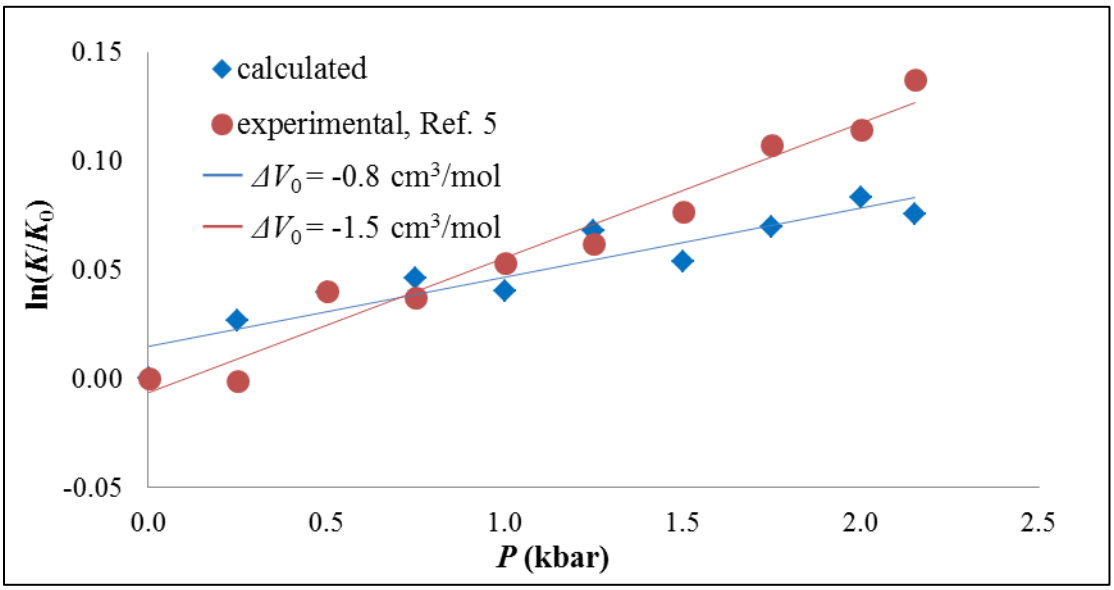

Figure 3.6. Calculated and experimental equilibrium constants at 298K and various pressures for ± *synclinal* conformational equilibrium in 2-chlorobutane (eq. 3.3). The indicated values of the conformational volume changes were obtained using eq. (3.1) from the slopes of the respective linear regressions.

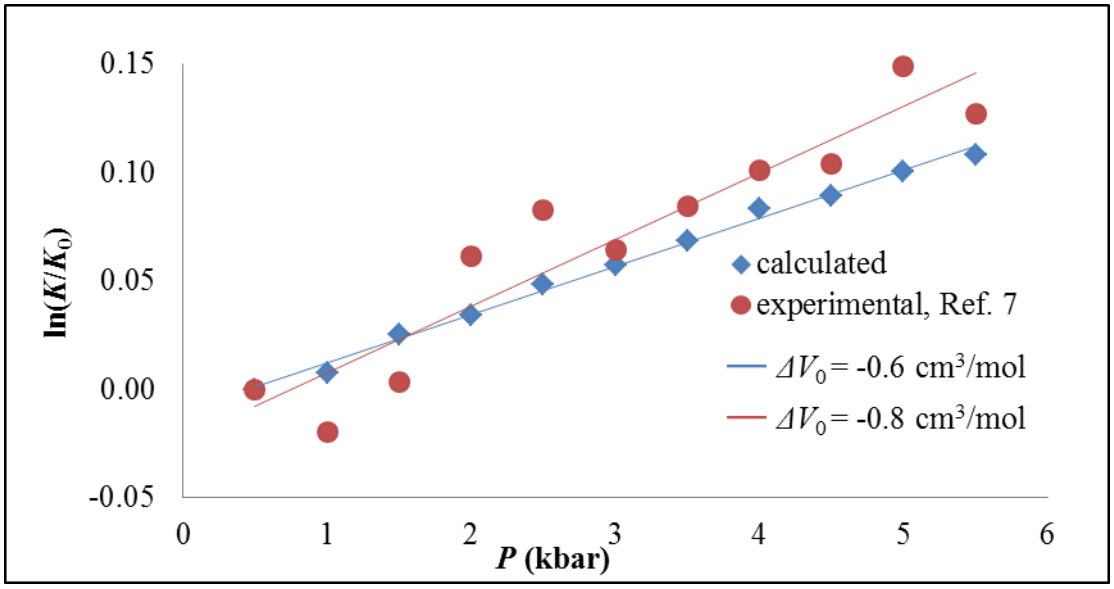

Figure 3.7. Calculated and experimental equilibrium constants at 298K and various pressures for *anti-gauche* conformational equilibrium in 1-bromobutane (eq. 3.6). The indicated values of the conformational volume changes were obtained using eq. (3.1) from the slopes of the respective linear regressions.

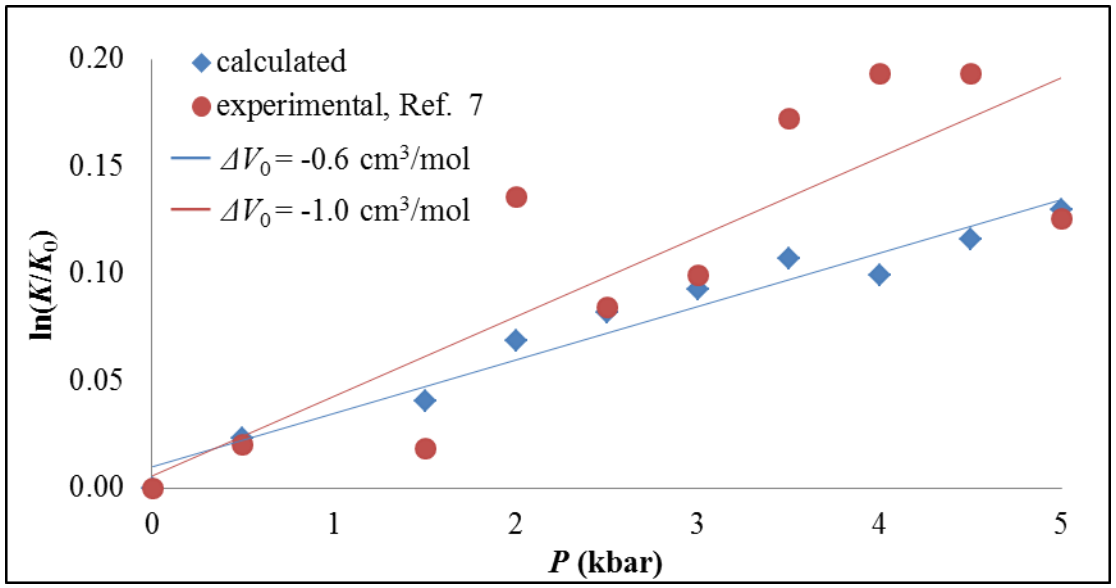

Figure 3.8. Calculated and experimental equilibrium constants at 298K and various pressures for *anti-gauche* conformational equilibrium in 1-bromopentane (eq. 3.6). The indicated values of the conformational volume changes were obtained using eq. (3.1) from the slopes of the respective linear regressions.

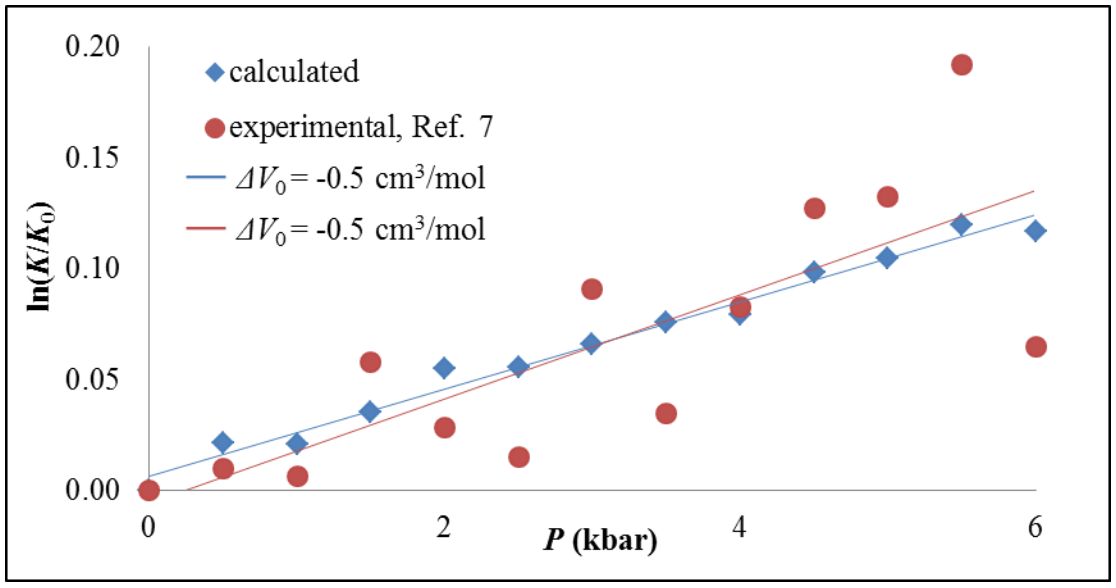

Figure 3.9. Calculated and experimental equilibrium constants at 298K and various pressures for *anti-gauche* conformational equilibrium in 1-bromohexane (eq. 3.6). The indicated values of the conformational volume changes were obtained using eq. (3.1) from the slopes of the respective linear regressions.

Although the idea of using linear regression for obtaining ΔV from $K(P)$ might seem reasonable, there is ample evidence in the literature that linear (and often quadratic) regression is inadequate for this purpose for the data spread over a wide pressure range.[8,9] As discussed in Section 1.4, a variety of more elaborate empirical fitting functions has been proposed for that purpose, the most reliable of which (see Chapter 5) are listed below starting with the quadratic eq. (3.7):[8]

$$\ln K/K_0 = a_1 P + a_2 P^2 \tag{3.7}$$

$$\ln K/K_0 = a_3 P/(1 + a_4 P) \tag{3.8}$$

$$\ln K/K_0 = a_1 P + a_3 P/(1 + a_4 P) \tag{3.9}$$

$$\ln K/K_0 = a_2 \ln(1 + a_4 P) \tag{3.10}$$

$$\ln K/K_0 = a_1 P + a_2 \ln(1 + a_4 P) \tag{3.11}$$

The ΔV values obtained from equations (3.7)-(3.11) fitted to the experimental and simulated $K(P)$ data of Figs. 3.5-3.9 are listed in Tables 3.4 and 3.5.

Table 3.4. Conformational volume changes, ΔV (in cm^3/mol), obtained from eq. (3.1) using linear regression and nonlinear functions (3.7)-(3.11) fitted to the ***experimental*** $K(P)$ data of Figs. 3.5-3.9.

System	Literature source	Fitting function					
		Linear	eq (3.7)	eq (3.8)	eq (3.9)	eq (3.10)	eq (3.11)
1,2-dichloroethane	Ref 3b	–2.7	–4.3	–4.2	–4.3	–4.2	–4.3
1,2-dichloroethane	Ref 3e	–0.6	–1.1	–2.0	–2.1	–2.3	–2.1
2-chlorobutane	Ref 5	–1.5	–1.1	–1.5	–1.1	–1.5	–1.5
1-bromobutane	Ref 7	–0.8	–1.6	–1.6	–1.6	–1.6	–[a]
1-bromopentane	Ref 7	–1.0	–1.2	–1.3	–1.2	–1.3	–1.2
1-bromohexane	Ref 7	–0.5	–0.6	–0.6	–[a]	–0.6	–[a]

[a] Failed fit (see text).

Table 3.5. Conformational volume changes, ΔV (in cm^3/mol), obtained from eq. (3.1) using linear regression and nonlinear functions (3.7)-(3.11) fitted to the ***simulated*** $K(P)$ data of Figs. 3.5-3.9.

System	Fitting function					
	Linear	eq (3.7)	eq (3.8)	eq (3.9)	eq (3.10)	eq (3.11)
1,2-dichloroethane	–1.8	–2.7	–3.0	–3.4	–3.2	–3.5
2-chlorobutane	–0.8	–1.3	–2.0	– [a]	–2.7	– [a]
1-bromobutane	–0.6	–0.7	–0.7	–0.7	–0.7	–0.7
1-bromopentane	–0.6	–0.9	–1.0	–0.9	–1.0	–0.9
1-bromohexane	–0.5	–0.6	–0.6	– [a]	–0.6	– [a]

[a] Failed fit (see text).

There was a notable difference in the case of 1,2-dichloroethane between ΔV values obtained using eqs. (3.7)-(3.11) and those assessed by linear regression, both for the volume changes derived from the experimental and simulated $K(P)$ data, with the simulated values matching very closely the average of the values obtained from two of the available experimental sources.[3b,e] In the case of monohalogenated hydrocarbons of Tables 3.3 and 3.4, this difference was no longer essential, which should likely be attributed to the smaller absolute values of ΔV resulting in a much lesser pressure dependence of K. In a few instances eqs. (3.9) and (3.11) failed to produce a reasonable fit and generated obviously wrong conformational volume changes. This is consistent with our analysis[8b], presented in Chapter 5 of this thesis, of the performance of various fitting functions, including eqs. (3.7)-(3.11), which indicates that tri-parametric eq. (3.9) and (3.11) tend to display an instability of the fit when the level of errors in $K(P)$ is relatively high.

3.2. Activation Volumes

So far, all calculations in this work using the MD displacement volume method have been carried out for stable systems well described by the OPLS force field[10]. However, neither OPLS nor any other common empirical force field[11] is parameterized

for TS's. Therefore, the major challenge in obtaining activation volumes from our MD simulations is the lack of available force field parameters for the TS's. Fortunately, this problem can be resolved using QM based approaches toward parameterization, which have become increasingly widespread in recent years.[12] In these approaches, force field parameters are obtained by fitting classical force fields to the QM deformation energies. We adopt this approach in order to generate the necessary OPLS parameters for transient species.

3.2.1. Parameterization of Transition States

In the OPLS force field, the total energy of a molecule can be separated into two contributions – intra- and intermolecular:

$$U = U^{inter} + U^{intra} \tag{3.12}$$

The intramolecular contribution U^{intra} includes bond angle, and out-of-plane deformation terms described by harmonic potentials and torsion terms described by a combination of cos functions of the torsion angles:

$$\begin{aligned} U^{intra} &= U_{bond} + U_{angle} + U_{oop} + U_{torsion} \\ U_{bond} &= \sum_{bonds} k_b (b - b_0)^2 \\ U_{angle} &= \sum_{angles} k_\theta (\theta - \theta_0)^2 \\ U_{oop} &= \sum_{angles} k_\psi (\psi - \psi_0)^2 \\ U_{torsion} &= \sum_{torsions} \sum_{n=1}^{4} \frac{V_n}{2} [1 + (-1)^{n+1} cos\{n(\varphi - \varphi_0)\}] \end{aligned} \tag{3.13}$$

The intermolecular contribution, U^{inter}, consists of van der Waals, U_{vdw}, and electrostatic interactions, U_{es}, between molecules and is represented by the Lennard-Jones and Coulomb potentials, respectively:

$$U^{inter} = U_{vdW} + U_{es}$$
$$U_{vdW} = U_{LJ} = \sum_{i=1}^{N} \sum_{j=i+1}^{N} \left(4\varepsilon_{ij} \left[\left(\frac{\sigma_{ij}}{r_{ij}} \right)^{12} - \left(\frac{\sigma_{ij}}{r_{ij}} \right)^{6} \right] \right) \quad (3.14)$$
$$U_{es} = \sum_{i=1}^{N} \sum_{j=i+1}^{N} \frac{q_i q_j}{4\pi\varepsilon_0 r_{ij}}$$

Though intermolecular parameters ε, σ, and q can also be parameterized using QM, in this work we rely on their values previously adapted from OPLS,[4] and focus primarily on obtaining the intramolecular parameters k_b, k_θ, k_ψ and V_n.

The required parameters were obtained by minimizing the function

$$\Phi^{intra} = \sum_{n=1}^{N_{conf}} \left(U_{n,QM}^{intra} - U_{n,MD}^{intra} \right)^2 \quad (3.15)$$

where N_{conf} is the number of sampled geometrical configurations of the target molecule, $U_{n,QM}^{intra}$ is the QM calculated energy, and $U_{n,MD}^{intra}$ is the intramolecular part of the classical force field described by eq. 3.13 obtained for n-th configuration. Configurations were sampled from an MD trajectory with the TS structure constrained along the reaction coordinate but flexible in all remaining degrees of freedom. The initial guess parameters were taken from OPLS. This approach is implemented in the program ForceBalance[12c,d] which was used for the parameterization of all TS in this work.

3.2.2. Calculation of Activation Volumes

Activation volumes were calculated according to eq. (1.4) as the differences $\Delta V^{\neq} = V^{\neq} - V_R$ for two non-polar reactions: Diels-Alder dimerization of isoprene, and hydrogen transfer from methane to methyl radical.

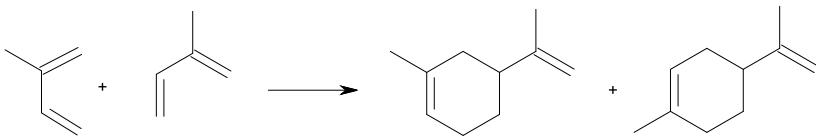

(3.16)

$$CH_3H + {}^{\bullet}CH_3 \longrightarrow CH_3^{\bullet} + HCH_3 \qquad (3.17)$$

The MD calculated activation volumes for reactions 3.16 and 3.17 are given in table 3.6 and show good agreement with the experimental data.

Table 3.6. Comparison of experimental ($\Delta V^{\neq}_{exp}$) and calculated ($\Delta V^{\neq}_{calc}$) activation volumes for reactions (3.16)-(3.17).

Reaction	Solvent	$\Delta V^{\neq}_{calc}$	$\Delta V^{\neq}_{exp}$
Dimerization of Isoprene	Bromobutane[a]	-31.0 ± 1.9	-33.9
Hydrogen Transfer	Hexane	-18.9 ± 2.2	~ -20[b]

[a] Kinetic data from ref. 13

[b] Estimated from experimental data for similar reactions[2]

3.3. Computational Details

MD simulations were performed using the GROMACS software package[14] for systems with 1000 molecules maintained at constant pressure and temperature conditions using Berendsen temperature and pressure coupling[15] with τ_T = 0.1 ps and τ_P = 1.0 ps. For the displacement volume calculations of conformational volumes, 10 molecules locked in the desired conformations by harmonic restraints (see Fig. 3.10) were added as solutes. For the activation volume calculations 1 molecule, either reactant or TS, was added as the solute. The MD trajectories were obtained via leap-frog integration[16] with a time step of 1 fs in a cubic box with periodic boundary conditions and an interaction cutoff of 1.0 nm

for Lennard-Jones interactions. The long-range electrostatic interactions were calculated using the particle mesh Ewald method[17] with a real-space cut off of 1.0 nm. The lengths of the trajectories were determined by the convergency of the calculated quantities and ranged from 0.8 to 1.5 ns for volume calculations and from 13 to 85 ns for equilibrium constant calculations. The OPLS force field[10] was used for organic molecules in all cases. Intramolecular parameters for TS were parameterized using ForceBalance[7d,e], with conformational sampling of 5000 configurations taken from an MD simulation of 1000 TS "molecules" at temperature and pressure conditions matching the experiment. Single point energy calculations for the conformers were performed using Gaussian 09 suite[18] at the B3LYP/6-31G++G(d,p) level.

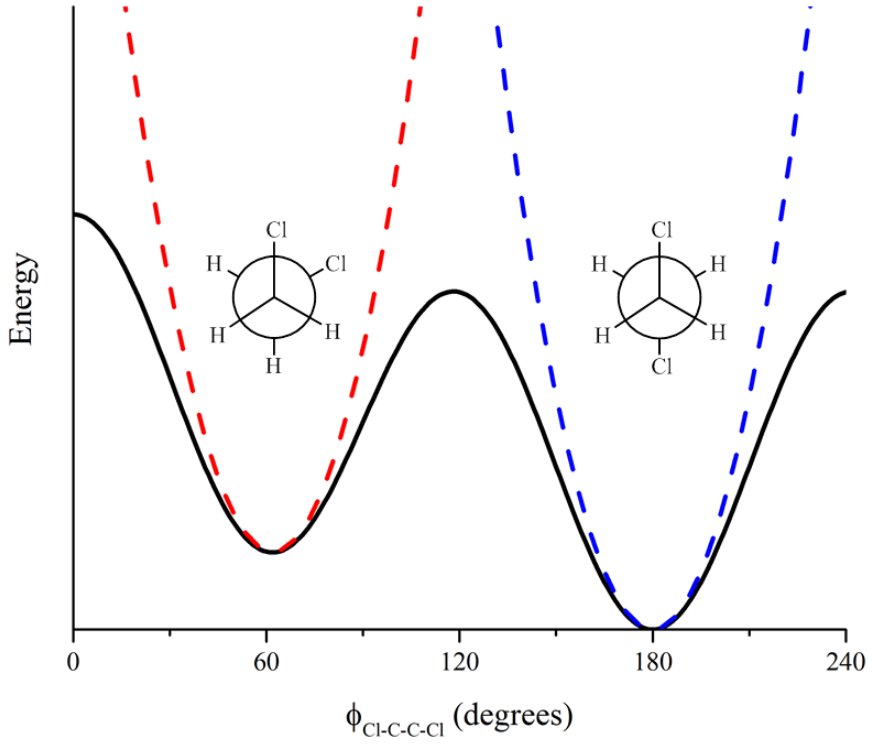

Figure 3.10. Torsional profiles of the unconstrained 1,2-dichloroethane and its harmonically restrained *anti* and *gauche* conformations.

3.4. Conclusion

A comparison of the data listed in Table 3.2-3.4 proves that ΔV values obtained by the displacement volume method and those assessed from the pressure dependence of the equilibrium constant, both experimental and simulated, match quite closely, which recommends the displacement volume technique as a reliable tool for theoretical assessment of the conformational volume changes. The rather quick convergence of the volume values obtained using this technique makes its application feasible for studying conformational equilibria in much more complex molecular systems than the halogenated hydrocarbons discussed here.

The choice of a fitting function for $K(P)$ remains an important issue in analysis of the experimental data. Quadratic equation (3.7) worked quite well for all conformational equilibria considered in this work, likely due to the fact that the absolute values of the conformational volume changes did not exceed 5 cm^3/mol, resulting in only slight curving of $K(P)$. For that reason even linear regression worked reasonably well. This situation is dramatically different from the case of the pressure dependence of the rate constants for reactions with significant activation volumes, where quadratic equation fails quite badly in its application to kinetic data over the pressure ranges exceeding 1-2 kbar.[8b] Chapter 5 of the thesis offers a thorough examination of this topic.

No less importantly, the results shown in Table 3.5 demonstrate that, paired with a reliable parameterization protocol, the displacement volume method can provide accurate values of theoretical activation volumes. These volumes are sensitive to the geometry of the TS and thus can be used, together with the high-pressure kinetic data, for the analysis of the reaction mechanisms, similar to the traditional analysis based on the comparison of the calculated and experimental activation energies.

3.5. References

1. (a) M. Planck, *Ann. Phys.* 1887, **268**, 462. (b) S.D. Hamann, *Physico-Chemical Effects of Pressure*; Academic Press: New York, 1957. (c) M.G. Gonikberg, *Chemical Equilibria and Reaction Rates at High Pressures*; National Science Foundation: Washington, DC, 1963. (d) N. S. Isaacs, Liquid Phase High Pressure Chemsitry; Wiley: New York, 1981.
2. W.J. le Noble, *Prog. Phys. Org. Chem.*, 1967, **5**, 207; (b) T. Asano and W.J. le Noble, *Chem. Rev.*, 1978, **78**, 407; (c) R. van Eldik, T. Asano and W.J. le Noble, *Chem. Rev*., 1989, **89**, 549; (d) A. Drljaca, C.D. Hubbard, R. van Eldik, T. Asano, M.V. Basilevsky and W.J. le Noble, *Chem. Rev.*, 1998, **98**, 2167.
3. (a) Y.Taniguchi, H. Takaya, P.T.T Wong and E. Whalley, *J. Chem. Phys.*, 1981, **75**, 4815; (b) H. Nomura, K. Murasawa, N. Ito, F. Iida and Y. Udagawa, *Bull. Chem. Soc. Jpn.*, 1984, **57**, 3321; (c) S. Ikawa and E. Whalley, *J. Chem. Phys*, 1984, **81**, 1620; (d) B.L. McClain and D. Ben-Amotz, *J. Phys. Chem. B*, 2002**, 106**, 7882; (e)R.J. Sabharwal, Y. Huang, and Y. Song, *J. Phys. Chem. B*, 2007**, 111**, 7267.
4. (a) E. Deglint, H. Martens, E. Edwards, N. Boon, P. Dance and N. Weinberg, *Phys. Chem. Chem. Phys.*, 2011, **13**, 438. (b) H. Wiebe, J. Spooner, N. Boon, E. Deglint, E. Edwards, P. Dance, N. Weinberg, *J. Phys. Chem. C*, 2012, **116**, 2240; (c) J. Spooner, H. Wiebe, N. Boon, E. Deglint, E. Edwards, B. Yanciw, B. Patton, L. Thiele, P. Dance, N. Weinberg, *Phys. Chem. Chem. Phys.*, 2012, **14**, 2264.
5. H. Nomura, Y. Udagawa and K. Murasawa, *J. Molec. Struct.*, 1985, **129**, 229.
6. H. Nomura and S. Koda, *Bull. Chem. Soc. Jpn.*, 1985, **58**, 2917.

7. D.J. Gardiner and R.W. Jackson, *J. Chem. Soc. Chem. Commun.*, 1981, **3**, 159.
8. (a) C.A.N. Viana and J.C.R. Reis, *Pure Appl. Chem.*, 1996, **68**, 1541; (b) J. Spooner and N. Weinberg, *Can. J. Chem*, 2017, **95**, 149.
9. (a) S.P. Sawin, *Ph.D. Thesis*; University of Illinois: Urbana, 1971. (b) C.A. Eckert, *Ann. Rev. Phys. Chem.*, 1972, **23**, 239; (c) H. Kelm and D.A. Palmer, In: *High Pressure Chemistry* (H. Kelm, ed.), Dordrecht: Reidel, 1978, 281; (d) B.S. El'yanov and E.M Gonikberg, *J. Chem. Soc. Faraday Trans.* 1, 1979, **75**, 172; (e) B.S. El'yanov and E.M. Vasylvitskaya, *Rev. Phys. Chem. Japan*, 1980, **50**, 169; (f) T. Asano and T. Okada, *J. Phys. Chem.*, 1984, **88**, 238; (g) C.A.N. Viana, A.R.T. Calado, and L.M.V. Pinheiro, *J. Phys. Org. Chem.*, 1995, **8**, 63.
10. (a) W.L. Jorgensen and J. Tirado-Rives, *J. Am. Chem. Soc*., 1988, **110**, 1657; (b) W.L. Jorgensen, D.S. Maxwell and J. Tirado-Rives, *J. Am. Chem. Soc.*, 1996, **118**, 11225.
11. (a) A.R. Leach, *Molecular Modelling: Principles and Applications*, 2nd ed., Prentice Hall: Upper Saddle River, NJ, 2001; (b) U. Burkert and N.L. Allinger *Molecular Mechanics*; American Chemical Society: Washington, D.C., 1982; (c) N.L. Allinger, Y.H. Yuh and J.-H. Lii, *J. Am. Chem. Soc*., 1989, **111**, 8551; (d) W.D. Cornell, P. Cieplak, C.I. Bayly, I.R. Gould, K.M. Merz, D.M. Ferguson, D.C. Spellmeyer, T. Fox, J.W. Caldwell and P.A. Kollman, *J. Am. Chem. Soc.*, 1995, **117**, 5179; (e) A.D. MacKerell, D. Bashford, M. Bellott, R.L. Dunbrack, J.D. Evanseck, M.J. Field, S. Fischer, J. Gao, H. Guo, S. Ha, D. Joseph-McCarthy, L. Kuchnir, K. Kuczera, F.T.K. Lau, C. Mattos, S. Michnick, T. Ngo, D.T. Nguyen, B. Prodhom, W.E. Reiher, B. Roux, M. Schlenkrich, J.C. Smith, R. Stote, J. Straub, M. Watanabe, J. Wiorkiewicz-

Kuczera, D. Yin and M. Karplus, *J. Phys. Chem. B*, 1998, **102**, 3586; (f) A.K. Rappe, C.J. Casewit, K.S. Colwell, W.A. Goddard III and W.M. Skiff, *J. Am. Chem. Soc.*, 1992, **114**, 10024; (g) T.A. Halgren, *J. Comput. Chem.*, 1996, **17**, 490; (h) X. Daura, A.E. Mark, W.F. van Gunsteren, *J. Comput. Chem.*, 1998, **19**, 535.

12. For some recent examples see (a) T.G.A. Youngs, M.G. Del Popolo and J. Kohanoff, *J. Phys. Chem. B*, 2006**, 110**, 5697; (b) S.K. Burger and G. A. Cisneros, *J. Comput. Chem.*, 2013, **34**, 2313; (c) L.-P. Wang, J. Chen and T. Van Voorhis, *J. Chem. Theory Comput.*, 2013, **9**, 452; (d) L.-P. Wang, T.J. Martinez, V.S. Pande, *J. Phys. Chem. Lett.* 2014, **5**, 1885; (e) S. Grimme, *J. Chem. Theory Comput.*, 2014, **10**, 4497; (f) L. Vanduyfhuys, S. Vandenbrande, T. Verstraelen, R. Schmid, M. Waroquier, V. Van Speybroeck, *J. Comput. Chem.*, 2015, **36**, 1015; (g) D.J. Cole, J.Z. Vilseck, J. Tirado-Rives, M.C. Payne and W.L. Jorgensen, *J. Chem. Theory Comput.*, 2016, **12**, 2312; (h) J.G. McDaniel, E. Choi, C.Y. Son, J.R. Schmidt, A. Yethiraj, *J. Phys. Chem. B*, 2016, **120**, 7024; (i) E. Hansen, A.R. Rosales, B. Tutkowski, P.-O. Norrby, O. Wiest, *Acc. Chem. Res.*, 2016, **49**, 996; (j) A. Madarász, D. Berta and R.S. Paton, *J. Chem. Theory Comput.*, 2016, **12**, 1833.
13. J. Rimmelin and G. Jenner, *Tetrahedron*, 1974, **30**, 3081.
14. (a) H.J.C. Berendsen, D. van der Spoel and R. van Drunen, *Comput. Phys. Commun.*, 1995, **91**, 43; (b) E. Lindahl, B. Hess and D. van der Spoel, *J. Mol. Model.*, 2001, **7**, 306; (c) D. van der Spoel, E. Lindahl, B. Hess, G. Groenhof, A. E. Mark and H.J. Berendsen, *J. Comput. Chem.*, 2005, **26**, 1701; (d) B. Hess, C. Kutzner, D. van der Spoel and E. Lindahl, *J. Chem. Theory Comput.*, 2008, **4**, 435.

15. H.J.C. Berendsen, J.P.M. Postma, W.F. van Gunsteren, A. DiNola and J.R. Haak, *J. Chem. Phys.*, 1984, **81**, 3684.

16. (a) L.Verlet, *Phys. Rev.*, 1967, **159**, 98; (b) A.R. Leach, *Molecular Modelling: Principles and Applications*, 2nd ed., Prentice Hall: Upper Saddle River, NJ, 2001.

17. T. Darden, D. York and L. Pedersen, *J. Chem. Phys*, 1993, **98**, 10089.

18. Gaussian 09, Revision **E.01**, M. J. Frisch, G. W. Trucks, H. B. Schlegel, G. E. Scuseria, M. A. Robb, J. R. Cheeseman, G. Scalmani, V. Barone, B. Mennucci, G. A. Petersson, H. Nakatsuji, M. Caricato, X. Li, H. P. Hratchian, A. F. Izmaylov, J. Bloino, G. Zheng, J. L. Sonnenberg, M. Hada, M. Ehara, K. Toyota, R. Fukuda, J. Hasegawa, M. Ishida, T. Nakajima, Y. Honda, O. Kitao, H. Nakai, T. Vreven, J. A. Montgomery, Jr., J. E. Peralta, F. Ogliaro, M. Bearpark, J. J. Heyd, E. Brothers, K. N. Kudin, V. N. Staroverov, R. Kobayashi, J. Normand, K. Raghavachari, A. Rendell, J. C. Burant, S. S. Iyengar, J. Tomasi, M. Cossi, N. Rega, J. M. Millam, M. Klene, J. E. Knox, J. B. Cross, V. Bakken, C. Adamo, J. Jaramillo, R. Gomperts, R. E. Stratmann, O. Yazyev, A. J. Austin, R. Cammi, C. Pomelli, J. W. Ochterski, R. L. Martin, K. Morokuma, V. G. Zakrzewski, G. A. Voth, P. Salvador, J. J. Dannenberg, S. Dapprich, A. D. Daniels, Ö. Farkas, J. B. Foresman, J. V. Ortiz, J. Cioslowski, and D. J. Fox, Gaussian, Inc., Wallingford CT, 2009.

19. W. Humphrey, A. Dalke and K. Schulten, *J. Mol. Graphics*, 1996, **14**, 33.

Chapter 4.

Reaction Profiles and Energy Surfaces of Compressed Species

4.1. Volume Profiles

As discussed in Section 1.3, the concept of a volume profile $V(x)$, describing how the volume of a reaction system changes along its reaction coordinate x, is frequently used in the mechanistic analysis of many chemical reactions.[1] In most cases, volume profiles are treated as discrete three-point schematics describing the volumetric properties of the reactant, transition, and product states.[2] A continuous-curve approach offers a significantly stronger alternative and has been explored in the past in the context of studies of high pressure effects on the structure and energy of transition states.[3] Until recently, this approach faced a major limitation stemming from the lack of an adequate computational technique to produce the necessary continuous volume function. However, now this no longer presents an obstacle[4] since our MD method can be used for calculations of volumes of transient species along the reaction path, thus giving the continous volume profile as $V(x) = V(\mathbf{Z}(x))$, where $\mathbf{Z}(x)$ is a transient structure sampled at point x along reaction coordinate. Correspondingly, an "adjusted" continuous volume profile $\Delta V(x) = V(x) - V(x_0)$, that measures change of volume relative to the reactant state $\mathbf{Z_0}$ is merely a difference.

$$\Delta V(x) = V(\mathbf{Z}(x)) - V(\mathbf{Z_0}) \qquad (4.1)$$

It follows from eq. 1.2, 1.4, and 4.1 that the activation volume $\Delta V^{\neq} = \Delta V(x^{\neq})$, and the reaction volume $\Delta V = \Delta V(x_P)$.

4.1.1. Bistable Diatomic

An example of a volume profile obtained using the above procedure is shown in Fig. 4.1 for a model bistable diatomic described by a quartic double-well potential

$$U(x) = \tfrac{1}{2}\lambda x^2\left(1-\gamma x^2\right) \qquad (4.2)$$

with λ = -3600 kJ mol^{-1} nm^{-2} and γ = 50 nm^{-2} (see Fig. 4.2). The variable bond length x serves as a reaction coordinate that describes the isomerization process between two states of the diatomic represented by two stable minima of potential (4.2) located at x=0.15 nm ("short state") and x=0.35 nm ("long state"). The minima are separated by a barrier of 9 kJ/mol with a TS at x=0.25 nm. MD simulations were performed at T = 300K and P = 1 kbar, under which conditions the solvent was liquid.[5]

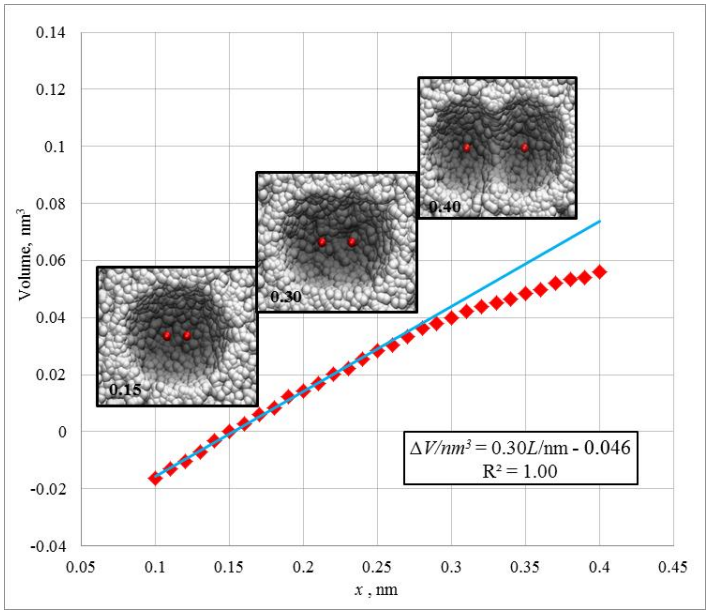

Figure 4.1. Volume profile $\Delta V(x)$ of a model diatomic at the reference pressure of 1 kbar (red diamonds). The linear profile predicted by Stearn-Eyring model is shown in blue for comparison. The insets, labeled by the values of x, illustrate the evolution of the sizes and shapes of the solvent cavity.

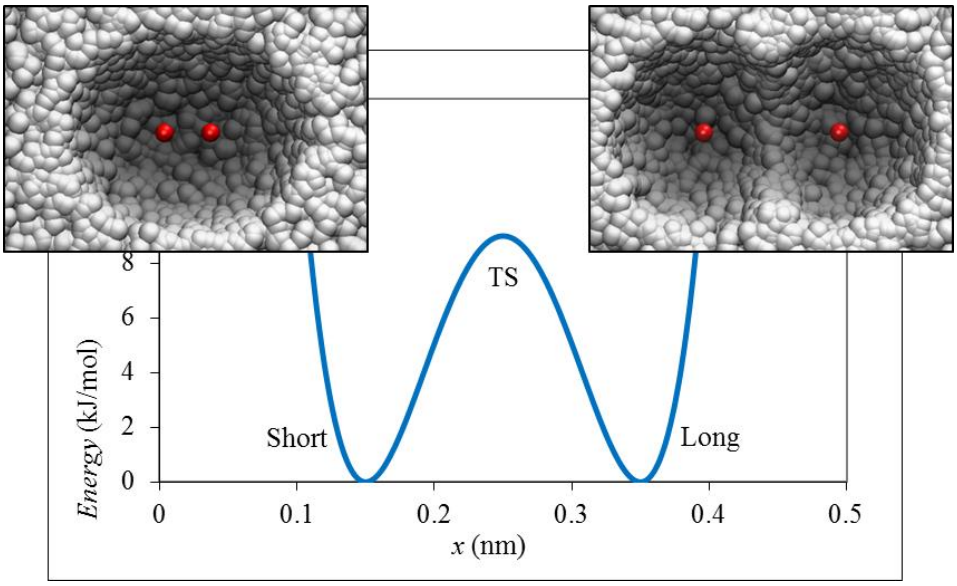

Figure 4.2. Energy profile of a model diatomic described by eq. (4.2). The insets show solvent cavities around the diatomic in its short and long states.

As can be seen from the insets in Fig. 4.1, the solvent cavities retain nearly constant cross-sections σ for x ranging between 0.1 and 0.3 nm. As a result, the volume profile for this system is well described by the linear equation $\Delta V(x) = \sigma(x\text{-}x_0)$ of the Stearn-Eyring model.[6] The radius of the circular cross-section estimated from this linear dependence is 0.31 nm. At $x > 0.3$ nm, a narrowing develops in the middle of the cavity, resulting in a marked nonlinearity of the volume profile.

4.1.2. Linear Triatomic System

The volume profile for the bistable diatomic is predictably a monotonic function of x since this variable describes the size of the system. The same can be expected for other simple processes, such as dissociation/association,[7] where a single distance parameter serves as a reaction coordinate for the duration of the entire process. The situation is quite different in most other cases, where the reaction coordinate involves more than one internal coordinate of a system. Substitution reactions constitute an important case; collinear exchange reactions A + BC → AB + C being a classic example of this type. A linear triatomic system ABC that undergoes this transformation is

described by two geometrical parameters – A-B distance R_{AB} and B-C distance R_{BC}. A typical potential energy surface[8] (PES) for a homonuclear case A = B = C is shown in Fig. 4.3 (the numerical values of the potential energy function $U(R_{AB},R_{BC})$ determining this PES can be found in the Appendix A).

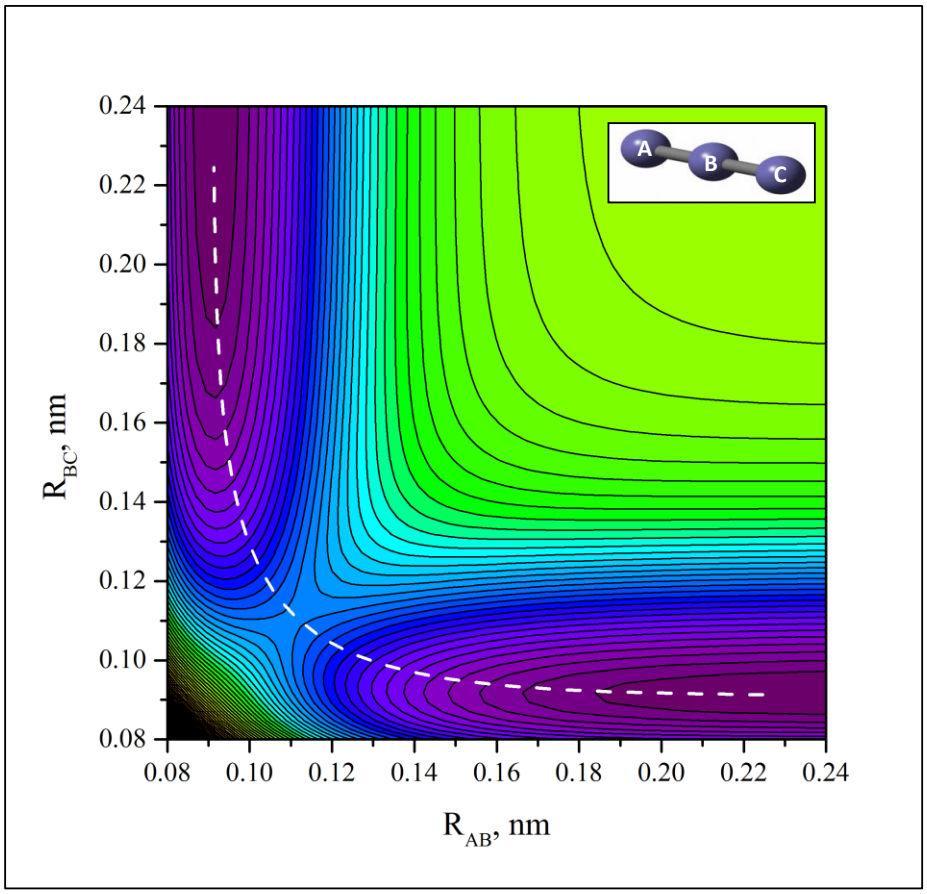

Figure 4.3. PES for model homonuclear linear triatomic system A-B-C (A = B = C). The white line is the BEBO reaction path

The reaction path can be approximated reasonably well by the Bond Energy Bond Order[9] (BEBO) parametric equation

$$\begin{cases} R_{AB} = \alpha - \beta ln(n) \\ R_{BC} = \alpha - \beta ln(1-n) \end{cases} \quad (4.3)$$

with α = 0.093 nm and β = 0.028 nm. The bond order parameter n can serve as a nonuniformly scaled reaction coordinate with values of n = 0, 0.5, and 1 for reactant, TS, and product, respectively. Alternatively, a uniformly scaled reaction coordinate x (with the reference x = 0 for TS) can be defined as a signed length of the reaction path.

$$x(n) = \beta \int_{0.5}^{n} \frac{\sqrt{\eta^2 + (1-\eta)^2}}{\eta(1-\eta)} d\eta \qquad (4.4)$$

The volume profile along coordinate x calculated for the above triatomic system at T = 300K and P = 1 kbar is shown in Fig. 4.4. As could be expected, the graph represents a curve with a minimum at x = 0 corresponding to the TS. Remarkably, the volume profile matches closely the linear dimension of the triatomic $L(x) = R_{AB}+R_{BC}$. The graph becomes linear if, instead of reaction coordinate x, the volume profile is plotted against parameter L (Fig. 4.5), as it was originally suggested by Stearn and Eyring.[6] The estimated radius of the circular cross-section in this case is 0.30 nm, which is consistent with the value found for the bistable diatomic.

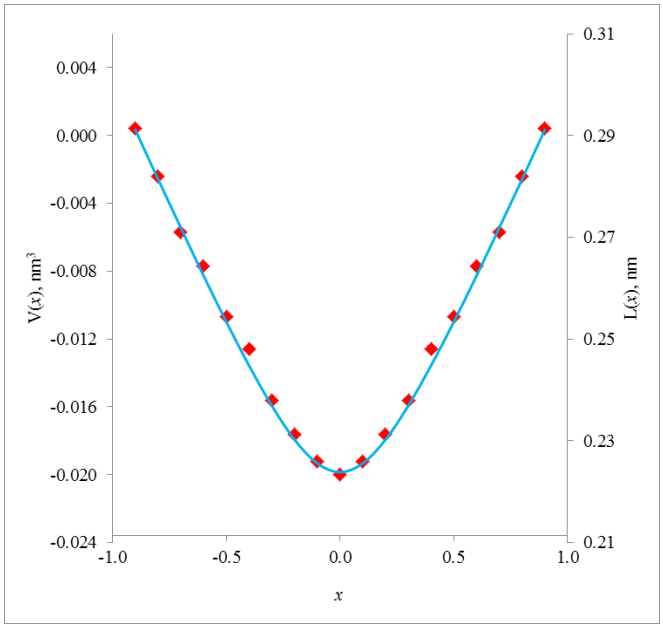

Figure 4.4. Volume profile $V(x)$ (red diamonds) and length profile $L(x)$ (blue line) for a model collinear triatomic exchange reaction at the reference pressure of 1 kbar.

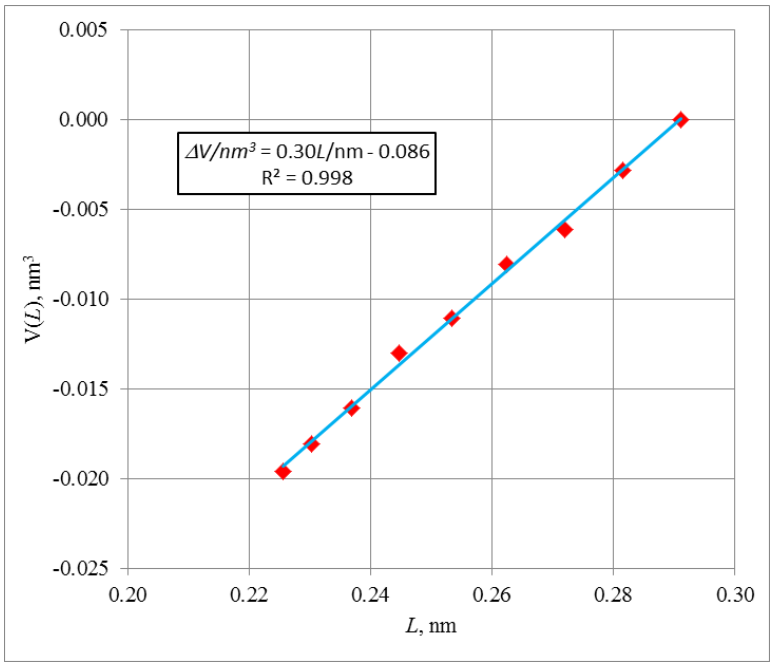

Figure 4.5. Volume profile $V(L)$ of a model triatomic at the reference pressure of 1 kbar (red diamonds). The linear profile predicted by Stearn-Eyring model[6] is shown in blue for comparison. Its equation and correlation coefficient are shown in the upper right part of the figure.

4.1.3. Stearn-Eyring Model

The Stearn-Eyring model, which has earlier been discussed in Section 1.2 and 2.1, gives a simple expression for a volume profile as a linear function of the size parameter $L(x)$

$$\Delta V(x) = \sigma[L(x) - L(x_0)] \qquad (4.5)$$

The requirement of $\sigma = const$ needs to be satisfied only for the part of the cavity adjacent to the reaction center. The rest of the system does not change in the course of reaction and its volume remains constant, thus giving zero contribution to the volume profile. As an illustration, we will consider the case of two reaction series of hydrogen atom abstraction by bromine radical from the aliphatic hydrogen of substituted toluenes:[10]

Series A: X-Ph-CH_2H + $Br^{\bullet}$ → X-Ph-$CH_2^{\bullet}$ + HBr

and

Series B: Ph-CY'Y"H + $Br^{\bullet}$ → Ph-CY'Y"$^{\bullet}$ + HBr

with X = H, *p*-CH_3, *m*-CH_3, *p*-Cl, *m*-Br, and Y'Y" = HH, CH_3H, CH_3CH_3, PhH. The images of the solvent cavities around the reactant state and TS of the unsubstituted toluene (X = H, Y'Y" = HH) are shown in Fig. 4.6. The major change in the cavity occurs in the course of reaction in the region adjacent to the reaction center C-H-Br (the "neck" of the rubber-duck-shaped cavity). The situation is similar in other reactions of series A and B (see Appendix B).

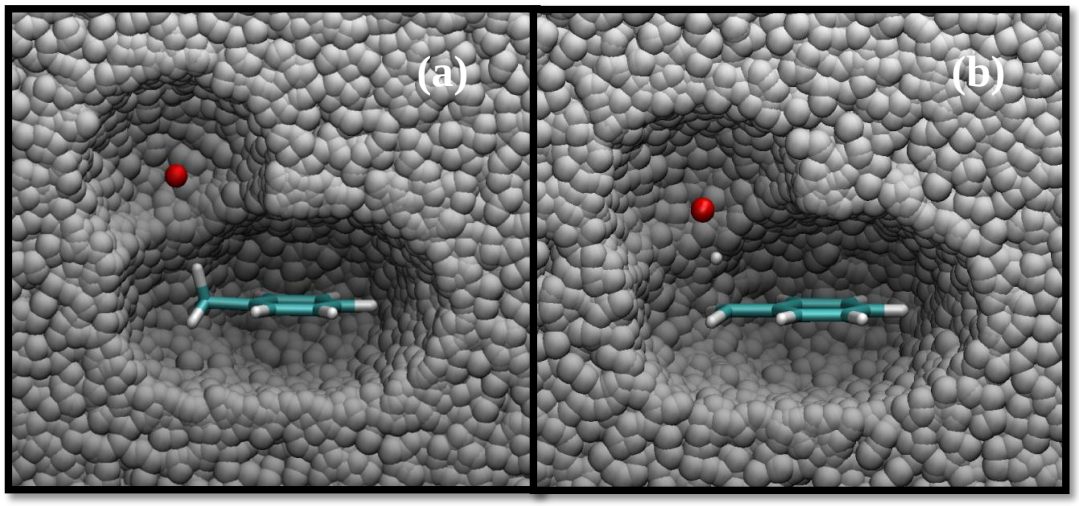

Figure 4.6. Solvent cavities around the reactant state (a) and TS (b) of abstraction of hydrogen atom (white) by bromine (red) from toluene (blue and white wire frame)

In all cases, the C-Br distance serves as the linear dimension parameter, $L = R_{CBr} = R_{CH} + R_{HBr}$. The values of R_{CH} and R_{HBr} for the B3LYP/6-31++G(d,p)-optimized[11] TSs of reactions of both series are listed in Table 4.1 along with the experimental values[10] of activation volume differences $\Delta\Delta V^{\neq} = \Delta V^{\neq} - \Delta V^{\neq}_{ref}$ determined with reference to the reaction of unsubstituted toluene. As can be seen from Fig. 4.7, these TSs cluster fairly close to the common BEBO reaction path

$$\begin{cases} R_{HBr} = 0.142 - 0.039ln(n) \\ R_{CH} = 0.108 - 0.039ln(1-n) \end{cases} \quad (4.6)$$

This allows one to use the same reaction coordinate x for all reactions of these series. If the Stearn-Eyring model applies, the value of $\Delta\Delta V^{\neq}$ can be expressed in terms of eq. (4.7) as

$$\Delta\Delta V^{\neq} = \Delta V(x^{\neq}) - \Delta V(x^{\neq}_{ref}) = \sigma[L(x^{\neq}) - L(x_0)] - \sigma_{ref}[L(x^{\neq}_{ref}) - L(x_0)] \quad (4.7)$$

where $x^{\neq}$ is the reaction coordinate of a TS, and x_0 is assumed to be the same for all reactions.

Table 4.1. B3LYP/6-31G++G(d,p)-optimized R_{CH} and R_{HBr} distances in TS's of hydrogen transfer reactions of series A and B and the experimental values[10] of activation volume differences $\Delta\Delta V^{\neq}$

	Substrate	R_{CH}, nm	R_{HBr}, nm	$\Delta\Delta V^{\neq}$, cm^3/mol
reference	toluene	0.1616	0.1534	0
Series A	*m*-xylene	0.1619	0.1535	1.5
	p-xylene	0.1628	0.1533	3.0
	m-bromotoluene	0.1589	0.1540	-3.0
	p-chlorotoluene	0.1601	0.1540	-1.2
Series B	ethylbenzene	0.1579	0.1546	-4.8
	cumene	0.1515	0.1570	-5.5
	diphenylmethane	0.1423	0.1624	-2.4

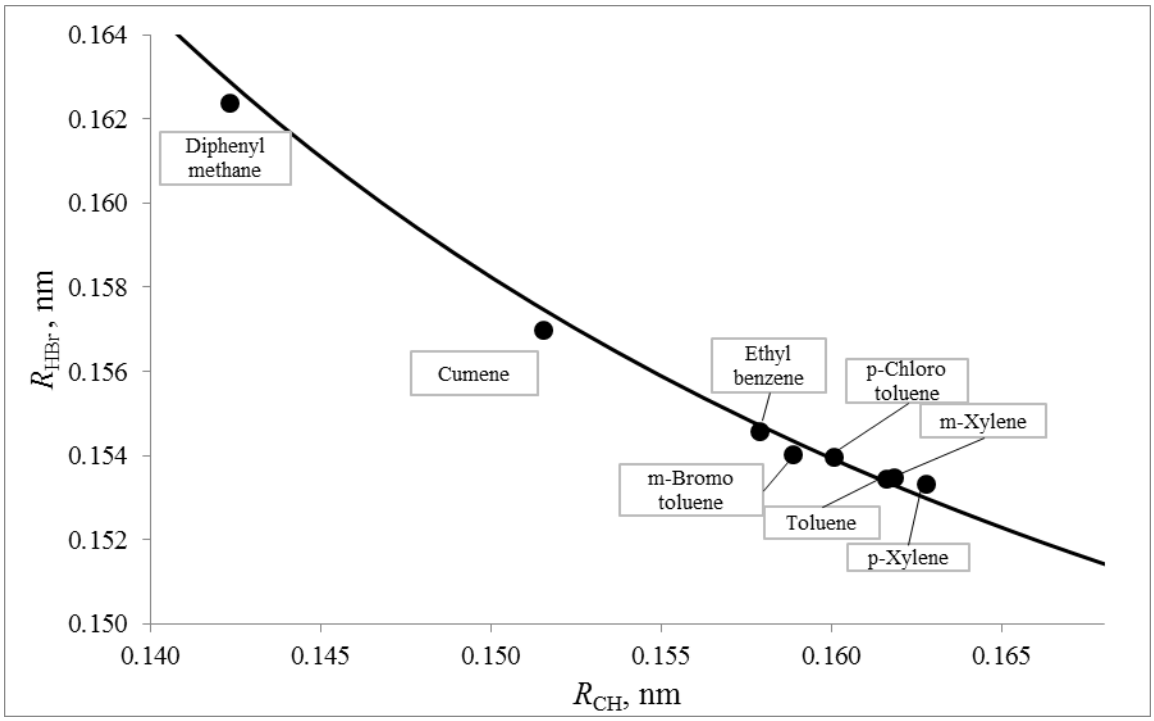

Figure 4.7. TSs for reactions of series A and B plotted in coordinates (R_{CH} , R_{HBr}) together with BEBO reaction path (4.7).

If the cavity cross-section σ for a given reaction is close to that of the reference reaction, σ_{ref}, then eq. (4.7) simplifies to

$$\Delta\Delta V^{\neq} = \sigma[L(x^{\neq}) - L(x^{\neq}_{ref})] = \sigma\Delta L^{\neq} \qquad (4.8)$$

That is, if σ is constant in a reaction series, the relative values of activation volumes, $\Delta\Delta V^{\neq}$, can be expected to be proportionate to the relative values of C-Br distances $\Delta L^{\neq}$ in the TS's. As can be seen in Fig. 4.8, such linear correlation is indeed observed for series A where cavity cross-sections are roughly equal due to the fact that substituents X are removed sufficiently far from the reaction center. In the case of series B, the substituents are introduced directly into the reaction center, which results in a substantial variation of σ and, consequently, in the loss of linearity between $\Delta\Delta V^{\neq}$ and $\Delta L^{\neq}$.

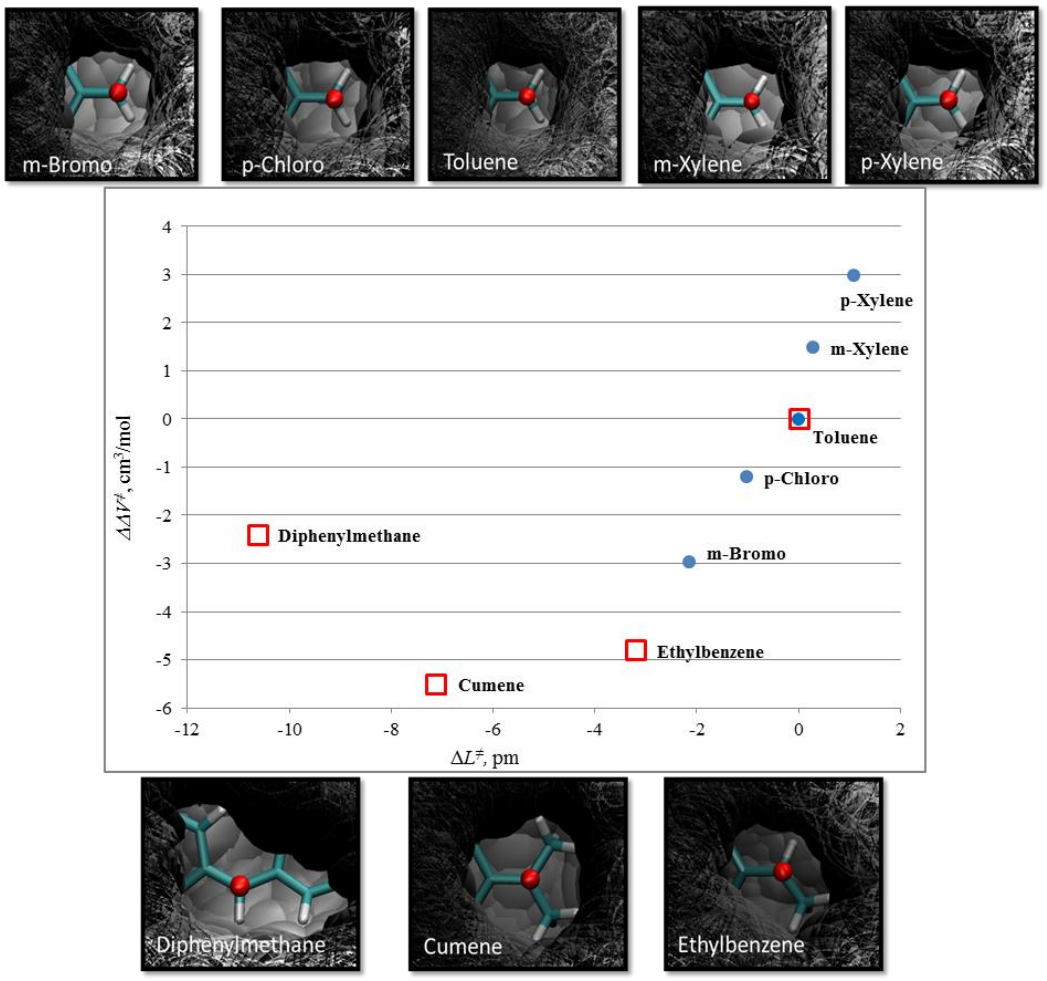

Figure 4.8. A plot of experimental activation volume differences,[10] $\Delta\Delta V^{\neq}$, *vs.* the differences in C-Br distances, $\Delta L^{\neq}$, in TSs for hydrogen abstraction by bromine radical from substituted toluenes: blue circles – Series A, red squares – Series B. The insets show solvent cavity cross-sections orthogonal to C-H-Br line and passing through H atom.

4.2. Reaction Profiles and Energy Surfaces for Model Systems

4.2.1. Reaction Profiles

Volume is an isothermal pressure derivative of Gibbs energy. Therefore, the Gibbs energy profile $G(x;P)$ at a given pressure P can be obtained from the Gibbs energy profile $G_0(x) = G(x;P_0)$ at a reference pressure P_0 by integration of the pressure dependent volume profile $V(x;P)$:

$$G(x;P) = G_0(x) + \int_{P_0}^{P} V(x;p)dp \tag{4.9}$$

If the pressure dependence of $V(x)$ can be neglected, eq.(4.9) reduces to a much simpler approximate relation

$$G(x;P) \approx G_0(x) + (P - P_0)V(x) \tag{4.10}$$

We used these equations to evaluate the effect of pressure on the shapes of reaction profiles for the short-to-long isomerization of a bistable diatomic and model collinear triatomic exchange reaction described in the previous section. The necessary reference Gibbs energy profiles $G_0(x)$ were obtained from the gas-phase energy profiles $U(x)$ by adding to them MD solvation Gibbs energies acquired by thermodynamic integration[13] at a reference pressure P_0 = 1 kbar. The results are shown in Fig. 4.9. The approximate pressure-dependent profiles $G(x;P)$ calculated using eq. (4.10) compare favorably with the exact profiles obtained directly from $U(x)$ using thermodynamic integration at the target pressure P.

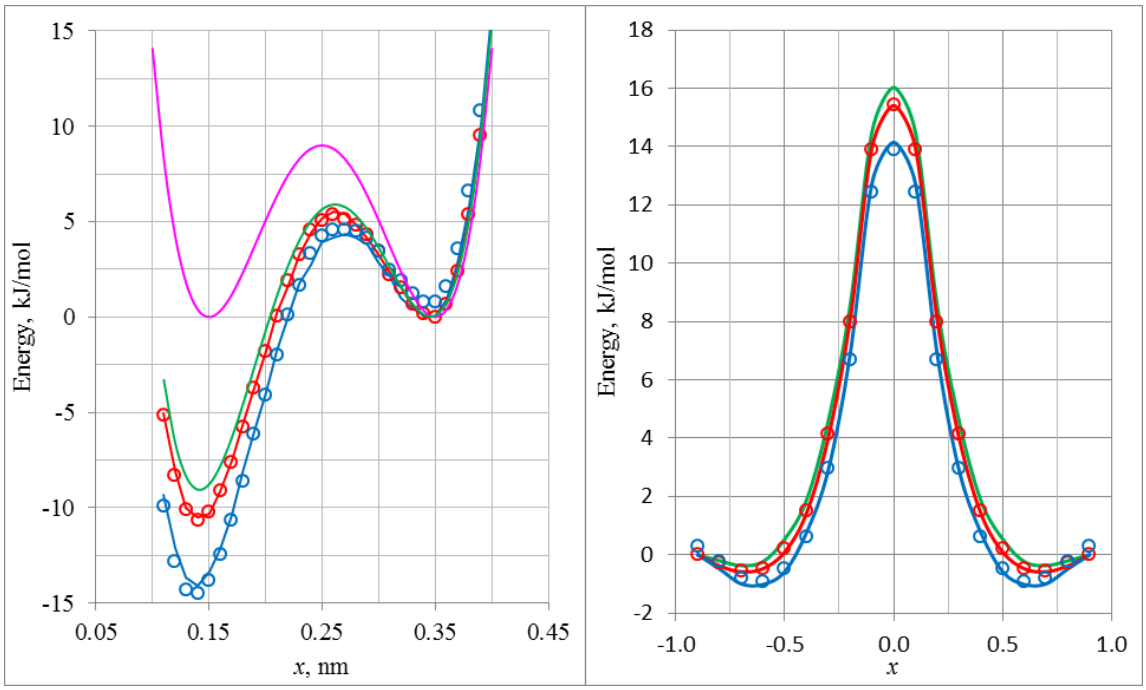

Figure 4.9. Exact and approximate energy profiles for a bistable diatomic (left) and a model collinear triatomic exchange reaction (right): magenta – gas-phase energy profile $U(x)$, eq. (4.2); green – reference Gibbs energy profile $G_0(x)$ at P_0 = 1 kbar; red $-G(x;P)$ at P = 1.5 kbar ; blue $-G(x;P)$ at P = 3 kbar; solid lines – exact $G(x;P)$; open circles – approximate $G(x;P)$, eq. (4.10).

Despite neglecting the pressure dependence of the volume profile, approximate equation (4.10) works quite well. This can probably be attributed to the fact that the major pressure-induced restructuring of the solute happens along its softest coordinate x, which is considered explicitly in the equation. This restructuring is substantial: both the barrier height and positions of stationary points (minima and TS) are affected by pressure. The direction of these shifts can be assessed using eq. (4.10).[3b] If $x = a_0$ is a stationary point of $G_0(x)$ and $x = a_P$ is the corresponding stationary point of $G(x;P)$, their relative shift $a_P - a_0$ can be estimated in the first iteration of the Newton-Raphson optimization[14] as

$$a_P - a_0 \approx -\left\{\left(\frac{dG(x;P)}{dx}\right)\Big/\left(\frac{d^2G(x;P)}{dx^2}\right)\right\}_{x=a_0} \tag{4.11}$$

By virtue of eq. (4.10) and since the first derivative of $G_0(x)$ at its stationary point a_0 is zero, eq. (4.11) reduces to eq. (4.12).

$$\begin{aligned} a_P - a_0 &\approx -(P - P_0)\left\{\left(\frac{dV(x)}{dx}\right)\Big/\left(\frac{d^2G(x;P)}{dx^2}\right)\right\}_{x=a_0} \\ &= -(P - P_0)V'(a_0)/G"(a_0;P) \end{aligned} \tag{4.12}$$

For reactant and product minima, the second derivative $G"(a_0;P)$ is positive. Therefore, for the bistable diatomic, where the volume profile $V(x)$ is an increasing function of x, both short- and long-state minima shift to the left with pressure. On the contrary, since $G"(a_0;P)$ is positive for the TS it shifts to the right. In the case of the triatomic exchange reaction, $V'(x)$ is negative for the reactant, positive for the product and zero for the TS. As a result, the reactant minimum moves to the right, the product shifts to the left, and the TS does not change its position with pressure.

4.2.2. Energy Surfaces

The bistable diatomic is a one-dimensional (1D) system and its energy profile $U(x)$ constitutes its full potential energy surface (PES). The situation is different for multidimensional systems, such as the linear triatomic system where the energy profile $U(x)$ is just a cross-section of its 2D PES. Solvation modifies this PES and, consequently, the reaction path, which redefines reaction coordinate x and energy profile $U(x)$. Compression is expected to further magnify this effect. Therefore, above a certain threshold, the effect of pressure on such systems is more appropriately described by its effect on their PES's rather than reaction profiles. Equations (4.9) and (4.10) can easily

be upgraded to a multidimensional case by simple replacement of reaction coordinate x with a multidimensional coordinate vector **x**:

$$\mathrm{G}(\mathbf{x};P) = G_0(\mathbf{x}) + \int_{P_0}^{P} V(\mathbf{x};p)dp \approx G_0(\mathbf{x}) + (P - P_0)V(\mathbf{x}) \tag{4.13}$$

V(**x**;P) and V(**x**) thus become multivariable functions and should therefore more appropriately be referred to as volume surfaces rather than volume profiles. We calculated the V(**x**) surface for the model linear triatomic for P_0 = 1 kbar and used it, in conjunction with eq. (4.13), to construct an approximate pressure-dependent Gibbs energy surface (GES) for this system at P = 3 kbar. The reference-pressure GES G_0(**x**) and the exact GES G(**x**;P) were obtained from the gas-phase PES U(**x**) of Fig. 4.3 by augmenting them with MD solvation Gibbs energies generated by thermodynamic integration at P_0 = 1 kbar and P = 3 kbar, respectively. The results are shown in Fig. 4.10. As can be seen from the figure and Table 4.2 listing parameters of the GES's, the exact and approximate surfaces are fairly similar.

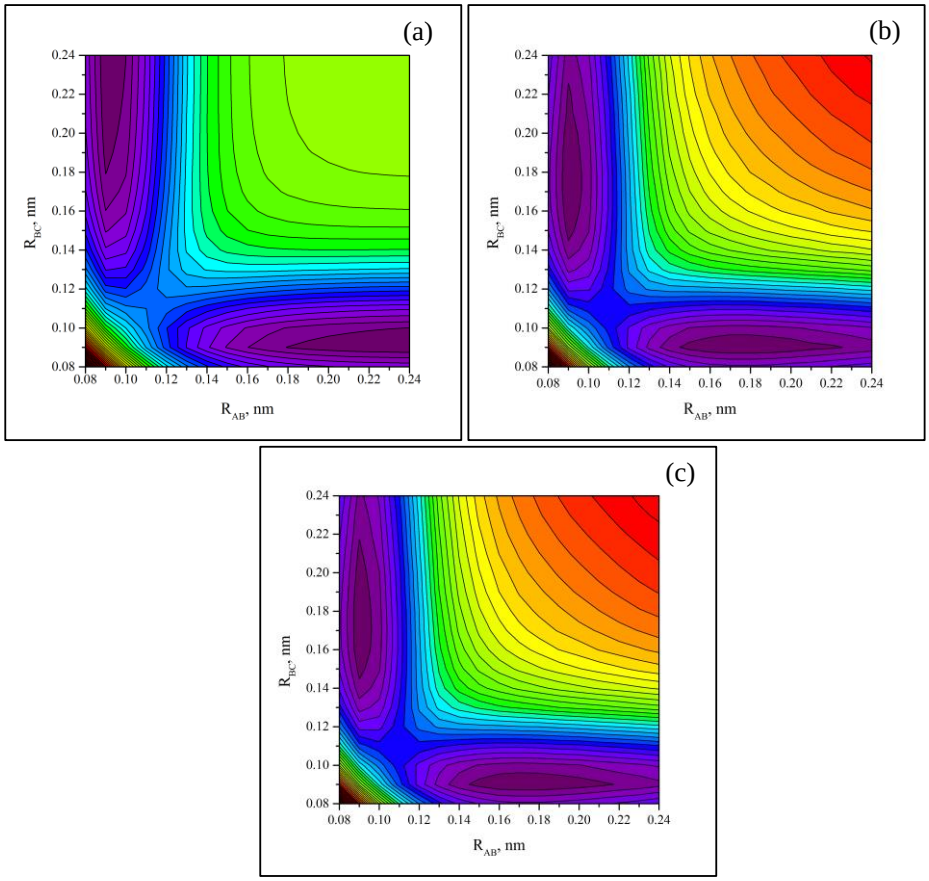

Figure 4.10. Reference 1 kbar GES $G_0(\mathbf{x})$ (a) and the exact (b) and approximate (c) pressure-dependent GES $G(\mathbf{x};P)$ of the model linear triatomic system at P = 3 kbar. The contour spacing is 2 kJ/mol.

Table 4.2. Geometrical parameters of stationary points and reaction barriers of three high pressure GES's for the collinear triatomic exchange reaction.

Pressure, kbar	Energy surface	Reactant		TS		Reaction barrier, kJ/mol
		R_{AB}, nm	R_{BC}, nm	R_{AB}, nm	R_{BC}, nm	
1.0	Reference GES (Fig 4.10a)	0.0916	0.1897	0.1094	0.1094	14.9
3.0	Exact GES (Fig. 4.10b)	0.0912	0.1737	0.1086	0.1086	13.4
	Approximate GES (Fig. 4.10c)	0.0914	0.1761	0.1085	0.1085	13.1

As in the case of Gibbs energy profiles, reaction barriers and stationary points of the GES's are strongly affected by pressure. The pressure-induced displacement of the stationary points is roughly described by eq. (4.14), generalizing eq. (4.12) to a multidimensional case:

$$\lambda_{iP} - \lambda_{i0} \approx -(P - P_0)\left\{\left(\frac{\partial V(\boldsymbol{x})}{\partial \lambda_i}\right)\Big/\left(\frac{\partial^2 G(\boldsymbol{x};P)}{\partial {\lambda_i}^2}\right)\right\}_{\boldsymbol{x}=\boldsymbol{a_0}} \tag{4.14}$$

where λ_{iP} and λ_{i0} are normal coordinates at the stationary points a and a_0 of $G(\mathbf{x};P)$ and $G_0(\mathbf{x})$. In the case of the triatomic described by the GES of Fig. 4.10, the normal modes for the TS are $\lambda_1 = L$ (the total length of the triatomic) and $\lambda_2 = x$ (the reaction coordinate). Since $\partial V/\partial x = 0$, $x^{\neq} = x^{\neq}_0$, *i.e.* the TS does not shift along the reaction coordinate in the multidimensional case either. At the same time, $\partial V/\partial L > 0$ and $\partial^2 G/\partial L^2 > 0$, and as a result, the TS is somewhat shifted with pressure in the diagonal direction toward the lower left corner. For the reactant and product minima, the normal modes are $\lambda_1 \approx R_{AB}$ and $\lambda_2 \approx R_{BC}$, and the minima shift in both directions due to the fact that $\partial G/\partial \lambda_i > 0$ and $\partial^2 G/\partial {\lambda_i}^2 > 0$. Since the second derivative of $G(\mathbf{x};P)$ along the reaction coordinate x is smaller than that across, both reactant and product minima are shifted toward the TS to a much greater degree than in the lateral direction. This lateral deformation of GES can likely be ignored at lower pressures and the reaction path remains practically unchanged, which makes volume and reaction profiles a meaningful tool for studying high pressure effects over the 0-10 kbar range. However, as we show below, the situation becomes dramatically different as pressure is further increased.

4.3. Energy Surfaces for Hydrogen Transfer and S_N2 Reactions at Extreme Pressures

To extend our study of high-pressure effects on the energy landscape we have chosen to look at two classes of system that are close realistic analogs of the model

triatomic system discussed in the previous sections: hydrogen transfer reactions X + HY → XH + Y between halogen atoms (X and Y = F, Cl, Br) or hydrocarbon systems R'-H-R" (R',R" = Me, Et, *i*-Pr), and anionic $X\text{-}CH_3\text{-}Y^-$ systems (X,Y = CN, F, Cl, Br) modeling S_N2 reactions.[15] We modeled the effect of extreme pressures on their PES's by embedding the reaction systems into compressed 1D and 3D neon matrices as shown in Figs 4.11 and 4.12. The PES were calculated by scanning R_{XH} and R_{HY} on a 25×25 grid with a step of 0.005 nm.

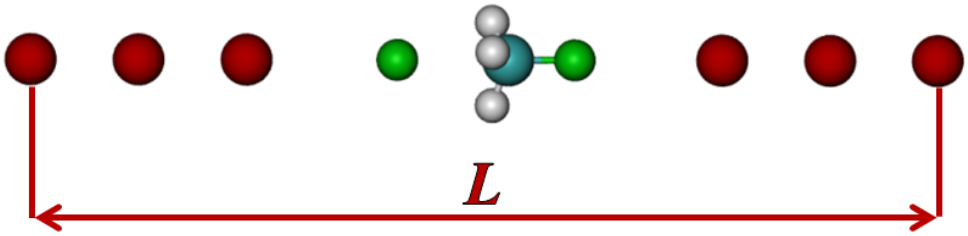

Figure 4.11. XCH_3X^- system in a 1D Ne matrix: X is green, C is cyan, H is white, Ne is red. Pressure exerted on the reaction system is generated by a compressed Ne chain with terminal atoms fixed at distance *L*.

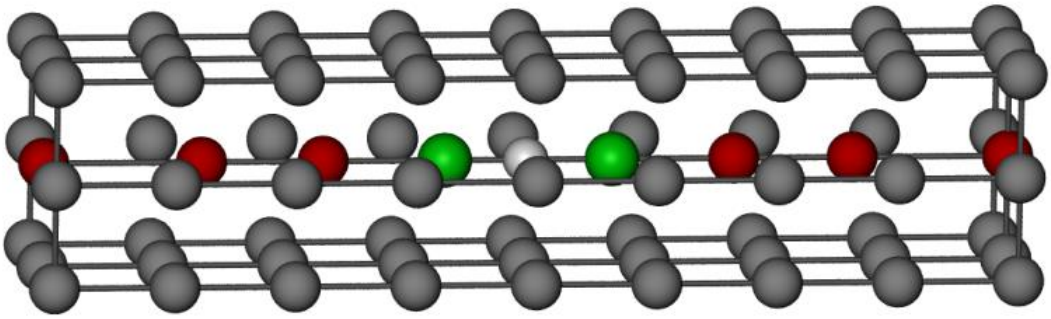

Figure 4.12. Linear X-H-X system in a 3D Ne matrix: X atoms are green, H atom is white, the Ne atoms of a 1D submatrix are red, and all other Ne atoms of the matrix are grey.

4.3.1. 1D Matrix

Reaction systems were inserted coaxially within a chain of Ne atoms (one to three Ne atoms on each side), and positions of the terminal Ne atoms were adjusted to attain

the desired degree of compression, while the geometry of the rest of the system was optimized. The PESs were then constructed by scanning the R_{XH} and R_{HY} parameters in X-H-Y, C-H distances, $R_{R'H}$ and $R_{HR''}$ in, R'HR'', or X-C and C-Y distances, R_{XC} and R_{CY}, in XCH_3Y^-, with positions of the terminal Ne atoms held fixed and the rest of the parameters of the system optimized. The force exerted onto the system was calculated as a negative derivative $F = -dU/dL$ of the optimized energy $U(L)$ with respect to distance L between terminal Ne atoms. We considered three regimes, referred to as low, medium, and high compression. For X-H-Y systems the regimes corresponded to compression forces of 0.15, 0.75, and 2.0 hartree/nm, while for the R'HR and XCH_3Y^- forces of 0.1, 0.5, and 1.0 hartree/nm were used. Compression of 0.1 hartree/nm is roughly equivalent to 100 kbar in the case of the F-H-F system (see Section 4.4.4.3). Varying the number of Ne atoms in the solvent matrix did not seem to have a significant effect on the energy surfaces (see Table 4.3).

Table 4.3. Parameters of the HF/6-31G PES of symmetric X-H-X systems (X = F, Cl, Br) embedded in Ne matrices of varying number of shells, with the outer shell frozen. Parameters of the gas-phase PES are also included for comparison.

System	Compression	Matrix size	Reactant		TS	
			R_{XH}, nm	R_{HX}, nm	R_{XH}, nm	Reaction barrier, kJ/mol
F-H-F	Zero	gas phase	0.092	0.214	0.113	152
	Low	1-shell	0.091	0.189	0.110	130
		2-shell	0.091	0.189	0.112	124
		3-shell	0.091	0.189	0.113	124
	Medium	1-shell	0.089	0.140	0.107	65
		2-shell	0.090	0.142	0.106	65
		3-shell	0.090	0.142	0.105	65
	High	1-shell	0.087	0.111	0.098	14
		2-shell	0.087	0.113	0.098	17
		3-shell	0.088	0.118	0.100	23
Cl-H-Cl	Zero	gas phase	0.130	0.301	0.154	82
	Low	1-shell	0.129	0.228	0.153	58
		2-shell	0.129	0.229	0.153	56
		3-shell	0.129	0.229	0.150	54
	Medium	1-shell	0.128	0.169	0.145	9
		2-shell	0.128	0.169	0.144	8
		3-shell	0.128	0.169	0.145	8
	High	1-shell	0.133	0.133	single minimum	no reaction
		2-shell	0.133	0.133		
		3-shell	0.135	0.135		
Br-H-Br	Zero	gas phase	0.141	0.280	0.167	56
	Low	1-shell	0.141	0.223	0.165	38
		2-shell	0.141	0.230	0.165	27
	Medium	1-shell	0.143	0.170	0.155	2
		2-shell	0.143	0.173	0.155	2
	High	1-shell	0.145	0.145	single minimum	no reaction
		2-shell	0.144	0.144		
		3-shell	0.144	0.144		

Table 4.4. Parameters of the HF/6-31G PES of asymmetric X-H-Y systems (X, Y = F, Cl, Br) embedded in the Ne matrix with the outer shell frozen. Parameters of the gas-phase PES are also included for comparison.

System	Compression	XH + Y		X + HY		TS		Reaction barrier, kJ/mol	
		R_{XH}, nm	R_{HY}, nm	R_{XH}, nm	R_{HY}, nm	R_{XH}, nm	R_{HY}, nm	XH + Y	X + HY
F-H-Cl	Gas phase	0.092	0.275	0.248	0.130	0.120	0.148	164	95
	Low	0.092	0.221	0.190	0.128	0.118	0.147	137	72
	Medium	0.090	0.177	0.149	0.125	0.116	0.138	77	19
	High	0.089	0.148	single minimum				no reaction	
F-H-Br	Gas phase	0.092	0.261	0.246	0.142	0.124	0.159	165	78
	Low	0.092	0.224	0.193	0.140	0.120	0.158	140	53
	Medium	0.089	0.158	single minimum				no reaction	
	High	0.089	0.152	single minimum				no reaction	
Cl-H-Br	Gas phase	0.130	0.272	0.295	0.142	0.159	0.163	80	60
	Low	0.129	0.241	0.231	0.141	0.155	0.162	65	40
	Medium	0.128	0.180	single minimum				no reaction	
	High	0.130	0.147	single minimum				no reaction	

The parameters of the stationary points obtained for symmetric and asymmetric systems are summarized in Tables 4.3-4.8. In all cases, pressure has a tremendous effect on the PES topography. With increasing pressure, the reactant and product minima shift toward the TS, as predicted by eq. (4.15), and the reaction barrier gets lower. At sufficiently high compressions the systems collapse into a single minimum. This behavior is common for both symmetric and asymmetric systems, with one notable difference, whereas the single minimum of a highly compressed PES for a symmetric system appears as the limit of the TS sequence; for the asymmetric system it appears as the limit for the sequence of the exothermic minima. The trends are illustrated in Fig. 4.13-4.16 by PES's for the representative F-H-F, F-CH_3-F^-, CH_3-H-CH_3, and F-CH_3-Cl^- systems. The full set of PES's for all A-B-C systems (A=X,R'; B=H,CH_3; C=Y,R'') systems at various compressions is included in Appendix C.

Table 4.5. Parameters of the B3LYP/6-31++G(d,p) PES of symmetric R'HR' systems (R' = Me, Et, i-Pr) embedded in compressing Ne matrices. Parameters of the zero-compression gas-phase PES are also included for comparison.

System	Compression	Reactant		TS	
		$R_{R'H}$, nm	$R_{HR'}$, nm	$R_{R'H}$, nm	Reaction barrier, kJ/mol
Me-H-Me	Zero	no minimum		0.135	64
	Low	0.110	0.220	0.135	45
	Medium	0.110	0.165	0.130	9
	High	0.120	0.120	single minimum	no reaction
Et-H-Et	Zero	no minimum		0.135	68
	Low	0.110	0.225	0.135	50
	Medium	0.110	0.165	0.125	14
	High	0.125	0.125	single minimum	no reaction
i-Pr-H-i-Pr	Zero	no minimum		0.135	70
	Low	0.110	0.230	0.135	54
	Medium	0.110	0.170	0.130	17
	High	1.15	1.35	1.25	2

Table 4.6 Parameters of the B3LYP/6-31++G(d,p) PES of asymmetric Me-H-R" systems (R" = Et, i-Pr) embedded in compressing Ne matrices. Parameters of the zero-compression gas-phase PES are also included for comparison.

System	Compression	Me-H + R"		Me + CH_3-R"		TS		Reaction barrier, kJ/mol	
		R_{MeH}, nm	$R_{HR"}$, nm	R_{MeH}, nm	$R_{HR"}$, nm	R_{MeH}, nm	$R_{HR"}$, nm	Me-H + R"	Me + H-R"
Me-H-Et	Zero	no minimum		no minimum		0.135	0.130	77	58
	Low	0.105	0.260	0.225	0.105	0.135	0.130	64	32
	Medium	0.105	0.170	single minimum				no reaction	
	High	0.105	0.140	single minimum				no reaction	
Me-H-iPr	Zero	no minimum		no minimum		0.140	0.130	84	49
	Low	0.108	0.228	0.213	0.108	0.138	0.128	72	25
	Medium	0.108	0.178	single minimum				no reaction	
	High	0.108	0.153	single minimum				no reaction	

Table 4.7 Parameters of the B3LYP/6-31++G(d,p) PES of symmetric X-CH_3-X^- systems (X = CN, F, Cl, Br) embedded in compressing Ne matrices. Parameters of the zero-compression gas-phase PES are also included for comparison.

System	Compression	Reactant		TS	
		R_{XC}, nm	R_{CX}, nm	R_{XC}, nm	Reaction barrier, kJ/mol
NC-CH_3-CN^-	Zero	0.150	0.300	0.210	167
	Low	0.150	0.295	0.205	159
	Medium	0.150	0.260	0.195	137
	High	0.100	0.240	0.185	121
F-CH_3-F^-	Zero	0.145	0.255	0.185	43
	Low	0.145	0.240	0.180	35
	Medium	0.145	0.215	0.180	25
	High	0.145	0.190	0.165	7
Cl-CH_3-Cl^-	Zero	0.185	0.320	0.235	37
	Low	0.185	0.295	0.235	33
	Medium	0.180	0.265	0.225	28
	High	0.180	0.240	0.205	20
Br-CH_3-Br^-	Zero	0.200	0.335	0.255	28
	Low	0.200	0.295	0.245	26
	Medium	0.200	0.270	0.230	18
	High	0.195	0.215	0.220	13

Table 4.8 Parameters of the B3LYP/6-31++G(d,p) PES of asymmetric X-CH_3-Y^- systems (X, Y = NC, F, Cl, Br) embedded in compressing Ne matrices. Parameters of the zero-compression gas-phase PES are also included for comparison.

System	Compression	X-CH_3 + Y		X + CH_3-Y		TS		Reaction barrier, kJ/mol	
		R_{XC}, nm	R_{CY}, nm	R_{XC}, nm	R_{CY}, nm	R_{XC}, nm	R_{CY}, nm	X-CH_3 + Y	X + CH_3-Y
NC-CH_3-F^-	Zero	0.145	0.265	0.265	0.150	0.200	0.185	130	60
	Low	0.140	0.290	0.255	0.145	0.200	0.185	126	53
	Medium	0.140	0.255	0.230	0.145	0.200	0.175	121	30
	High	0.140	0.230	0.215	0.140	0.190	0.160	117	12
NC-CH_3-Cl^-	Zero	0.145	0.315	0.320	0.185	0.235	0.210	190	24
	Low	0.145	0.300	0.280	0.185	0.220	0.205	187	20
	Medium	0.140	0.275	0.240	0.185	0.215	0.200	179	7
	High	0.140	0.255	0.220	0.180	0.210	0.190	177	1
NC-CH_3-Br^-	Zero	0.145	0.345	0.305	0.200	0.240	0.225	204	13
	Low	0.145	0.300	0.280	0.200	0.235	0.225	198	18
	Medium	0.145	0.290	0.260	0.200	0.225	0.220	191	4
	High	0.14	0.265	single minimum				no reaction	
F-CH_3-Cl^-	Zero	0.14	0.33	0.245	0.19	0.215	0.21	109	2
	Low	0.14	0.305	0.24	0.19	0.215	0.195	100	1
	Medium	0.14	0.285	single minimum				no reaction	
	High	0.14	0.265	single minimum				no reaction	
F-CH_3-Br^-	Zero	0.145	0.315	single minimum				no reaction	
	Low	0.145	0.29	single minimum				no reaction	
	Medium	0.14	0.28	single minimum				no reaction	
	High	0.14	0.255	single minimum				no reaction	
Cl-CH_3-Br^-	Zero	0.185	0.34	0.305	0.205	0.24	0.245	46	20
	Low	0.185	0.31	0.295	0.2	0.235	0.245	40	17
	Medium	0.18	0.28	0.26	0.2	0.23	0.22	31	11
	High	0.175	0.26	0.24	0.195	0.205	0.215	27	9

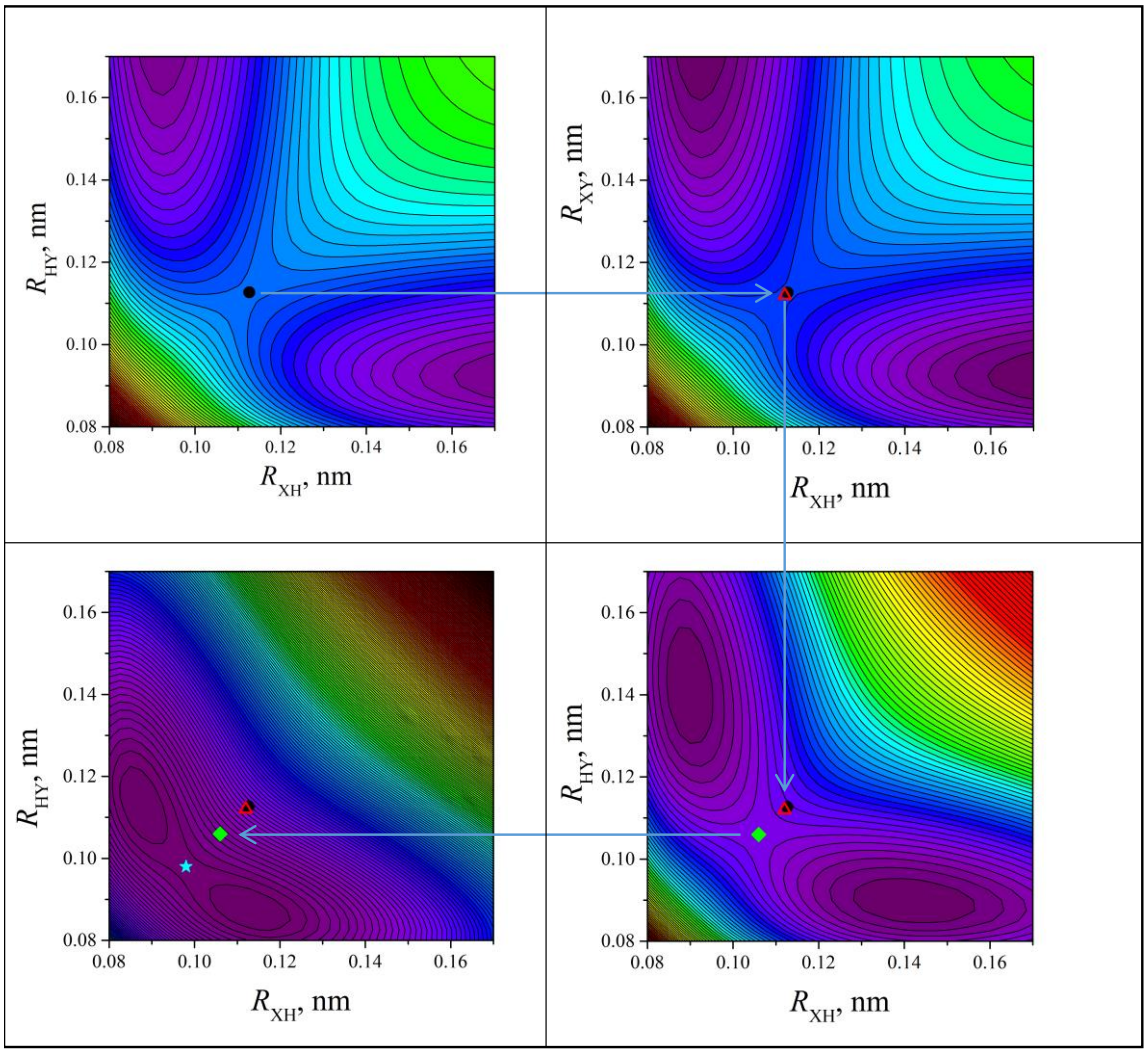

Figure 4.13. PES for FHF system at ambient conditions (a), low compression (b), medium compression (c), and high compression (d). The corresponding TS positions (marked by symbols) shift in the diagonal direction with increasing pressure. The arrows project TS positions between lower and higher compression PES's. The contour spacing is 10 kJ/mol.

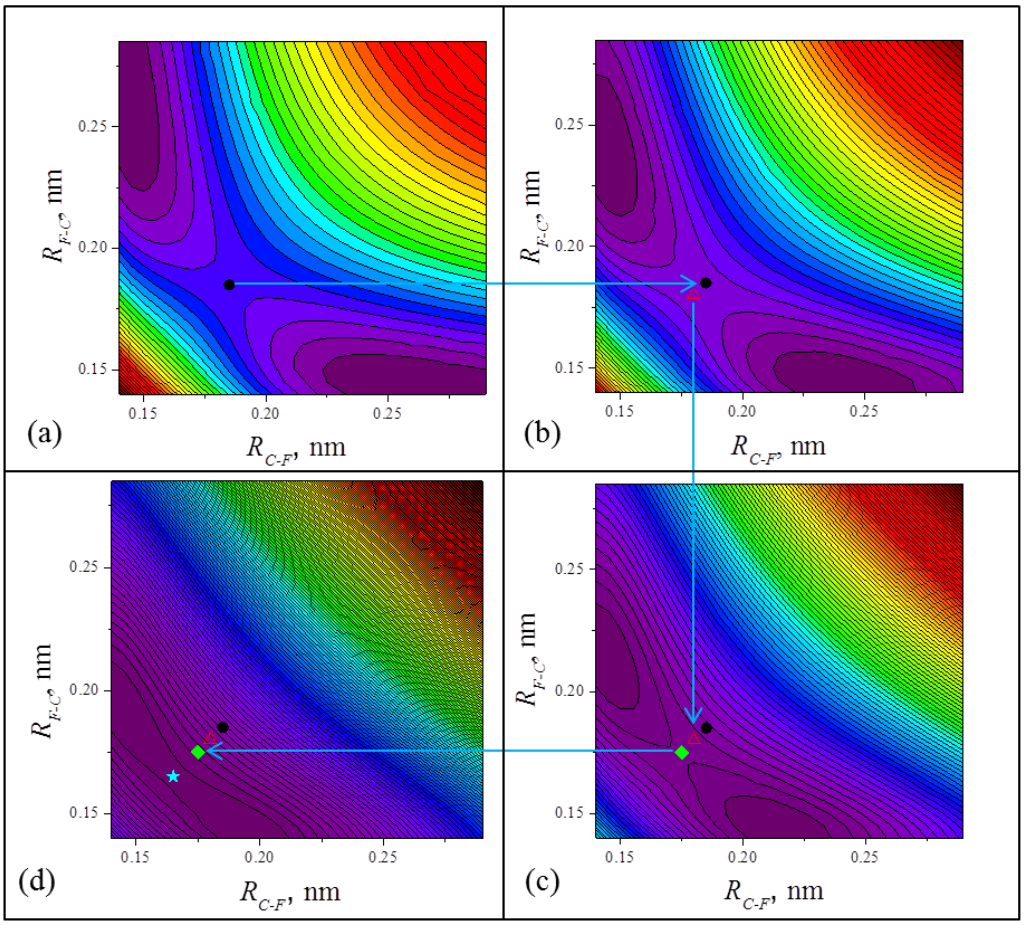

Figure 4.14. PES for F-CH_3-F^- system at ambient conditions (a), low compression (b), medium compression (c), and high compression (d). The corresponding TS positions (marked by symbols) shift in the diagonal direction with increasing pressure. The arrows project TS positions between lower and higher compression PESs. The contour spacing is 10 kJ/mol.

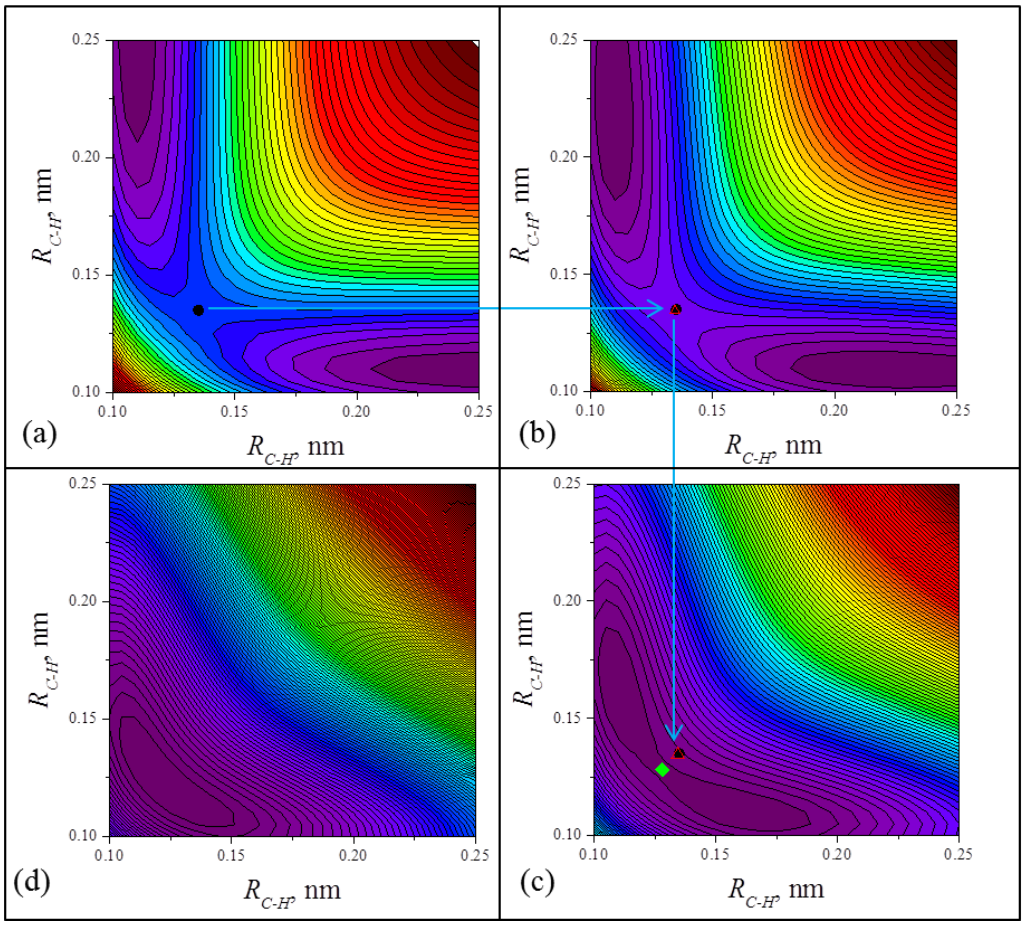

Figure 4.15. PES for CH_3-H-CH_3 system at ambient conditions (a), low compression (b), medium compression (c), and high compression (d). The corresponding TS positions (marked by symbols) shift in the diagonal direction with increasing pressure. The arrows project TS positions between lower and higher compression PESs. At high compression the system collapses into a single minimum. The contour spacing is 10 kJ/mol.

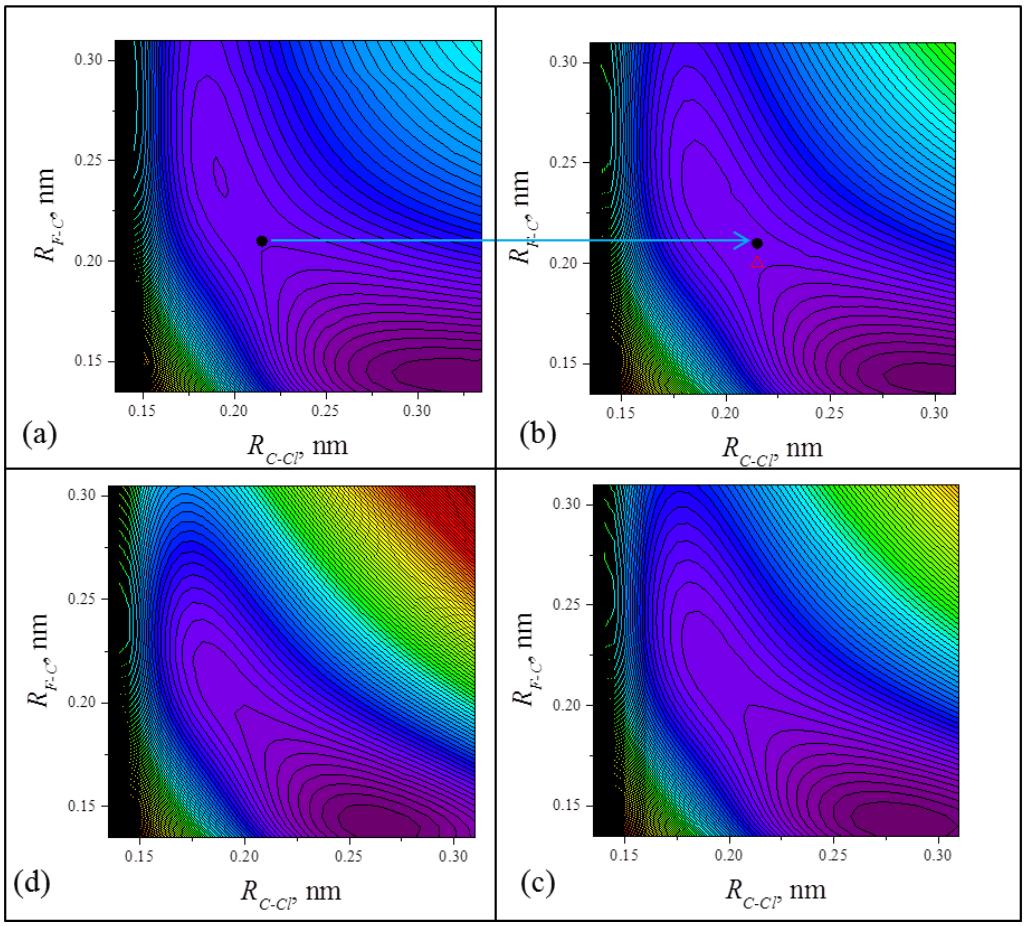

Figure 4.16. PES for F-CH_3-Cl^- system at ambient conditions (a), low compression (b), medium compression (c), and high compression (d). The corresponding TS positions are marked by symbols. The arrows project TS positions between lower and higher compression PES's. At medium and high compression the TS has been annihilated and the system collapses into the endothermic minimum. The contour spacing is 10 kJ/mol.

At lower compressions, the reaction paths are fairly similar to the zero-pressure paths despite the notable shift of reactant and product minima along the reaction coordinate. However, as pressure increases and deformation of the PES becomes more significant, the reaction paths shift in the diagonal direction towards the lower left corner. Symmetric systems show a progression of the TS position diagonally collapsing to a symmetric single minimum, while the TS for asymmetric systems collapses to the exothermic minimum. This behaviour is illustrated in Figure 4.17.

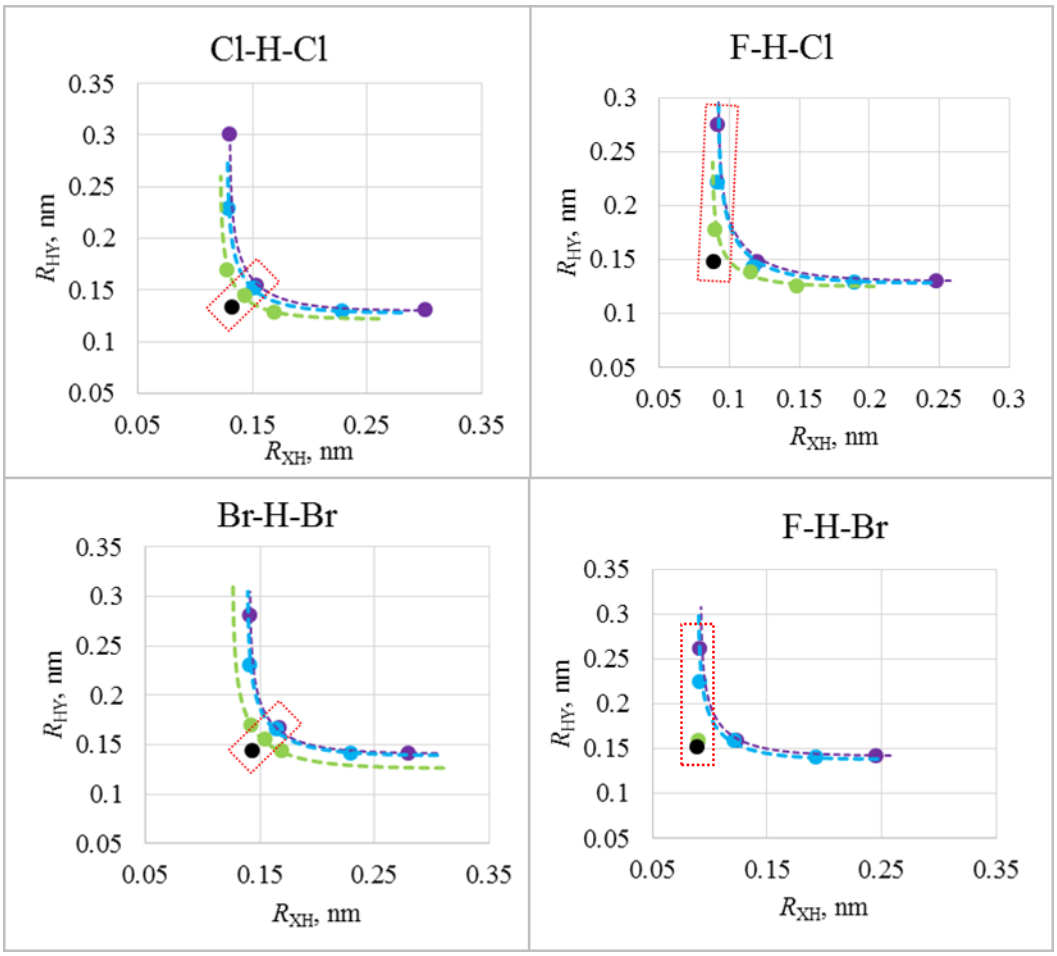

Figure 4.17. Plots of the minima and TS positions for symmetric and asymmetric X-H-Y systems at ambient conditions (purple), and low (blue), medium (green), and high (black) compression. The red boxes highlight the sequence of the stationary points (TSs for symmetric and exothermic minima for asymmetric systems) leading to a single minimum at high compressions. The dashed lines are BEBO reaction paths.

It is interesting to note that the energy profiles along the reaction pathways for the A-B-C reaction systems are reasonably well represented by a combination of two parabolic diabatic terms, which is consistent with the fact that hydrogen and alkyl transfer reactions obey the Marcus relationship.[19] The two-parabola model seems to offer an easy pictorial interpretation of the observed trends in the pressure dependencies of reaction profiles, as illustrated by an example for three XHY systems (X,Y = F,Cl) shown in Fig. 4.18. As two parabolas are shifted by pressure toward each other, the reaction barrier roughly estimated by their crossing point gets smaller. The TSs of a symmetric XHX

system remain exactly in the middle, between reactant and product minima, up to the moment when the two parabolas fully overlap and these two minima collapse into a single one, thus fully eliminating the TS and reaction barrier. The situation is somewhat different for asymmetric XHY systems, where the TS and reaction barrier disappear when the minimum of the "endothermic" parabola crosses the branch of the "exothermic" parabola, thus leaving the exothermic minimum the only stable state on the PES, with the remainder of the "endothermic" parabola manifesting itself as a dissymmetric shoulder on the reaction profile.

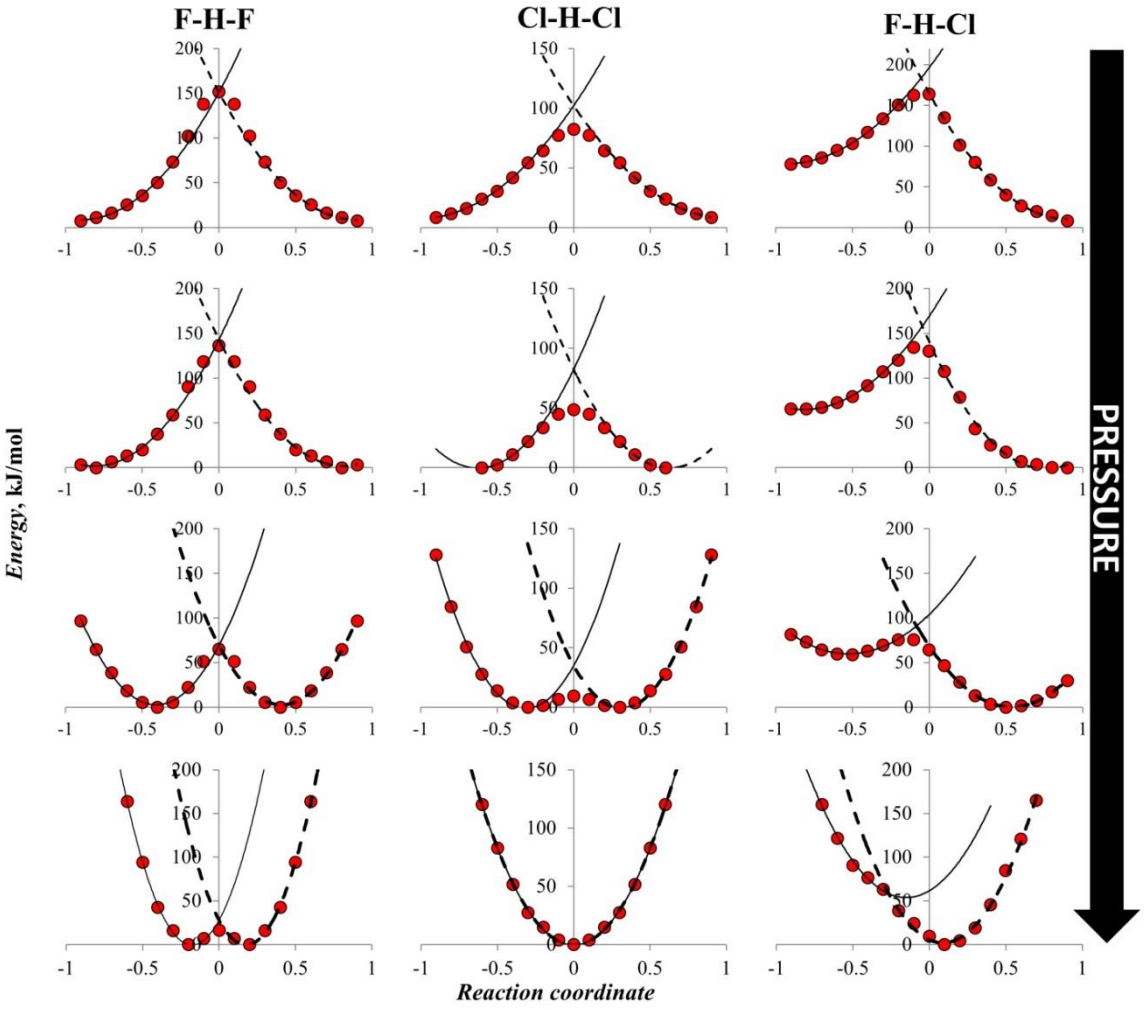

Figure 4.18. Reaction profiles for X-H-Y systems at different levels of compression. Red circles represent adiabatic QM energy profiles along scaled reaction coordinate; solid and dashed lines represent parabolic approximations for diabatic terms describing the reactant and product state, respectively.

The pressure dependencies of the reaction barriers for symmetric systems are shown in Fig. 4.19. Radical systems displayed a stronger pressure dependence than the anionic system, which could be traced to a lesser shift of the reactant minimum along the reaction coordinate in the latter, as predicted by eq. (4.14) for stiffer systems (see Fig. 4.20 where the energy profiles for the radical and anionic systems are compared at the bottom of their reactant wells).

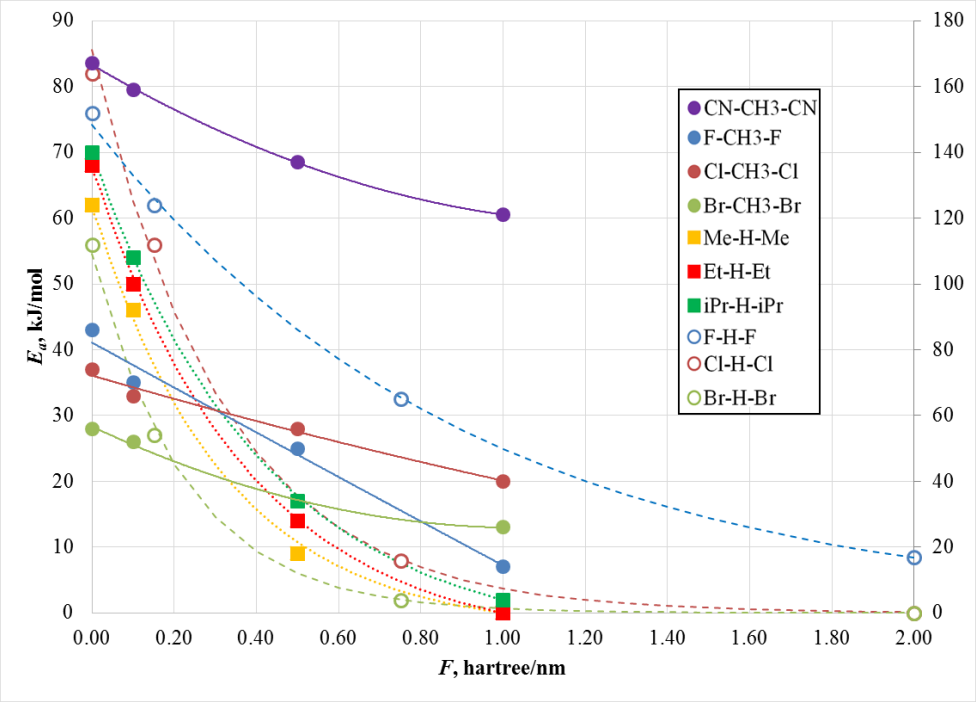

Figure 4.19. The dependence of the reaction barriers E_a on the strength of compression force F for symmetric exchange reaction systems: open circles – XHX, filled circles – XCH_3X^-, filled squares – R'HR". The graphs for $CNCH_3CN^-$ and FHF are plotted with a reference to the secondary energy axis.

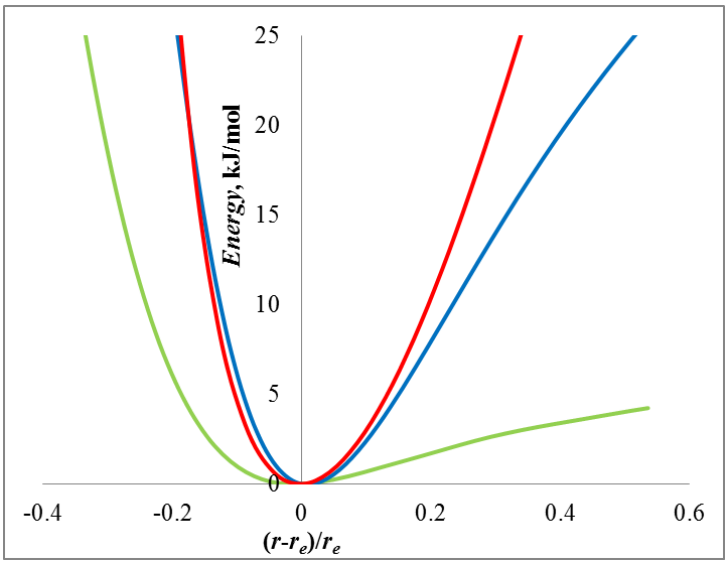

Figure 4.20. Energy profiles at the bottom the reactant wells for FH–F (green), $FH–F^-$ (red) and $FCH_3–F^-$ (blue) systems. The horizontal axis is a scaled displacement from the equilibrium distance r_e.

The activation energies $E_{ABC}(P)$ for asymmetric A-B-C systems obeyed the Marcus relation[20]

$$E_{ABC} = \frac{E_{ABA} + E_{CBC}}{2}\left(1 + \frac{1}{2}\frac{E_{ABC} - E_{CBA}}{E_{ABA} + E_{CBC}}\right)^2 \tag{4.15}$$

at various pressures, as evidenced by the linear correlation of Fig. 4.21 between their values obtained by direct QM calculations and from eq. (4.15).

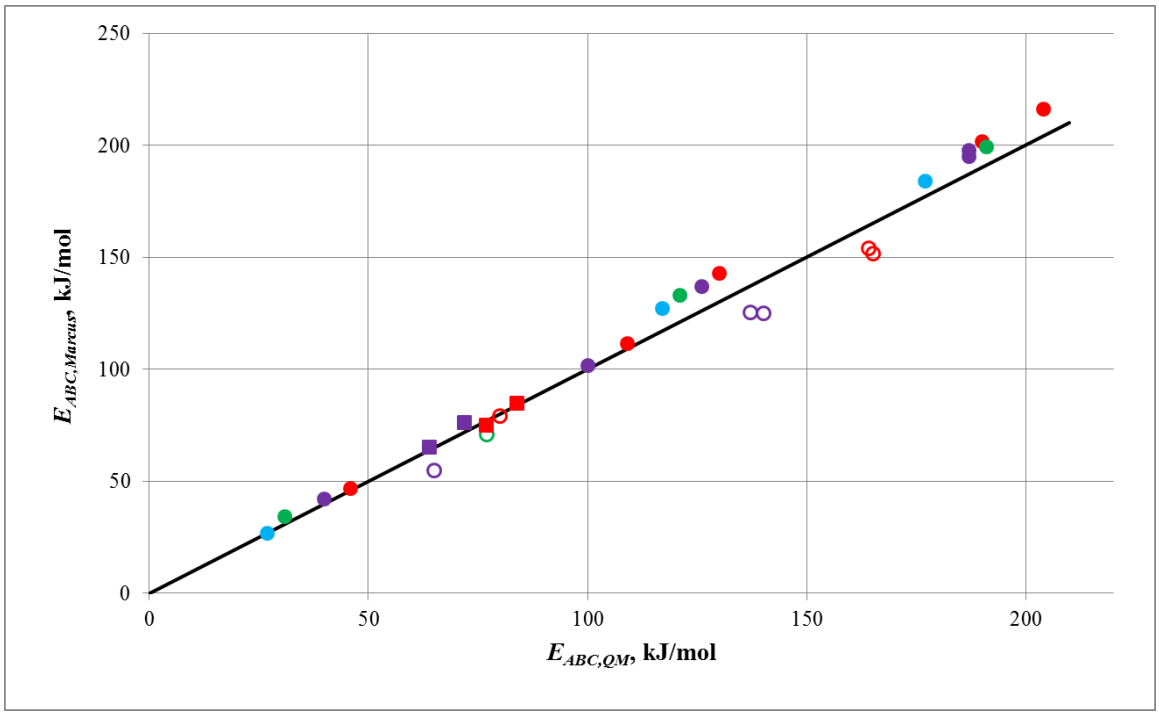

Figure 4.21. Correlation between reaction barriers E_{ABC} for A-B-C systems (A=X,R'; B=H,CH_3; C=Y,R") obtained by direct QM calculations and from the Marcus relation: open circles – XHY (X,Y=F,Cl,Br), filled circles – XCH_3Y^- (X,Y=F,Cl,Br), filled squares – R'HR" (R',R"=Me,Et), red – zero compression, purple – low compression, green – medium compression, blue – high compression.

4.3.2. Approximate Energy Surfaces

Since approximate eq. (4.13) offers a considerable computational saving in comparison to the full quantum-mechanical calculations, it is important to know if the description of high-pressure PESs provided by this equation is sufficiently accurate. We investigated this for the X-H-X systems. Since all calculations in this section refer to zero temperature, the Gibbs energy function $G(\mathbf{x};P)$ reduces to the enthalpy function $H(\mathbf{x};P)$. In addition, for a 1D model, the expansion work term $PV(\mathbf{x})$ becomes $FL(\mathbf{x})$, where $L(\mathbf{x})$ is the linear size of the system and F is the compression force, playing the roles of 1D volume and 1D pressure, respectively. By virtue of the linearity of the X-Y-H system, $L(R_{XH},R_{HY}) = R_{XH} + R_{HY}$ and, with $T = 0$ and $P_0 = 0$, eq. (4.13) turns into

$$H(R_{XH},R_{HY};F) \approx U_0(R_{XH},R_{HY}) + F\times L(R_{XH},R_{HY}) = U_0 + F\times(R_{XH}+R_{HY}) \quad (4.16)$$

The approximate high-pressure PES's $H(R_{XH},R_{HY};F)$ were derived from the zero-pressure PES $U_0(R_{XH},R_{HY})$ using eq. (4.16) and showed a remarkable similarity to the exact PES described in the previous subsection. Parameters of the approximate PES's for symmetric X-H-X systems are listed in Table 4.9 in comparison with the corresponding parameters of the exact PESs.

Table 4.9. Parameters of the approximate PES of symmetric X-H-X systems (X = F, Cl, Br) obtained using eq. (4.16). The figures in parentheses represent their relative deviation from the corresponding parameters of the exact PES listed in Table 4.3.

System	Compression	Reactant		TS	
		R_{XH}, nm	R_{HX}, nm	R_{XH}, nm	Reaction barrier, kJ/mol
F-H-F	Low	0.091 (0%)	0.185 (2%)	0.110 (2%)	115 (7%)
	Medium	0.089 (1%)	0.144 (1%)	0.106 (0%)	63 (3%)
	High	0.088 (1%)	0.117 (4%)	0.110 (12%)	20 (18%)
Cl-H-Cl	Low	0.129 (0%)	0.231 (1%)	0.151 (1%)	50 (11%)
	Medium	0.128 (0%)	0.170 (1%)	0.143 (1%)	8 (0%)
	High	0.133 (0%)	0.133 (0%)	single min	no reaction
Br-H-Br	Low	0.141 (0%)	0.231 (0%)	0.164 (1%)	33 (22%)
	Medium	0.142 (1%)	0.173 (0%)	0.154 (1%)	2 (0%)
	High	0.143 (1%)	0.143 (1%)	single min	no reaction
Average deviation		0.5%	1%	2%	7%

4.3.3. 3D Matrix

The 1D model of Fig. 4.11 was adequate to describe the effects of the longitudinal compression but left the lateral compression of a reaction system outside of its scope. It was also unsuitable for calculation of the pressure equivalent of a given compression force. To address these issues, we considered a 3D matrix built by encasing the linear model in a rectangular 3×3×9 prism of uniformly spaced Ne atoms as shown in Fig. 4.12.

As in the case of the 1D matrix, the compressing forces were calculated as negative partial derivatives of energy with respect to the linear dimensions of the prism: $F_i = -dU/dL_i$ ($i = x,y,z$). The pressure equivalents were found by dividing the forces by the appropriate cross-section areas to which the forces were applied. Both isotropic ($P_x = P_y = P_z$) and axially anisotropic ($P_x \neq P_y = P_z$) compressions were considered for the symmetric F-H-F system aligned along the x axis. The resulting PES's were very similar to those shown in Fig. 4.13 for the 1D matrix, at least in the part of the PES adjacent to the reaction path. As an example, a comparison of the PES generated for the F-H-F system at medium compression in the 1D and 3D matrices is shown in Fig. 4.22 (PES for low and high compression can be found in Appendix D). The PES were similar due to the fact that while the longitudinal compression by a 3D matrix had a profound effect on the PES topography, the effect of the lateral compression by that matrix was rather marginal.

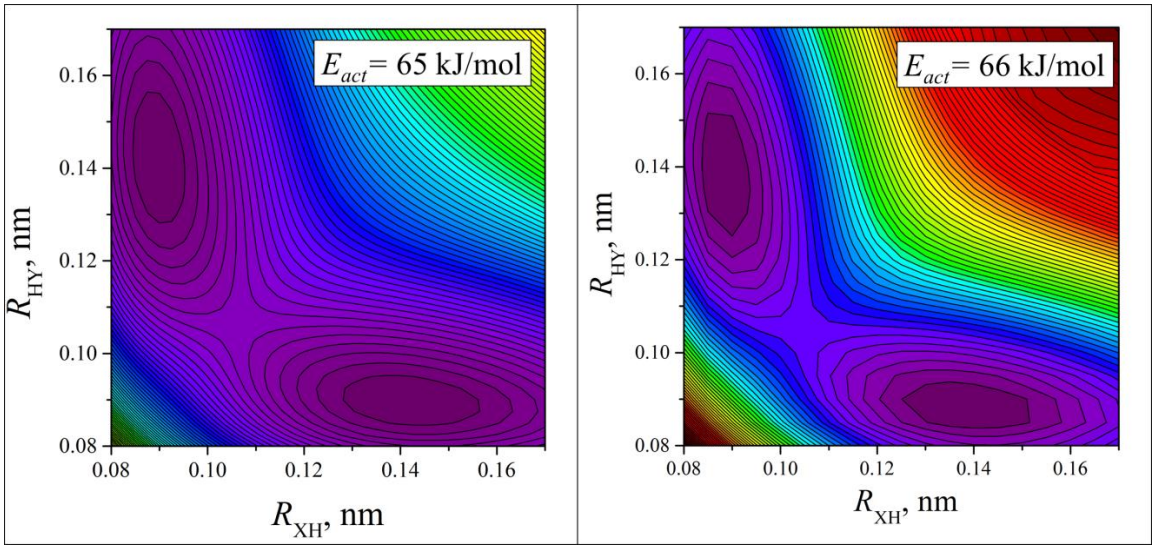

Figure 4.22. PES for F-H-F system at medium compression generated using the 1D matrix (left) and 3D matrix (right). The contour spacing is 10 kJ/mol.

4.4. Linear H_3^- System

Recent studies of potassium, rubidium, cesium, and barium polyhidrides[21] have observed the formation of a symmetric linear H_3^- anion at elevated pressures. At lower pressures this ion disproportionated into a linear $H^-\cdots H_2$ complex, stable at ambient

conditions.[22] The exact pressure of this transition depended on the nature of the metal cation and crystal stoichiometry, and for RbH_5 it was about 300 kbar.[23] To check the accuracy of the predictions based on our system-in-matrix calculations, we optimized the geometry of the linear H-H-H^- system embedded in a compressed 3D Ne matrix, as shown in Fig. 4.12 for F-H-F. The calculations were performed with PBE/6-311++G(d,p) to match the level of theory used in Refs. 21 and 22b. The results presented in Fig. 4.23 predict a transition to the symmetric H_3^- anion above 300 kbar.

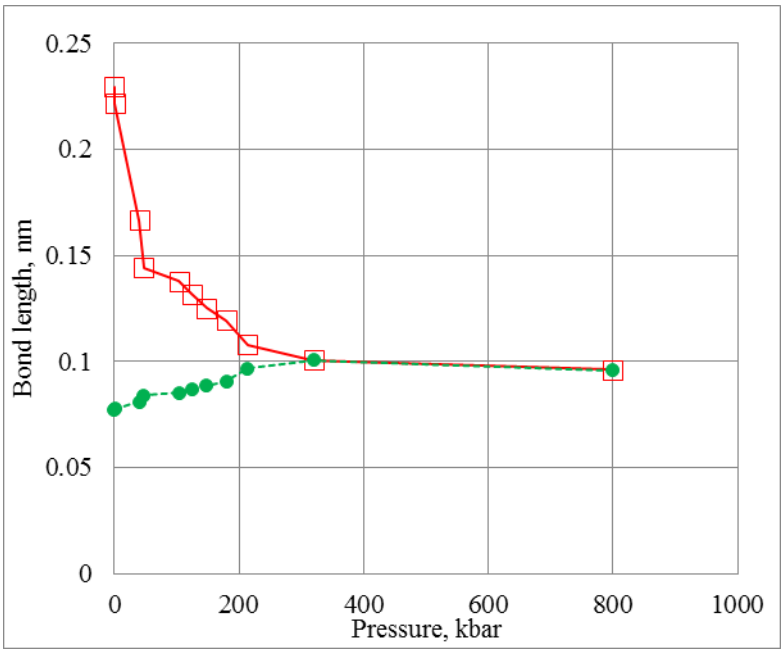

Figure 4.23. Pressure dependence of the lengths of long (red squares) and short (green circles) HH bonds in the H-H-H^- system.

4.5. Conclusion

The reported results indicate that reaction profiles and energy surfaces of compressed systems can undergo a tremendous change with pressure, sometimes resulting in the complete annihilation of the reaction barrier separating reactants and products. Softer systems with lower activation barriers undergo a transition to a single-minimum state at lower pressures as evidenced by the comparison of the radical X-H-Y and R′-H-R″ systems to the stiffer anionic X-CH_3-Y^- systems. Unsaturated systems

represent another example of softer species. It has been argued earlier[3b] that the reaction barrier for Diels-Alder dimerization of cyclopentadiene gets reduced from about 70 kJ/mol at ambient conditions to 20 kJ/mol at 50 kbar. If a high-pressure single minimum replaces the barrier of a thermoneutral process, as in the case of symmetric X-H-X systems, the high pressure species associated with that minimum are unstable at low pressures when the barrier is restored. The transition between high- and low-pressure forms is therefore expected to be reversible in such cases, as it was with the H_3^- anion in polyhidrides.[21] On the contrary, for exothermic processes, where high pressures simultaneously eliminate the barrier and the endothermic minimum, the high-pressure state is associated with the exothermic minimum and therefore remains stable at lower pressures. An example of this kind is high pressure polymerization of aromatic compounds,[24] where static pressure of 100-350 kbar eliminates the barrier separating the endothermic minimum of the monomer state and the exothermic minimum of the polymer state.

Approximate expressions (4.13) and (4.16), together with the compressed matrix approach used in this work promise remarkable saving and computational efficiency in producing high-pressure reaction profiles and energy surfaces, the knowledge of which is crucial to understanding reactivity and spectral properties of compressed species.

4.6. References

1. (a) W. J. le Noble and H. Kelm, *Angew. Chem., Int. Ed. Engl.*, 1980, **19**, 841; (b) R. van Eldik and H. Kelm, *Rev. Phys. Chem. Japan*, 1980, **50**, 185; (c) R. van Eldik and C.D. Hubbard, *S. Afr. J. Chem.*, 2000, **53**, 139; (d) R. van Eldik and C.D. Hubbard, *Adv. Phys. Org. Chem.*, 2006, **41**, 1; (e) C.D. Hubbard, and R. van Eldik, *Inorg. Chim. Acta*, 2010, **363**, 2357.

2. (a) W. J. le Noble, *Rev. Phys. Chem. Jpn.*, 1980, **50**, 207; (b) W. J. le Noble and H. Kelm, *Angew. Chem., Int. Ed.*, 1980, **19**, 841; (c) R. van Eldik, H. Kelm, *Rev. Phys. Chem. Jpn.*, 1980, **50**, 185; (d) R. van Eldik, C. D. Hubbard, *Afr. J. Chem.*, 2000, **53**, 139; (e) R. van Eldik and C. D. Hubbard, *Adv. Phys. Org. Chem.*, 2006, **41**, 1; (f) C. D. Hubbard and R. van Eldik, *Inorg. Chim. Acta*, 2010, **363**, 2357.
3. (a) W.J. le Noble, *Rev. Phys. Chem. Jap.*, 1980, **50**, 207; (b) M.V. Basilevsky, N. Weinberg, V.M. Zhulin, *J. Chem. Soc. Faraday Trans. 1*, 1985, **81,** 875.
4. J. Spooner, B. Yanciw, B. Wiebe and N. Weinberg, *J. Phys. Chem. A*, 2014, **118**, 765.
5. J. Nicolas, K. Gubbins, W. Streett and D. Tildesley, *Mol. Phys.*, 1979, **37**, 1429.
6. A. E. Stearn and H. Eyring, *Chem. Rev.*, 1941, **29**, 509.
7. (a) I.S. Crick and P.A. Tregloan, *Inorg. Chim. Acta*, 1988, **142**, 291; (b) M. Zhang, R. van Eldik, J.H. Espenson and A. Bakac, *Inorg. Chem.*, 1994, **33**, 130.
8. P.W. Atkins and J. De Paula, *Physical Chemistry*, 9th ed., Oxford University Press: Oxford, N.Y., 2010.
9. H.S. Johnston, *Gas Phase Reaction Rate Theory*, Ronald Press Co.: NY, 1966
10. (a) V.M. Zhulin, M.Ya. Botnikov and I. Milyavskaya, *Russian Chem. Bull.*, 1975, **24**, 424; (b) V.M. Zhulin, M.Ya. Botnikov, I. Milyavskaya, *Russian Chem. Bull.*, 1975, **24**, 1038; (c) V.M. Zhulin, M.Ya. Botnikov, I. Milyavskaya, *Russian Chem. Bull.*, 1977, **26**, 517.
11. Although somewhat inadequate for open-shell systems, B3LYP/6-31G++G(d,p) calculations produce good geometry and decent energy parameters for the TS of hydrogen transfer from the methyl group[12].

12. (a) J. Zheng, Y. Zhao and D.G. Truhlar, *J. Phys. Chem. A*, 2007, **111**, 4632; (b) A.G. Vandeputte, M.K. Sabbe, M.-F. Reyniers, V. van Speybroeck, M. Waroquier, G.B. Marin, *J. Phys. Chem. A*, 2007, **111**, 11771.
13. A.R. Leach, *Molecular Modelling: Principles and Applications*, 2nd ed., Prentice Hall: Upper Saddle River, NJ, 2001.
14. R.L. Burden and J.D. Faires, *Numerical Analysis*, 9th ed., Brooks/Cole: Boston, 2011.
15. Although the importance of polar solvent-solute interactions dramatically changing the shape of the S_N2 PES has long been recognized,[16] the solvent effects on the TS structure are rather limited,[17] and the gas-phase calculations[18] remain a useful and widely exploited proxy for the solution reactions, when limited to the central barrier segment of the PES, between the minima of reactant and product complexes.
16. (a) J. Chandrasekhar, S.F. Smith, W.L. Jorgensen, *J. Am. Chem. Soc.*, 1984, **106**, 3049; (b) J. Chandrasekhar, S.F. Smith and W.L. Jorgensen, *J. Am. Chem. Soc.*, 1985, **107**, 154.
17. W.L. Jorgensen and J.K. Buckner, *J. Phys. Chem.*, 1986, **90**, 4651.
18. (a) S. Wolfe and C.-K. Kim, *J. Am. Chem. Soc.*, 1991, **113**, 8056; (b) R. Boyd, C.-K. Kim, Z. Shi, N. Weinberg and S. Wolfe, *J. Am. Chem. Soc.*, 1993, **115**, 10147; (c) R.A. Poirier, Y Wang and K.C. Westaway, *J. Am. Chem. Soc.*, 1994, **116**, 2526; (d) M.N. Glukhovtsev, A. Pross and L. Radom, *J. Am. Chem. Soc.*, 1995, **117**, 2024; (e) M.N. Glukhovtsev, A. Pross and L. Radom, *J. Am. Chem. Soc.*, 1996, **118**, 6273; (f) G.E. Davico and V.M. Bierbaum, *J. Am. Chem. Soc.*, 2000, **122**, 1740; (g) K.C.

Westaway, *Adv. Phys. Org. Chem.*, 2006, **41**, 217; (h) K.C. Westaway, *J. Label. Compd. Radiopharm.*, 2007, **50**, 989.

19. (a) R.A. Marcus, *J. Phys. Chem.* 1968, **72**, 891; (b) A.O. Cohen, R.A. Marcus, *J. Phys. Chem.* 1968, **72**, 4249; (c) A.J. Kresge, *Acc. Chem. Res.* 1975, **8**, 354; (d) W.J. Albery, *Ann. Rev. Phys. Chem.*, 1980, **31**, 227; (e) S. Wolfe, D.J. Mitchell and H.B. Schlegel, *J. Am. Chem. Soc.*, 1981, **103**, 7694; (f) M.M. Kreevoy, D. Ostovic, I.-S.H. Lee, D.A. Binder and G.W. King, *J. Am. Chem. Soc.*, 1988, **110**, 524; (g) R.A. Marcus, *Angew. Chem., Int. Ed.*, 1993, **32**, 1111.
20. (a) R. Marcus, *J. Phys. Chem.*, 1968, **72**, 891; (b) R. Marcus, *Faraday Symposia Chem. Soc*., 1975, **10**, 60.
21. (a) J. Hooper and E. Zurek, *J. Phys. Chem. C*, 2012, **116**, 13322; (b) J. Hooper and E. Zurek, *Chem. Eur. J.*, 2012, **18**, 5013-5021; (c) A. Shamp, J. Hooper, E. Zurek, *Inorg. Chem.*, 2012, **51**, 9333; (d) J. Hooper, B. Altintas, A. Shamp and E. Zurek, *J. Phys. Chem. C*, 2013, **117**, 2982.
22. (a) M. Ayouz, O. Dulieu, R. Guérout, J. Robert and V. Kokoouline, *J. Chem. Phys.*, 2010, **132**, 194309; (b) C.F. Matta, L. Huang and L. Massa, *J. Phys. Chem. A*, 2011, **115**, 12451.
23. Estimated from the RbH_5 graph of Fig. 3 in Ref. 21b.
24. (a) H.G. Drickamer, *Science*, 1967, **156**, 1183; (b) V.C. Bastron and H.G. Drickamer, *J. Solid State Chem.*, 1971, **3**, 550; (c) P. Pruzan, J.C. Chervin, M.M. Thiery, J.P. Itie, J.M. Besson, J.P. Forgerit and M. Revault, *J. Chem. Phys.*, 1990, **92**, 6910; (d) M. Santoro, L. Ciabini, R. Bini and V. Schettino, *J. Raman Spectrosc.*, 2003, **34**, 557.

Chapter 5.

A Comparative Analysis of Empirical Equations Describing Pressure Dependence of Reaction Rate Constants

5.1. Introduction

It has been shown in Chapter 3 of this thesis that our MD displacement volume model can be used to obtain accurate theoretical activation and reaction volumes. The usefulness of these calculated volumes for mechanistic analysis crucially depends on the availability and precision of the experimental ΔV and $\Delta V^{\neq}$. As discussed in Section 1.4, the latter are usually obtained from kinetic or equilibrium data by differentiation of empirical analytical functions ln $k(P)$ or ln $K(P)$ fitted to the experimental data[1]. Since these functions utilize different analytical expressions, *the values of the activation and reaction volumes obtained from the same experimental data set using different equations can vary substantially*[1c-f]. Earlier[2], various empirical equations (eleven most common of them are listed in Table 1.4[3], which is reproduced here for convenience as Table 5.1) were analyzed in the context of their common features and their relationship to the volume changes in reactions. In the present study, we discuss the limits within which these equations remain physically meaningful, and assess how the level of errors in the experimental data and the choice of equations affect the accuracy of determination of activation and reaction volumes. Although in our analysis we refer specifically to $\Delta V^{\neq}$, the same expressions, results, and conclusions equally apply to ΔV.

Table 5.1. Most common empirical equations describing pressure dependence of rate and equilibrium constants and their classification[2].

	Equation	Type
E1	$\ln k/k_0 = a_1P + a_2P^2$	Polynomial eq. (1.9)/(1.10a)
E2	$\ln k/k_0 = a_1P + a_3P^3$	
E3	$\ln k/k_0 = a_1P + a_2P^2 + a_3P^3$	
E4	$\ln k/k_0 = a_3P/(1+a_4P)$	Hyperbolic eq. (1.9)/(1.10b)†
E5	$\ln k/k_0 = a_1P + a_3P/(1+a_4P)$	
E6	$\ln k/k_0 = a_2\ln(1+a_4P)$	Logarithmic eq. (1.9)/(1.10c)
E7	$\ln k/k_0 = a_1P + a_2\ln(1+a_4P)$	
E8	$\ln k/k_0 = a_1P + a_3P\ln(1+a_4P)$	
E9	$\ln k/k_0 = a_1P + a_2(1+a_4P)\ln(1+a_4P)$	
E10	$\ln k/k_0 = a_1P + a_2\ln(1+a_4P) + a_3P\ln(1+a_4P)$	
E11	$\ln k/k_0 = a_1P + a_2P^{1.523}$	Pseudo-logarithmic

† Without loss of generality, a_2 in the equations of hyperbolic type can be assumed to be equal to zero if a_3 is appropriately adjusted. Equation E5 thus represents the most general form of a hyperbolic equation (1.9)/(1.10b).

5.2. General properties and comparison of empirical functions describing pressure dependence of the rate and equilibrium constants

General behavior of ln*k* as a function of pressure can be characterized by the signs and asymptotic values of its pressure derivatives – activation volume $\Delta V^{\neq}$ (eq. (1.4)), compressibility coefficient of activation[4]

$$\Delta\beta^{\neq} = \left(\frac{\partial \Delta V^{\neq}}{\partial P}\right)_T = -RT\left(\frac{\partial^2 lnk}{\partial P^2}\right)_T \qquad (5.1)$$

and hypercompressibility coefficient of activation

$$\Delta\xi^{\neq} = \left(\frac{\partial \Delta\beta^{\neq}}{\partial P}\right)_T = -RT\left(\frac{\partial^3 lnk}{\partial P^3}\right)_T \qquad (5.2)$$

The values of $\Delta V^{\neq}$ at zero and infinite pressure, $\Delta V_0^{\neq}$ and $\Delta V_\infty^{\neq}$, in their relationships to parameters a_i of eqs E1-E11 are listed in Table 5.2 together with similar expressions for higher order derivatives $\Delta\beta_0^{\neq}$ and $\Delta\xi_0^{\neq}$.

Table 5.2. Activation volumes, and compressibility and hypercompressibility coefficients of activation for empirical functions listed in Table 1 (see also Table 6 in Ref. 2).

Equation	$\Delta V_0^{\neq}/RT$ (Ref. 2)	$\Delta V_\infty^{\neq}/RT$ (Ref. 2)	$\Delta\beta_0^{\neq}/RT$ (this work)	$\Delta\xi_0^{\neq}/RT$(this work)
E1	$-a_1$	$\pm\infty$	$-2a_2$	0
E2	$-a_1$	$\pm\infty$	0	$-6a_3$
E3	$-a_1$	$\pm\infty$	$-2a_2$	$-6a_3$
E4	$-a_3$	0	$2a_3a_4$	$-6a_3a_4^2$
E5	$-(a_1+a_3)$	$-a_1$	$2a_3a_4$	$-6a_3a_4^2$
E6	$-a_2a_4$	0	$a_2a_4^2$	$-2a_2a_4^3$
E7	$-(a_1+ a_2a_4)$	$-a_1$	$a_2a_4^2$	$-2a_2a_4^3$
E8	$-a_1$	$\pm\infty$	$-2a_3a_4$	$3a_3a_4^2$
E9	$-(a_1+a_2a_4)$	$\pm\infty$	$-a_2a_4^2$	$a_2a_4^3$
E10	$-(a_1+a_2a_4)$	$\pm\infty$ or $-a_1$ [†]	$a_2a_4^2-2a_3a_4$	$-2a_2a_4^3+3a_3a_4^2$
E11	$-a_1$	$\pm\infty$	$\pm\infty$	$\pm\infty$

Since the overall shape of functions E1-E11 depends on their parameters a_i, it is of interest to assess general constraints on these parameters, within which these functions demonstrate a physically reasonable behavior in describing the pressure dependence of ln*k*. The following would seem to be a set of natural requirements if dynamic effects of solvent[5] are unimportant:

1. ln*k* is a monotonic function of pressure, *i.e.* $\Delta V^{\neq}$ retains its sign over a range of pressures where eq (1.7) is valid. That is,

$$\Delta V^{\neq}/\Delta V_0^{\neq} \geq 0 \qquad (5.3)$$

2. The relative value $\Delta V^{\neq}/\Delta V_0^{\neq}$ of $\Delta V^{\neq}$ with respect to its reference value $\Delta V_0^{\neq}$ at zero pressure is a decreasing function of pressure, *i.e.*

$$\Delta\beta^{\neq}/\Delta V_0^{\neq} < 0 \qquad (5.4)$$

It follows directly from (5.3) and (5.4) that at high pressures $\Delta V^{\neq}$ asymptotically approaches its finite limit $\Delta V_\infty^{\neq}$, such that $0 \leq \Delta V_\infty^{\neq}/\Delta V_0^{\neq} < 1$.

3. Consistently with that, the graph of $\Delta V^{\neq}(P)/\Delta V_0^{\neq}$ is a concave curve of positive curvature, *i.e.*

$$\Delta\xi^{\neq}/\Delta V_0^{\neq} > 0 \qquad (5.5)$$

Inspection of Table 5.2 reveals that, strictly speaking, only equations E4-E7 can satisfy condition $0 \leq \Delta V_\infty^{\neq}/\Delta V_0^{\neq} < 1$ and thus demonstrate correct asymptotic behavior at infinite pressure. This is not surprising since none of the equations E1-E11 was intended to describe the rate constants at extreme pressures, which makes the above condition somewhat excessive. However, it is important to know the range of pressures over which conditions (5.3)-(5.5) are satisfied and to determine the validity threshold P_{max}, above which at least one of these conditions is violated. Such thresholds, together with the constraints on parameters a_i of equations E1-E11 imposed by conditions (5.3)-(5.5), are obtained in Appendix E and summarized in Table 5.3.

Table 5.3. The summary of constraints and thresholds for equations E1-E11.

Equation	P_{max}	Constraints
E1	eq. (A5)	$a_1a_2 < 0$
E2	eq. (A7)	$a_1a_3 < 0$
E3	eq. (A8)	$a_1a_2 < 0$ and $a_1a_3 < 0$
E4	$+\infty$	$a_4 > 0$
E5	$+\infty$	$a_4 > 0$ and $a_1a_3 > 0$
E6	$+\infty$	$a_4 > 0$
E7	$+\infty$	$a_4 > 0$ and $a_1/(a_2a_4) > -1$
E8	eq. (A24)	$a_4 > 0$ and $a_1a_3 > 0$
E9	eq. (A26)	$a_4 > 0$, $a_1/(a_2a_4) < -1$, and $a_1a_2 < 0$
E10	$+\infty$ or eq. (A29)	eqs. (A27)-(A30)
E11	eq. (A35)	$a_1a_2 < 0$

In the case of equations E1-E9, the relationships of Table 5.2 can be inverted to produce expressions for coefficients a_i in terms of physical parameters $\Delta V_0^{\neq}$, $\Delta\beta_0^{\neq}$, and $\Delta\xi_0^{\neq}$ (see Appendix F). One, therefore, can compare equations E1-E9 by plotting them for the same set of physical parameters. Such plots are presented in Fig. 5.1 for a series of different pressure ranges. As a prototype model reaction, we chose high-pressure *Z/E*-isomerization of 4-(dimethylamino)-4'-nitroazobenzene, for which equations E5 and E7, fitted to the experimental data[1e] over a 0-4 kbar pressure range, give close values of $\Delta V_0^{\neq}$, $\Delta\beta_0^{\neq}$, and $\Delta\xi_0^{\neq}$ listed in Table 5.4. In our graphs, we used the rounded averages of these values.

Table 5.4. Equation coefficients and physical parameters for *Z/E* isomerization of 4-(dimethylamino)-4'-nitroazobenzene[1e]

Equation	Equation coefficients†				Physical parameters† at 25ºC		
	a_1	a_2	a_3	a_4	$\Delta V_0^{\neq}$	$\Delta\beta_0^{\neq}$	$\Delta\xi_0^{\neq}$
E5	0.1977		0.8105	0.2325	–25.0	9.3	–6.5
E7	0.05706	2.266		0.4223	–25.1	10.0	–8.5
Rounded average					–25	10.	–7.5

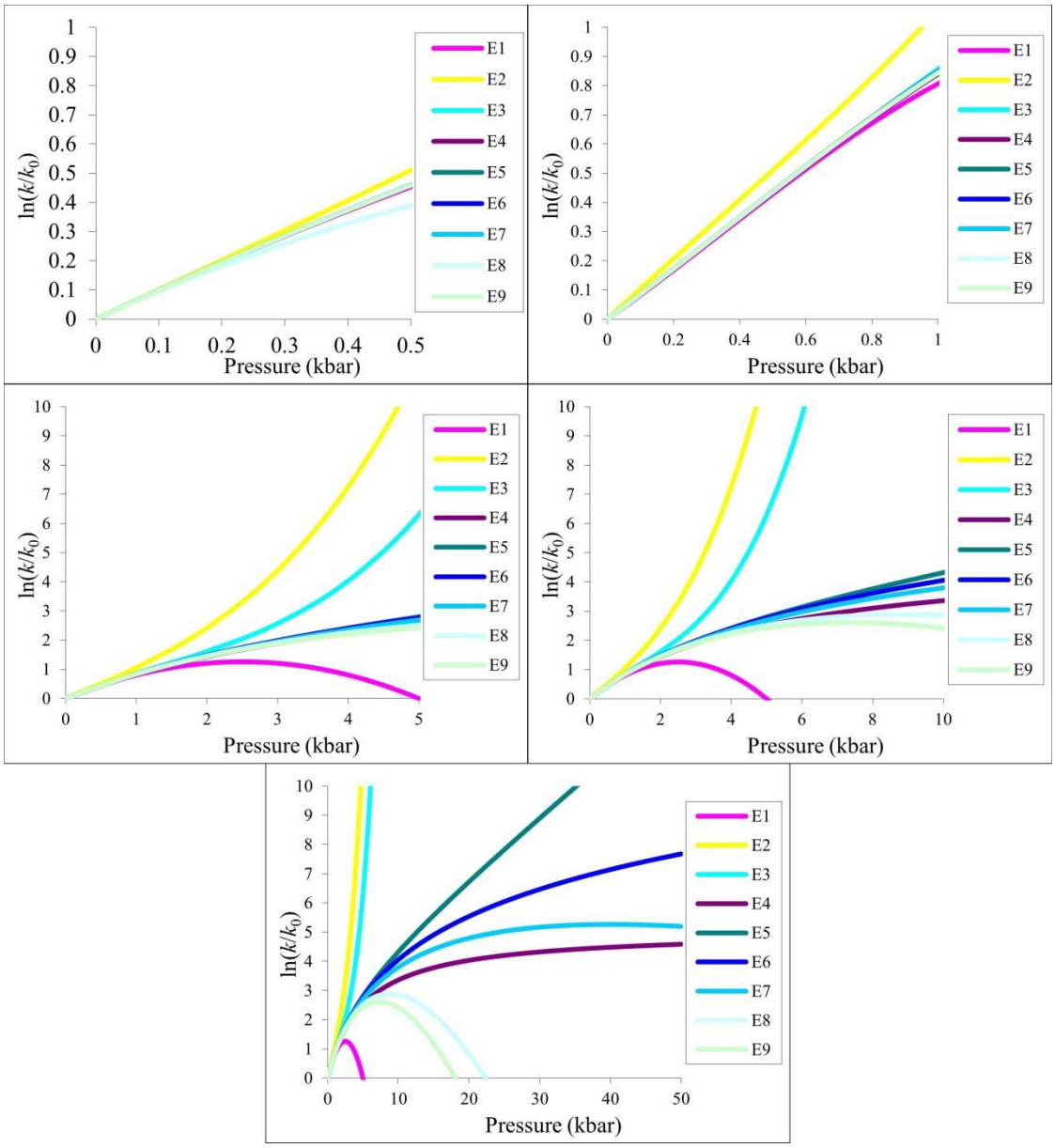

Figure 5.1. Graphs of equations E1-E9 for $\Delta V_0^{\neq}$ = –25 cm^3mol^{-1}, $\Delta\beta_0^{\neq}$= 10. $cm^3mol^{-1}kbar^{-1}$, and $\Delta\xi_0^{\neq}$ = –7.5 $cm^3mol^{-1}kbar^{-2}$. Pressure ranges: (*a*) 0 to 0.5 kbar; (*b*) 0 to 1 kbar; (*c*) 0 to 5 kbar; (*d*) 0 to 10 kbar; (*e*) 0 to 50 kbar.

5.2.1. Graphs

As can be seen from Fig. 5.1, for a relatively narrow pressure range of 0 to 0.5 kbar the graphs cluster relatively close to each other. They remain close up to 1 kbar, although E2 start departing notably from the rest of equations. When the pressure range is

extended to 5 kbar, two more graphs split off and start demonstrating counter-intuitive unphysical behavior: cubic equations E2 and E3 produce curves that are concave up, whereas quadratic equation E1 passes its maximum and starts dipping down. Equations E4-E9 remain close at 5 kbar, but visibly deviate from each other by 10 kbar. Most of them also start showing unphysical behavior at higher pressures, and by the time the pressure range exceeds 50 kbar, only equations E4 and E6 remain physically reasonable[6].

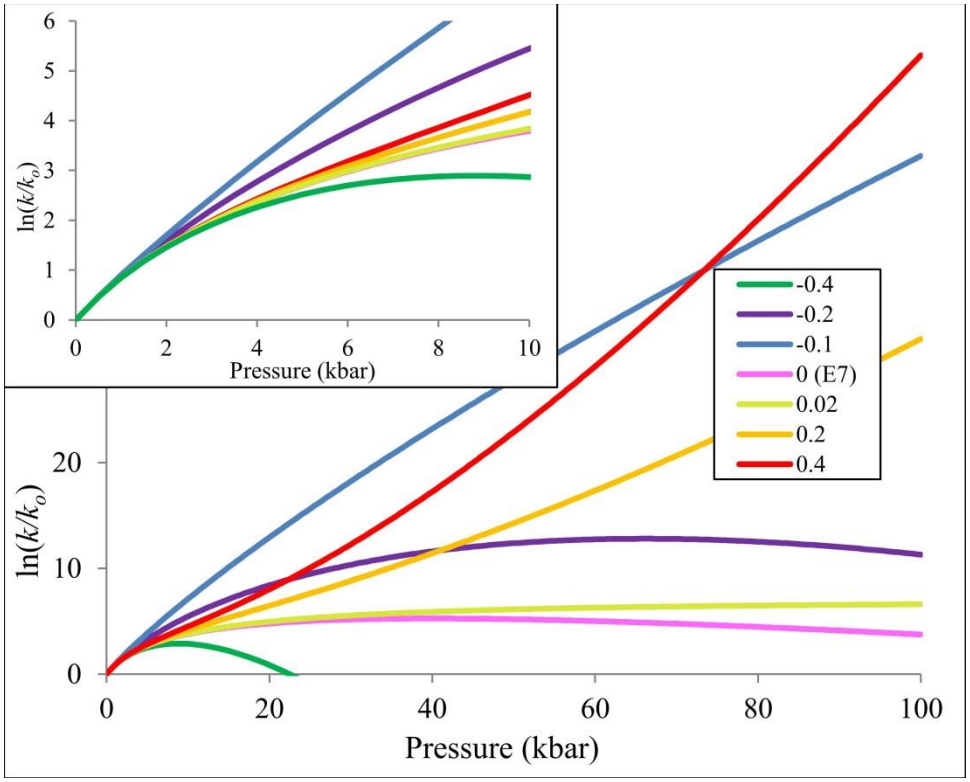

Figure 5.2. Graphs of equation E10 for $\Delta V_0^{\neq} = -25$ cm^{3}mol^{-1}, $\Delta\beta_0^{\neq} = 10$. cm^{3}mol^{-1}kbar^{-1}, $\Delta\xi_0^{\neq} = -7.5$ cm^{3}mol^{-1}kbar^{-2}, with the free parameter a_3 = -0.4, -0.2, -0.1, 0, 0.02, 0.2, and 0.4. In the case of a_3=0 equation E10 reduces to equation E7.

Since equation E10 contains four parameters, only three of them can be expressed in terms of $\Delta V_0^{\neq}$, $\Delta\beta_0^{\neq}$, and $\Delta\xi_0^{\neq}$, leaving the fourth parameter free. A family of E10 curves consistent with the selected $\Delta V_0^{\neq}$, $\Delta\beta_0^{\neq}$, and $\Delta\xi_0^{\neq}$values is shown in Fig. 5.2, where a_3 is chosen as an independent parameter. As can be seen from the figure, the shapes of the graphs vary significantly on a wider pressure range, depending on the value of the free parameter a_3. In the shown examples, only the curves with a_3 = -0.1 and 0.02 display

physically reasonable behavior over the 0-100 kbar range, the curves with a_3 = -0.4, -0.2 and 0 possess maxima, and the curves with a_3 = 0.2 and 0.4 possess inflection points. At the same time, at lower pressures (see the inset), all curves of the family cluster closely, and since E10 reduces to E7 when a_3 = 0, all these E10 curves are also quite close to E1-E9 curves when pressures do not exceed 1 kbar.

Equation E11 demonstrates unphysical behavior at zero pressure by producing infinite compressibility and hypercompressibility coefficients, and therefore the data on $\Delta\beta_0^{\neq}$ or $\Delta\xi_0^{\neq}$ cannot be used to estimate its second coefficient a_2. Fig. 3 shows a family of E11 curves parametrized by a_2. With the exception of a_2 = -0.04, all shown curves possess maxima on the 0-100 kbar pressure range. To get closer to curves of Fig. 1, say, the E7 curve, the value of a_2 needs to become as low as -0.2. This is accompanied with a significant shift of the curve maximum to lower pressures: $P_{max} \approx$ 40kbar for a_2 = -0.1 and 10 kbar for a_2 = -0.2, *i.e.* P_{max} is approximately proportional to the reciprocal square of a_2, as predicted by eq. (A35) for E11, the exponent a_4 of which is close to 1.5 (a_4 = 1.523).

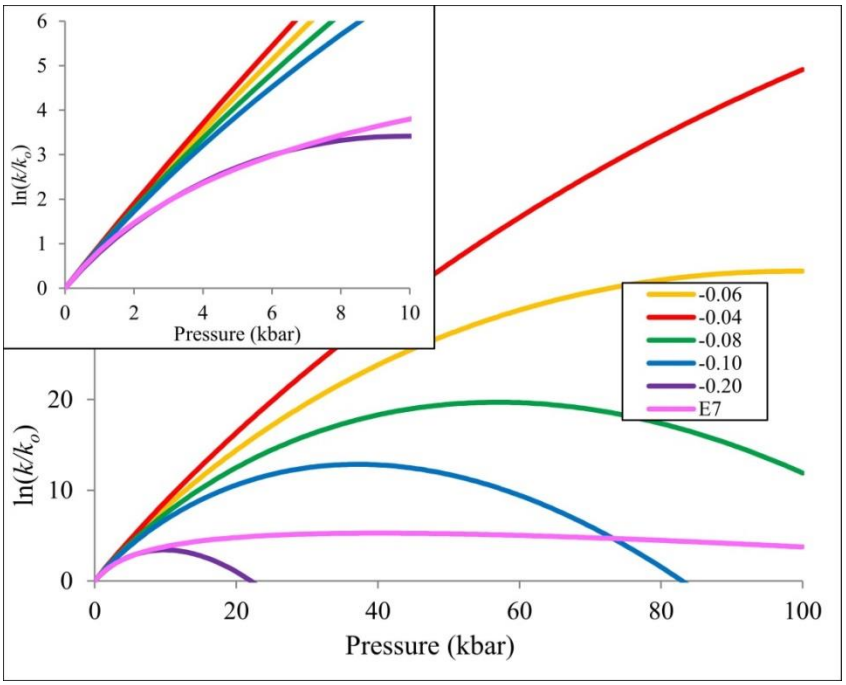

Figure 5.3. Graphs of equation E11 for $\Delta V_0^{\neq}$ = –25 cm^3mol^{-1} and a_2 = -0.20, -0.10, -0.08, -0.04, and -0.06. The graph of equation E7 for $\Delta V_0^{\neq}$ = –25 cm^3mol^{-1}, $\Delta\beta_0^{\neq}$= 10. $cm^3mol^{-1}kbar^{-1}$, $\Delta\xi_0^{\neq}$ = –7.5 $cm^3mol^{-1}kbar^{-2}$ is included for comparison

5.2.2. Statistical Comparison

Since experimental errors are unavoidable in kinetic data, it is of interest to assess to what degree these errors can interfere with discrimination between equations E4-E11. To incorporate the effect of random errors, we started with "ideal" rate constants $\kappa(P)$ described by these equations and added relative random errors σz of a given level σ to simulate "experimental" rate constants $k(P)$:

$$k(P) = \kappa(P)(1 + \sigma z) \qquad (5.6)$$

The sets of 50 data points uniformly distributed over a given pressure range were generated for each equation with a random number z drawn from a standard normal distribution, $z \sim N(0, 1)$. The data sets were produced for three different pressure ranges (P = 0-1 kbar, 0-5 kbar, and 0-10 kbar) and three increasing levels of errors (σ = 1%, 5%,

and 10%) and compared using a paired t-test ($p < 0.05$). The t-statistic for comparison of a given pair of equations *a* and *b* (*a*,*b* = E4-E11) was calculated as

$$\tau = \frac{|\overline{d_{ab}}|}{S_d/\sqrt{n}} \tag{5.7}$$

where $\overline{d_{ab}}$ and s_d are, respectively, the mean and the standard deviation of the relative differences

$$d_{ab}(P) = \frac{k_a(P) - k_b(P)}{\frac{1}{2}\left(k_a(P) + k_b(P)\right)} \tag{5.8}$$

and $n = 50$ is the size of the compared data sets. The results are listed in Table 5.5 for various pressure ranges and levels of errors. It appears that, with few exceptions, the data sets for the lower pressure range of 0-1 kbar are not statistically different. On the contrary, for 0-10 kbar range the data sets are statistically different in most cases. The switch of behavior occurs at about 5 kbar, which is consistent with the general behavior of the functions shown in Fig. 5.1. It is worth noting that sometimes the functions of different types (*e.g.* hyperbolic function E4 and logarithmic function E6) appear to be closer to each other than to functions of their own type.

Table 5.5. Paired t-statistics calculated using eq. (5.7) for data sets generated by equations E4-E8 (50 data points evenly spread over the respective pressure range). The criterion identifying two data sets as statistically distinguishable at 95% confidence level is $\tau > 2.00$ (shaded cells).

		1% Error				5% Error				10% Error			
Pressure range	Equation	**E5**	**E6**	**E7**	**E8**	**E5**	**E6**	**E7**	**E8**	**E5**	**E6**	**E7**	**E8**
0-1 kbar	E4	1.87	0.23	1.20	1.57	2.77	1.07	1.99	0.26	2.88	1.18	2.09	0.51
	E5		1.40	0.50	3.06		1.19	0.57	1.92		1.11	0.56	1.76
	E6			0.80	1.94			0.54	0.91			0.48	0.79
	E7				2.69				1.41				1.24
0-5 kbar	E4	7.07	7.80	7.09	10.18	4.69	5.29	3.40	4.31	2.13	2.61	1.15	1.94
	E5		0.91	6.25	3.82		0.65	2.55	1.35		0.84	1.01	0.05
	E6			8.04	4.45			3.06	2.25			1.69	0.89
	E7				0.59				0.57				0.82
0-10 kbar	E4	8.24	9.02	8.97	0.66	7.68	8.61	7.21	0.17	6.77	7.31	5.10	0.19
	E5		5.53	7.21	6.40		3.57	6.93	6.00		1.97	5.76	5.34
	E6			8.74	6.53			7.87	6.45			5.03	6.05
	E7				5.56				4.76				3.72

5.3. Accuracy of Determination of Activation and Reaction Volumes

Notwithstanding their asymptotic behavior at extreme pressures, most of the functions listed in Table 5.1 remain suitable for calculation of activation volumes from experimental kinetic data not exceeding 10 kbar. However, in order to rely on these experimentally determined $\Delta V^{\neq}$ values as a quantitative tool for mechanistic analysis, one must have a better understanding of how the accuracy of their determination may be affected by the choice of a fitting function and by the level of experimental errors in the kinetic data. Different fitting equations may demonstrate different tolerance to the level of experimental errors and this tolerance could also vary depending on the pressure range. To assess the situation, a full control over the error level in the kinetic data is important, which is impossible in the real life experiment. Therefore, we resorted to a model approach similar to the one used in Section 5.2 and generated simulated "experimental" rate constants $k(P)$ using eq. (5.6) with functions E4-E8 for $\Delta V_0^{\neq}$=-25 cm^3/mol, $\Delta\beta_0^{\neq}$ = 10. $cm^3mol^{-1}kbar^{-1}$, and $\Delta\xi_0^{\neq}$ = −7.5 $cm^3mol^{-1}kbar^{-2}$ (Table 5.4). The simulated kinetic data were produced for three different pressure ranges (P = 0-1 kbar, 0-5 kbar, and 0-10 kbar) and three increasing levels of errors (σ = 1%, 5%, and 10%). In each specific case (*i.e.* for each combination of a specific *generating* equation E4-E8, a given pressure range, and a selected error level) the "experimental" data were produced in quintuplicate, thus emulating five repeated series of experimental measurements. These data were then approximated by each of the *fitting* equations E1-E11 using the least squares procedure. The values of activation volumes and their errors obtained by averaging the fitted parameters over the five repeated sets of "measurements" are summarized in Tables 5.6 (self-fitting) and 5.7-5.9 (cross-fitting). The extended versions of these tables including the results for individual data sets and the optimized values of fitting parameters a_i can be found in the Supplementary Information.

5.3.1. Self-fitting

Table 5.6 shows the values of activation volumes predicted when the fitting functions and the generating equations were identical. The results listed in the table indicate that at 1% error level equations E4-E8 accurately reproduce $\Delta V_0^{\neq}$ to within 0.6 cm^3/mol of the expected value of –25 cm^3/mol. The quality of the self-fit remained generally good when the level of experimental errors was increased to 5% with the data spread over a sufficiently wide pressure range (0-5 or 0-10 kbar). However, for a narrower range of 0-1 kbar, only equations E4 and E6 recovered the proper values of activation volumes, whereas equations E5, E7, and E8 demonstrated a significant instability, further increasing with the increasing level of errors. Widening of the pressure range helped in reducing this instability and for the 0-10 kbar range all equations produced reasonable values of $\Delta V_0^{\neq}$. When fitting 0-10 kbar data with higher error levels, regressions tended to underestimate activation volumes, whereas for 0-5 kbar range they showed an opposite trend toward overestimating $\Delta V_0^{\neq}$. Overall, equations E4 and E6 demonstrated a higher level of stability, probably due to the fact that these equations use fewer fitting parameters – two for E4 and E6, compared to three for E5, E7, and E8.

Table 5.6. Activation volumes (cm^3/mol) obtained by fitting equations E4-E8 to kinetic data generated using these equations with $\Delta V_0^{\neq} = -25$ cm^3mol^{-1}, $\Delta\beta_0^{\neq} = 10.$ $cm^3mol^{-1}kbar^{-1}$, $\Delta\xi_0^{\neq} = -7.5$ $cm^3mol^{-1}kbar^{-2}$ over various pressure ranges and various levels of random relative errors (see text for details).

Pressure range	Equation	Error level		
		1%	5%	10%
0-1 kbar	E4	-25.0 ± 0.3	-24 ± 1	-24 ± 2
	E5	-24.7 ± 0.6	-36 ± 18	-54 ± 43
	E6	-24.8 ± 0.3	-24 ± 1	-24 ± 2
	E7	-24.7 ± 0.6	-39 ± 22	-80 ± 90
	E8	-24.7± 0.6	-44 ± 31	-45 ± 38
0-5 kbar	E4	-25.6 ± 0.9	-26 ± 1	-27 ± 3
	E5	-24.9 ± 0.4	-25 ± 1	-25 ± 3
	E6	-25.2 ± 0.3	-26 ± 1	-27 ± 3
	E7	-24.9 ± 0.4	-25 ± 1	-25 ± 3
	E8	-24.9 ± 0.4	-25 ± 1	-25 ± 3
0-10 kbar	E4	-25.0 ± 0.2	-24.9 ± 0.9	-24.7 ± 2
	E5	-24.8 ± 0.3	-24 ± 1	-23 ± 2
	E6	-25.0 ± 0.2	-24.9 ± 0.9	-25 ± 2
	E7	-24.8 ± 0.3	-24 ± 1	-23 ± 2
	E8	-24.8 ± 0.3	-24 ± 1	-23 ± 3

The high quality of fit for a given pressure range did not guarantee the proper behavior of the fitted function outside of the range of fitting. For example, although equation E5 fitted well the 1%-error data set on the 0-1 kbar range and predicted an accurate activation volume of -24.7 cm^3/mol, it demonstrates unphysical behavior outside of the fitting range of pressures (Fig. 5.4), reaching a maximum at 3.5 kbar.

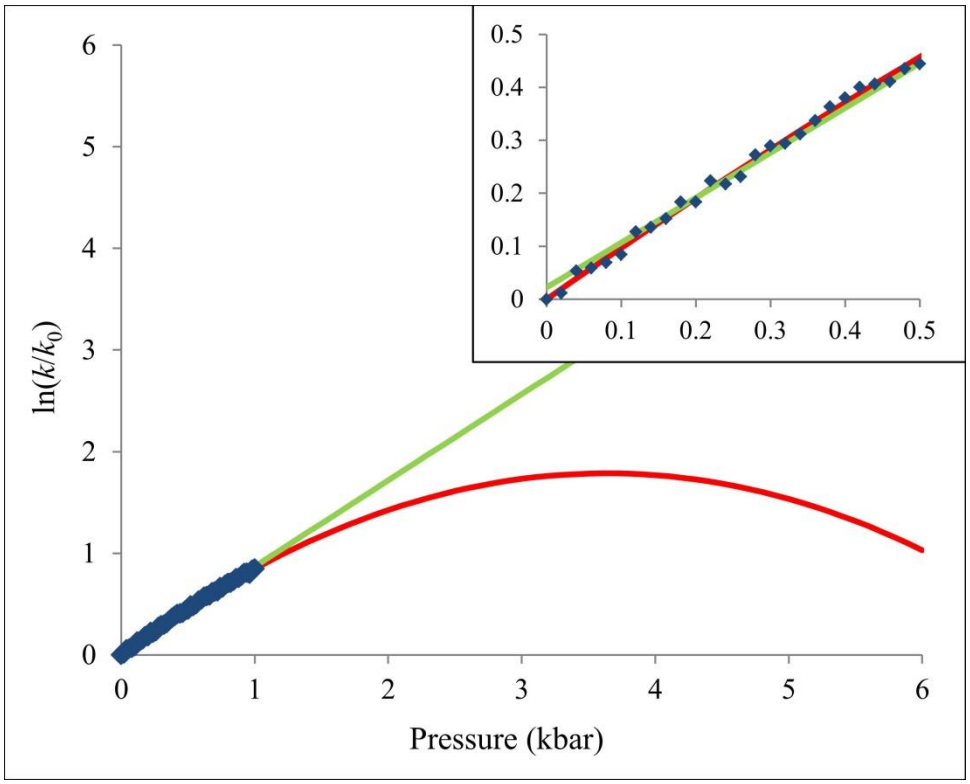

Figure 5.4. Fit of E5 (red line) to the data generated using E5 for the pressure range 0-1kbar with relative error of 1% (blue diamonds). The best linear fit (green line) is shown for comparison. Although the E5 curve fits the data well over the range of 0-1 kbar, it shows unphysical behavior as its starts descending at pressures exceeding 4 kbar.

Poor performance of equations E4-E8 in self-fitting to the 0-1 kbar range data with high error level can be traced to the fact that, as it can be seen in Fig. 5.1, their graphs are quasi-linear for the set of physical parameters for $\Delta V_0^{\neq}$=-25 cm^3/mol, $\Delta\beta_0^{\neq}$ = 10. cm^{3}mol^{-1}kbar^{-1}, and $\Delta\xi_0^{\neq}$ = −7.5 cm^{3}mol^{-1}kbar^{-2} used to generate simulated kinetic data. As a result, to recover the proper value of the activation volume, these data need to be approximated by a quasi-linear fitting function. When the level of errors is low, the curving of the data set is sufficiently distinct to support determination of the nonlinear regression parameter a_4. However, as the error level increases, the accuracy of such determination decreases. In the case of equations E4 and E6, the a_4 parameter becomes small, turning them into linear functions a_3P and $a_2\ln(1+a_4P) \approx a_2a_4P$, respectively. Three-parametric equations E5, E7, and E8 are more flexible and thus more prone to

bend in response to errors in the data, which results in large variations in the predicted activation volumes. Fig. 5.5 shows an example of how E5 is able to contort in the low pressure region, which in this particular case produces an error of over 85 cm^3/mol in the estimated activation volume. In comparison, linear regression gives a much better estimate with an error of only 5.4 cm^3/mol.

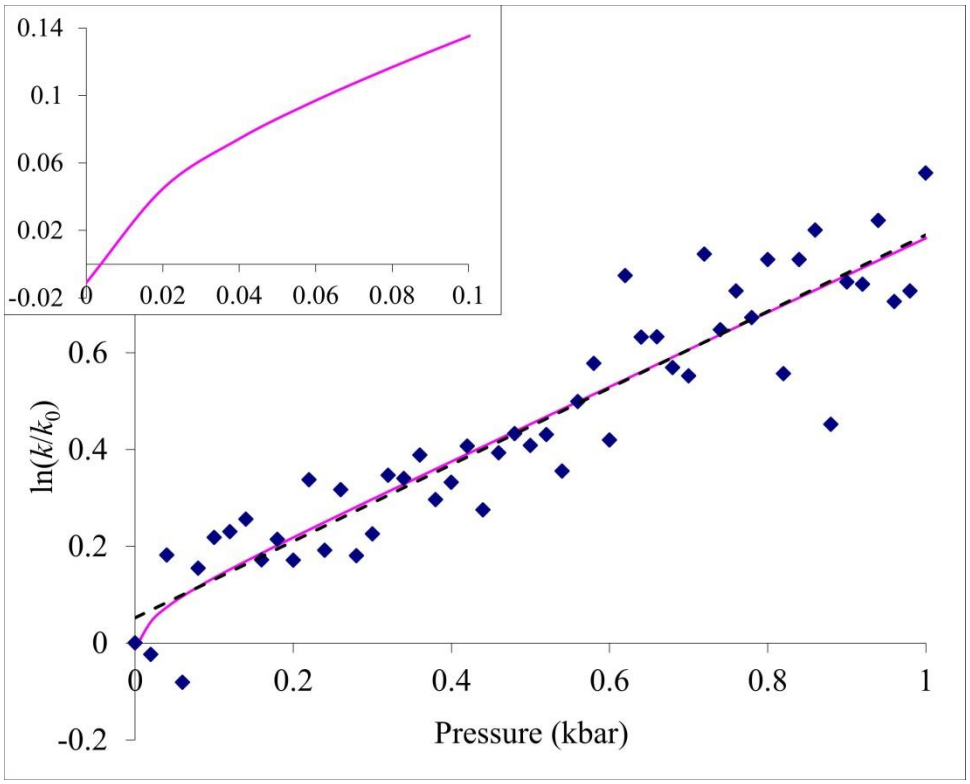

Figure 5.5. Fit of E5 (magenta line) to the data generated using E5 for the 0-1kbar pressure range with a relative error of 10% (blue diamonds). Sudden curving of an almost linear E5 graph in the lower pressure region results in a significant overestimation of the activation volume determined by the slope of the graph. Linear regression (dashed line), included for comparison, gives a better estimate for the activation volume.

5.3.2. Cross-fitting

Functions, other than E4-E8, are frequently used to approximate equilibrium and rate constants[9]. We therefore expand the scope of discussion to include an analysis of the performance of all functions E1-E11. Tables 5.7-5.9 show the values of activation volumes obtained by fitting functions E1-E11 to the data sets generated using equations

E4-E8. In general, the results and trends observed are qualitatively similar to those seen for the self-fitting data listed in Table 5.6.

As a rule, the choice of generator equation did not have much effect on the results, which is consistent with the statistical similarity of the simulated kinetic data sets (see Table 5.5). Equations E1-E2 and E11, graphs of which visibly deviate from those of equations E4-E8 (see Fig. 5.1), typically performed poorer. With the exception of E1-E2, all equations performed better on 1%-error data sets. Less flexible two-parametric equations E4 and E6 were better in the 0-1 kbar range at higher error levels, whereas more flexible functions E5 and E7-E10 demonstrated very low levels of accuracy in their prediction of activation volumes for this pressure range. As the pressure range widened to 0-5 or 0-10 kbar, performance of the latter significantly improved, whereas that of the former somewhat deteriorated. The most general logarithmic equation E10 showed rather poor performance, giving unacceptably large errors in the estimated activation volumes. Simple quadratic equation E1 worked remarkably well on the 0-1 kbar range, however it did not perform as well outside that range, as it has been noted on multiple occasions in the past[5e,10].

Table 5.7. Activation volumes (cm^3/mol) obtained by fitting equations E1-E11 to the data generated using equations E4-E8 with parameters $\Delta V_0^{\neq} = -25\ cm^3mol^{-1}$, $\Delta\beta_0^{\neq} = 10.\ cm^3mol^{-1}kbar^{-1}$, $\Delta\xi_0^{\neq} = -7.5\ cm^3mol^{-1}kbar^{-2}$ for different levels of errors and the pressure range of 0-1kbar**.** The cells containing the results of self-fitting are shown in bold. In the cases of inconsistency of self-fitting, the equations showing such instability were not included as a generating equations and the respective rows were omitted from the table.

		Fitting Equation										
Error level	Generating Equation	**E1**	**E2**	**E3**	**E4**	**E5**	**E6**	**E7**	**E8**	**E9**	**E10**	**E11**
1%	**E4**	-24.4 ± 0.2	-22.9 ± 0.2	-24.6 ± 0.7	**-24.9 ± 0.3**	-24.7 ± 0.6	-25 ± 0.3	-24.7 ± 0.6	-24.8 ± 0.6	-24.8 ± 0.6	-24.6 ± 0.8	-27 ± 0.3
	E5	-24.4 ± 0.2	-22.9 ± 0.2	-24.5 ± 0.7	-24.7 ± 0.2	**-24.7 ± 0.6**	-24.9 ± 0.3	-24.7 ± 0.6	-24.7 ± 0.7	-24.8 ± 0.7	-24.7 ± 0.9	-26.8 ± 0.3
	E6	-24.4 ± 0.2	-23.1 ± 0.2	-24.5 ± 0.7	-24.7 ± 0.2	-24.7 ± 0.6	**-24.8 ± 0.3**	-24.7 ± 0.6	-24.7 ± 0.6	-24.8 ± 0.7	-24.6 ± 0.9	-26.7 ± 0.3
	E7	-24.4 ± 0.2	-22.9 ± 0.2	-24.5 ± 0.7	-24.7 ± 0.2	-24.7 ± 0.6	-24.9 ± 0.3	**-24.7 ± 0.6**	-24.7 ± 0.6	-24.8 ± 0.7	-24.6 ± 0.9	-26.8 ± 0.3
	E8	-24.5 ± 0.2	-23.1 ± 0.2	-24.5 ± 0.7	-24.8 ± 0.2	-24.7 ± 0.6	-24.9 ± 0.3	-24.7 ± 0.6	**-24.7 ± 0.6**	-24.8 ± 0.6	-24.6 ± 0.8	-26.8 ± 0.3
5%	**E4**	-24 ± 1	-22.7 ± 0.7	-23 ± 4	**-24 ± 1**	-36 ± 16	-24 ± 1	-38 ± 20	-46 ± 33	-44 ± 31	-28 ± 16	-26 ± 2
	E6	-24 ± 1	-22.9 ± 0.7	-23 ± 4	-24 ± 1	-37 ± 18	**-24 ± 1**	-39 ± 24	-43 ± 30	-42 ± 28	-28 ± 17	-26 ± 2
10%	**E4**	-23 ± 2	-23 ± 1	-21 ± 7	**-23 ± 2**	-54 ± 42	-24 ± 2	-74 ± 83	-47 ± 40	-45 ± 38	-34 ± 33	-25 ± 3
	E6	-23 ± 2	-23 ± 1	-21 ± 7	-24 ± 2	-54 ± 44	**-24 ± 2**	-86 ± 108	-44 ± 40	-43 ± 35	-34 ± 33	-25 ± 3

Table 5.8. Activation volumes (cm^3/mol) obtained by fitting equations E1-E11 to the data generated using equations E4-E8 with parameters $\Delta V_0^{\neq} = -25$ cm^3mol^{-1}, $\Delta\beta_0^{\neq} = 10.$ $cm^3mol^{-1}kbar^{-1}$, $\Delta\xi_0^{\neq} = -7.5$ $cm^3mol^{-1}kbar^{-2}$ for different levels of errors and the pressure range of 0-5kbar. The cells containing the results of self-fitting are shown in bold. In the cases of inconsistency of self-fitting, the equations showing such instability were not included as a generating equations and the respective rows were omitted from the table.

		Fitting Equation										
Error	Generating Eq.	**E1**	**E2**	**E3**	**E4**	**E5**	**E6**	**E7**	**E8**	**E9**	**E10**	**E11**
1%	**E4**	-20.4 ± 0.3	-16.7 ± 0.1	-23.9 ± 0.9	**-25.6 ± 0.9**	-25.3 ± 1	-28.4 ± 1	-25.6 ± 1	-26.2 ± 1	-26.5 ± 1	-24.8 ± 0.6	-26.6 ± 0.6
	E5	-20.2 ± 0.1	-17.2 ± 0.1	-23.3 ± 0.2	-23.1 ± 0.2	**-24.9 ± 0.4**	-24.5 ± 0.3	-25.2 ± 0.4	-26.1 ± 0.5	-26.5 ± 0.6	-24.6 ± 0.4	-25.2 ± 0.2
	E6	-20.7 ± 0.1	-17.6 ± 0.1	-23.5 ± 0.2	-23.7 ± 0.2	-24.7 ± 0.3	**-25.2 ± 0.3**	-24.9 ± 0.4	-25.5 ± 0.4	-25.8 ± 0.5	-24.6 ± 0.4	-25.9 ± 0.2
	E7	-20.4 ± 0.1	-17.1 ± 0.1	-23.4 ± 0.2	-24.1 ± 0.2	-24.7 ± 0.3	-26 ± 0.3	**-24.9 ± 0.4**	-25.5 ± 0.4	-25.8 ± 0.5	-24.6 ± 0.4	-25.9 ± 0.2
	E8	-21.1 ± 0.1	-17.4 ± 0.1	-23.7 ± 0.2	-25.9 ± 0.2	-24.5 ± 0.3	-28.5 ± 0.3	-24.6 ± 0.3	**-24.9 ± 0.4**	-25.1 ± 0.4	-24.5 ± 0.4	-27.4 ± 0.2
5%	**E4**	-20.6 ± 0.6	-16.9 ± 0.4	-24 ± 1	**-26 ± 1**	-25 ± 2	-29 ± 2	-25 ± 2	-25 ± 2	-26 ± 2	-24.1 ± 1	-27 ± 0.9
	E5	-20.5 ± 0.6	-17.4 ± 0.4	-24 ± 1	-24 ± 1	**-25 ± 2**	-25 ± 1	-25 ± 2	-25 ± 2	-26 ± 2	-24 ± 1	-26 ± 0.9
	E6	-21.1 ± 0.6	-17.8 ± 0.4	-24 ± 1	-24 ± 1	-25 ± 2	**-26 ± 1**	-25 ± 2	-25 ± 2	-25 ± 2	-24 ± 2	-27 ± 0.9
	E7	-20.8 ± 0.6	-17.3 ± 0.4	-24 ± 1	-25 ± 1	-25 ± 2	-27 ± 1	**-25 ± 2**	-25 ± 2	-25 ± 2	-23 ± 2	-27 ± 0.9
	E8	-21.5 ± 0.6	-17.6 ± 0.4	-24 ± 1	-27 ± 1	-25 ± 1	-30 ± 2	-25 ± 2	**-25 ± 2**	-25 ± 2	-22 ± 4	-28 ± 0.9
10%	**E4**	-21 ± 1	-17.1 ± 0.7	-24 ± 2	**-27 ± 3**	-25 ± 3	-30 ± 3	-25 ± 3	-25 ± 3	-25 ± 3	-22 ± 5	-28 ± 2
	E5	-21 ± 1	-17.6 ± 0.7	-24 ± 2	-25 ± 2	**-25 ± 3**	-27 ± 3	-25 ± 3	-25 ± 3	-26 ± 3	-22 ± 5	-27 ± 2
	E6	-22 ± 1	-18.1 ± 0.7	-24 ± 2	-25 ± 2	-25 ± 3	**-27 ± 3**	-25 ± 3	-25 ± 3	-25 ± 3	-19 ± 8	-27 ± 1
	E7	-21 ± 1	-17.6 ± 0.7	-24 ± 2	-26 ± 2	-25 ± 3	-28 ± 3	**-25 ± 3**	-25 ± 3	-25 ± 3	-19 ± 8	-27 ± 2
	E8	-22 ± 1	-17.8 ± 0.7	-24 ± 2	-28 ± 2	-25 ± 3	-31 ± 3	-25 ± 3	**-25 ± 3**	-25 ± 3	-19 ± 7	-29 ± 2

Table 5.9. Activation volumes (cm^3/mol) obtained by fitting equations E1-E11 to the data generated using equations E4-E8 with parameters $\Delta V_0^{\neq} = -25$ cm^3mol^{-1}, $\Delta\beta_0^{\neq} = 10.$ $cm^3mol^{-1}kbar^{-1}$, $\Delta\xi_0^{\neq} = -7.5$ $cm^3mol^{-1}kbar^{-2}$ for different levels of errors and the pressure range of 0-10kbar**.** The cells containing the results of self-fitting are shown in bold. In the cases of inconsistency of self-fitting, the equations showing such instability were not included as a generating equations and the respective rows were omitted from the table.

		Fitting Equation										
Error	Generating Eq.	**E1**	**E2**	**E3**	**E4**	**E5**	**E6**	**E7**	**E8**	**E9**	**E10**	**E11**
1%	**E4**	-15.5 ± 0.1	-12 ± 0.1	-20.5 ± 0.1	**-25.0 ± 0.2**	-24.7 ± 0.4	-32.3 ± 0.3	-25.6 ± 0.5	-30.2 ± 0.8	-32 ± 1	-25 ± 0.4	-15.0 ± 0.2
	E5	-16.00 ± 0.04	-13.31 ± 0.02	-20.3 ± 0.1	-19.7 ± 0.1	**-24.8 ± 0.3**	-21.8 ± 0.2	-25.9 ± 0.3	-33.7 ± 0.3	-40.0 ± 0.7	-25.1 ± 0.4	-20.6 ± 0.1
	E6	-16.80 ± 0.04	-13.68 ± 0.02	-20.9 ± 0.1	-21.9 ± 0.1	-24.1 ± 0.2	**-25 ± 0.2**	-24.8 ± 0.3	-28.1 ± 0.4	-29.4 ± 0.4	-24.9 ± 0.4	-22.1 ± 0.1
	E7	-16.24 ± 0.04	-12.91 ± 0.02	-20.6 ± 0.1	-23 ± 0.1	-24 ± 0.2	-27.5 ± 0.2	**-24.8 ± 0.3**	-28.3 ± 0.4	-29.8 ± 0.4	-24.9 ± 0.4	-21.9 ± 0.1
	E8	-17.31 ± 0.04	-12.82 ± 0.02	-21.4 ± 0.1	-32.4 ± 0.2	-23.3 ± 0.2	-45.4 ± 0.4	-23.7 ± 0.2	**-24.8 ± 0.3**	-25.3 ± 0.3	-24.8 ± 0.4	-24.9 ± 0.1
5%	**E4**	-15.5 ± 0.2	-12 ± 0.1	-20.4 ± 0.6	**-24.9 ± 0.9**	-24 ± 1	-32 ± 2	-25 ± 1	-29 ± 2	-31 ± 2	-26 ± 3	-15.0 ± 0.6
	E5	-16 ± 0.2	-13.4 ± 0.1	-20.1 ± 0.6	-19.7 ± 0.5	**-24 ± 1**	-21.8 ± 0.7	-25 ± 2	-48 ± 34	-50 ± 31	$>1{\cdot}10^5$	-20.6 ± 0.3
	E6	-16.9 ± 0.2	-13.7 ± 0.1	-20.7 ± 0.6	-21.9 ± 0.6	-23 ± 1	**-24.0 ± 0.9**	-24 ± 1	-27 ± 2	-28 ± 2	-25 ± 2	-22.2 ± 0.3
	E7	-16.3 ± 0.2	-13 ± 0.1	-20.4 ± 0.6	-22.9 ± 0.7	-23 ± 1	-27 ± 1	**-24 ± 1**	-27.1 ± 2	-28 ± 2	-25 ± 2	-22.0 ± 0.3
	E8	-17.4 ± 0.2	-12.9 ± 0.1	-21.2 ± 0.6	-32 ± 1	-22.9 ± 0.9	-45 ± 2	-23 ± 1	**-24.1 ± 1**	-25 ± 1	-22 ± 4	-25.0 ± 0.3
10%	**E4**	-15.6 ± 0.4	-12.1 ± 0.2	-20 ± 1	**-25 ± 2**	-23 ± 2	-32 ± 3	-24 ± 3	-27.3 ± 4	-29 ± 4	-25 ± 3	-15 ± 1
	E5	-16.1 ± 0.4	-13.4 ± 0.2	-20 ± 1	-20 ± 1	**-23 ± 2**	-22 ± 2	-24 ± 3	-44.8 ± 33	-31 ± 5	-26 ± 3	-21 ± 0.7
	E6	-16.9 ± 0.4	-13.8 ± 0.2	-20 ± 1	-22 ± 1	-23 ± 2	**-25 ± 2**	-23 ± 3	-25.3 ± 4	-26 ± 4	-24 ± 3	-22.2 ± 0.7
	E7	-16.4 ± 0.4	-13 ± 0.2	-20 ± 1	-23 ± 1	-23 ± 2	-27 ± 2	**-23 ± 3**	-25.5 ± 4	-26 ± 4	-24 ± 3	-22.2 ± 0.7
	E8	-17.4 ± 0.4	-12.9 ± 0.2	-21 ± 1	-32 ± 2	-22 ± 1	-44 ± 4	-23 ± 2	**-23 ± 3**	-23 ± 3	2 ± 55	-25.0 ± 0.7

5.3.3. Data Pooling: El'yanov-Gonikberg Approach

An interesting approach toward reducing the errors of determination of activation volumes was proposed by El'yanov and Gonikberg[1cd]. It is based on an earlier observation[11] that the pressure dependence of rate and equilibrium constants for a series of similar processes can be described by the equation

$$ln\frac{k}{k_0} = \left(-\frac{\Delta V_0^{\neq}}{RT}\right)\Phi(P) \qquad (5.9)$$

where $\Phi(P)$ is a universal function, common for all processes of a given type, and values of $\Delta V_0^{\neq}$ vary for specific processes of a series. In accordance with (5.1) and (5.3), the universality of function $\Phi(P)$ implies that compressibility, $\Delta\beta_0^{\neq}/\Delta V_0^{\neq}$, and hypercompressibility, $\Delta\xi_0^{\neq}/\Delta V_0^{\neq}$, are the same for all reactions of a given sufficiently narrowly defined class. Consistency of eqs. (1.3) and (5.9) also requires that $d\Phi/dP = 1$ at P = 0. Specific expressions for E4-E8 in El'yanov-Gonikberg format are listed in the Appendix G.

Since only $\Delta V_0^{\neq}$ is a reaction-specific parameter and function $\Phi(P)$ is common for the entire series, the El'yanov-Gonikberg approach opens a possibility of pooling data obtained for different reactions and different pressure ranges. It has been argued[1cd] that such data pooling increased stability of $\Delta V_0^{\neq}$ predictions for Diels-Alder reactions[12]. One might hope, therefore, that this approach could remediate the instability noted for self-fitting of E4-E8 in the case of high level of errors in the simulated data. To test this, we applied this approach to our simulated data generated for the 0-1 kbar and 0-5 ranges with 10% error level. The results are listed in Tables 5.10 and 5.11. As in Tables 5.6-5.9, the values reported are mean $\Delta V_0^{\neq}$ and their standard deviations were obtained over five replicated sets of simulated data.

Table 5.10. Activation volumes (cm^3/mol) obtained by fitting equations E4-E8 to kinetic data generated using these equations with $\Delta V_0^{\neq} = -25$ cm^3mol^{-1}, $\Delta\beta_0^{\neq} = 10.$ $cm^3mol^{-1}kbar^{-1}$, $\Delta\xi_0^{\neq} = -7.5$ $cm^3mol^{-1}kbar^{-2}$ over pressure range of 0-5 kbar with 10% error. The El'yanov-Gonikberg function $\Phi(P)$ was parameterized by fitting more accurate 0-5 kbar data with 1% error.

Equation	Fitting Procedure	
	Self-fitting (Table 5.6)	El'yanov-Gonikberg data pooling
E4	-27 ± 3	-25±0.4
E5	-25 ± 3	-24.68±0.04
E6	-27 ± 3	-25.0±0.4
E7	-25 ± 3	-24.7±0.4
E8	-25 ± 3	-24.7±0.4

Table 5.11. Activation volumes (cm^3/mol) obtained by fitting equations E4-E8 to kinetic data generated using these equations $\Delta V_0^{\neq} = -25$ cm^3mol^{-1}, $\Delta\beta_0^{\neq} = 10.$ $cm^3mol^{-1}kbar^{-1}$, $\Delta\xi_0^{\neq} = -7.5$ $cm^3mol^{-1}kbar^{-2}$ over pressure range of 0-1 kbar with 10% error. The El'yanov-Gonikberg function $\Phi(P)$ was parameterized by fitting data of the same accuracy (10% error) but for a wider pressure range of 0-5 kbar.

Equation	Fitting Procedure	
	Self-fitting (Table 5.6)	El'yanov-Gonikberg data pooling
E4	-24 ± 2	-26±2
E5	-54 ± 43	-24±2
E6	-24 ± 2	-26±2
E7	-80 ± 90	-24±2
E8	-45 ± 38	-24±2

Table 5.10 refers to a case, where function $\Phi(P)$ is parameterized using accurate data "collected" over a 0-5 kbar range with an error of 1% and then used to obtain $\Delta V_0^{\neq}$ for the data set spread over the same pressure range but with an error of 10%. This mimics a situation where kinetic data for various reactions of a series are characterized by substantially different error levels. As can be seen from the table, such an approach allows one to increase the accuracy of $\Delta V_0^{\neq}$ for a less accurate set by pooling it with a more accurate set. Similarly, Table 5.11 demonstrates that pooling data sets with different pressure ranges, allows one to "transfer" higher stability of the solution of a wider (0-5

kbar) pressure range onto a narrower (0-1 kbar) pressure range and thus significantly increase the accuracy of the predicted $\Delta V_0^{\neq}$ for the latter.

5.4. Analysis of Experimental Data

Although the use of simulated data offers a unique degree of control over their physical parameters and error levels, it is significantly more interesting and important to see how equations E1-E11 perform as regression functions in fitting real experimental data. In this section, we discuss their performance in application to some Diels-Alder[12a,13], Menshutkin[10], and solvolysis[14] reactions, kinetic data for which are available in the literature for a wide range of pressures.

5.4.1. Diels-Alder Reactions.

The results for three Diels-Alder reactions in various solvents are listed in Table 5.12. The error level estimated by the standard deviations of fit ranged between 1% and 15%.

Table 5.12. Activation volumes (cm^3/mol) obtained from fitting equations E1-E11 to data for Diels-Alder reactions

Reaction	Isoprene-Maleic Anhydride Addition	Dimerization of Isoprene		Dimerization of Cyclopentadiene	
Solvent (T, °C)	Ethyl acetate (35°C)[a]	Isoprene (60°C)[b]	Bromobutane (40°C)[c]	Cyclopentadiene (20°C)[d]	Chlorobutane (20°C)[e]
Pressure Range	0-6 kbar	0-8 kbar	0-8 kbar	0-4 kbar	0-3 kbar
Error Level	2 %	15 %	5 %	4 %	1 %
E1	-30.2	-30.4	-26.7	-27.1	-21.9
E2	-26.9	-26.3	-22.3	-24.4	-21.0
E3	-34.6	-25.1	-33.1	-32.4	-21.4
E4	-32.4	-32.8	-32.3	-28.8	-22.1
E5	-37.2	-30.4	-35.9	-36.1	-21.9
E6	-33.4	-33.8	-34.8	-29.4	-22.1
E7	-37.8	-30.4	-36.2	-37.8	-21.9
E8	-40.2	-30.4	-36.7	-115.0	-19.4
E9	-41.0	-30.4	-37.4	-135.9	-21.9
E10	$>1\cdot10^5$	-20.8	-33.1	-37.9	-21.9
E11	-35.8	-36.9	-33.9	-31.5	-23.5

[a] Kinetic data from ref. 12a
[b] Kinetic data from ref. 13a
[c] Kinetic data from ref. 13b
[d] Kinetic data from ref. 13c
[e] Kinetic data from ref. 13d

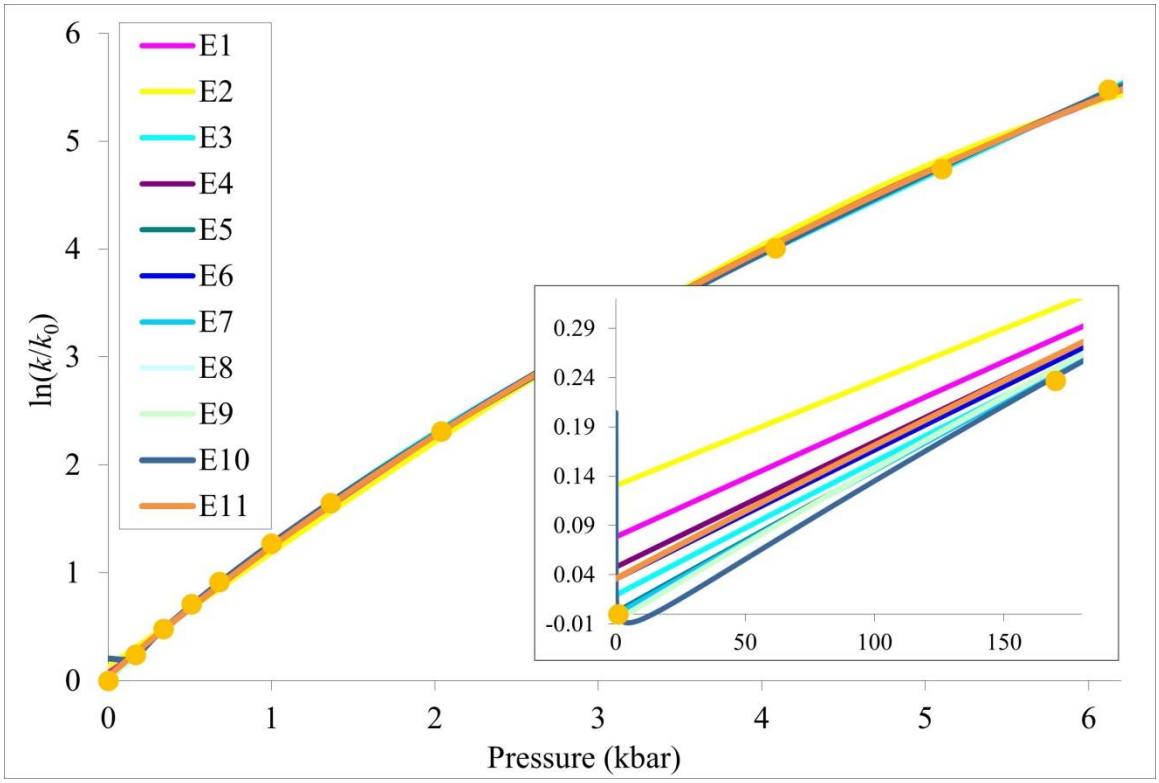

Figure 5.6. Fit of E1-E11 to the kinetic data for the Diels-Alder addition of maleic anhydride to isoprene in ethyl acetate[12a].

Although all functions perform comparably well over the full range of pressures, the values of the obtained activation volumes vary in some cases quite dramatically. As with the simulated data discussed in the previous section, this can be attributed to the difference in behavior of functions E1-E11 in the low pressure region. As shown in Fig. 5.6, only equations E5, E7, and E8 demonstrated proper behaviour at low pressures, producing consistent values of activation volumes of -37 to -40 cm^3/mol for addition of maleic anhydride to isoprene. Function E10, although showing an equally good fit on the low pressure range, bent at 0 and predicted an absurd $\Delta V_0^{\neq}$ value of $1x10^5$ cm^3/mol. Like in the similar cases previously observed in the self-fitting of E5 and E7 to the simulated data (Table 5.6), this happened due to a collapse of the optimization process resulting in an excessively large value of parameter a_4, precipitating catastrophic behavior of the fitting function near zero. Other obviously wrong values of activation volumes, generated

by E8-E9 for cyclopentadiene dimerization, could be traced to the same origin. The remaining $\Delta V_0^{\neq}$ values were not unreasonable, however their relatively large variance necessitated further steps in selecting the most reasonable figures. Visual inspection of the behavior of the fitting functions identified equation E5 and E7 as the most promising candidates. These equations produced consistently close values of activation volumes for all Diels-Alder reactions included in Table 5.12.

As described in the previous section, the use of El'yanov-Gonikberg eq. (5.11) allowed us to increase the accuracy of $\Delta V_0^{\neq}$ for a less accurate set of simulated data by pooling it with a more accurate data set. We therefore applied this approach here to the experimental kinetic data on Diels-Alder reactions in an attempt to improve the performance of equations E4-E9. Function $\Phi(P)$ was parameterized in two different ways – by simultaneous fitting to all reactions included in Table 5.12 and by fitting to the more accurate maleic anhydride plus isoprene data. The results are listed in Table 5.13.

Table 5.13. Activation volumes (cm^3/mol) obtained from fitting equations E4-E9 to data for five Diels-Alder reactions using El'yanov-Gonikberg data pooling. Function $\Phi(P)$ was parametrized by simultaneous fitting to all reactions included in Table 12 and by fitting to the more accurate maleic anhydride plus isoprene data. Also included are the theoretical values of activation volumes previously obtained using molecular dynamics simulations.

Reaction	Dimerization of Isoprene				Dimerization of Cyclopentadiene			
Solvent (T, °C)	Isoprene (60°C)[b]		Bromobutane (40°C)[c]		Cyclopentadiene (20°C)[d]		Chlorobutane (20°C)[e]	
Source of $\Phi(P)$	All reactions	Isoprene + Maleic Anhydride	All reactions	Isoprene + Maleic Anhydride	All reactions	Isoprene + Maleic Anhydride	All reactions	Isoprene + Maleic Anhydride
E4	-34.4	-32.0	-29.3	-27.2	-28.4	-27.2	-24.5	-23.6
E5	-32.5	-35.8	-27.8	-30.6	-26.7	-31.3	-23.3	-26.9
E6	-35.8	-32.8	-30.6	-28.0	-29.6	-27.9	-25.5	-24.3
E7	-32.5	-36.4	-27.8	-31.1	-26.7	-31.8	-23.3	-27.4
E8	-32.8	-30.3	-28.0	-26.0	-26.7	-25.3	-23.3	-22.2
E9	-32.8	-39.6	-28.0	-33.9	-26.9	-34.2	-23.4	-29.6
MD[e]			-29.0		-35.8		-30.1	

[a] Kinetic data from ref. 12a

[b] Kinetic data from ref. 13a

[c] Kinetic data from ref. 13b

[d] Kinetic data from ref. 13c

[e] Kinetic data from ref. 13d

[e] Data from ref.15

For comparison, the theoretical values of activation volumes obtained using molecular dynamics simulations[15] were also included in the table. As expected, the El'yanov-Gonikberg data pooling eliminated unreasonable $\Delta V_0^{\neq}$ values generated by equations E8-E9 for cyclopentadiene dimerization. It also considerably increased the absolute values of the predicted activation volumes for this reaction in chlorobutane. The consistency of the $\Delta V_0^{\neq}$ values produced by different fitting functions increased due to data pooling for all reactions. However, the results of molecular dynamics simulations better matched the data obtained using $\Phi(P)$ parameterized by fitting to the more accurate maleic anhydride plus isoprene data. Equation E9 in El'yanov-Gonikberg format worked surprisingly well, particularly with maleic anhydride - isoprene parameterization of $\Phi(P)$.

5.4.2. Menshutkin Reaction.

Experimental data[10] for the Menshutkin reaction of tri-n-propyl amine with methyl iodide in various solvents were fitted with functions E1-E11. The results are shown in Table 5.14.

Table 5.14. Activation volumes (cm^3/mol) obtained by fitting equations E1-E11 to data for the Menshutkin reaction of tri-n-propyl amine with methyl iodide in various solvents at 30°C[10].

Solvent	Propionitrile	Cyclohexanone	Dichloromethane	Nitrobenzene	Nitromethane	Acetone	
Error Level	4 %	2 %	5 %	2 %	3 %	4 %	
Pressure Range	0-2 kbar	0-2 kbar	0-2kbar	0-1 kbar	0-2 kbar	0-1.5 kbar	0-7 kbar
E1	-29.5	-30.4	-31.3	-27.0	-31.9	-28.4	-18.5
E2	-26.1	-26.4	-28.0	-26.3	-26.4	-25.7	-15.0
E3	-23.9	-27.9	-28.9	-22.6	-27.4	-29.2	-25.6
E4	-31.4	-33.4	-33.2	-27.0	-38.5	-29.9	-25.0
E5	-29.5	-30.4	-31.3	-27.0	-31.9	-29.4	-32.9
E6	-32.2	-34.8	-34.0	-27.1	-41.4	-30.5	-28.8
E7	-29.5	-30.4	-31.3	-27.0	-31.9	-29.4	-33.5
E8	-19.9	-30.4	-170.0	-27.0	-30.7	-29.5	-126.1
E9	-19.9	-30.4	-31.3	-27.0	-30.7	-29.5	-168.5
E10	-23.9	-27.9	-28.9	-22.6	-27.4	-29.5	-29.5
E11	-35.4	-37.2	-37.1	-28.2	-41.4	-33.0	-24.3

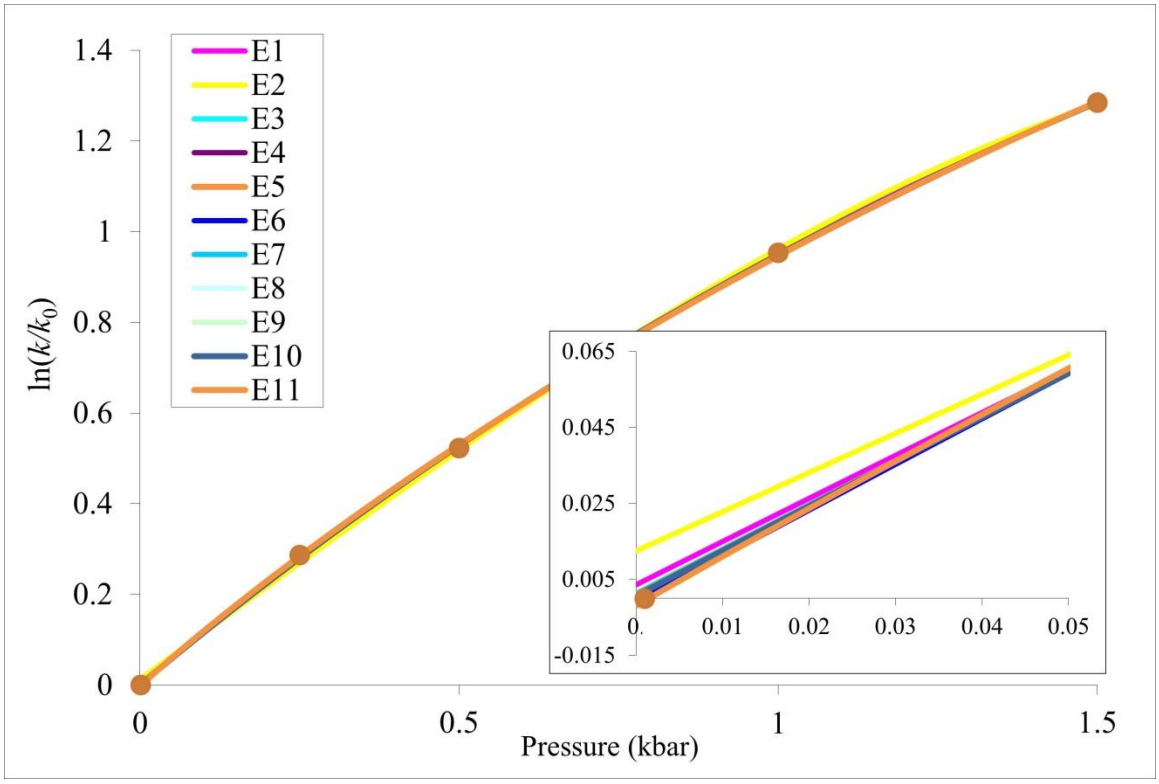

Figure 5.7. Fit of E1-E11 to kinetic data for the Menshutkin reaction between tri-n-propyl amine with methyl iodide in acetone[10] over the pressure ranges of 0-1500 kbar.

A value of -28.6 cm^3/mol was reported[10] for the activation volume of the reaction in acetone by fitting E1 to the data limited to a maximum pressure of 1.5 kbar (Fig. 5.7). It was noted, however, that this fitting function no longer worked at higher pressures, when compression of the solvent exceeded 10%. Fitting data for different solvents with E1-E11 over a pressure range of up to 2 kbar (see Table 5.14) reveals that E1 produces a similar quality of fit and comparable activation volumes when compared to the other well behaved equations, such as E4-E8 with E5. As in previous cases, equations E2-E3 and E10-E11 produced substantially more inferior results.

On a wider pressure range of 0-7 kbar, the failings of the polynomial equations, predicting activation volumes of significantly smaller absolute values, became clear (Fig. 5.8); the complete cubic function E3 , despite showing a much smaller change in $\Delta V_0^{\neq}$,

adopted an unphysical curvature. Equations E8-E9 predicted substantially different and obviously wrong values of $\Delta V_0^{\neq}$; and only equations E5-E7 retained a reasonable stability of the results. Although El'yanov-Gonikberg data pooling with $\Phi(P)$ parameterized by fitting to all reactions (see Table 5.15) partially resolved the problem of obviously unacceptable values for E8-E9 it did not fully eliminate the disparity of values for E4-E9. As in the case of Diels-Alder reactions, equations E5 and E7 produced consistently close values of activation volume for all solvents when data pooling was applied.

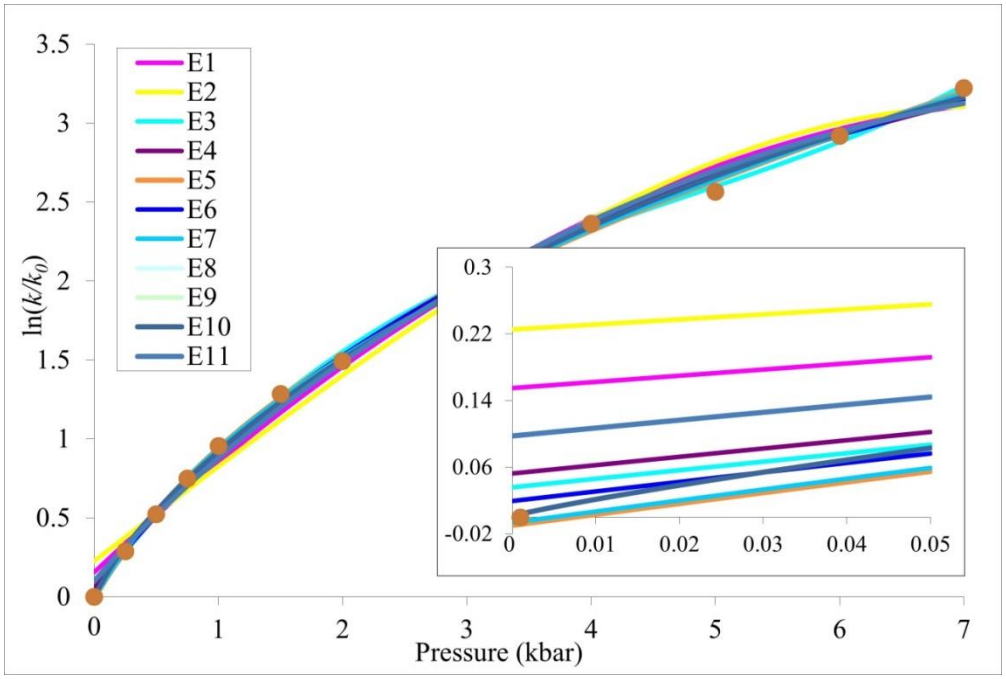

Figure 5.8. Fit of E1-E11 to kinetic data for the Menshutkin reaction between tri-n-propyl amine with methyl iodide in acetone[10] over the pressure ranges of 0-7 kbar.

Table 5.15. Activation volumes (cm^3/mol) obtained by fitting equations E4-E9 to data for the Menshutkin reaction of tri-n-propyl amine with methyl iodide in various solvents at 30°C[10] using the El'yanov-Gonikberg data pooling with $\Phi(P)$ parameterized by fitting to all reactions.

Solvent	Propionitrile	Cyclohexanone	Dichloromethane	Nitrobenzene	Nitromethane	Acetone
Pressure Range	0-2 kbar	0-2 kbar	0-2kbar	0-1 kbar	0-2 kbar	0-7 kbar
E4	-28.1	-27.9	-31.3	-29.1	-24.1	-26.9
E5	-33.1	-33.1	-36.8	-32.8	-28.6	-31.8
E6	-31.3	-31.3	-35.1	-31.6	-27.1	-30.1
E7	-33.8	-33.8	-37.8	-33.6	-29.1	-32.3
E8	-37.1	-37.1	-41.3	-37.3	-31.8	-34.6
E9	-39.8	-39.6	-44.3	-39.8	-34.1	-36.8

5.4.3. Solvolysis.

The data for the two solvolysis reactions discussed here – methanolysis of ethyl chloride[14a] and allyl bromide[14b] – are particularly interesting due to the extremely wide range of pressures over which their kinetics was measured. Not surprisingly, the results of fitting shown in Table 5.16 are much more dispersed than for the previously discussed Diels-Alder and Menshutkin reactions. The plots shown in Fig. 5.9 clearly display the unphysical behavior of many functions over the entire pressure range – E1-E2, E8-E9, E11 possess maxima and E3 has an inflection point. The graphs of functions E4-E7 and E10 look reasonable over the entire range, including the lower pressure region; E7 and E10 appear undistinguishable. The $\Delta V_0^{\neq}$ values produced by E6, E7, and E10 are very close for allyl bromide, but are much more disperse for ethyl chloride. Fitting of E8 and E9 results in an unbounded a_4 parameter, leading to extremely unreasonable values of predicted activation volumes for both reactions. The El'yanov-Gonikberg treatment that resolved this issue in the case of Diels-Alder and Menshutkin reactions, does not seem possible in this case due to the lack of data necessary for pooling.

Table 5.16. Activation volumes (cm^3/mol) obtained from fitting equations E1-E11 to data for Methanolysis reactions.

Reactant (T, °C)	Ethyl Chloride (65 °C)[a]	Allyl Bromide (23 °C)[b]
Pressure Range	0-31 kbar	0-45 kbar
Error Level	3 %	3 %
E1	-11.0	-8.0
E2	-8.7	-6.0
E3	-16.4	-12.8
E4	-17.9	-19.8
E5	-29.1	-26.6
E6	-24.1	-31.7
E7	-33.9	-31.9
E8	-123.8	-92.2
E9	-122.6	-108.7
E10	-28.6	-31.3
E11	-15.0	-11.6

[a] Kinetic data from Ref 14a

[b] Kinetic data from Ref 14b

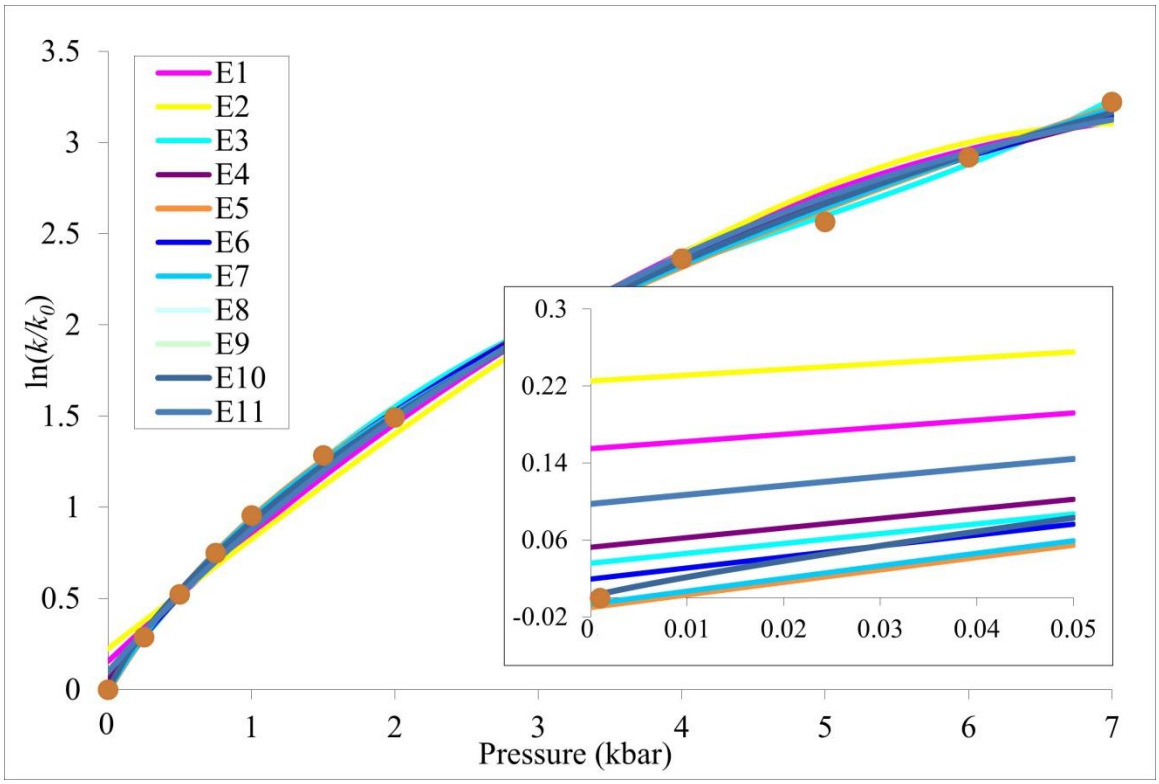

Figure 5.9. Fit of E1-E11 to the kinetic data for the methanolysis of allyl bromide at 23°C[14b].

5.5. Concluding Remarks

The presented study of the general properties of equations E1-E11 and their performance as regression functions reveals that, although none of these equations is universally good, they remain, when applied properly, a useful tool for analysis of the experimental data on high-pressure kinetics or equilibria. The following is a summary of general observations and recommendations.

1. All equations E1-E11 perform equally well if both the pressures and the level of experimental errors are sufficiently low (0-1kbar; 1-2%).
2. Simple quadratic equation E1 works remarkably well on 0-1 kbar range, even if the level of experimental errors is relatively high, which makes it a better choice over that range compared to equations, such as E4-E10, that include nonlinear parameter a_4 and are more sensitive to the level of experimental errors.

3. Equations E2-E3 and E10 should generally be avoided since they are prone to display unphysical behavior in many cases. Although this could reasonably be expected for cubic equations E2 and E3, it might seem somewhat more surprising for E10, the instability of which apparently arises from its excessive flexibility due to a greater number of adjustable parameters.
4. Equations E4-E9, and especially E5-E7, appear to be the most reliable on wider pressure ranges, substantially exceeding 1 kbar. However, their behavior becomes rather unpredictable on narrower pressure ranges when the level of errors is high.
5. El'yanov-Gonikberg data pooling offers an excellent tool for correcting this instability and significantly improves the quality of predictions based on equations E4-E9. With data pooling, functions E5, E7, and E9 seem to perform the best.

Based on the above, it seems that equations E2-E3 and E10-E11 are less suitable for the purpose of obtaining activation or reaction volumes from experimental data. We also suggest the following to improve the quality of volumes predicted using the remaining functions E1 and E4-E9: For narrow pressure ranges, use quadratic equation E1. For wider pressure ranges, fit all functions E1 and E4-E9 to the experimental data and identify any irregularities in their appearances by visual inspection of their plots, paying particular attention to the presence of maxima or inflection points and unusual behavior in the vicinity of P = 0. Use data pooling to obtain more robust predictions.

5.6. References

1. (a) C.A. Eckert, *Ann. Rev. Phys. Chem.*, 1972, **23**, 239; (b) H. Kelm and D.A. Palmer, In: *High Pressure Chemistry* (H. Kelm, ed.), Dordrecht: Reidel, 1978, 281; (c) B.S. El'yanov and E.M.Gonikberg, *J. Chem. Soc., Faraday Trans.* 1, 1979, **75**, 172; (d) B.S. El'yanov and E.M. Vasylvitskaya, *Rev. Phys. Chem. Japan*, 1980, **50**, 169; (e) T. Asano and T. Okada, *J. Phys. Chem.*, 1984, **88**, 238; (f) C.A.N. Viana, A.R.T. Calado, and L.M.V. Pinheiro, *J. Phys. Org. Chem.*, 1995, **8**, 63.

2. C.A.N. Viana and J.C.R.Reis, *Pure Appl. Chem.*, 1996, **68**, 1541 and references therein.
3. We omitted the trivial linear equation $\ln k = a_0 + a_1 P$.
4. D.R. Stranks, *Pure Appl. Chem.*, 1974, **38**, 303.
5. (a) M.V. Basilevsky, V.M. Ryaboy, and N.N. Weinberg, *J. Phys. Chem.*, 1991, **95**, 5533; (b) H. Sumi and T. Asano, *J. Chem. Phys.*, 1995, **102**, 9565; (c) T. Asano and H. Sumi, Chem. Phys. Lett., 1998, **294**, 493; (d) N. Weinberg, *Rev. High Press. Sci. Tech.*, 1998, **8**, 86; (e) A. Drljaca, C. D. Hubbard, R. van Eldik, T.Asano, M. V. Basilevsky and W. J. le Noble, *Chem. Rev.*, 1998, **98**, 2167; (f) T. Asano, *Pure Appl. Chem.*, 1999, **71**, 1691; (g) Y. Goto, T. Takahashi, Y. Ohga, T. Asano, M. Hildebrand, and N. Weinberg, *Phys. Chem. Chem. Phys.*, 2003, **5**, 1825; (h) H. Kono, H. Osako, M. Sasaki, T. Takahashi, Y. Ohga, T. Asano, M. Hildebrand, and N.N. Weinberg, *Phys. Chem. Chem. Phys.*, 2004, **6**, 2260.
6. At pressures approaching and exceeding 100 kbar when the strength of intermolecular interactions reaches the level of intramolecular forces, completely new patterns of chemical reactivity are revealed[7] due to significant deformation of the energy surfaces of reaction systems.[8]
7. See for example R. J. Hemley, *Annu. Rev. Phys. Chem.*, 2000, **51**, 763; R. Bini, M. Ceppatelli, M. Citroni, V. Schettino, *Chem. Phys.*, 2012, **398**, 262 and references therein.
8. J. Spooner, B. Yanciw, B. Wiebe and N. Weinberg, *J. Phys. Chem., A* 2014, **118**, 765; J. Spooner, B. Smith N. and Weinberg, *Can. J. Chem.*, 2016, **94**, 1057

9. R. Lohmuller; D.D. Macdonald, M. Mackinnon, and J.B. Hyne, Can. J. Chem., 1978, **56**, 1739.
10. S.P. Sawin, Ph.D. Thesis, University of Illinois, Urbana (1971).
11. B.S. El'yanov and M.G. Gonikberg, *Zh. Fiz. Khim.*, 1962, **36**, 604; B.S. El'yanov and M.G. Gonikberg, *Izv. Akad. Nauk SSSR Ser. Khim.*, 1967,1044 ; B.S. El'yanov, *Austr J Chem*, 1975, **28**, 933
12. (a) R. A. Grieger and C. A. Eckert, *AIChE J., 1970,* **16**, *766; (b)* R. A. Grieger and C. A. Eckert, *Trans. Faraday. Soc., 1970,* **66**, *2579; (c)* R. A. Grieger and C. A. Eckert, *J. Amer. Chem. Soc., 1970*, **92**, 7149; (d) R. A. Grieger and C. A. Eckert, *Ind. and Eng. Chem. (Fundamentals)*, 1971, **10**, 369.; (e) B.E. Poling and C. A. Eckert, *Ind. and Eng. Chem. (Fundamentals)*, 1972, **11**, 451; (f) J. R. McCabe and C. A. Eckert, *Ind. and Eng. Chem. (Fundamentals)*, 1974, **13b**, 766.
13. (a) C. Walling, J. Peisach,. *J. Am. Chem. Soc.*, 1958, **80**, 5819; (b) J. Rimmelin and G. Jenner, *Tetrahedron*, 1974, **30**, 3081; (c) B. Raistrick, R. H. Sapiro and D. M. Newitt, *J. Chem. Soc.*, 1939,**61**, 1761; (d) C. Walling and H. J. Schugar, J. Am. Chem. Soc., 1963, **85**, 607.
14. (a) H. G. David, S. D. Hamann, and S. J. Lake, *Aust. J. Chem.*, 1955, **8**, 285; (b) H. G. David and S. D. Hamann, *Discuss. Faraday Soc***.,** 1956, **22**, 114.
15. (a) J. Spooner, H. Wiebe, N. Boon, E. Deglint, E. Edwards, B. Yanciw, B. Patton, L. Thiele, P. Dance, N. Weinberg, *Phys. Chem. Chem. Phys.*, 2012, **14**, 2264 (b) H. Wiebe, J. Spooner, N. Boon, E. Deglint, E. Edwards, P. Dance, N. Weinberg, *J. Phys. Chem. C*, 2012, **116**, 2240.

Chapter 6.

Concluding remarks

6.1. Summary of achievements

The work presented in this thesis clearly demonstrates the utility of our computational techniques in gaining understanding and predicting of the behaviour of chemical systems under pressure. The ability to accurately calculate molecular volumes using our MD displacement volume model is at the heart of our methodology. Figure 6.1 summarizes six of the main applications[1] of the displacement volume model to date – four of them have been discussed in the preceding chapters of this thesis; while the others remain the focus of investigation by other members of our research group. The application of the method to the study of protein folding has already shown promising results.[1c]

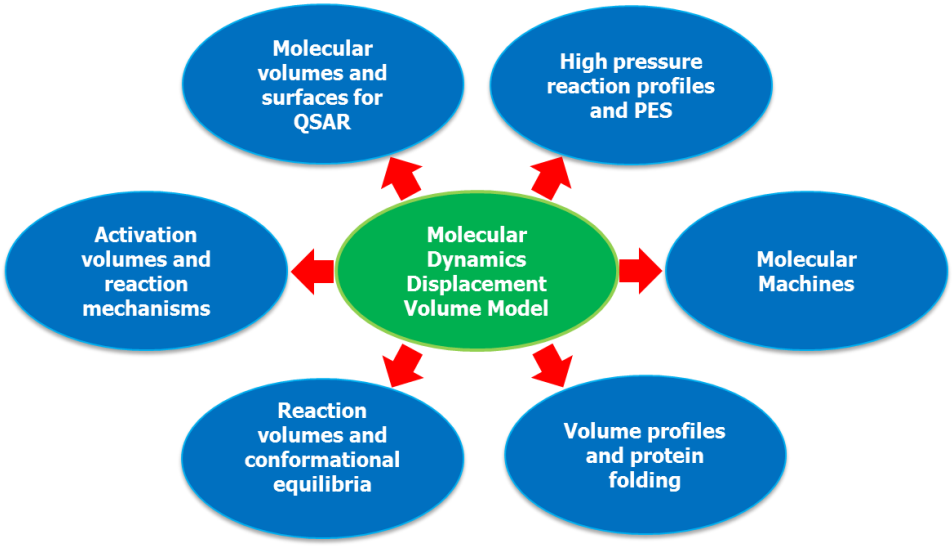

Figure 6.1. Various applications[1] based the MD displacement volume method[2]

6.2. Future work

The next natural step is to further develop and improve our methodology in its application to various interesting types of reactions, on which pressure has a profound effect[3] (see Table 1.2). Among those various cases, electron transfer reactions, for which a wealth of experimental high-pressure data is available,[4] present a particular challenge for the classical MD simulations since they are not readily suited to study these processes.

As discussed in section 2.1.6, the main instrument currently used to interpret high pressure effects in electron transfer processes is the Stranks-Hush-Marcus theory.[5] Predictions of this theory have shown good agreement with experiment for many outer-sphere electron transfer systems.[4] However, this approach does not offer a recipe for calculation of the effects of solvent/solute restructuring that goes beyond a simple change in ionic radii of the solute in a structureless solvent. Our MD displacement volume method is perfectly suited for describing the omitted effects of solute restructuring and specific solvation. However, to be used as a viable alternative to the Stranks-Hush-Marcus treatment, it needs to be augmented with an MD-based description of nonequilibrium solvation to replace the continuum solvent model.

The discrete solvent approach that we use to describe nonequilibrium polarization of the medium, playing the central role in Marcus theory, utilizes a procedure, similar to the one previously used to model nonequilibrium solvation by viscous solvents.[6] In an equilibrium MD simulation, the total energy of a solvent-solute system is described as a trajectory average that depends on both the solvent trajectory, $\boldsymbol{X}(t)$, and solute trajectory, $\boldsymbol{x}(t)$:

$$E = \langle E(\boldsymbol{x}(t), \boldsymbol{X}(t)) \rangle \tag{6.1}$$

Due to solvent-solute interactions, both of these trajectories and, as a result, the total energy are parametrically dependent on the solute parameters (such as solute charge

distribution). If such solute parameter is labeled as q, the equilibrium energy of the solvent-solute system is

$$E(q) = \langle E(\boldsymbol{x}(t|q), \boldsymbol{X}(t|q)) \rangle \tag{6.2}$$

If a solvent trajectory is generated for the solute parameter $q = Q$ and the solute with $q = Q$ is removed and replaced by the solute with $q \neq Q$, which no longer matches the previously generated solvent trajectory $\boldsymbol{X} = \boldsymbol{X}(t\,|Q)$, the resulting construct represents a situation of nonequilibrium solvation, and the energy of such system is

$$E(q, Q) = \langle E(\boldsymbol{x}(t|q), \boldsymbol{X}(t|Q)) \rangle \tag{6.3}$$

This approach is illustrated in Fig. 6.2 for a model example of electron transfer between donor, M^{Z_1} (charge Z_1), and acceptor, M^{Z_2} (charge Z_2) where solute parameter q describes the charge distribution of the solute ion pair: $q_1 = Z_1+q$; $q_2=Z_2–q$. In the reactant state $q_1 = Z_1$ and $q_2 = Z_2$ (q=0), whereas in the product state $q_1 = Z_1+1$ and $q_2 = Z_2–1$ (q=1). Nonequilibrium solvent trajectories corresponding to various intermediate states of partial charge transfer $q_1 = Z_1+Q$; $q_2 = Z_2–Q$ ($0<Q<1$) can be generated by varying the solvent coordinate Q. Solvent trajectories thus produced are then recombined with the solute in either reactant or product state to give diabatic Marcus-type energy profiles.

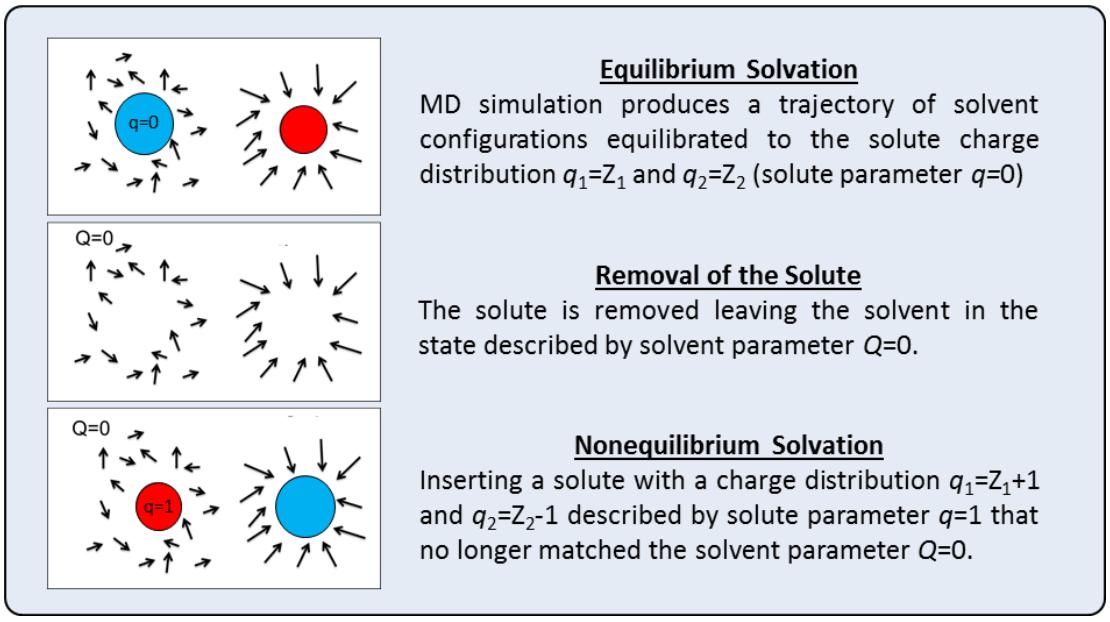

Figure 6.2. Schematic representation of a construct describing nonequilibrium solvation of solute with charge distribution parameter q = 1not matching the solvent parameter Q = 0.

Our preliminary results using this approach for a simple system of two structureless ions in aqueous solution with charges 2+ and 3+ at an interionic separation of 5 nm are compared in Fig. 6.3 to the curves generated using the Marcus equation[5]

$$\Delta G = (\Delta e)^2 \left(\frac{1}{2a_1} + \frac{1}{2a_2} - \frac{1}{\sigma}\right)\left(\frac{1}{\varepsilon_o} - \frac{1}{\varepsilon}\right) \qquad (6.4)$$

where Δe is the amount of charge transferred, a_1 and a_2 are the Born radii of the donor and acceptor ions, and sigma is the internuclear separation distance equal to the sum of the two radii. The close match of the MD results and the prediction of Marcus theory is very encouraging and we hope that we will soon be in a position to formulate a consistent numerical procedure to cover the entire range of homogeneous high pressure reactions with a proper balance in description of structural and solvent effects.

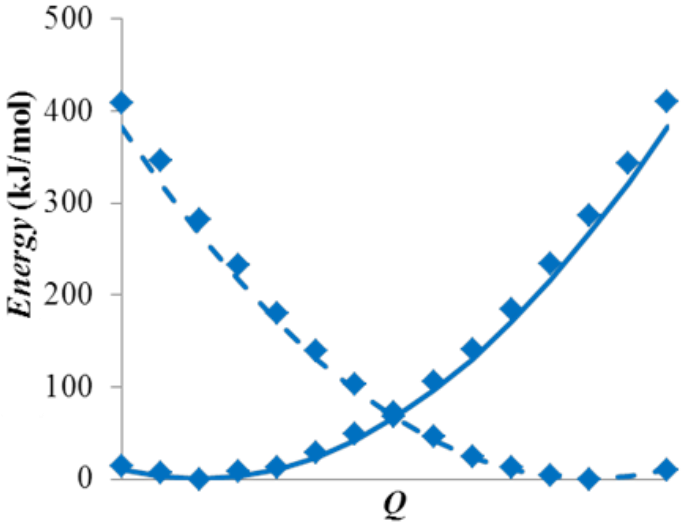

Figure 6.3. MD generated free energy profiles for the pair of 2+/3+ structureless ions in aqueous solution (diamonds), with corresponding Marcus energy curves calculated using eq. 6.4 (lines).

6.3. References

1. (a) P. Ebrahimi, J. Spooner, N. Weinberg, E. Plettner, *Chemosphere*, 2013, **93**, 54. (b) J. Spooner, B. Yanciw, B. Wiebe and N. Weinberg, *J. Phys. Chem. A* 2014, **118**, 765. (c) H. Wiebe and N. Weinberg, *J. Chem. Phys.*, 2014, **140**, 124105. (d) J. Spooner, B. Smith, N.Weinberg, *Can. J. Chem.*, 2016, **94**, 1057 (e) H. Wiebe, M. Louwerse, N. Weinberg, *J Chem Phys.*, 2017, **146**, 104107.
2. J. Spooner, H. Wiebe, N. Boon, E. Deglint, E. Edwards, B. Yanciw, B. Patton, L. Thiele, P. Dance, N. Weinberg, *Phys. Chem. Chem. Phys.*, 2012, **14**, 2264; H. Wiebe, J. Spooner, N. Boon, E. Deglint, E. Edwards, P. Dance, N. Weinberg, *J. Phys. Chem. C*, 2012, **116**, 2240
3. (a) W.J. le Noble, *Prog. Phys. Org. Chem.*, 1967, **5**, 207; (b) T. Asano and W.J. le Noble, *Chem. Rev.*, 1978, **78**, 407; (c) R. van Eldik, T. Asano and W.J. le Noble,

Chem. Rev., 1989, **89**, 549; (d) A. Drljaca, C.D. Hubbard, R. van Eldik, T. Asano, M.V. Basilevsky and W.J. le Noble, *Chem. Rev.*, 1998, **98**, 2167.

4. (a) T. Swaddle, *Inorg. Chem.*, 1990, **29**, 5018; (b) T. Swaddle, *J. Mol. Liq.*, 1995, **65/66**, 237; (c) T. Swaddle, *Can. J. Chem.*, 1996, **74**, 631; (d) T. Swaddle and P. Tregloan, *Coord. Chem. Rev.*, 1999, **187**, 255; (e) T. Swaddle, *Chem. Rev.*, 2005, **105**, 2573.
5. D.R. Stranks, *Pure Appl. Chem.*, 1974, **38**, 303.
6. M. Dhaliwal, M.V. Basilevsky, N. Weinberg, *J. Chem. Phys.*, 2007, **126**, 234505; L. Huber, E. Edwards , M.V. Basilevsky, N. Weinberg, *Mol. Phys.*, 2009, **107**, 2283; H. Wiebe, M. Prachnau, N. Weinberg, *Can. J. Chem.*, 2013, **91**, 787.

Appendix A.

Numerical Values of the Potential Energy Function for the Model Triatomic of Section 4.1.2.

		R_{AB}, nm																	
		0.08	**0.09**	**0.1**	**0.11**	**0.12**	**0.13**	**0.14**	**0.15**	**0.16**	**0.17**	**0.18**	**0.19**	**0.2**	**0.21**	**0.22**	**0.23**	**0.24**	**0.25**
R_{BC}, nm	**0.08**	99.46	68.91	49.16	35.83	26.76	20.58	16.38	13.51	11.55	10.20	9.28	8.65	8.21	7.92	7.71	7.56	7.45	7.36
	0.09	68.91	47.00	33.48	23.88	16.9	11.88	8.32	5.80	4.04	2.79	1.93	1.32	0.89	0.59	0.37	0.21	0.09	0.00
	0.1	49.16	33.48	25.97	20.66	16.08	12.36	9.50	7.36	5.80	4.66	3.84	3.25	2.82	2.50	2.27	2.10	1.97	1.87
	0.11	35.83	23.88	20.66	20.00	18.71	16.79	14.89	13.27	11.97	10.97	10.21	9.64	9.22	8.90	8.66	8.47	8.33	8.22
	0.12	26.76	16.9	16.08	18.71	21.01	21.66	21.3	20.58	19.81	19.10	18.50	18.02	17.63	17.32	17.09	16.9	16.76	16.65
	0.13	20.58	11.88	12.36	16.79	21.66	24.76	26.18	26.69	26.77	26.67	26.50	26.32	26.15	26.00	25.88	25.77	25.68	25.61
	0.14	16.38	8.32	9.05	14.89	21.3	26.18	29.00	30.5	31.28	31.67	31.86	31.94	31.96	31.95	31.93	31.9	31.87	31.84
	0.15	13.51	5.8	7.36	13.27	20.58	26.69	30.5	32.69	33.94	34.66	35.08	35.32	35.46	35.53	35.57	35.59	35.59	35.59
	0.16	11.55	4.04	5.80	11.97	19.81	26.77	31.28	33.94	35.52	36.46	37.03	37.38	37.59	37.72	37.80	37.84	37.87	37.89
	0.17	10.2	2.79	4.66	10.97	19.10	26.67	31.67	34.66	36.46	37.55	38.22	38.64	38.91	39.07	39.18	39.25	39.29	39.32
	0.18	9.28	1.93	3.84	10.21	18.50	26.5	31.86	35.08	37.03	38.22	38.97	39.44	39.74	39.93	40.05	40.14	40.19	40.23
	0.19	8.65	1.32	3.25	9.64	18.02	26.32	31.94	35.32	37.38	38.64	39.44	39.94	40.26	40.48	40.62	40.71	40.77	40.81
	0.2	8.21	0.89	2.82	9.22	17.63	26.15	31.96	35.46	37.59	38.91	39.74	40.26	40.61	40.83	40.98	41.08	41.15	41.2
	0.21	7.92	0.59	2.50	8.9	17.32	26.00	31.95	35.53	37.72	39.07	39.93	40.48	40.83	41.06	41.22	41.33	41.40	41.45
	0.22	7.71	0.37	2.27	8.66	17.09	25.88	31.93	35.57	37.8	39.18	40.05	40.62	40.98	41.22	41.38	41.49	41.57	41.62
	0.23	7.56	0.21	2.10	8.47	16.9	25.77	31.9	35.59	37.84	39.25	40.14	40.71	41.08	41.33	41.49	41.6	41.68	41.74
	0.24	7.45	0.09	1.97	8.33	16.76	25.68	31.87	35.59	37.87	39.29	40.19	40.77	41.15	41.40	41.57	41.68	41.76	41.82
	0.25	7.36	0.00	1.87	8.22	16.65	25.61	31.84	35.59	37.89	39.32	40.23	40.81	41.2	41.45	41.62	41.74	41.82	41.87

Appendix B.

Solvent Cavities Around the Reactant State and TS of the Substituted Toluene Systems.

Reactant State (left) and TS (right)

B.1 Series A: m-xylene

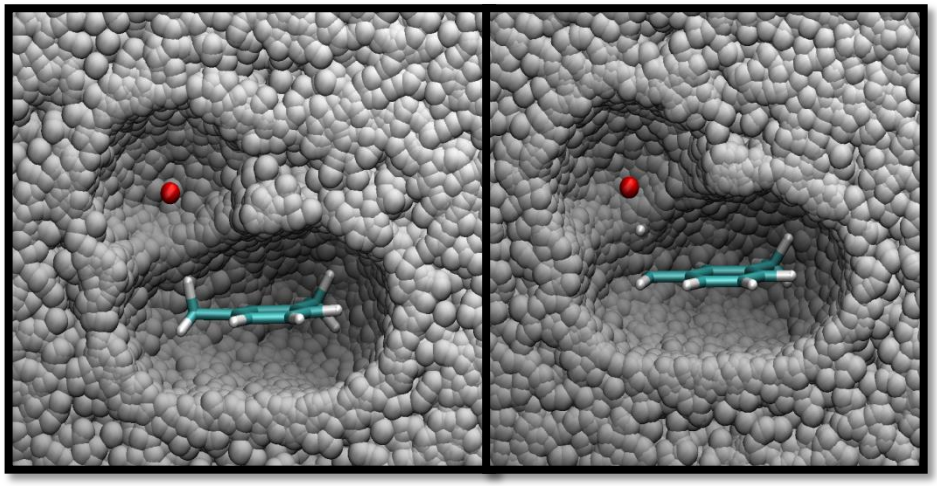

B.2 Series A: p-xylene

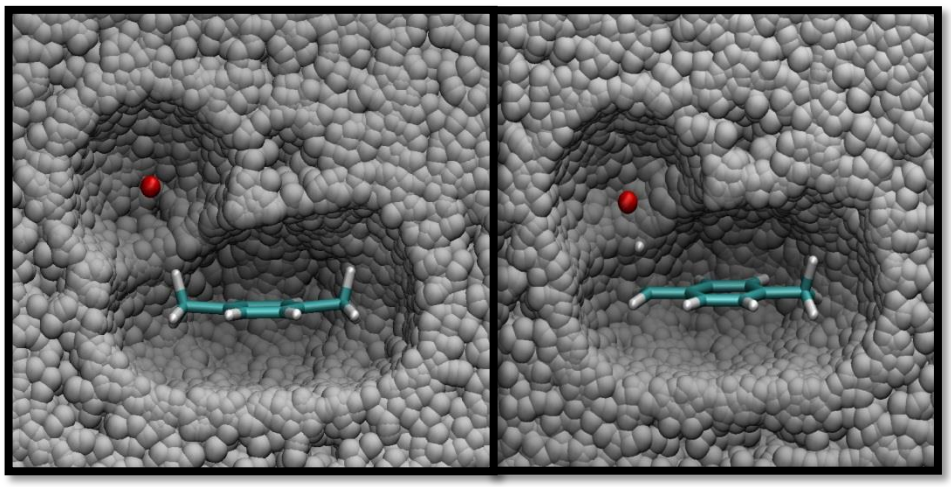

B.3 Series A: m-bromotoluene

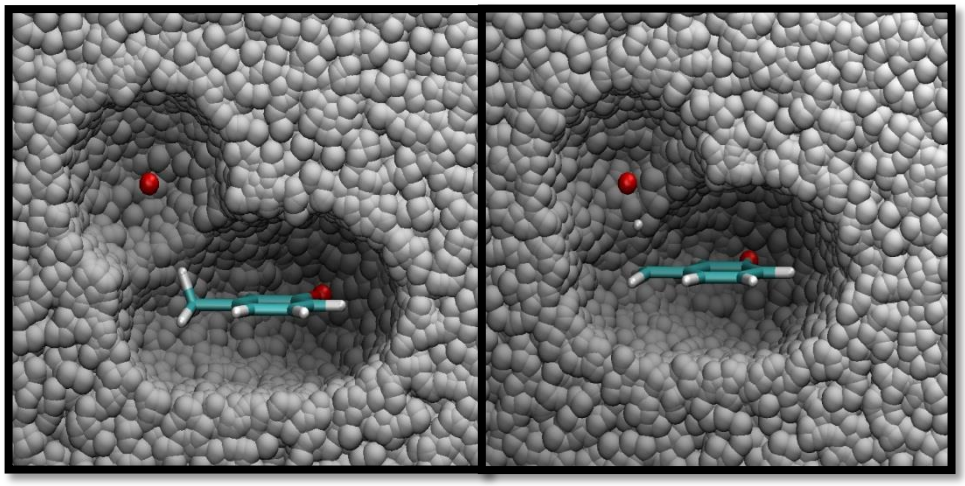

B.4 Series A: p-chlorotoluene

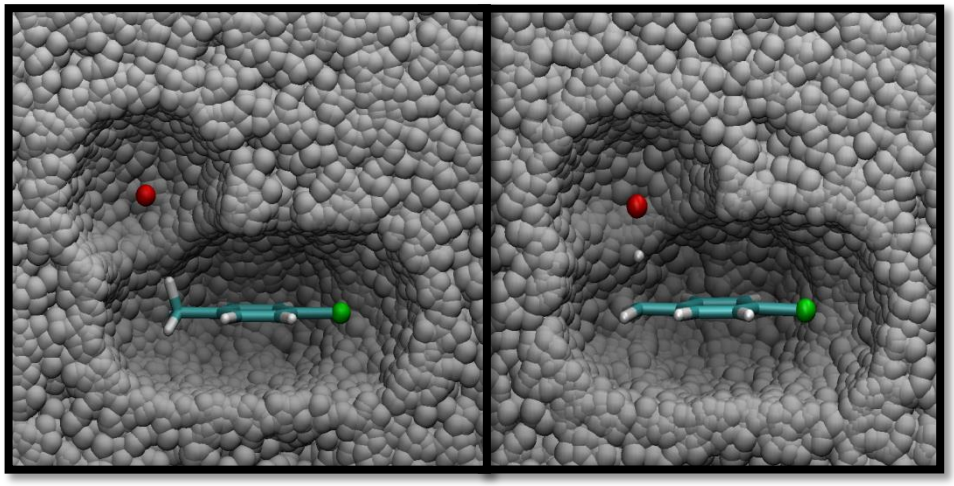

B.5 Series B: ethylbenzene

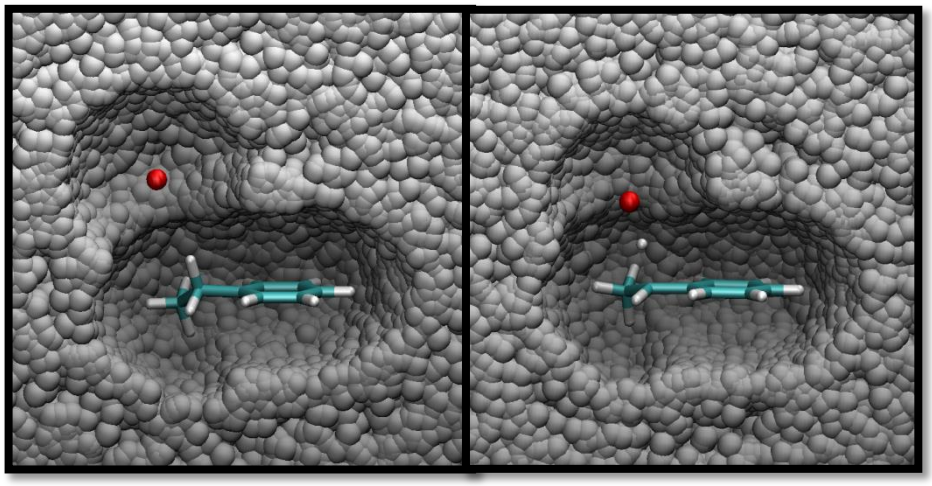

B.6 Series B: cumene

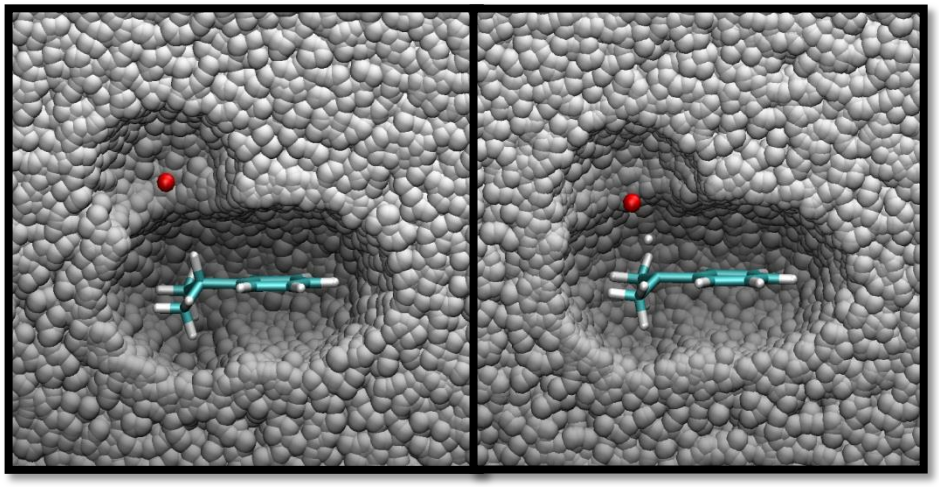

B.7 Series B: diphenylmethane

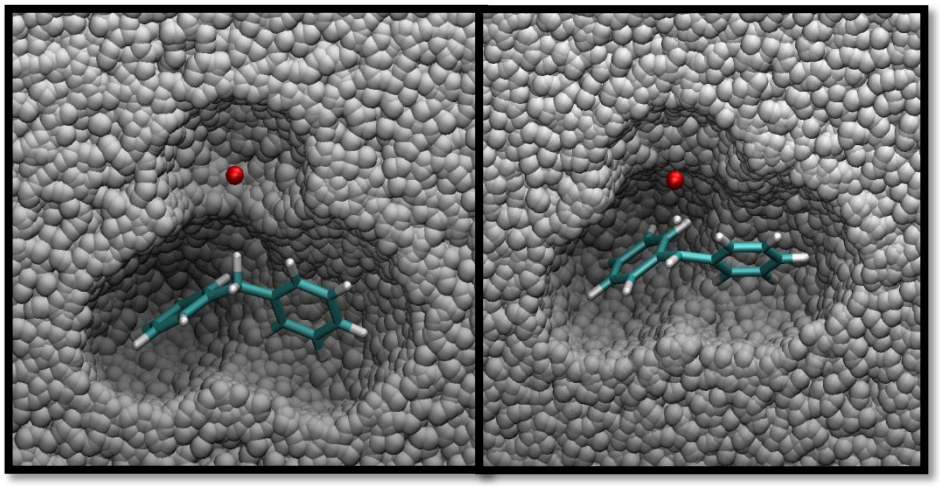

Appendix C.

Compressed PES's for A-B-C systems embedded in 1D Ne matrix.

C.1 PES for BrHBr at low (A) medium (B) and high (C) compression. The contour spacing is 10 kJ/mol.

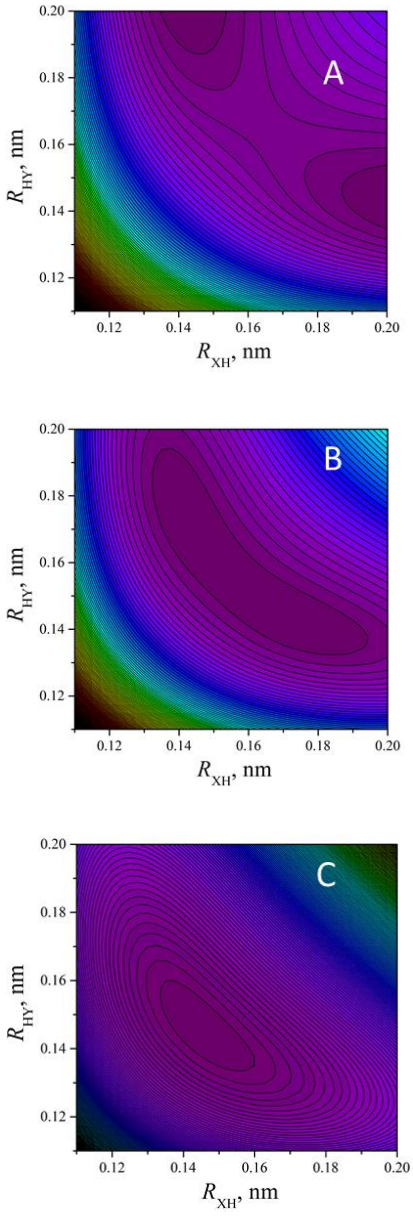

C.2 PES for ClHCl at low (A) medium (B) and high (C) compression. The contour spacing is 10 kJ/mol.

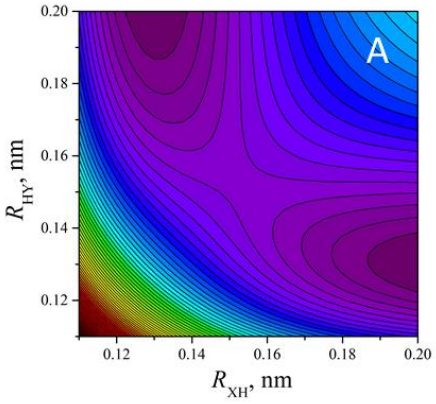

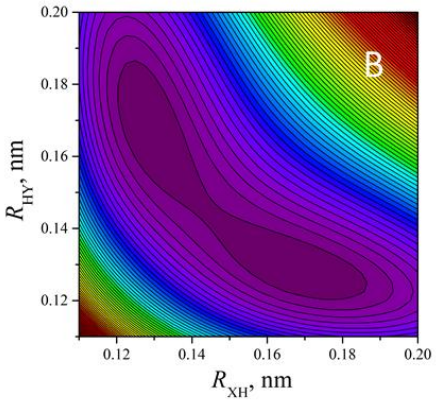

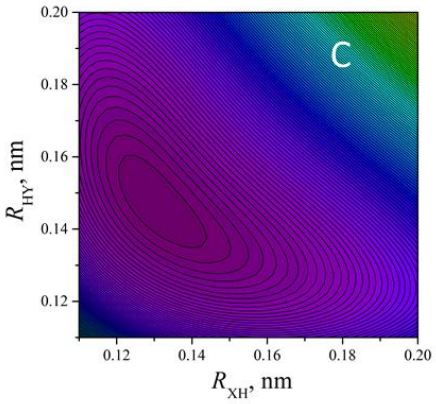

C.3 PES for ClHBr at low (A) medium (B) and high (C) compression. The contour spacing is 10 kJ/mol.

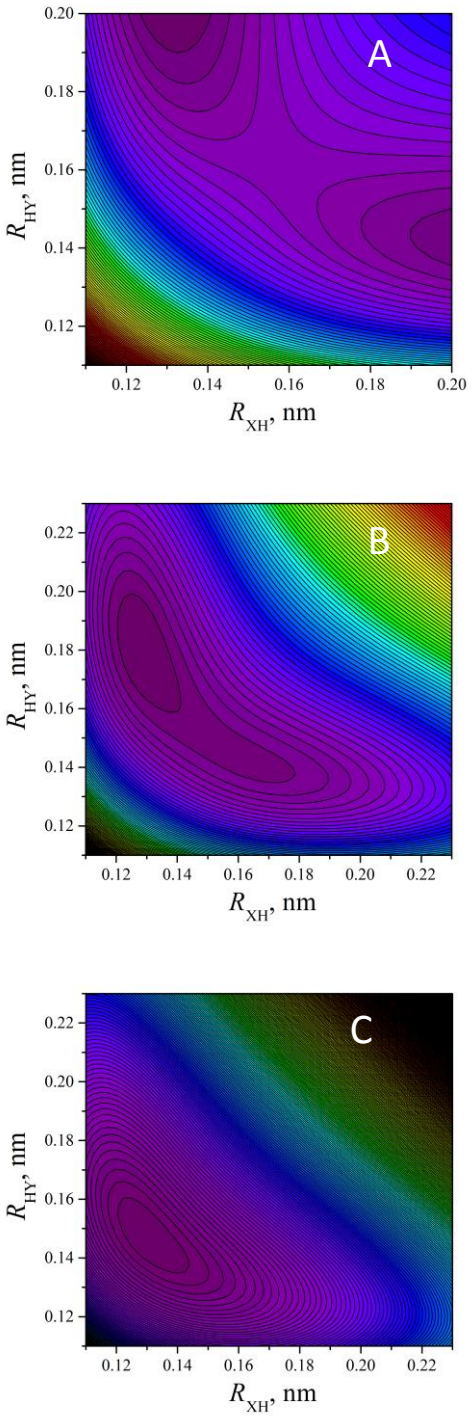

C.4 PES for FHBr at low (A) medium (B) and high (C) compression. The contour spacing is 10 kJ/mol.

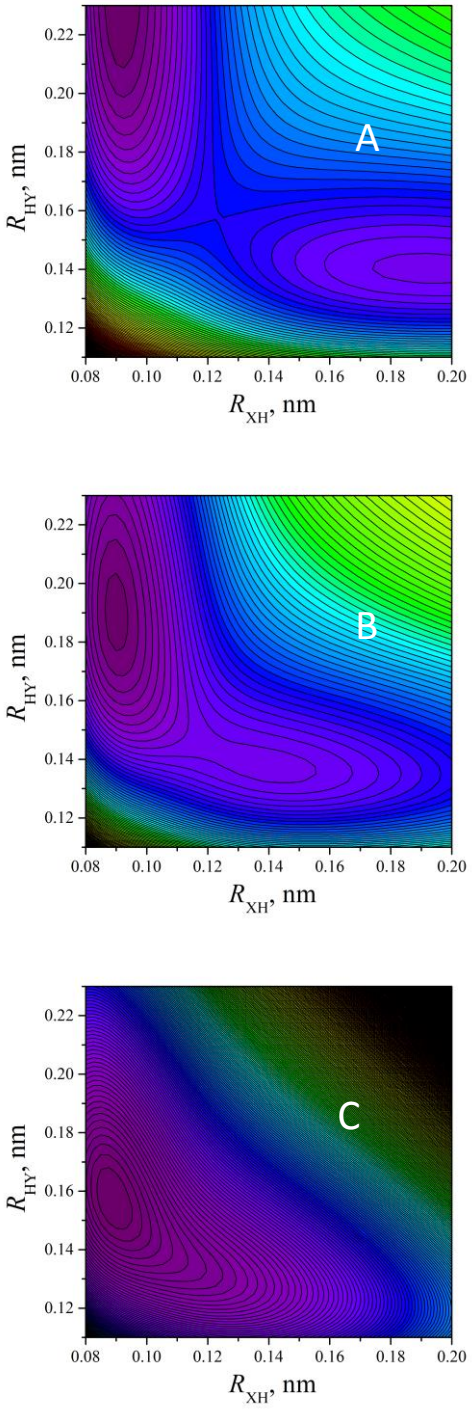

C.5 PES for FHCl at low (A) medium (B) and high (C) compression. The contour spacing is 10 kJ/mol.

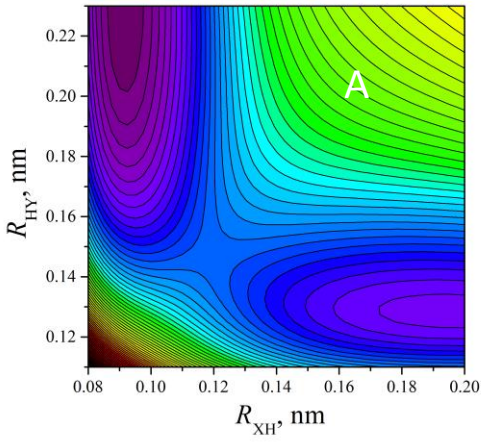

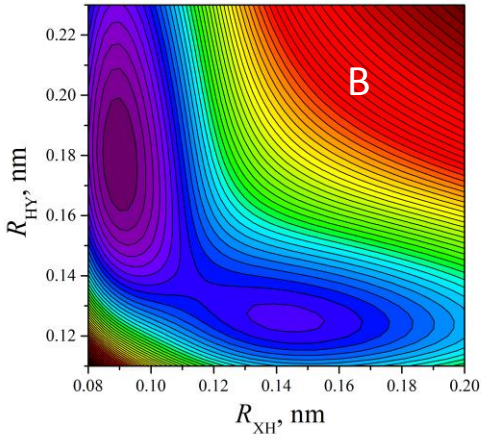

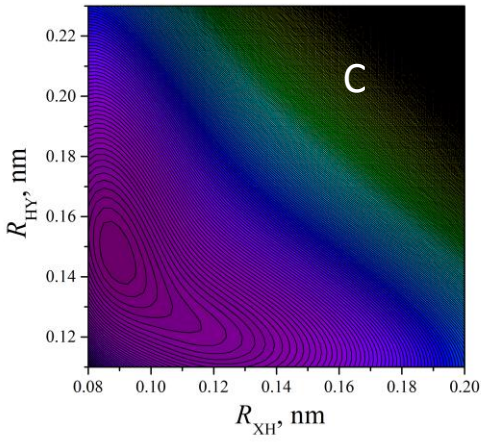

C.6 PES for CN-CH_3-CN at low (A) medium (B) and high (C) compression. The contour spacing is 10 kJ/mol.

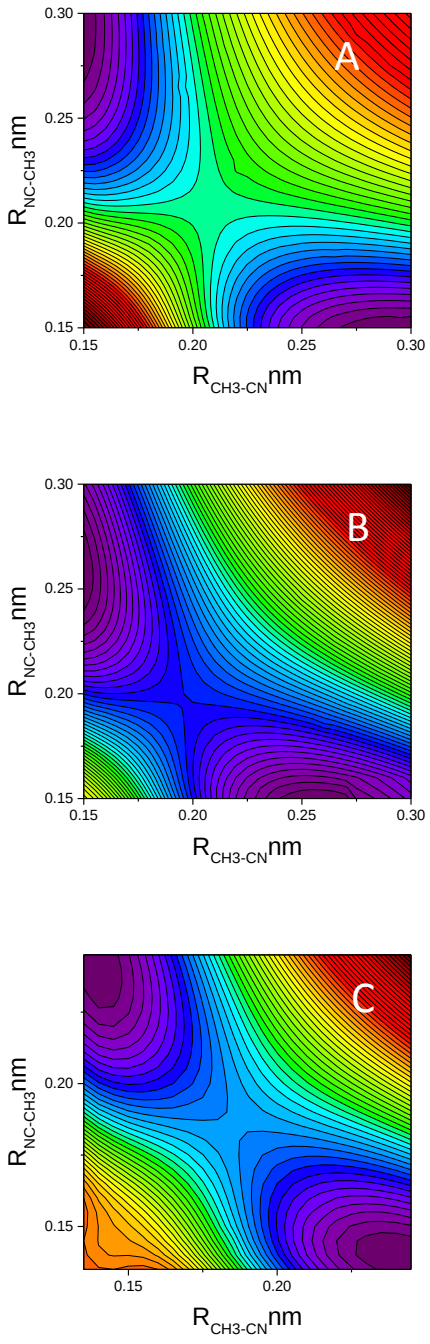

C.7 PES for Cl-CH_3Cl at low (A) medium (B) and high (C) compression. The contour spacing is 10 kJ/mol.

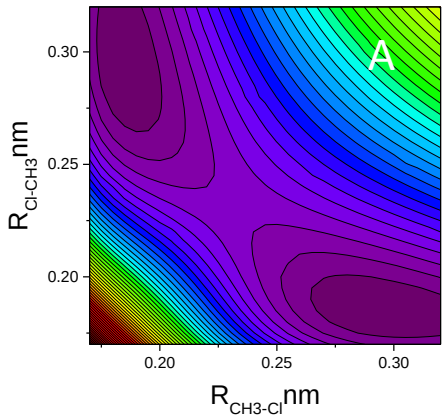

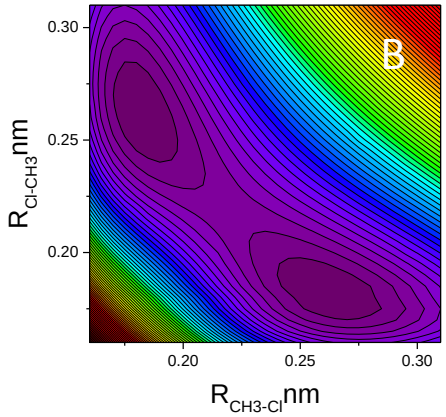

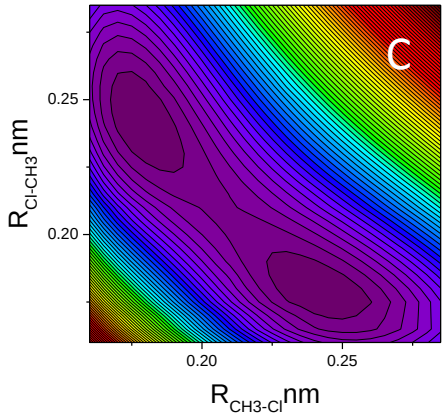

C.8 PES for Br-CH_3-Br at low (A) medium (B) and high (C) compression. The contour spacing is 10 kJ/mol.

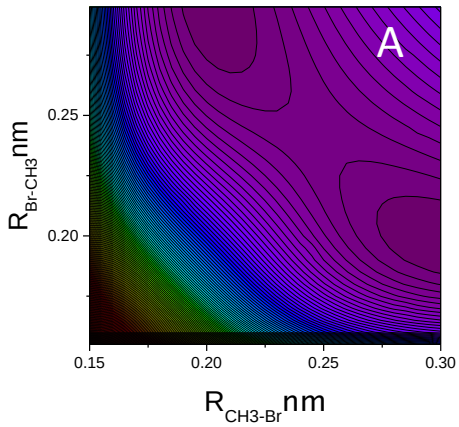

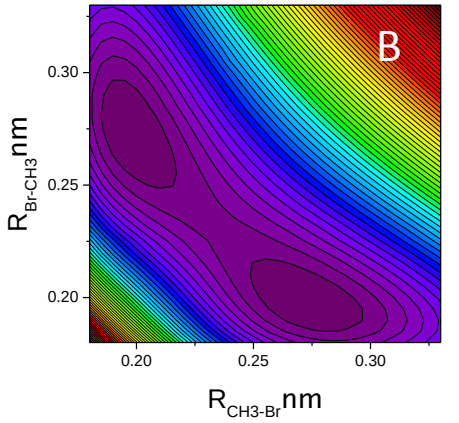

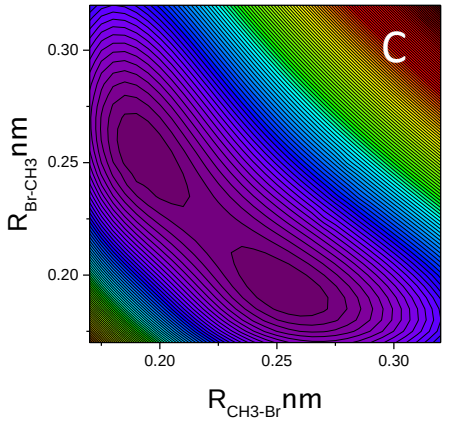

C.9 PES for NC-CH3-Cl at low (A) medium (B) and high (C) compression. The contour spacing is 10 kJ/mol.

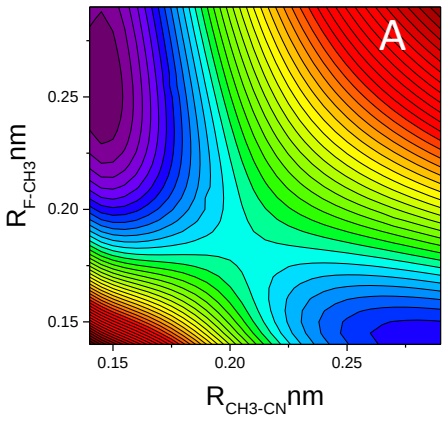

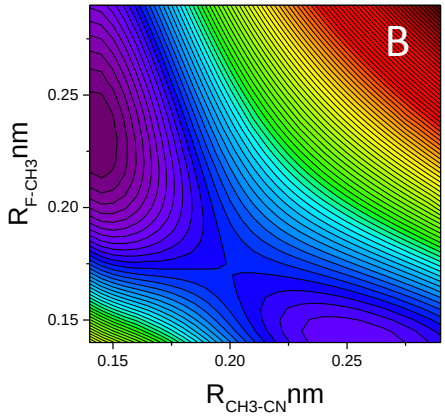

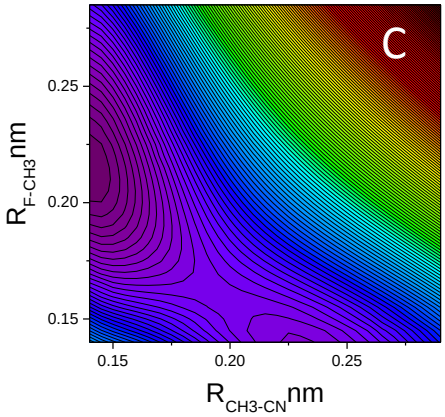

C.10 PES for NC-CH_3-Cl at low (A) medium (B) and high (C) compression. The contour spacing is 10 kJ/mol.

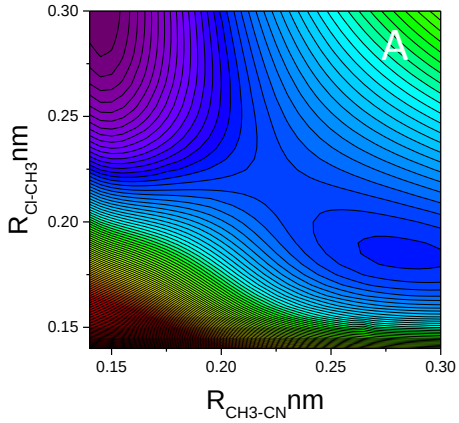

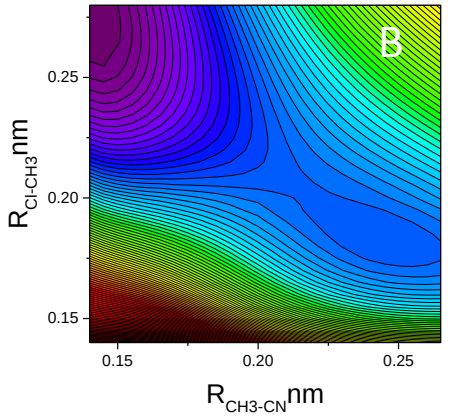

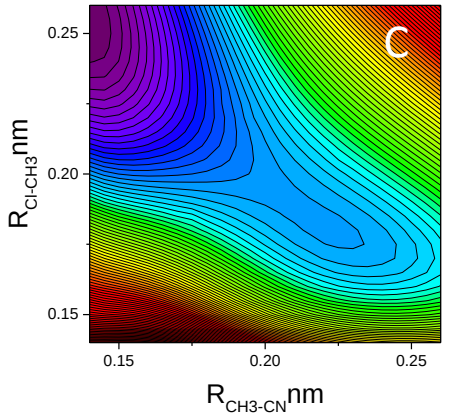

C.11 PES for NC-CH_3-Br at low (A) medium (B) and high (C) compression. The contour spacing is 10 kJ/mol.

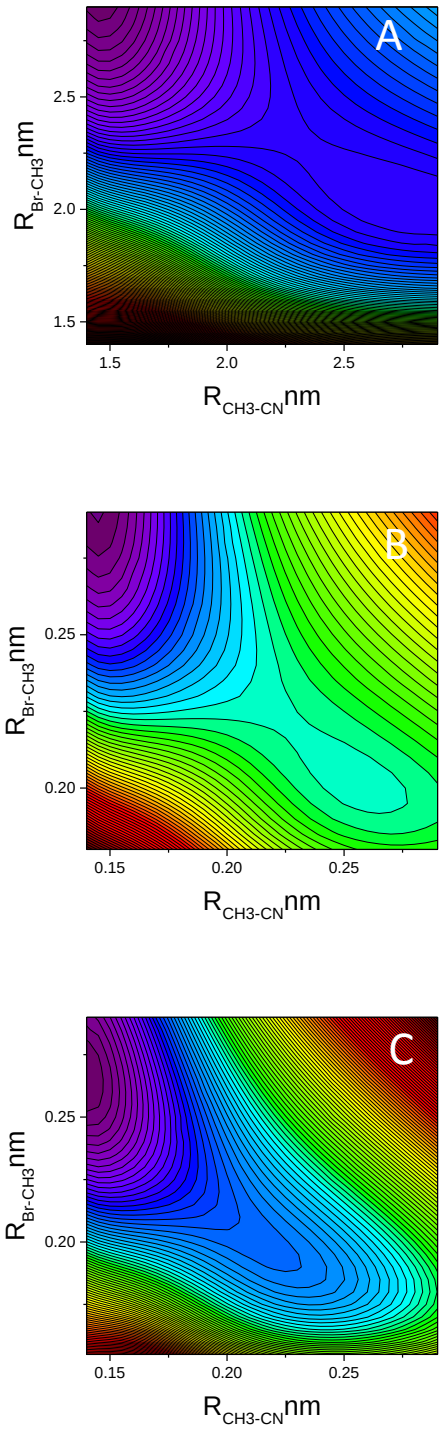

C.12 PES for F-CH_3-Br at low (A) medium (B) and high (C) compression. The contour spacing is 10 kJ/mol.

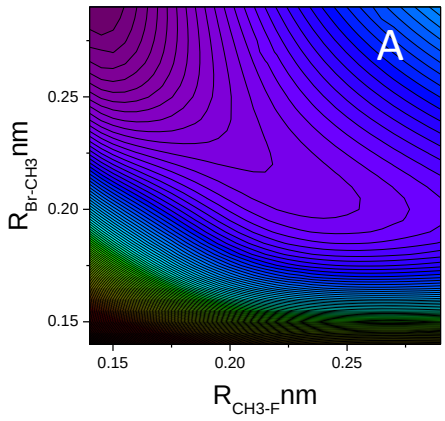

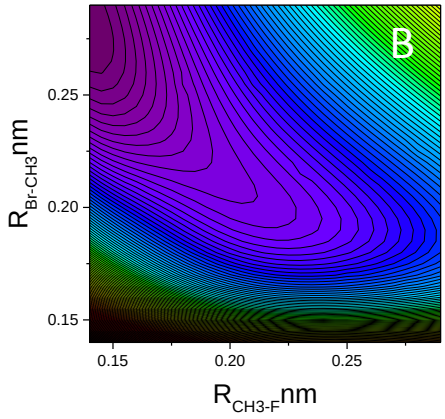

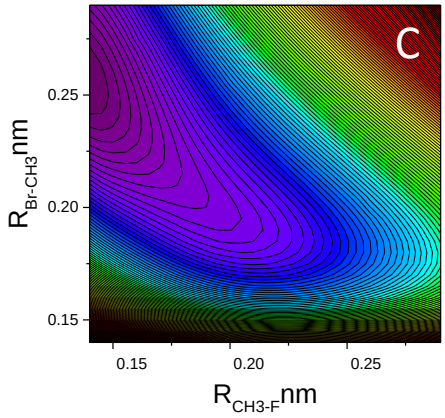

C.13 PES for Cl-CH_3-Br at low (A) medium (B) and high (C) compression. The contour spacing is 10 kJ/mol.

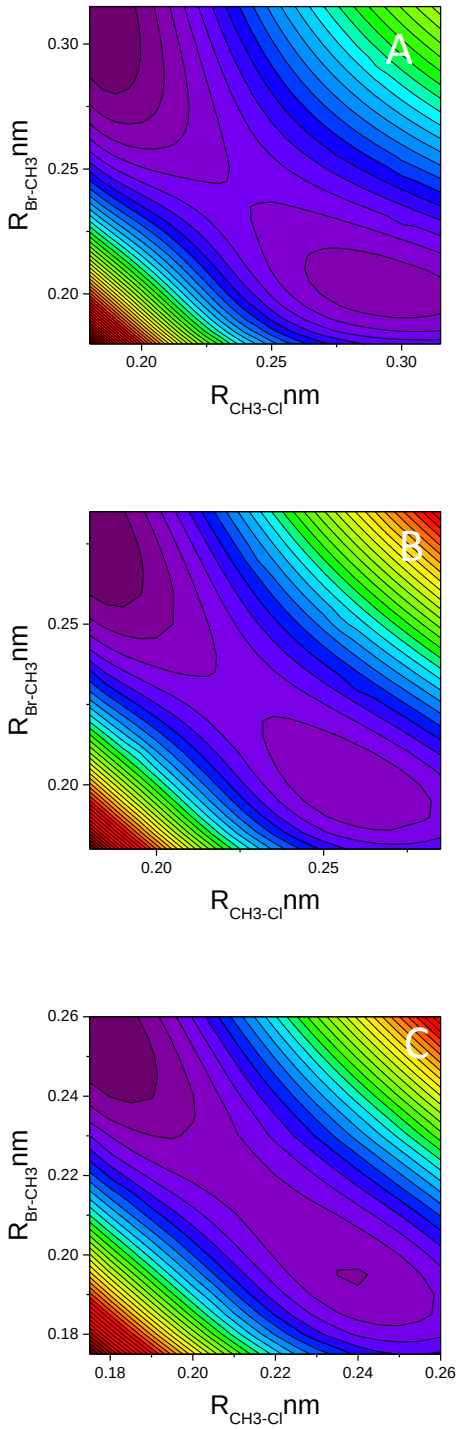

C.14 PES for Et-H-Et at low (A) medium (B) and high (C) compression. The contour spacing is 10 kJ/mol.

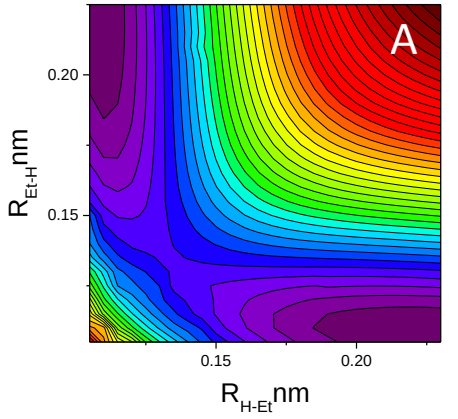

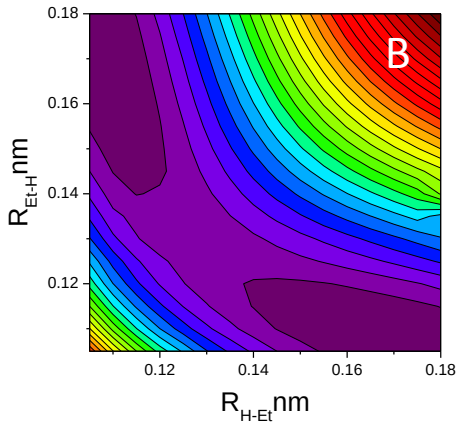

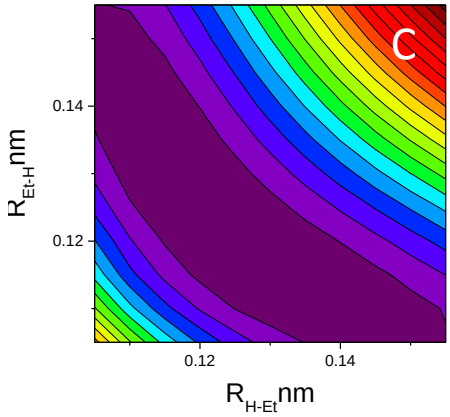

C.15 PES for Et-H-Me at low (A) medium (B) and high (C) compression. The contour spacing is 10 kJ/mol.

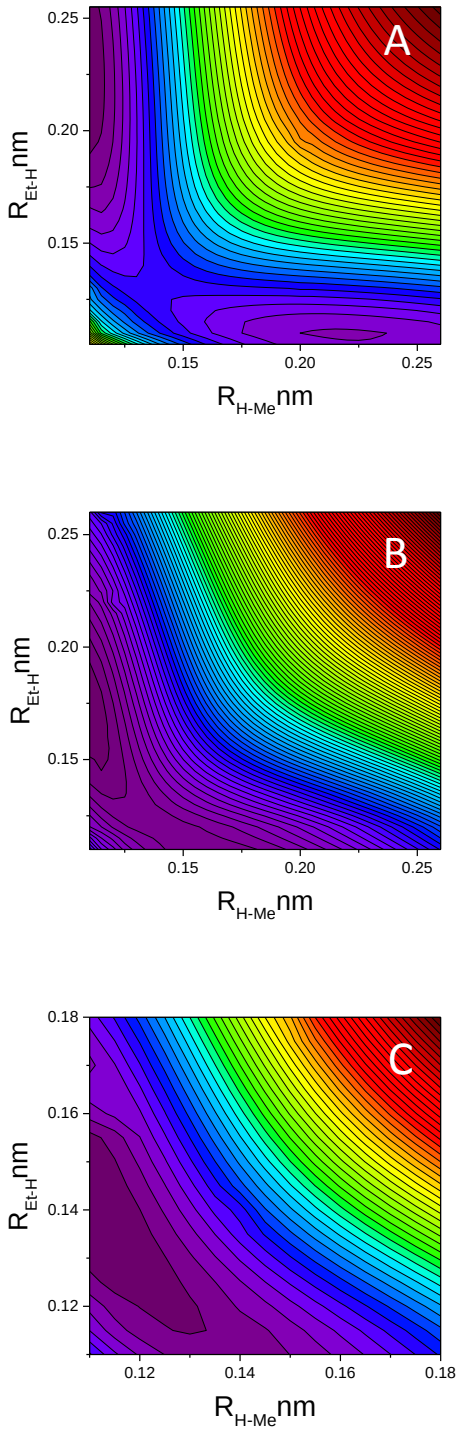

C.16 PES for Me-H-iPr at low (A) medium (B) and high (C) compression. The contour spacing is 10 kJ/mol.

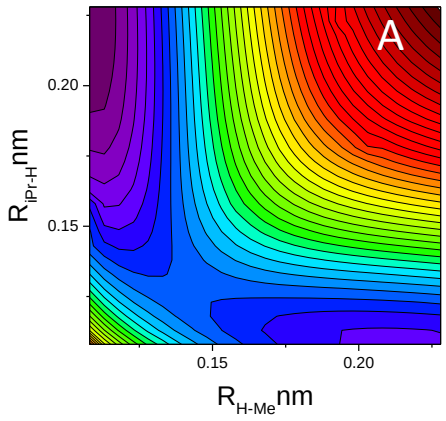

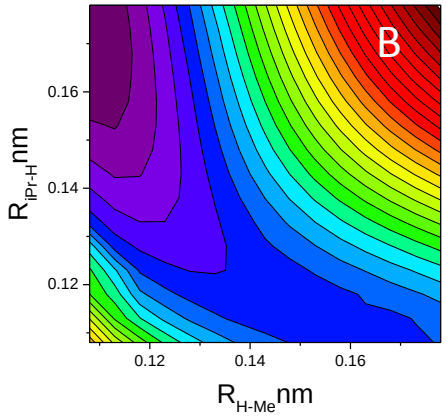

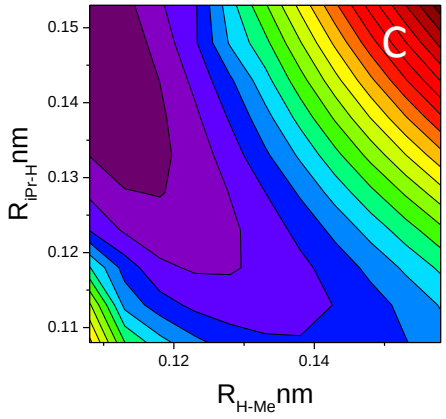

Appendix D.

PES for the F-H-F System Embedded in a 3D Ne Matrix.

D.1 PES for the FHF system at isotropic low (A) medium (B) and high (C) compression. The contour spacing is 10 kJ/mol.

Note the change in length scale between plots A-C.

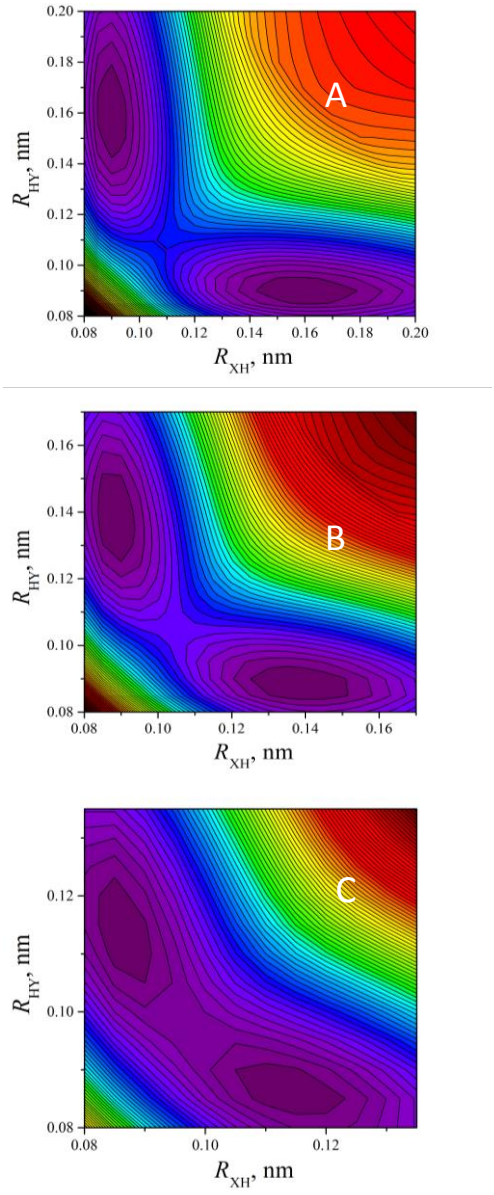

Appendix E.

Validity Thresholds and Parameter Constraints of equations E1-E11

Polynomial equations E1-E3. It follows from eqs. (1.9) and (1.10a) that in the case of polynomial equations E1-E3 conditions (5.3)-(5.5) take the form of eqs. (A1)-(A3)

$$\frac{\Delta V^{\neq}}{\Delta V_0^{\neq}} = 1 + \frac{2a_2}{a_1} P + \frac{3a_3}{a_1} P^2 \geq 0 \tag{A1}$$

$$\frac{\Delta \beta^{\neq}}{\Delta V_0^{\neq}} = \frac{2a_2}{a_1} + \frac{6a_3}{a_1} P < 0 \tag{A2}$$

$$\frac{\Delta \xi^{\neq}}{\Delta V_0^{\neq}} = \frac{6a_3}{a_1} > 0 \tag{A3}$$

Taken at $P = 0$, condition (A2) requires that

$$\frac{a_2}{a_1} < 0 \qquad \text{or} \qquad a_1 a_2 < 0 \tag{A4}$$

Equation E1 does not satisfy requirement (A3) and hence condition (5.5) since $a_3 = 0$. Condition (A2), and hence (5.4), are satisfied if requirement (A4) is imposed. If, in addition,

$$P \leq P_{\max} = -\frac{a_1}{2a_2} \tag{A5}$$

conditions (5.3) and (A1) are also satisfied

Similarly, (5.4)/(A2) and (5.5)/(A3) are inconsistent for equation E2 since $a_2 = 0$. However, condition (5.5) alone still can be satisfied, provided that

$$\frac{a_3}{a_1} < 0 \qquad \text{or} \qquad a_1 a_3 < 0 \tag{A6}$$

in which case eq. (A1) produces the pressure threshold

$$P \leq P_{\max} = \sqrt{-\frac{a_1}{3a_3}} \tag{A7}$$

within which conditions (5.3) and (A1) are also satisfied.

Finally, in the case of equation E3 conditions (A1)-(A3), and hence (5.3)-(5.5), are satisfied for

$$P \le P_{\max} = -\frac{a_2}{3a_3}\left(1-\sqrt{1-\frac{3a_1a_3}{a_2^2}}\right) \text{ if } \qquad 3a_1a_3 \le a_2^2$$

or (A8)

$$P \le P_{\max} = -\frac{a_2}{3a_3} \text{ if } \qquad 3a_1a_3 > a_2^2$$

Hyperbolic equations *E4-E5.* In the case of hyperbolic equations conditions (5.3)-(5.5) take the form of eqs. (A9)-(A11)

$$\frac{\Delta V^{\neq}}{\Delta V_0^{\neq}} = \frac{a_1(1+a_4P)^2 + a_3}{(a_1+a_3)(1+a_4P)^2} \ge 0 \tag{A9}$$

$$\frac{\Delta \beta^{\neq}}{\Delta V_0^{\neq}} = -\frac{2a_3a_4}{(a_1+a_3)(1+a_4P)^3} < 0 \tag{A10}$$

$$\frac{\Delta \xi^{\neq}}{\Delta V_0^{\neq}} = \frac{6a_3a_4^2}{(a_1+a_3)(1+a_4P)^3} > 0 \tag{A11}$$

which are satisfied for any pressure if $a_4 > 0$ and $a_1a_3 \ge 0$

Logarithmic equations *E6-E10.* In this case, conditions (5.3)-(5.5) take the form of eqs. (A12)-(A14)

$$\frac{\Delta V^{\neq}}{\Delta V_0^{\neq}} = \frac{a_1 + a_3\ln(1+a_4P)}{a_1+a_2a_4} + \frac{a_2a_4 + a_3a_4P}{(a_1+a_2a_4)(1+a_4P)} \ge 0 \tag{A12}$$

$$\frac{\Delta \beta^{\neq}}{\Delta V_0^{\neq}} = \frac{2a_3a_4 - a_2a_4^2 + a_3a_4^2P}{(a_1+a_2a_4)(1+a_4P)^2} < 0 \tag{A13}$$

$$\frac{\Delta \xi^{\neq}}{\Delta V_0^{\neq}} = \frac{-3a_3a_4^2 + 2a_2a_4^3 - a_3a_4^3P}{(a_1+a_2a_4)(1+a_4P)^3} > 0 \tag{A14}$$

It obvious from eq. (A12), that logarithmic equations have proper asymptotic behavior at infinite pressure only if $a_3 = 0$ (equations E6 and E7).

Since $1+a_4P>0$ and $a_4^2>0$, eqs. (A12)-(A14) reduce to

$$1+\frac{a_3}{a_1+a_2a_4}\left[\left(\frac{a_1}{a_3}+1\right)a_4P+(1+a_4P)\ln(1+a_4P)\right]\geq 0 \qquad \text{(A15)}$$

$$\frac{2a_3a_4-a_2a_4^2}{a_1+a_2a_4}+\frac{a_3}{a_1+a_2a_4}a_4^2P<0 \qquad \text{(A16)}$$

$$\frac{3a_3-2a_2a_4}{a_1+a_2a_4}+\frac{a_3}{a_1+a_2a_4}a_4P<0 \qquad \text{(A17)}$$

Taken at $P = 0$, eqs. (A16) and (A17) give the following constraints on parameters a_i:

$$\frac{2a_3a_4-a_2a_4^2}{a_1+a_2a_4}<0 \qquad \text{(A18)}$$

$$\frac{3a_3-2a_2a_4}{a_1+a_2a_4}<0 \qquad \text{(A19)}$$

which for $a_3 = 0$ (equations E6-E7) further reduce to

$$\frac{a_2a_4^2}{a_1+a_2a_4}>0 \quad \text{(A20)}$$

$$\frac{a_2a_4}{a_1+a_2a_4}>0 \quad \text{(A21)}$$

It follows from inequalities (A20)-(A21) that for E6-E7

$$a_4>0 \quad \text{and} \quad \frac{a_1}{a_2a_4}>-1 \qquad \text{(A22)}$$

With these constraints, conditions (A12)-(A14), and hence (5.3)-(5.5), are satisfied for the entire range of pressures.

Similarly, for $a_2 = 0$ (equation E8) inequalities (A18)-(A19) produce constraints

$$a_4>0 \quad \text{and} \quad a_1a_3<0 \qquad \text{(A23)}$$

which guarantee the validity of conditions (A13)-(A14) for all pressures. Condition (A12), although violated at sufficiently high pressures, is obeyed for pressures below the threshold P_{max} satisfying condition

$$\frac{a_1 + a_3 \ln\left(1 + a_4 P_{\max}\right)}{a_3} = -\frac{a_4 P_{\max}}{\left(1 + a_4 P_{\max}\right)} \tag{A24}$$

Again, for $a_3 = a_2 a_4$ (equation E9) eqs. (A18)-(A19) lead to

$$a_4 > 0\,, \quad \frac{a_1}{a_2 a_4} < -1\,, \quad \text{and} \quad a_1 a_2 < 0 \tag{A25}$$

With these constraints, conditions (A13)-(A14) are valid for the entire range of pressures and condition (A12) for

$$P \le P_{\max} = \frac{1}{a_4}\left[\exp\left(-\frac{a_1 + a_2 a_4}{a_2 a_4}\right) - 1\right] \tag{A26}$$

In the general case of equation E10 with four independent parameters, it is difficult to obtain individual constraints on these parameters. To simplify the analysis of this equation we will assume that $a_4 > 0$ as in all other cases of logarithmic equations. If, in addition,

$$\frac{a_3}{a_1 + a_2 a_4} < 0 \tag{A27}$$

then eq. (A18) follows from eq. (A19) and inequalities (A16)-(A17), and hence conditions (A13)-(A14), are satisfied for the entire range of pressures if eq. (A18) is obeyed.

If, on the other hand,

$$\frac{a_3}{a_1 + a_2 a_4} > 0 \tag{A28}$$

then eq. (A19) follows from eq. (A18), and inequalities (A16)-(A17) are satisfied for a limited range of pressures

$$P \le P_{\max} \le \frac{a_2}{a_3} - \frac{2}{a_4} \tag{A29}$$

if eq, (A19) is obeyed. Since $P_{\max} > 0$, it follows from eq. (A29) that

$$\frac{a_2 a_4}{a_3} > 2 \tag{A30}$$

Pseudo-logarithmic equation *E11.* For this equation conditions (5.3)-(5.5) take the form of eqs. (A31)-(A33)

$$\frac{\Delta V^{\neq}}{\Delta V_0^{\neq}} = 1 + \frac{a_2 a_4}{a_1} P^{a_4 - 1} \geq 0 \tag{A31}$$

$$\frac{\Delta \beta}{\Delta V_0^{\neq}} = \frac{a_2 a_4 (a_4 - 1)}{a_1} P^{a_4 - 2} < 0 \tag{A32}$$

$$\frac{\Delta \xi}{\Delta V_0^{\neq}} = \frac{a_2 a_4 (a_4 - 1)(a_4 - 2)}{a_1} P^{a_4 - 3} > 0 \tag{A33}$$

which result in the following set of constraints:

$$a_1 a_2 < 0 \quad \text{and} \quad 1 < a_4 < 2 \tag{A34}$$

Under these constraints, conditions (A32) and (A33) are satisfied for the entire range of pressures exceeding zero, and condition (A31) for

$$P \leq P_{\max} = \left(- \frac{a_1}{a_2 a_4} \right)^{\frac{1}{a_4 - 1}} \tag{A35}$$

Appendix F.

Inverse of Table 5.2.

Equation	a_1	a_2	a_3	a_4
E1	$-\alpha$	$-\beta/2$	0	0
E2	$-\alpha$	0	$-\gamma/6$	0
E3	$-\alpha$	$-\beta/2$	$-\gamma/6$	0
E4	0	0	$-\alpha$	$-\beta/2\alpha$
E5	$3\beta^2/2\gamma-\alpha$	0	$-3\beta^2/2\gamma$	$-\gamma/3\beta$
E6	0	$-\alpha^2/\beta$	0	$-\beta/\alpha$
E7	$-\alpha+2\beta^2/\gamma$	$4\beta^3/\gamma^2$	0	$-\gamma/2\beta$
E8	$-\alpha$	0	$3\beta^2/4\gamma$	$-2\gamma/3\beta$
E9	$-\alpha-\beta^2/\gamma$	$-\beta^3/\gamma^2$	0	$-\gamma/\beta$

Appendix G.

Explicit Expressions for Equations E4-E9 in their El'yanov-Gonikberg Format.

For consistency with eqs (1.9) function $\Phi(P)$ of eq (5.9) has to be presentable as

$$\Phi(P) = b_1 P + b_2 f(P) + b_3 P f(P) \qquad \text{(G1)}$$

where *f*(*P*) is described by eq (1.10) with nonlinear parameter a_4. Linear coefficients b_i of eq (G1) can be obtained from the corresponding coefficients a_i of eq (1.9) by scaling: $b_i = -a_i RT/\Delta V_0^{\neq}$. Condition $d\Phi/dP = 1$ at P = 0 translates into a constraint on b_i, specific forms of which for equations E4-E8 are listed in Table 5.2 together with their explicit expressions for these equations in El'yanov-Gonikberg format.

Table G1 Constraints on parameters b_i of function $\Phi(P)$ stipulated by the condition $d\Phi/dP = 1$ at P = 0 for empirical equations E4-E8 and their explicit expressions in El'yanov-Gonikberg form (eqs. 5.9 and G1).

	Constraints	Equations
E4	$b_3 = 1$	$\ln k/k_0 = \left(-\frac{\Delta V_0^{\neq}}{RT}\right) P/(1 + a_4 P)$
E5	$b_1 = 1 - b_3$	$\ln k/k_0 = \left(-\frac{\Delta V_0^{\neq}}{RT}\right)((1 - b_3) + b_3 P/(1 + a_4 P))$
E6	$b_2 = 1/a_4$	$\ln k/k_0 = \left(-\frac{\Delta V_0^{\neq}}{RT}\right)\left(\frac{\ln(1 + a_4 P)}{a_4}\right)$
E7	$b_1 = 1 - b_2 a_4$	$\ln k/k_0 = \left(-\frac{\Delta V_0^{\neq}}{RT}\right)((1 - b_2 a_4) P + b_2 \ln(1 + a_4 P))$
E8	$b_1 = 1$	$\ln k/k_0 = \left(-\frac{\Delta V_0^{\neq}}{RT}\right)(P + b_3 P \ln(1 + a_4 P))$

Appendix H.

Table of a_i Parameters of Equations E1-E11 Generated From Table 5.4.

Equation	Equation Coefficients†			
	a_1	a_2	a_3	a_4
E1	1.0084	-0.2017		
E2	1.0084		0.0504	
E3	1.0084	-0.2017	0.0504	
E4			1.0084	0.2000
E5	0.2017		0.8067	0.2500
E6		2.5211		0.4000
E7	-0.0672	2.8684		0.3750
E8	1.0084		-0.4034	0.5000
E9	1.5463	-0.7171		0.7500
E10	0.1580	2.1694	-0.0893	0.3920
E11	1.0084	-0.2000		

† Pressure in kbar; $\Delta V_0^{\neq}$ in cm^3mol^{-1}; $\Delta\beta_0^{\neq}$ in $cm^3mol^{-1}kbar^{-1}$; $\Delta\xi_0^{\neq}$ in $cm^3mol^{-1}kbar^{-2}$